

Durham E-Theses

Design and optimisation of THz and mm-wave components for communications

VANESSA JAYNE FENLON

How to cite:

FENLON, VANESSA JAYNE (2023) Design and optimisation of THz and mm-wave components for communications. Doctoral thesis, Durham University.

Use policy

The full-text may be used and/or reproduced, and given to third parties in any format or medium, without prior permission or charge, for personal research or study, educational, or not-for-profit purposes provided that:

- a full bibliographic reference is made to the original source
- a <https://etheses.durham.ac.uk/id/eprint/14933/> is made to the metadata record in Durham E-Theses
- the full-text is not changed in any way

The full-text must not be sold in any format or medium without the formal permission of the copyright holders.

Please consult the [full Durham E-Theses policy](#) for further details.

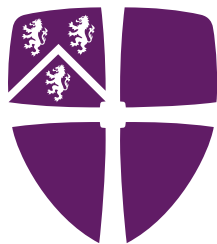
Design and optimisation of THz and mm-wave components for communications

Vanessa Jayne Fenlon

A Thesis submitted for the degree of Doctor of Philosophy

Department of Engineering

Durham University



Durham
University

Department of Engineering

Dedicated to

Granddad

xox

Abstract

This thesis proposes millimetre-wave (mm-wave) and terahertz (THz) components that can be used in highly integrated systems. These components have been designed for low cost and ease of manufacture using traditional manufacturing techniques, such as printed circuit board (PCB) printing and microlithography. The proposed frequency regions pose unique challenges, including high water-vapor attenuation [1] and the need for micro-scale components. This can limit the achievable power transfer, thereby lowering the signal-to-noise ratio (SNR) associated with components. Components have therefore been highly optimised for power efficiency to compensate for this.

A genetic algorithm (GA), Agenoria, written and revised by the author throughout this work, is presented that can optimise a variety of passive mm-wave and THz components. This uses pre-written FDTD software, Lucifer, which was previously designed in-house, to simulate component performance. A GA is chosen, as compared to other numerical methods, they are more likely to scale well to THz frequencies due to being able to optimise within many constraints at once. The challenge of manufacturing at the micrometre scale can be avoided by specifying constraints such as minimum feature size.

Agenoria is tested on a series of planar patch antennas with varying frequency responses. The first is a broadband antenna, optimised between 100 GHz and 5.0 THz, where 79% of the spectrum shows some improvement. The second antenna is optimised for a single peak at 1.0 THz. The evolved antenna's simulated power output is considerably higher than that of the reference case, with an improvement at 1 THz of 267%. The third antenna is a dual peak

antenna, with peaks optimised at 1.0 THz and 1.2 THz showing a 4,510% and 250% improvement on the reference case from the first generation.

One candidate antenna design, the broadband antenna, was then fabricated and experimentally verified, both in-house by the author. Due to the extremely broadband nature of the antenna, it was not possible to validate the simulated performance across the entire frequency range. Therefore, the verification was completed at a frequency band of 0.8 THz to 1.0 THz, within the optimised range. A vector network analyser (VNA) with two bidirectional VDI WR 1.0 frequency extenders with high-gain horn antennas operating between 0.75 THz and 1.10 THz was used for testing. The antenna transmission and angular dependence was measured and found to concur with simulated results for both the evolved antennas and a reference plain patch antenna. Feedline losses were investigated using the experimental set-up shown in Figure 61. The calculated loss of the microstrip line, connecting the antenna pairs, is 0.79 ± 0.06 dB/mm, which shows promisingly low losses. The combination of these antenna measurements verifies the simulation output within the region 0.8 THz to 1.0 THz. This provides strong evidence that the simulations would match experimental results across the entire simulated range.

In addition, a simple modulation platform for THz communications has been developed to be used in conjunction with WR1.0-VNAX frequency extenders. This consists of an on-off switching board, designed and simulated for a 12.3 GHz carrier wave, corresponding to the RF input of the extender modules, and a power detector board, designed for the LO output of the extenders. These components were designed using traditional techniques, such as transmission line theory, and optimised using Keysight Advanced Design System (ADS) Method of Moments (Momentum) electromagnetic simulator.

The power detector was successfully designed and fabricated in house. It was characterised, and a clear peak seen between 310 and 320 MHz, of 1.38 V at 314 MHz. This PCB was then used in the characterisation of the on-off keying capabilities of the VNA and extender heads. The switch was found to work best at 10 kHz but can modulate the VNA 12.3 GHz input at frequencies between 1 Hz and 1 MHz.

A series of frequency multipliers and mixers were also produced. The frequency multipliers were designed and simulated in the 10 to 30 GHz frequency range. Simulations consistently showed a strong third harmonic while others were successfully filtered by on-chip microstrip filters. However, the preliminary experimental results show a stronger effect of the filter output due to tolerances than had been predicted.

The frequency mixers were designed for two consecutive frequency ranges. The low frequency mixers, combining 2 GHz and 1.685 GHz signals, had a measured output power of -42.3 dBm at 0.315 GHz, where the mixer is optimised for. A mid-frequency mixer, designed to combine frequencies of 20 GHz and 18 GHz to produce a 2 GHz output signal, produced an output power of -45.8 dBm at the optimised frequency.

Table of Contents

Abstract.....	3
Table of Contents.....	6
List of Figures.....	10
Acknowledgements.....	10
Copyright.....	11
Publication List.....	12
Journal Papers.....	12
Conference Papers.....	12
Chapter 1: Introduction.....	13
1.1 Structure of Thesis.....	15
Chapter 2: Theory.....	17
2.1 Transmission Lines.....	17
2.1.1 Transmission Line Basics.....	18
2.1.2 Microstrip.....	20
2.1.3 Coplanar waveguide.....	22
2.2 Filters.....	24
2.2.1 Design Methodology.....	25
2.2.2 Stub Filter.....	26
2.2.3 Coupled Line Bandpass Filter.....	27
2.2.4 Coplanar waveguide filters.....	28
2.3. Multipliers.....	29
2.3.1 Passive Multipliers.....	29
2.3.2 Active Multipliers.....	31
2.4. Mixers.....	31
2.4.1 Mixer Overview.....	32
2.4.2 Single-ended Diode Mixer.....	33
2.4.3 Balanced Mixer.....	35
2.4.4 Double Balanced Mixer.....	36
2.5 Antennas.....	36

2.5.1 Antenna Basics	37
2.5.2 Dipole Antenna	39
2.5.3 Horn Antenna.....	41
2.5.4 Array Antenna.....	43
2.5.5 Microstrip/ Patch Antenna	44
2.6 Conclusion.....	45
Chapter 3: Numerical Methods	46
3.1 Finite Difference Time Domain	46
3.1.1 The Finite Difference Time Domain Method	47
3.1.2 Lucifer.....	48
3.2 Method of Moments.....	51
3.2.1 Matlab.....	52
3.2.2 Agilent Advanced Design System.....	52
3.3 Conclusion.....	53
Chapter 4: Measurement Techniques and Fabrication Methods	54
4.1 Measurement Techniques	54
4.1.1 Vector Network Analyser	56
4.1.2 Frequency Extenders.....	57
4.1.3 Calibration.....	58
4.1.4 Additional equipment	59
4.2 Fabrication Techniques	59
4.2.1 Lithography	60
4.2.2 Optical Lithography Limitations	61
4.2.3 Printed Circuit Boards	62
4.3 Conclusion.....	67
Chapter 5: Genetic Algorithms	68
5.1 Background	68
5.2 Introduction to Genetic Algorithms.....	70
5.2.1 Genetic Operators.....	73
5.2.2 Algorithm Termination.....	75
5.3 Agenesis	75
5.3.1 File Allocation.....	77
5.3.2 Initialisation.....	78
5.3.3 Genetic Operators.....	80

5.4 Conclusion.....	84
Chapter 6: Antenna Optimisation.....	85
6.1 Patch Antenna Principles	85
6.2 Application of Genetic Algorithm	87
6.3 Algorithm Examples	89
6.3.1 A broadband patch antenna optimized from 100 GHz to 5.00 THz.....	90
6.3.2 A single peak patch antenna optimized for at 1.00 THz	94
6.3.3 A dual peak patch antenna optimized for 1.00 THz and 1.20 THz.....	98
6.4 Conclusion.....	103
Chapter 7: Antenna Fabrication, Testing and Results	104
7.1 Antenna Fabrication.....	105
7.1.1 Fabrication Process	106
7.1.3 Fabricated Antenna.....	107
7.2 Antenna and Feedline Characterisation	109
7.2.1 Experimental configuration	109
7.2.2 Antenna Transmission.....	111
7.2.3 Feedline losses	112
7.3 Radiation Pattern	114
7.3.1 Experimental Configuration	114
7.3.2 Comparison of Simulated and Experimental Measured Angular Dependence	116
7.4 Calibration.....	117
7.5 Conclusion.....	118
7.5.1 Experimental Adjustments.....	119
Chapter 8: On-Off Modulation.....	122
8.1 Concept.....	122
8.2 RMS Detector	124
8.3 On-Off Modulator	126
8.3.1 On-Off Modulator Design	126
8.3.2 Simulation	128
8.3.3 Fabrication	129
8.3.4 On-Off Modulator Characterisation.....	130
8.3.5 Extender head modulation	131
8.4 Conclusion.....	132
Chapter 9: Frequency Multipliers	134

9.1 Experimental Procedure	135
9.2 Multiplier Design.....	136
9.3 Diodes	138
9.4 Filters.....	142
9.4.1 Filter A.....	143
9.4.2 Filter B	145
9.5 Conclusion.....	149
Chapter 10: Frequency Mixers.....	150
10.1 Design.....	151
10.1.1 Rat Race Mixer	152
10.1.2 Simulation and Optimisation	153
10.1.3 Fabrication	153
10.1.4 Experimental Procedure	153
10.2 2 GHz Mixer.....	154
10.2.1: On FR4 Substrate	154
10.2.2 On RT/Duroid 5870 Substrate.....	159
10.3 20 GHz Mixer.....	162
10.4 Conclusion.....	165
Chapter 11: Conclusions and Further Work	167
11.1 Conclusions	167
11.2 Further Work.....	169
Appendices.....	171
Appendix 1: Increasing frequency range of Matlab Antenna Toolbox.....	171
Appendix 2: Fabrication procedure for terahertz antennas.....	171
Bibliography	173

List of Figures

Acknowledgements

I would like to start by thanking my supervisors, Claudio Balocco and Andrew Gallant. I don't think I've yet found a question Claudio couldn't answer, and his explanations and accompanying diagrams have been invaluable to my knowledge of post-5G communications and to this thesis. However, this project would not have stayed on track without Andrew, especially keeping us going through the endless lockdowns, and checking in to make sure I was enduring!

Thank you to Jim and the team at Viper RF for both your financial contribution and your industrial expertise. My thanks also go to Sana Salous for allowing me the use of her communications laboratory for frequency multiplier testing. And thank you to Saied El-faitori and Mohamed Abdulali for putting aside your time to help with my experiment.

I would also like to thank Mike Cooke, our experimental officer, who made endless amounts of time for my questions on fabrication, and who taught me everything I could want to know about working in a clean room. To this end, I would also like to thank Iman Frozanpoor and Alejandro Galan Gonzalez who always had a spare pair of hands when I needed them and made my time in the office so much more enjoyable.

Ian Hutchinson, Ian Garrett, and the entire electronics workshop have been extraordinary helpful in fabricating the PCBs seen in this thesis and the tea breaks spent in the workshop certainly made lockdown working a lot more fun. However, Neil Clarey deserves the largest thanks of all. The few final results shown here could never begin to encompass the number of hours he put into fabricating tiny structures, and soldering components he could barely see!

Copyright

The copyright of this thesis rests with the author. No quotation from it should be published without the author's prior written consent and information derived from it should be acknowledged.

Publication List

Journal Papers

V.J. Fenlon, M. Cooke, J. Mayock, A.J. Gallant and C. Balocco “Genetic Algorithms for the Design of Planar THz Antenna” *Journal of Applied Physics*. vol. 132, no. 16, 2022. [Featured].

Conference Papers

The work in this thesis has featured in the following publications:

V.J. Fenlon, M. Cooke, J. Mayock, A.J. Gallant and C. Balocco “Verification of THz genetic algorithm using a VNA” 2021 46th International Conference on Infrared, Millimeter and Terahertz Waves (IRMMW-THz), IEEE, 2021.

V.J. Fenlon, M. Cooke, A.J. Gallant and C. Balocco “Genetic Algorithms for the Design of THz Components” 2020 45th International Conference on Infrared, Millimeter, and Terahertz Waves (IRMMW-THz), IEEE, 2020.

J. McCubbin, V.J. Fenlon and C. Balocco “Impedance Matching Networks Designed by Evolutionary Algorithms” 2019 44th International Conference on Infrared, Millimeter, and Terahertz Waves (IRMMW-THz), IEEE, 2019.

V.J. Fenlon, R. Lees, P.S. Stefanova, A.K. Klein, A.J. Gallant and C. Balocco “Evolutionary Optimisation of THz components” 2018 43rd International Conference on Infrared, Millimeter, and Terahertz Waves (IRMMW-THz), IEEE, 2018.

Chapter 1: Introduction

Globally, there is a clear increase in mobile network data traffic, which has doubled in the past two years alone. The increase is visible in our day to day lives, from our home devices being connected to the internet of things, to the increase in smart phone usage and the digitalisation of industries [2]. As the number of connected devices increases, the amount of available spectrum is decreasing. Spectrum scarcity is causing communications engineers to branch into previously unexplored regions of the spectrum, such as terahertz (0.1 to 10 THz [3]) and mm-wave (0.03 to 0.3 THz). In the UK, the roll out of 5G is already well underway, which while currently focused on the 700 MHz and 3.6 GHz to 2.8 GHz bands, the UK regulator Ofcom has begun a consultation to make mm-wave spectrum in the 26 GHz and 40 GHz bands available for 5G communications by 2024 [4].

The Ericsson 2022 mobility report states *“5G is scaling faster than any previous mobile generation and we expect 5G subscriptions to reach 1 billion by the end of 2022”* [2]. However, this part of the spectrum has limited bandwidth and so research into mm-wave and terahertz communications circuits is ongoing. Components in the unlicensed wireless band at 60 GHz are being investigated, with approximately 7 GHz of bandwidth available [5]. However, it is expected that data rates above 100 Gbps will be achieved by using frequencies above 100 GHz [6]. Therefore, the THz gap is increasingly being scouted for 6G potential [7], with speeds of up to 46 Gbps already demonstrated for wireless communications at 0.4 THz.

The mm-wave and THz frequency ranges pose unique challenges, including high water-vapor attenuation [1] and the need for micro-scale components, which can limit the achievable power transfer. There is also larger noise associated with components and larger path loss due to the shorter wavelengths [8]. Components therefore need to be highly optimised for power efficiency to compensate for this. Additionally, this frequency band lies at the transition between lower frequencies used for electronics and higher frequencies for optics. To adapt current electronic components, they must be downsized to micrometre dimensions, greatly complicating fabricating procedures. Alternatively, by adjusting photonic components to lower frequencies, the energy required for electron transition decreases below that caused by external thermal fluctuations. Therefore, transitions due to optical input are impossible to detect unless the components are cooled to cryogenic temperatures [9].

Viable methods to breach the terahertz gap include direct signal generation at these frequencies [9]. Sources include backward wave oscillators, laser sources and gyrotrons. However, these are all bulky and either require vacuum generation or constant cooling. One option to enter the terahertz gap is to use non-linear electronic components. These are most commonly diodes and can be used in frequency mixers or multipliers to generate harmonics that can be isolated via filtering [9]. These have been used, for example, in heterodyne receivers inside the Atacama Large Millimetre Array to downconvert THz emissions from space to analysable frequencies [10].

More recently, mm-wave and terahertz research has moved into integrated circuit development [9] which is incredibly useful for small, hand-held communications devices. Passive circuit elements, such as filters and impedance matching networks can be combined on chip with multipliers, mixers and antennas, which massively reduces wired transmission distances and therefore internal power losses. In addition, all components are pre-aligned, with less external connections, therefore reliability and repeatability are improved [9].

This thesis proposes mm-wave and terahertz components that can be used in small hand-held devices, fabricated using traditional microfabrication techniques and can be easily integrated with other components. The optimisation techniques built into Keysight ADS (Advanced Design Software) [11] and a genetic algorithm are employed for the purpose of designing these components.

1.1 Structure of Thesis

Chapter 2 presents the theory underpinning the work in this thesis. First the history and basics of transmission lines and waveguides are covered, followed by filters and their design methodology. Then, mixers and multipliers and their respective history and operating principles are presented. The final section covers antenna theory. This chapter gives an overview of each of the components that appear in detail in the thesis.

Chapter 3 presents the numerical methods and software used in this thesis. These are the finite difference time domain (FDTD) method, as used in Lucifer, and the method of moments (MOM), as used in Matlab and Keysight ADS (Advanced Design Software).

Chapter 4 is an overview of the techniques employed for experimental work in this thesis. This chapter can be split into two principal topics: measurement techniques, and fabrication methods. Experimental work at post-5G frequencies requires state-of-the-art equipment and processes, as devices are increasingly miniaturised and require high-rate analysis tools. The techniques outlined in this chapter are used throughout the thesis and are not particular to any one experiment.

Chapter 5 introduces the concept of a genetic algorithm (GA), and presents Agenoria, a GA developed for the purpose of optimising electromagnetic components without requiring prior in-depth knowledge of their operating procedure.

Chapter 6 presents the optimisation of antennas using a GA. The antennas presented here are planar patch antennas. Conventionally, the patch is continuous, but this limits the performance of the antenna to narrow-band operation. By creating apertures in the patch, the antenna bandwidth can be extended, and its impedance tailored. This technique has been used before, such as by Islam [12]. This section investigates the viability in using genetic algorithms to design the location of these apertures.

Chapter 7: presents the validation of Agenoria, a GA introduced in Chapter 5, by experimentally verifying the simulation results of an evolved antenna. In this chapter, the fabrication method, experimental configuration, and results are also presented. The antenna

is a broadband patch antenna, optimised from 0.1 GHz to 5.0 GHz, as presented in Chapter 6.4.1.

In Chapter 8 an on-off modulator design is presented with accompanying simulations for a 12.3 GHz carrier wave. This has been fabricated and tested both alone and in conjunction with a mm-wave VNA and terahertz frequency extenders. A PCB power detector is also presented in this chapter, for the analysis of the output of the modulator.

Chapter 9 reports on the viability of using diodes as a non-linear component to produce a passive diode tripler. This chapter describes the design, optimisation and experimental verification of the multipliers. First, the experimental procedure is outlined. Then the anti-parallel diode tripler is described. A combination of three filter designs and three diode types are fabricated for a total of nine multipliers. Finally, the simulation and experimental results of these nine boards are presented.

Chapter 10 describes the design, fabrication, and testing of a system used to downconvert between 20 GHz and 315 MHz. This is split between two planar balanced mixers. The first has inputs 20 GHz and 18 GHz and will be filtered for an output of 2 GHz. The second has inputs 2 GHz and 1.685 GHz and will be filtered at 315 MHz.

Chapter 11 presents the conclusions and further work of the thesis.

Chapter 2: Theory

This chapter first covers the history and basics of transmission lines. These form the basis from which all circuits are designed, and underpin the results presented in this thesis. The theory of microstrip transmission lines and coplanar waveguides is also presented.

The second section of this chapter introduces filters and their design methodology. Three filter types are covered in detail; these are stub, coupled line bandpass and coplanar waveguide filters. Multipliers and their theory are then introduced. This section is split into passive and active multipliers. However, only passive multiplier designs are featured in this thesis and therefore more attention is given to these.

The fourth section covers the theory of mixers. Specifically focusing on single ended, balanced and double-balanced mixers. This final mixer type is the forerunner to the rat-race mixer featured in Chapter 10. The final theory section is that of antennas. A brief overview of dipole, horn, array and microstrip antennas is covered. The theory covered here is intended to give background to the antenna designs shown in Chapters 5-7.

2.1 Transmission Lines

Early RF systems mostly utilise three types of structure: waveguides, parallel or two-wire lines, and coaxial lines. Waveguides can have low losses, high power transfer and complete shielding, but are often bulky and expensive to manufacture at lower frequencies. Parallel

lines are cheap to manufacture but provide no shielding. Alternatively, coaxial lines are shielded, so experience lower losses per electrical length. However, both parallel and coaxial lines are unsuitable for the aggressive integration required by modern systems [13].

The flat-strip coaxial transmission line was designed by V. H. Rumsey and H. W. Jamieson during World War II for a production antenna system as a power division network, which was published by the Combined Research Group NRL during this time [14]. Microstrip lines were developed later, in the early 1950s by ITI laboratories [15] and have become an often-preferred medium for microwave integrated circuits [16].

Planar transmission lines, such as coplanar waveguides and microstrip lines, provide a good alternative to these traditional structures, which can experience high losses at THz frequencies. Planar lines allow for very compact systems as they can be manufactured directly on a substrate with other components and easily integrated with external devices. In addition, coplanar waveguides and microstrip lines are both open structures, and so can be easily manufactured with microlithography techniques.

2.1.1 Transmission Line Basics

A transmission line is a structure designed to guide electromagnetic waves, ideally with as little loss as possible. They are most seen in the power lines in our towns and cities and common types include ladder line, twisted pair and coaxial cable. In traditional circuit theory, signals are assumed to be quasi-static, which enables a description of circuits based on voltages and currents independent of each other. When the wavelength of the signal involved is of the same order of magnitude of the physical circuit, this theory is no longer sufficient.

Transmission line theory is an extension of circuit theory and is usually considered when the dimensions of the system are comparable to a quarter wavelength. This was originally considered for long range communications, but as the wavelengths used for communications have gotten shorter, transmission between local equipment must be considered.

The transmission line model represents a real line in terms of an infinite series of two-port components, such as seen in Figure 1. The resistance per unit length, R , models the Ohmic losses in the conductor (which also accounts for the skin effect); L is the inductance per unit

length; the conductance per unit length, G , models losses in the dielectric; and C is the capacitance per unit length.

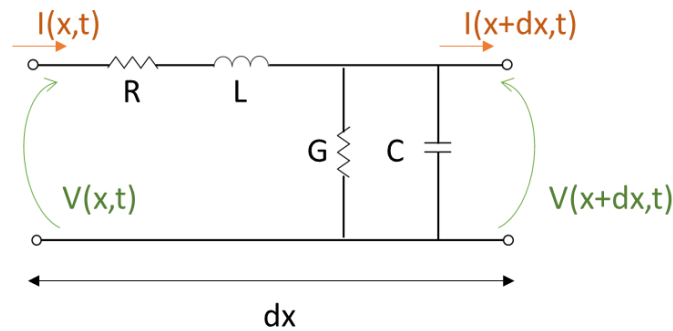


Figure 1: Transmission parameters for an infinitesimally small section of transmission line. This model is used to outline the Telegrapher's equations. $I(x)$ and $V(x)$ are the current and voltage at position x along the line, the parameters, R , L , G and C allow the calculation of $I(x+dx)$ and $V(x+dx)$ which are the current and voltages displaced dx from position x .

Assuming the system is linear, and the signals are sinusoidal with angular frequency ω , Heaviside's Telegrapher's equations can be used to describe the Voltage and Current across a transmission line, in terms of distance and time [17],

$$\frac{\partial V(x)}{\partial x} = -(R + j\omega L)I(x) \quad (2.1)$$

$$\frac{\partial I(x)}{\partial x} = -(G + j\omega C)V(x) \quad (2.2)$$

where the harmonic component $e^{i\omega t}$ is an implicit component of $I(x)$ and $V(x)$. This allows the calculation of the voltage and currents in the transmission line to be calculated for any given distance. The imaginary part of the calculation (either $\omega LI(x)$ or $\omega CV(x)$) are dependent on the frequency ω of the transmission, and therefore can consider systems where the dimensions are comparable to the propagation wavelength.

For the mm-wave and sub-mm systems considered in this thesis, the wavelength is in the centimetre region, and so even transmission across a PCB must be analysed using transmission line theory. There are three basic ways that an electromagnetic wave can propagate along a transmission line. These are described by the relative direction of the electric and magnetic vectors to the direction of propagation:

TE (transverse electric) mode: The electric field vector is always perpendicular to the direction of propagation.

TM (transverse magnetic) mode: The magnetic field vector is always perpendicular to the direction of propagation.

TEM (transverse electromagnetic) mode: Both the electric and magnetic field vectors are perpendicular to the direction of propagation. These can only be supported in transmission lines that consist of two or more conductors.

2.1.2 Microstrip

A microstrip is a commonly used planar transmission line configuration, due to being easy to integrate with other devices; simple to fabricate with standard fabrication techniques such as PCB printing and photolithography; and finally, easily miniaturised, which also makes it highly adaptable to post-5G frequencies.

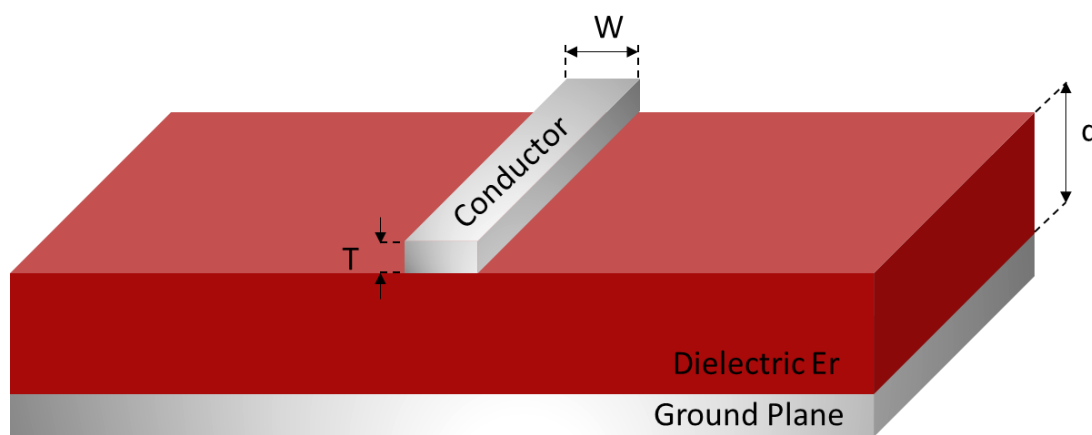


Figure 2: Diagram of a microstrip transmission line, showing conductor (thickness ' T ', width ' W '), dielectric substrate (depth ' d '), and ground plane.

A microstrip line consists of a rectangular metal waveguide, on top of a grounded dielectric substrate. One disadvantage of microstrip lines is the ground plane is located underneath the dielectric. This means shunt connection of circuit components can be difficult and makes waveguide parameters dependant on a non-variable substrate thickness [18].

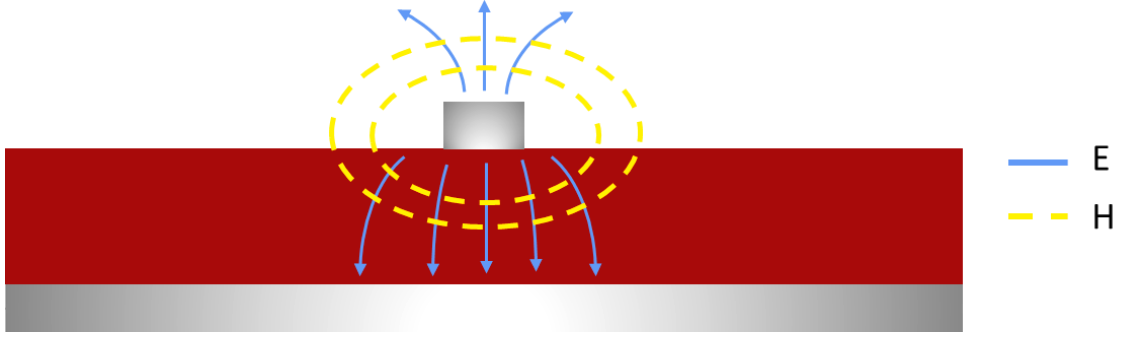


Figure 3: Diagram of the Electric, E , and Magnetic, H , fields of a microstrip transmission line.

If the dielectric material is air, the microstrip would act as a simple TEM transmission line. However, by introducing a material with non-unity dielectric constant, there is a difference in dielectric constant above and below the conductor. As shown in Figure 3, the microstrip induces electric and magnetic fields in both regions. Due to the difference in dielectric constant, the electric fields above and below the conductor have different phase velocity, and therefore cannot support a pure TEM mode. However, if most of the electric field is confined in the dielectric, then the transmission mode can be described as quasi-TEM. This implies the fields acts closely enough to those in the static (phase matched) case. Therefore, it is easy to approximate phase velocity, propagation constant and characteristic impedance. Additionally, the dimensions the microstrip are much smaller than the wavelength, to ensure multiple modes are not present in the dielectric [13].

The characteristic impedance, Z_0 , of a given microstrip transmission line is [13],

$$Z_0 = \begin{cases} \frac{60}{\sqrt{\epsilon_e}} \ln \left(\frac{8d}{W} + \frac{W}{4d} \right) & \text{for } \frac{W}{d} \leq 1 \\ \frac{120\pi}{\sqrt{\epsilon_e} \left[W/d + 1.393 + 0.667 \ln \left(W/d + 1.444 \right) \right]} & \text{for } \frac{W}{d} \geq 1 \end{cases} \quad (2.3)$$

Where W and d are the width and depth dimensions respectively, as shown in Figure 2. The effective permittivity, ϵ_e , is the dielectric constant of an equivalent homogenous medium to the air and dielectric filled regions. For a microstrip, this can be defined as [13],

$$\epsilon_e = \frac{\epsilon_r + 1}{2} + \frac{\epsilon_r - 1}{2} \left(\frac{1}{\sqrt{1 + 12d/W}} \right) \quad (2.4)$$

Where ϵ_r is the relative permittivity of the substrate, which is frequency dependant and must be measured, rather than calculated, for the frequency of operation.

The propagation velocity can be described as [13],

$$v_p = \frac{c}{\sqrt{\epsilon_e}} \quad (2.5)$$

where c is the speed of light. The equations for characteristic impedance and phase velocity can be rearranged to provide a useful first approximation of microstrip line dimensions. This provides a basis from which to optimise in simulation.

2.1.3 Coplanar waveguide

Coplanar waveguides are used for fabricating complicated, often active, circuitry. The centre conductor and ground planes are in close proximity, as shown in Figure 4, which makes it easy to fabricate components with access to both.

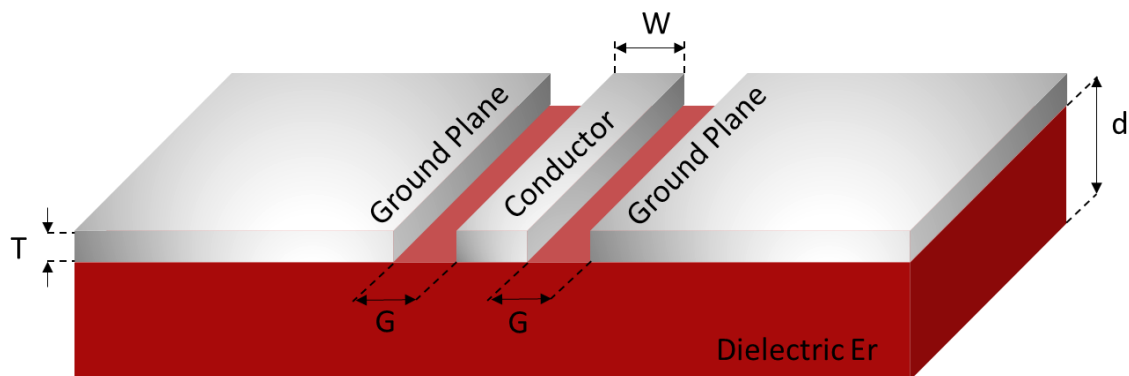


Figure 4: Diagram of a coplanar waveguide, showing conductor (width ' w ') at gap (' g ') from surrounding ground plane (with thickness ' T ') and dielectric substrate (depth ' d ').

Due to the planar nature of the structure, the width between the ground plane and transmission line can be easily varied. This means coplanar waveguide parameters are not sensitive functions of substrate thickness. For example, the ratio of the width, W , to the gap, G , controls the characteristic impedance [18].

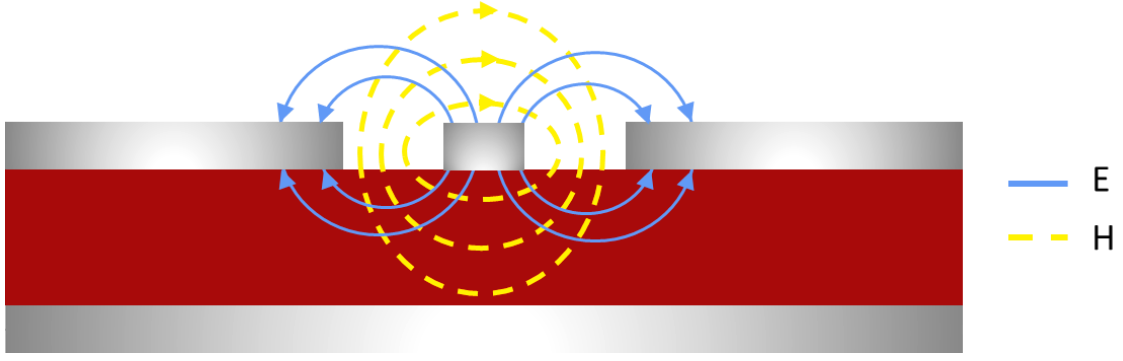


Figure 5: Diagram of the Electric, E, and Magnetic, H, fields of a coplanar waveguide.

As in the case of the microstrip line, the coplanar waveguide also acts in quasi-TEM mode. The electric fields are aligned from the conductor towards the ground planes, and the magnetic fields are in closed loops around the conductor. This means the propagation velocity can be defined, as in the microstrip case, by equation 2.5. The effective dielectric constant for a coplanar waveguide, ϵ_e is given by [19],

$$\epsilon_e = \frac{\epsilon_r + 1}{2} \quad (2.6)$$

where ϵ_r is the relative permittivity of the substrate.

The characteristic impedance of the coplanar waveguide is [19],

$$Z_c = \begin{cases} \frac{Z_0}{4\sqrt{\epsilon'_r}} \left(\frac{1}{\pi} \ln \left(2 \frac{1 + \sqrt{k}}{1 - \sqrt{k}} \right) \right) & \text{for } 0.7 \leq k < 1 \\ \frac{Z_0}{4\sqrt{\epsilon'_r}} \left(\frac{1}{\pi} \ln \left(2 \frac{1 + \sqrt{k}}{1 - \sqrt{k}} \right) \right)^{-1} & \text{for } 0 \leq k < 0.7 \end{cases} \quad (2.7)$$

where [19],

$$k = \frac{1}{\cosh \left(\frac{\pi W}{4d} \right)} \quad (2.8)$$

where W and d are the width and depth dimensions respectively, as shown in Figure 4.

2.2 Filters

Filters are a 2-port network with a controlled frequency response. They provide transmission in required frequency regions and attenuation otherwise. Common types are high-pass, low-pass, band-stop and band-pass. High-pass and low-pass filters respectively transmit all frequencies above or below a specific cut-off frequency. Band-stop filters attenuate all frequencies within a specified frequency region, and for band-pass the opposite is true. These are a feature of most RF systems as they greatly reduce wasted energy in transmission and allow ease of received signal processing [20].

RF filters first became of interest in the late 19th Century when long-distance transmission lines for telegraphy and telephony were causing high levels of signal damping. Pupin's work in 1899 [21], optimising intervals between lengths of coil spaced along transmission cables, was the first to show substantial reduction in damping, and therefore was the first successful introduction of an RF filter [20].

Pupin's work was expanded by Reed [22] to express the transmission line in terms of characteristic impedances. This is a first-order approximation that assumes the filter is terminated by its characteristic impedance at all frequencies, and this does not vary with frequency. This gives the assumption that there is no damping (apart from parasitic losses) at the pass band. Reed's method was called "*image-parameter theory*" by Sidney Darlington [23] and used in low frequency filters in radio and telephony. However, complex filter characteristics are achieved by combining basic filters together. Therefore, this technique cannot optimise simultaneously over the complete operating range. This makes for a slow optimisation as can require repeated iterations to achieve the desired frequency response [13].

Butterworth was the first to deviate from image-parameter theory and use transfer functions to design filters [24]. This technique was adapted by Darlington, who published his 'insertion-loss theory' in 1939, which made it possible to accurately design the transfer function of the filter [23]. This simplifies the approach by starting with known low-pass-filters with normalised impedance and frequency. Most usually, a 1Ω input impedance with a cut-off frequency of $\omega c = 1$ rad/sec. The approach uses transformations to scale the known filters to the desired impedance and frequency [13] and is fully described in Matthaei [25].

Most filters today are designed using CAD packages, based on the insertion-loss method. However, because of introduction of new materials and the incorporation of active devices in filter circuits, microwave filter design is still an active research area.

2.2.1 Design Methodology

At microwave frequencies, the size of circuit components becomes significant compared to the wavelength, and the purchasing of miniaturised, high frequency components can be costly (if at all possible, with the desired characteristics). One alternative to traditional components (resistors, capacitors and inductors) is to use distributed elements. These are sections of transmission line, with their length in the order of magnitude of the wavelength of the filter such that have the properties of lumped components. Common examples of these are open-circuited or short-circuited transmission line stubs. At microwave frequencies, the wavelength is in the order of a few cm, meaning these equivalent components can be made to fit onto a PCB.

Richard's transformation can be used to convert lumped elements into distributed elements [26]:

$$\Omega = \tan(\beta l) = \tan\left(\frac{\omega l}{v_p}\right) \quad (2.9)$$

This equation maps between the frequency planes ω and Ω . β is the imaginary part of the propagation factor (otherwise known as the phase constant), l is length of line and v_p is the phase velocity.

The description of the reactance of an inductor, X_L , can be rewritten in terms of Ω using Richard's conversion [26].

$$jX_L = j\Omega Z_0 = jZ_0 \tan \beta l \quad (2.10)$$

where Z_0 is the characteristic impedance of the transmission line [26],

$$Z_0 = \sqrt{\frac{L}{C}} = \frac{1}{Y_0} \quad (2.11)$$

where L and C respectively are the inductance and capacitance per unit length and Y_0 is the characteristic admittance of the transmission line.

The susceptance of a capacitor, B_C , can also be rewritten in terms of Ω [26].

$$jB_C = j\Omega Y_0 = jY_0 \tan \beta l \quad (2.12)$$

From equations 2.10 and 2.12, it can be concluded that, assuming unity filter impedance, an inductor can be replaced with a short-circuited stub with length βl and characteristic impedance L , and a capacitor can be replaced with an open-circuited stub of length βL . And characteristic impedance $1/C$ [13].

2.2.2 Stub Filter

Coupled line filters are microstrip transmission lines with short or open-circuited stubs perpendicular to the direction of transmission. The stubs are a multiple of $\lambda/4$ of the frequencies that require attenuation, so each open stub attenuates a wavelength that is four times its length, this is because the total travelled length is $\lambda/2$, and so the returning wave is out of phase with the main path. This is the opposite for a grounded stub as this produces a $\lambda/2$ reflection at the end of the stub, meaning the returning wave is in phase. The stubs are placed a quarter wavelength apart and depending on whether they are grounded or not, gives the behaviour of a parallel or series circuit, respectively.

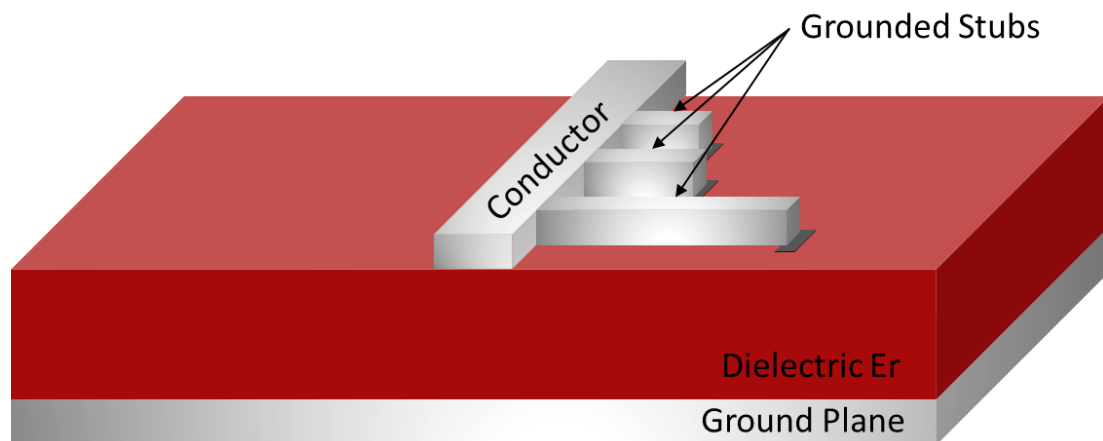


Figure 6: Diagram of a microstrip stub filter, showing grounded stubs, conductor and grounded dielectric substrate. The filtered wavelengths are a quarter of the stub length.

An improvement on the standard rectangular stub filter is the radial stub filter, as shown in Figure 7.

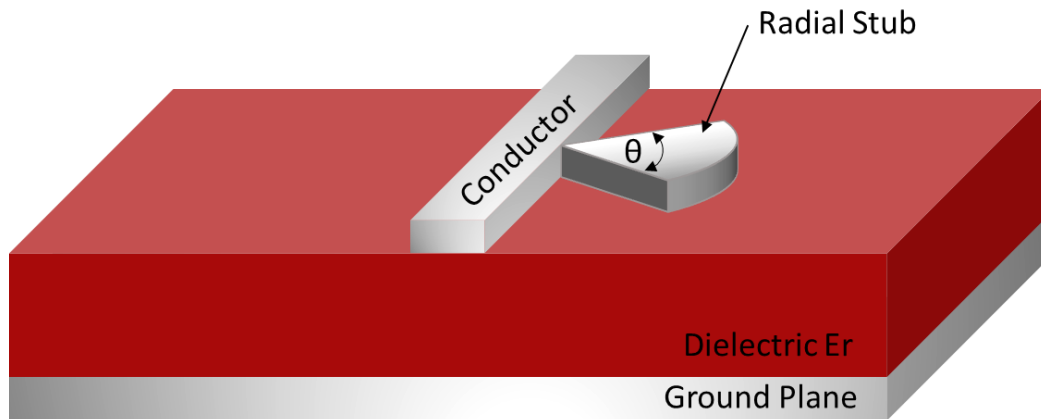


Figure 7: Diagram of a radial microstrip stub filter, showing radial stub, conductor and grounded dielectric substrate. The radial nature gives a broadband wavelength attenuation.

The key advantage of the radial stub is the increased bandwidth of the stopband, due to the collection of wavelengths accounted for in the varying width stub, due to the varying impedance along its length. The outer radius of the stub determines the attenuation frequency and the angle, θ , affects the bandwidth. Another improvement over the rectangular stub filter, is that the radial stub is connected at a concentrated point. This accurately defines the location of the short circuit and is useful when predicting circuit characteristics or combining multiple filters [27].

2.2.3 Coupled Line Bandpass Filter

Coupled line bandpass filters can be fabricated as part of a microstrip line. As shown in Figure 8, they consist of cascaded line segments with a long section of transmission line between consecutive filter sections. Small gaps between neighbouring transmission line sections allow only a narrowband of frequencies to pass. This leads to a highly selective narrowband filter. However, precise manufacturing of the gap size is required to provide an accurately tuned frequency response.

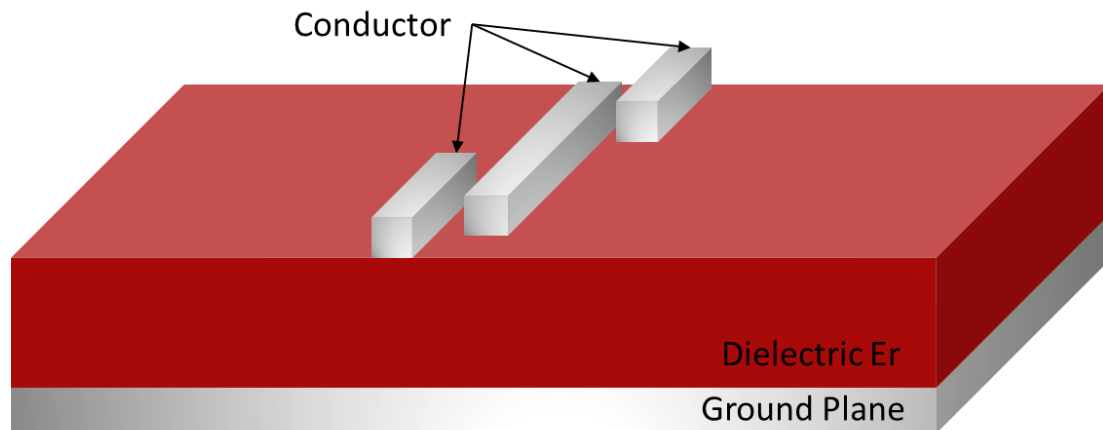


Figure 8: Diagram of a coupled line bandpass filter, showing a cascaded transmission line and grounded dielectric substrate. This has a narrowband response, with non-attenuated wavelengths proportional to the gap between conducting strips.

2.2.4 Coplanar waveguide filters

Coplanar waveguides are simple to integrate with filter structures as they are planar, making it easy to connect circuit elements in series or shunt configurations. Figure 3 outlines a gap-coupled resonator as presented by Matthaei [25].

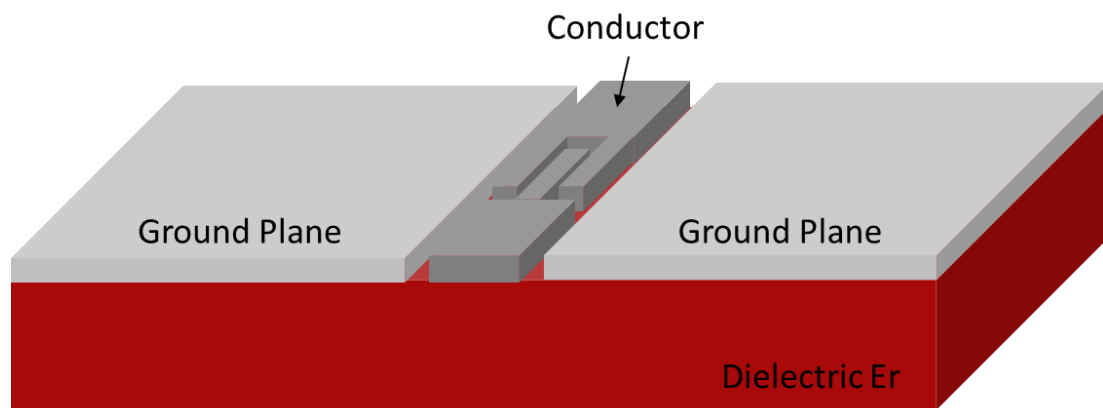


Figure 9: Diagram of a coplanar waveguide filter, specifically a gap-coupled resonator. This gap only allows wavelengths proportional to its width to pass.

The conductor in Figure 9 is split into two sections, with an electrically thin gap between. This gap only allows wavelengths proportional to its width to pass, and thus acts as a strict narrowband filter. This is similar to the coupled line bandpass filter shown in Figure 8, with a more compact conduction line to remain within the constraints of the same-surface ground plane [18].

2.3. Multipliers

Millimetre-wave and terahertz radiation can be produced in multiple ways such as via gyrotrons and laser sources. However direct signal generation at high frequencies is expensive and too bulky to be considered for hand-held devices. A common alternative to producing high frequency signals is to multiply lower frequency signals using frequency multipliers to achieve the desired rate.

Frequency multipliers rely on non-linear circuits to distort an input signal and generate harmonics. The multiplication factor depends on which harmonics are generated due to the distortion. A bandpass filter is then used to isolate the required harmonic.

Most multipliers are doublers or triplers, which amplify the second and third harmonics respectively. Higher harmonics can be selected but the output amplitude would be greatly reduced. The input is usually a sine wave, which only contains the fundamental frequency. By distorting the signal, harmonics are generated. If the distortion produced an ideal rectangular wave, the 2nd harmonic would peak when the duty cycle is 25% and the 3rd harmonic when the duty cycle is 16%.

There are two main types of frequency multipliers, namely passive and active. Passive multipliers solely rely on the power from the RF input to produce the harmonic content. Active multipliers have an external DC power source.

2.3.1 Passive Multipliers

Most diode frequency multipliers are one of two types: varistor or varactor. Varistor multipliers use Schottky barrier diodes to act as a voltage-dependant resistor with non-linear $I-V$ characteristics. These characteristically have a large bandwidth but poor conversion efficiency: doublers have a theoretical loss of 6.0 dB loss, see equation 2.16, but usually exhibit closer to 10 dB. Varactor multipliers use diodes to act as a voltage-controlled capacitor. These typically have good conversion efficiency but must be imbedded inside a tuned circuit, causing their performance to only be optimised over a very narrow bandwidth. The performance of these capacitor-based multipliers decreases at higher frequencies, as parasitic capacitances cause increased impedance. Therefore, varactor multipliers lose their

non-resistive advantage over varistor multipliers at high millimetre wave frequencies, and varistors become the clear choice.

Figure 10 shows a conceptual circuit of a varistor multiplier, that can be used to determine the efficiency of the multiplier for each harmonic.

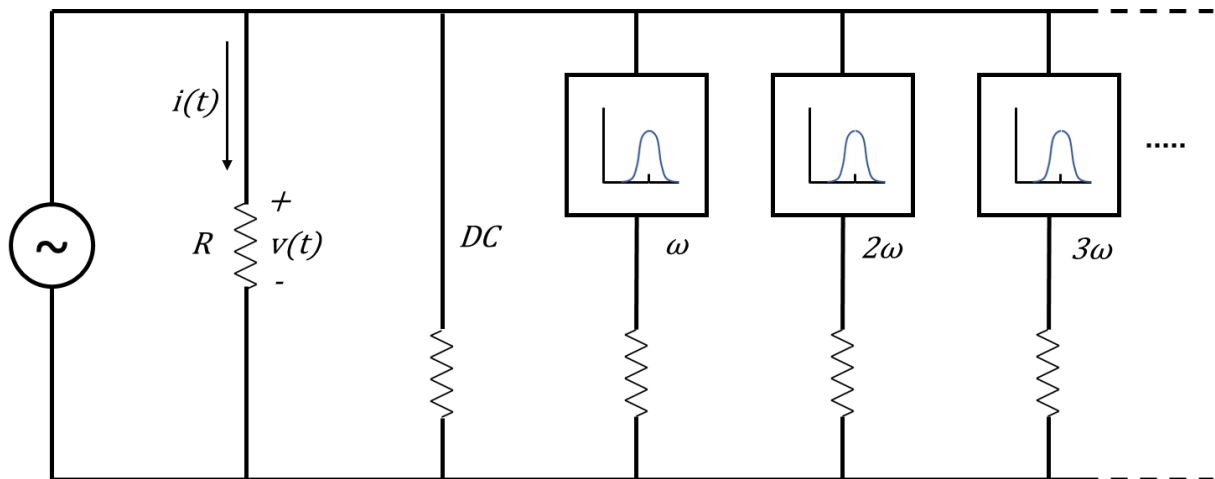


Figure 10: Conceptual Circuit for the derivation of efficiency in a resistive frequency multiplier. Remade from reference [13]. This can be used to derive the efficiency of each harmonic (ω , 2ω , 3ω , etc.), as seen in equations 2.13 to 2.16.

To calculate the efficiency of the varistor multiplier, the total power in the system can be first derived [13]:

$$\sum_{m=0}^{\infty} m^2 P_m = \frac{1}{2\pi\omega} \int_{t=0}^T \frac{\partial i}{\partial v} \left(\frac{\partial v(t)}{\partial t} \right)^2 dt \quad (2.13)$$

where m is the harmonic number and P_m is the power associated with that harmonic. $v(t)$ and $i(t)$ are the resistor voltage and current and ω is the source frequency.

For positive nonlinear resistors, this integral will always be positive, thus [13]

$$\sum_{m=0}^{\infty} m^2 P_m \geq 0. \quad (2.14)$$

Only the input harmonic, ω , and the desired harmonic, $m\omega$, are not terminated in a resistive load. Therefore equation 2.14 can be reduced to show the power efficiency of any harmonic [13],

$$\left| \frac{P_m}{P_1} \right| \leq \frac{1}{m^2}. \quad (2.15)$$

Therefore, the efficiency decreases with the square of the multiplication factor. For a frequency doubler or tripler, the efficiency is 1/4 or 1/9 respectively. The minimum carrier-to-noise degradation (CNR), in dB, from an ideal frequency multiplier is [13],

$$CNR = 20 \log m \quad (2.16)$$

A doubler has a CNR of 6.0 dB and a tripler 9.5 dB. This performance can be improved by using two diodes in balanced configuration, as shown in Section 9.2 with an anti-parallel arrangement, which rejects all even harmonics of the input frequency.

2.3.2 Active Multipliers

Active frequency multipliers have an external power source to assist the amplification of the required harmonic. Passive multipliers will always experience loss, whereas these can provide broadband conversion gain while achieving good DC to RF efficiency. However, higher levels of noise are introduced compared to their passive counterparts. Active multipliers are usually based on either FET (field effect transistor) or BJT (bipolar junction transistor) technology.

They can make very effective doublers, but when implemented as triplers it can be difficult to filter the unwanted harmonics as the fundamental harmonic is also amplified. The complications arising from designing the output network makes it hard to optimise for efficiency and to reduce the risk of instability. This makes active triplers significantly more expensive than their passive alternatives [28].

2.4. Mixers

Mixers are described in Pozar [13] as *“a three-port device that uses a nonlinear or time-varying element to achieve frequency conversion”*. They are a vital part of most microwave systems as it is both difficult to generate and analyse the RF signal directly. The principle of mixing signals can be traced back to the early 1900's. However, interest in the field spiked in World War II, where military radars were being produced for microwave frequencies [29].

A mixer takes two inputs at different frequencies and produces an output that contains both the sum and the difference of the input frequencies. This is usually done by harnessing the

nonlinearity of a diode or transistor. This produces a range of products and harmonics of the input frequencies and so must be used in conjunction with an output filter to select the desired frequency [13].

2.4.1 Mixer Overview

Figure 11 (a) shows an upconverter, where the intermediate frequency, f_{IF} , is combined with the local oscillator frequency, f_{LO} , to produce the RF output, f_{RF} . These are normally used in place of a multiplier to “upconvert” a modulated baseband signal to a higher transmission frequency. Figure 11(b) shows a downconverter, where the RF input, f_{RF} , is combined with the local oscillator frequency, f_{LO} , to produce the IF output, f_{IF} . This can be used to “downconvert” a received RF signal to a lower baseband frequency for ease of analysis.

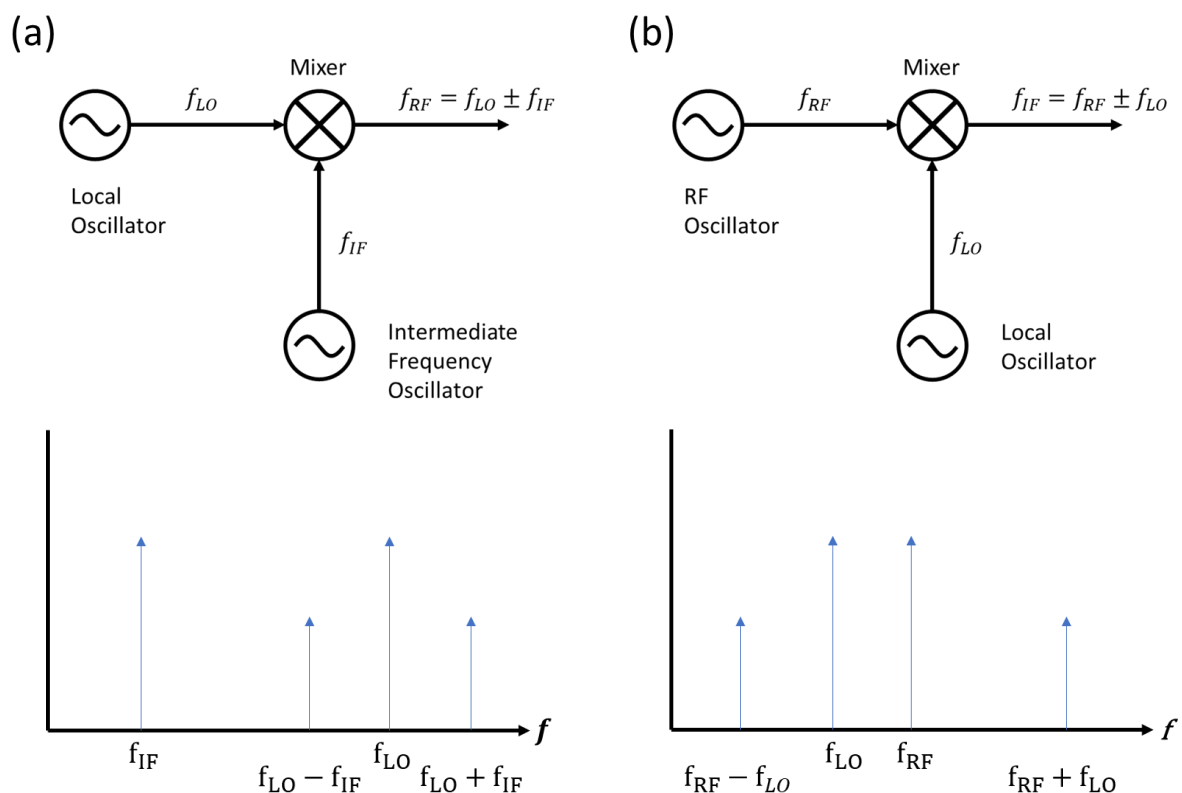


Figure 11: Diagram of frequency mixers, upconverter shown in (a) and downconverter in (b). Frequencies of inputs and outputs shown. Each mixer shown with respective output spectrum underneath. Recreated from [13].

In both instances, the input signal and reference will be passed to the output. As will both the positive and negative products and harmonics. The upconverter (Figure 11(a)) requires a filter at the RF frequency to “select” the required output and ensure power is not wasted in

transmitting unwanted frequencies. The same logic applies to the IF output of the downconverter (Figure 11(b)).

Mixers rely on multiplying the RF and LO inputs through a non-linear device. These can be described as [13]:

$$v_{RF} = V_{RF0} \cos(\omega_{RF}t) \quad (2.17)$$

$$v_{LO} = V_{LO0} \cos(\omega_{LO}t) \quad (2.18)$$

Therefore, when multiplied [13],

$$\begin{aligned} v_{RF} \times v_{LO} &= V_{RF0} \cos(\omega_{RF}t) \times \cos(\omega_{LO}t) V_{LO0} \\ &= \frac{1}{2} V_{RF0} V_{LO0} \cos((\omega_{RF} - \omega_{LO})t) + \frac{1}{2} V_{RF0} V_{LO0} \cos((\omega_{RF} + \omega_{LO})t) \end{aligned} \quad (2.19)$$

Which after an IF filter, only transmits the difference of the signals (i.e. the IF component) and not the sum [13]:

$$v_{IF} \propto \frac{1}{2} V_{RF0} V_{LO0} \cos((\omega_{RF} - \omega_{LO})t) \quad (2.20)$$

This is not strictly equal as it does not account for the conversion loss of the mixer.

2.4.2 Single-ended Diode Mixer

The simplest type of mixer is the single-ended diode mixer, which can be seen in Figure 12. This relies on the non-linearity of a diode to multiply the two inputs.

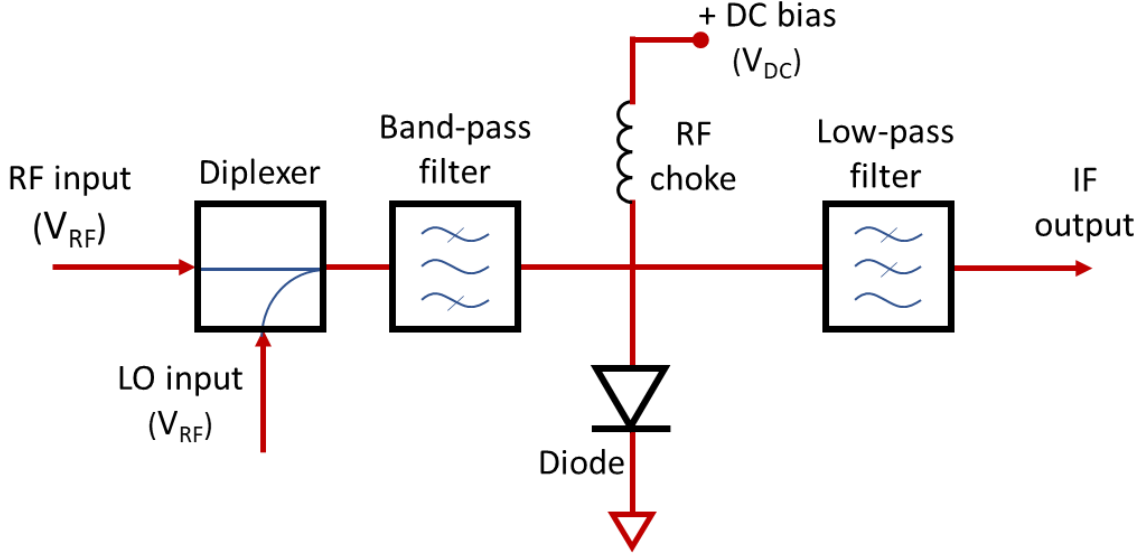


Figure 12: Circuit for a single-ended diode mixer. The two inputs are combined using a diplexer, filtered and then mixed using the non-linear nature of a diode, recreated from [13].

The diode is biased at V_{DC} and the DC choke stops RF and LO inputs being passed to the DC bias input. The voltage across the diode is the sum of the RF and LO inputs [13]:

$$v(t) = v_{RF} + v_{LO} = V_{RF0} \cos(\omega_{RF}t) + V_{LO0} \cos(\omega_{LO}t) \quad (2.21)$$

The equation for the diode current, $i_D(t)$, due to a voltage, $(v(t))$, is given by [13]:

$$i_D(t) = I_D(V_{D0}) + G_d v(t) + \frac{G'_d}{2!} v(t)^2 + \dots \quad (2.22)$$

where, the dynamic conductance of the diode, G_d , can be described by the junction resistance [13],

$$G_d = \frac{1}{R_j} = \frac{dI}{dV} \quad (2.23)$$

and the second derivative of the dynamic conductance is [13]:

$$G'_d = \frac{d^2I}{d^2V} \quad (2.24)$$

The square of the voltage can be calculated to find the remaining terms [13]:

$$\begin{aligned} v(t)^2 &= [V_{RF0} \cos(\omega_{RF}t) + V_{LO0} \cos(\omega_{LO}t)]^2 \\ &= V_{RF0}^2 (1 + \cos(2\omega_{RF}t)) + V_{LO0}^2 (1 + \cos(2\omega_{LO}t)) \\ &\quad + 2V_{RF0}V_{LO0} [\cos((\omega_{RF} - \omega_{LO})t) + \cos((\omega_{RF} + \omega_{LO})t)] \end{aligned} \quad (2.25)$$

If ω_{RF} and ω_{LO} are similar, then except for the component $\omega_{RF} - \omega_{LO}$ all other components produced by the diode nonlinearity are at a much higher frequency and are therefore filtered by the low pass filter shown in Figure 12. The output IF current of the single-ended diode mixer is therefore [13]:

$$i_{IF}(t) = G'_d V_{RF0} V_{LO0} \cos((\omega_{RF} - \omega_{LO})t) \quad (2.26)$$

And conversion gain is [13],

$$G_{CG} = \left| \frac{i_{IF}}{V_{RF0}} \right| = G'_d V_{LO0} \quad (2.27)$$

The disadvantage of this mixer is the strong LO component on the output. This is difficult to filter as has greater magnitude than the other components [30].

2.4.3 Balanced Mixer

Non-linear devices used in the fabrication of frequency mixers are usually diodes and field effect transistors (FETs). However, balanced mixers can be produced using ring hybrids. An example of a balanced mixer designed using a 180° hybrid is shown in Figure 13.

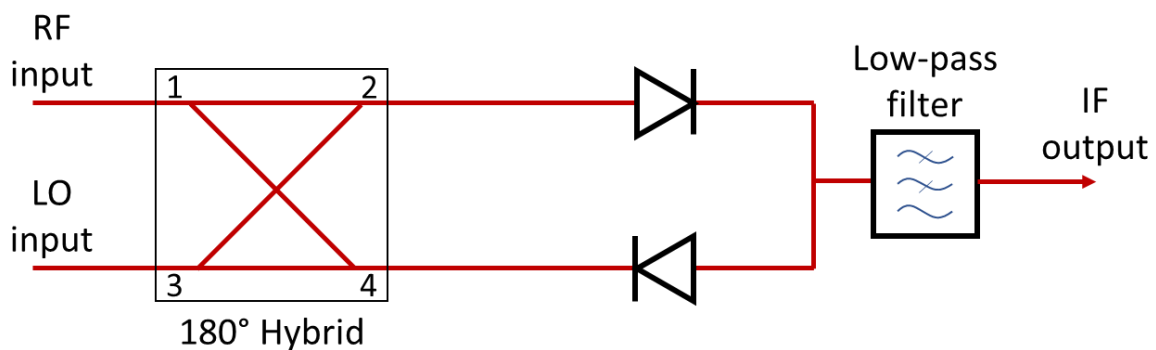


Figure 13: Balanced mixer circuit using a 180° hybrid and diode configuration as a mixer, relying on quarter wavelength spacing inside the hybrid to add or subtract the input waveforms, followed by a low-pass filter to isolate the desired output, recreated from [13].

These devices rely on the spacing between ports being a quarter wavelength. Thus, at each port, the RF or LO waveform are either positive or negative. This can be used to add or subtract the waveforms from each other, and therefore can function as a mixer. This is used in Chapter 10 for the design of a rat race mixer and is explored in more detail there.

2.4.4 Double Balanced Mixer

An example of a double balanced mixer can be seen in Figure 14.

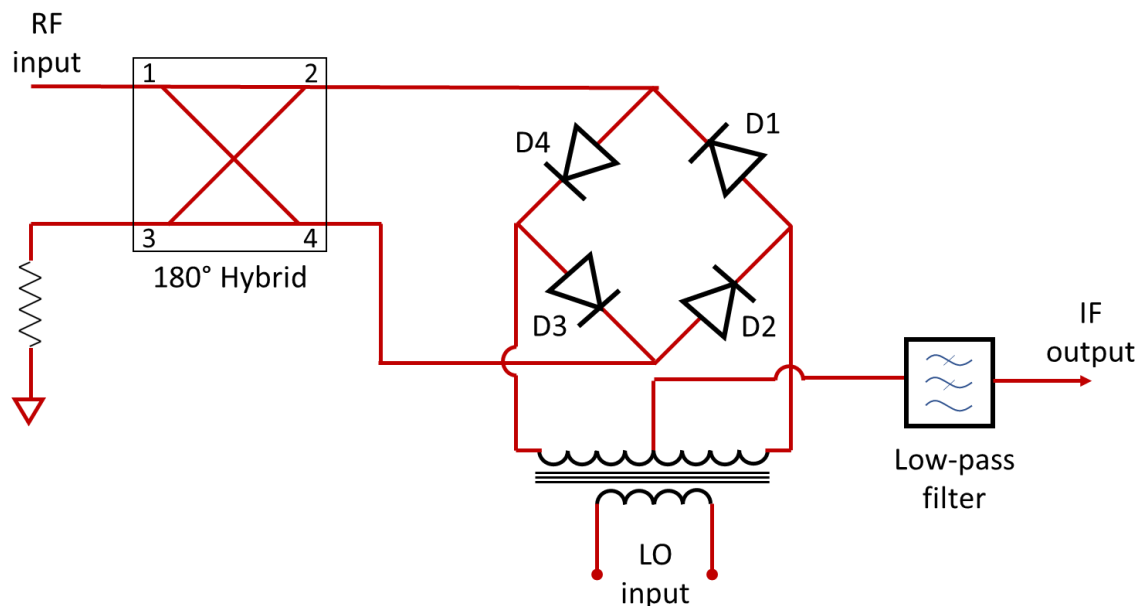


Figure 14: Double balanced mixer circuit. This combines the 180° hybrid shown in Figure 12 with a diode ring. This has the advantage of automatically filtering both the LO and RF components from the output, recreated from [13].

The LO input switches the diodes D1 and D2 on together, and then the diodes D3 and D4. The point between D1 and D4 is a virtual earth to the RF signal, due to layout of the 180° hybrid. Therefore, by switching the diode pairs on and off with the LO input, the RF input is switched alternately to ground. When not switched to ground, the RF signal is routed to the IF output via the low-pass filter. Therefore, the output at the IF port is the RF input multiplied by the LO waveform [31].

This layout has the advantage that both the LO and RF inputs are completely removed from the output, and no additional filtering is required. However, due to the increased complexity of this circuit compared to that in Figure 13, it is perhaps simpler to add an RF filter to the balanced mixer circuit.

2.5 Antennas

The introduction of electronic communication by Samuel Morse in 1844 saw a wired telegraphy transmission from Baltimore to Washington, DC. This is a clear precursor to today's

wireless communications when combined with the presentation of the well-known 'Maxwell's Equations' by James Clerk Maxwell in 1864, which introduced the electromagnetic theory that still underpins the communications industry today [32].

The first antennas were dipole antennas produced by Heinrich Hertz in 1887 [33] and presented in 1889 [34]. These proved the existence of electromagnetic waves predicted by James Clerk Maxwell in 1865 [35]. Practical use of antennas began with Guglielmo Marconi around 1896 for wireless telegraphy with Morse code [36]. Marconi was also subsequently responsible for the first transatlantic radio transmission [32].

The requirements for wireless transmission were increased during World War II, and the resulting invention of microwave devices enabled the development of radar [32]. This was a system whereby aircraft or ships could be detected using pulsed RF waves, transmitted via antenna that had reflected off the detected object. Radar is now used for applications such as weather detection, car speed checks and locating hidden pipes.

Post-World War II saw improvements in broadcast television and fiber optic communications before the reinvention of the wireless with the introduction of cellular telephones in the 1980s [32]. Around this time, antennas such as the corner reflector, printed antennas and phased arrays were introduced [37].

For the last 30 years, the size of antennas has been substantially decreasing to reflect the increasing frequencies used in transmission standards for broadband cellular networks, i.e., 2G to 5G.

2.5.1 Antenna Basics

An antenna is a device used to convert between propagating electromagnetic waves and electric currents moving in a conductor. In transmission, electric currents are converted to electromagnetic waves, and vice versa in reception. Antennas can be designed to transmit and receive electromagnetic waves in a particular direction (directional antennas) or in all directions equally (omnidirectional antennas).

Key features of an antenna include the impedance, bandwidth, efficiency, gain and directivity. The antenna impedance is the ratio of voltage to current across the antenna terminals. The

bandwidth is the frequency range over which the antenna radiates. The efficiency is a measure of the radiated power relative to the input power. The gain is a measure of the radiated power in a given direction, and the directivity measures how “directional” the gain is. This can be shown by plotting the radiation pattern of the antenna, which is a visualisation of the gain over a variety of angles and can be plotted in 2D or 3D (An 3D example is shown in Figure 16). Additionally, the beamwidth, angle covered by the region of peak gain, and sidelobes (secondary, smaller peak gain regions) can be clearly shown using radiation patterns.

The radiation pattern usually shows the antenna output in the far field. This is the power radiated at a distance greater than $2D^2/\lambda$, where D is the maximum linear dimension of the antenna. In this region the power density decreased with the square of the distance. The near field is any distance closer than $2D^2/\lambda$, which is more complex to consider due to the presence of both reactive (those directly due to the antenna) and radiative (those spreading out from the reactive region) fields.

Antennas can also be described by their polarisation. As all electromagnetic plane waves can have an associated polarisation, which specifies the orientation of the oscillations, the antenna polarisation is which of these the antenna is most sensitive to. This includes linear, circular and elliptical polarization.

The simplest example of an antenna is a metal pole with length characterised by the wavelength (λ) of the propagation (usually $\lambda/2$), as seen in Figure 15. The dimensions of an antenna are usually restricted to greater than a quarter wavelength, as high directivity and efficiency are difficult to achieve in antennas smaller than this.

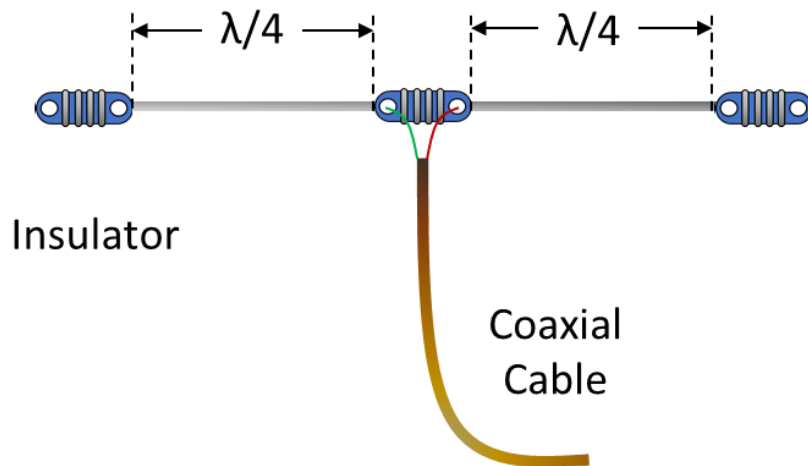


Figure 15: Example of a basic, dipole antenna, centrally fed via coaxial cable, with quarter wavelength elements.

The antenna is constructed of an array of elements, electrically connected to the antenna terminals. Components not connected to the antenna, such as parabolic reflectors and horns, may be added to direct the electromagnetic radiation towards the antenna. This increases the efficiency by recreating the radiation pattern of the antenna. The radiation pattern is the directional variation in intensity of the radiation transmitted from the antenna.

2.5.2 Dipole Antenna

The dipole antenna is only effective at the wavelength, or intervals of this, that it was designed for. It consists of two identical conductive elements placed end-to-end with a feed line in the centre. An example can be seen in Figure 15. The most common type is a half-wave dipole, with elements of length $\lambda/4$. A standing wave is set-up along the antenna when excited by an electromagnetic wave with wavelength λ . The dipole antenna only has regions of low or no transmission along the length of the element. This can be seen in the radiation pattern shown in Figure 16.

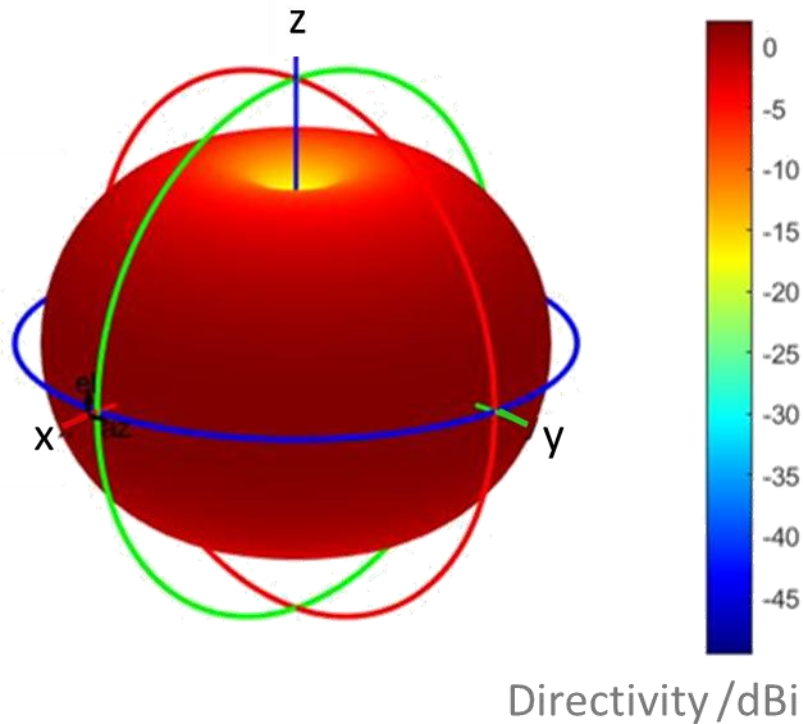


Figure 16: The radiation pattern of a centrally fed dipole antenna with 1 m ($\lambda/4$) elements simulated in Matlab antenna toolbox at 75 MHz. The dipole is orientated along the z-axis.

Though the dipole antenna is a complete antenna, it can also be used as part of the feed for more complicated structures, such as in the Yagi Uda antenna. These were invented in 1926 by H Yagi and Shintaro Uda [38] and are commonly seen attached to houses as TV antennas.

This is an iconic example of an array antenna, which combines many antennas (in this case, dipoles) into a single, more effective structure. The dipoles are arranged so that there is positive interference between the elements, making a series of parallel resonant structures [39].

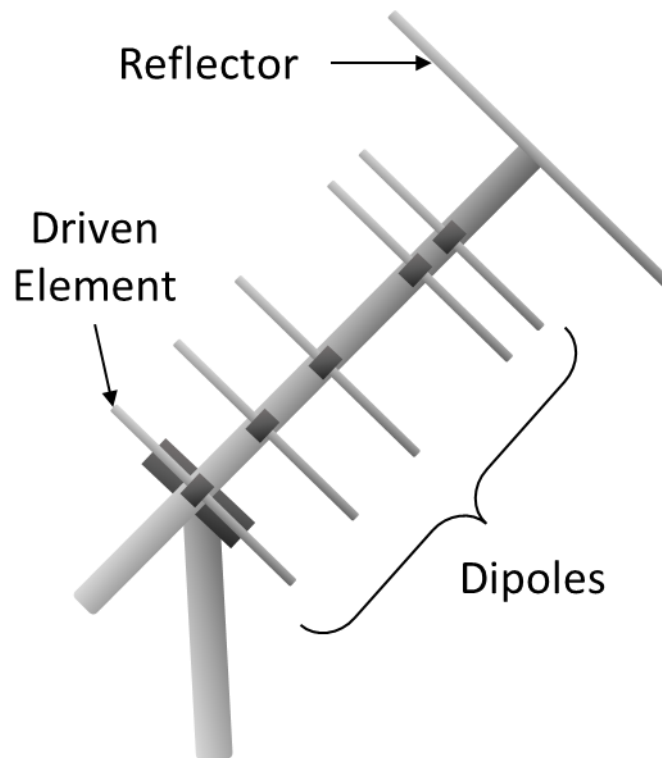


Figure 17: Example of a Yagi Uda antenna, with dipole elements and reflector labelled.

The reflector was designed during World War II alongside radar, horn, and array antennas [32]. The reflector element, shown in Figure 17 is slightly longer than the dipoles and placed opposite the intended transmission direction. The reflector increases the gain in the direction of interest, by reflecting transmitted radiation to cause positive interference.

These antennas are popular as they are highly directional and cheap, but they do only provide a very small bandwidth.

2.5.3 Horn Antenna

The horn antenna was invented by both Wilmer Barrow and G.C. Southworth, independently, in 1938 [40]. A horn is a metal waveguide, shaped as its namesake suggests, to direct electromagnetic waves into a beam. An example can be seen in Figure 18. They increase the amount of radiation collected onto the surface of the antenna, and as such have a much-increased bandwidth from previous antennas.

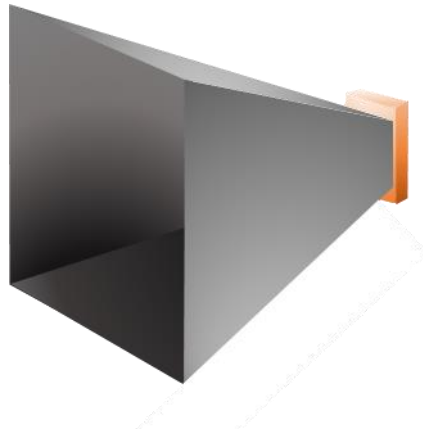


Figure 18: Example of a horn antenna. Its shape is used to increase the amount of electromagnetic radiation incident to a collecting antenna at the back (shown in orange in figure).

Horn antennas have characteristic truncated rectangular prism shape with dimensions proportional to the propagation wavelength. In this thesis we use Virginia Diodes WR-1.0 Horn Antennas to transmit THz frequencies. The dimensions of this horn, with front and side projections, can be seen in Figure 19.

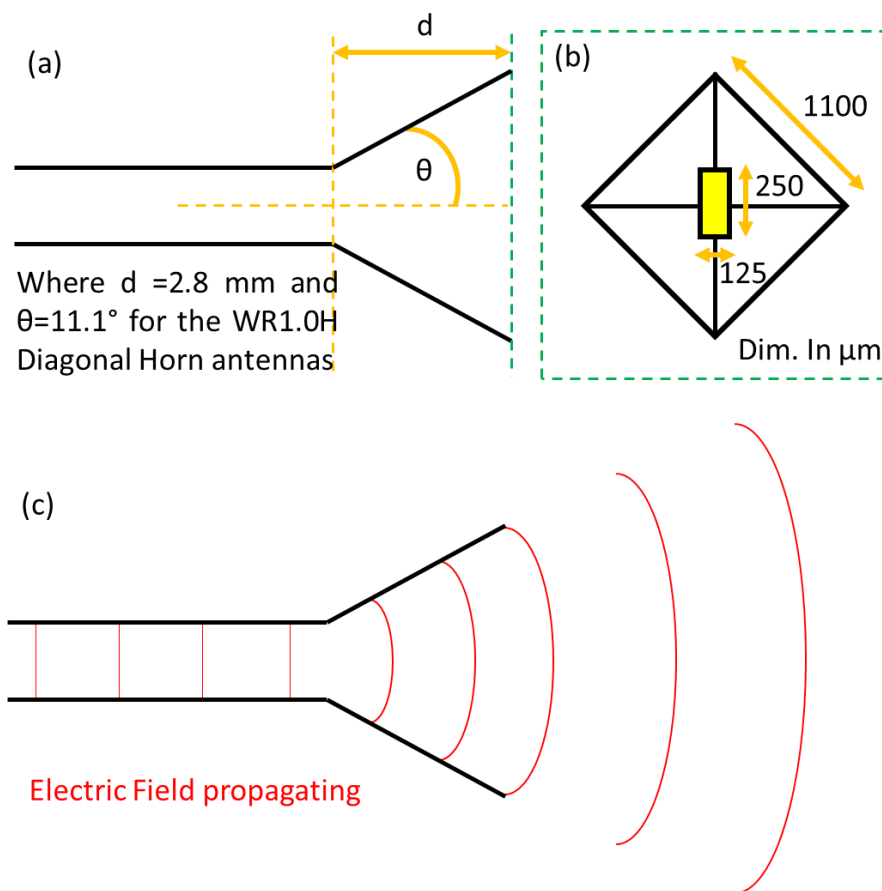


Figure 19: (a) Side-on diagram of horn antenna with central waveguide. Cross section of end of horn shown in (b) with rectangular waveguide central shown in yellow. (c) shows the electric field propagating in the horn. Dimensions are of a Virginia Diodes WR-1.0 Horn Antenna [41].

Figure 19(a) and (b) show the dimensions of a Virginia Diodes WR-1.0 horn antenna [41], which is used for experiments in Chapter 7. The horn is centrally fed with a TE₀₁ waveguide, shown in yellow in Figure 19(b). The electric fields propagating both in the waveguide and radiated through the horn antenna is shown in Figure 19(c).

2.5.4 Array Antenna

Array antennas are a combination of smaller, less effective elements, that combine to produce a structure of centrally fed antennas with higher gain and improved directivity compared to its individual components. The array and its feedlines are arranged to ensure that each of the elements receives a current with a specific phase. This ensures that the electromagnetic radiation transmitted by each element constructively interferes with the radiation transmitted by consecutive elements, in the direction of interest. The design also specifies where destructive interference is required. This beam shape selection ensures the array antenna has higher gain and directivity than a singular element could produce. An example of an array antenna can be seen in Figure 20, as shown the feed lines are often arranged in a grid structure to allow all elements to be attached to the feed.

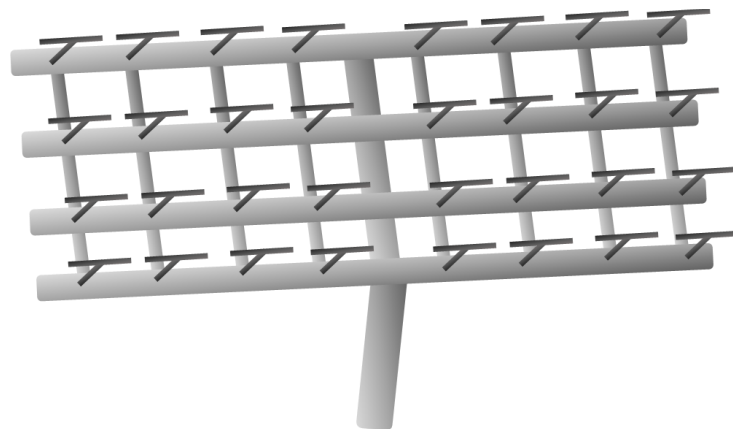


Figure 20: Example of an array antenna. These are a collection of smaller antennas, centrally fed and combined to produce a single structure with high gain and improved directivity.

In modern systems each element can be tuned to allow the radiation pattern of the overall antenna to be adjusted in real time. These are called programmable antenna arrays and elements are either adjusted in position (mechanically) or in component values (electrically). The key advantage of these structures is they allow wide beam steering; however, they can be bulky and expensive to implement. A current area of research is reducing these disadvantages by integrating metasurfaces into the array [42].

A key measure of an array antenna is the Array Factor. This is a function of the individual antenna locations and their feeds. This can be adjusted to optimise the overall array antenna's performance, such as the beam width and gain.

2.5.5 Microstrip/ Patch Antenna

Most of the antenna designs covered here are not convenient to integrate when scaled down to the sizes required for microwave frequencies. For this, a host of new more compact designs have been introduced in the last 20 years. These include patch [43], planar bowtie [44], leaky wave [45] and photonic antennas [46]. For this thesis, we are interested in planar antennas, that can be fabricated using traditional microfabrication techniques and easily reduced to THz scales.

Antennas in smart phones need to be small, flat and easily integrated. The most common mobile phone antenna is the patch antenna, proposed by Howell [43] in 1975. It consists of a dielectric substrate sandwiched between a flat metallic ground plane and a "patch" of metal.

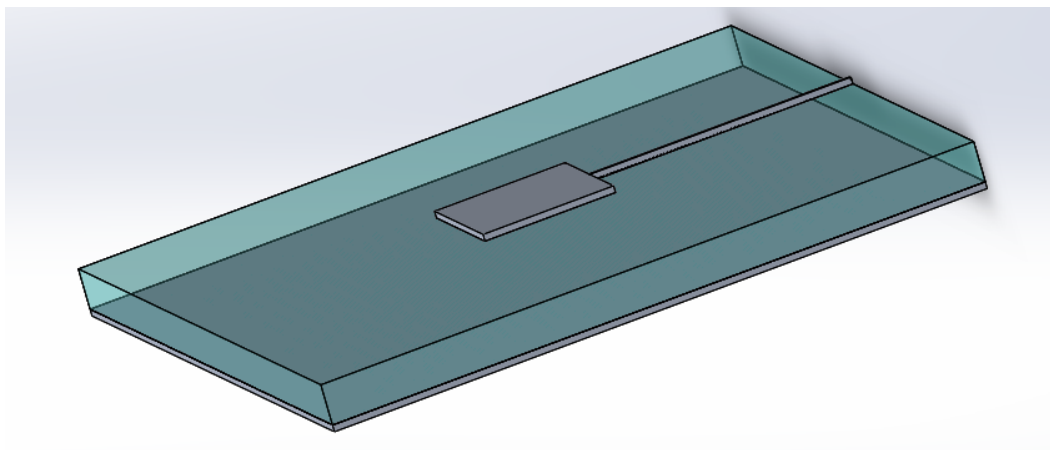


Figure 21: Example of a patch or microstrip antenna, which is a low-profile antenna with metallic ground plane underneath, substrate in middle, and patch on top.

These are popular as they are two dimensional and can be easily manufactured through PCB techniques (lithography). Kleine-Ostmann and Nagatsuma [47] states planar structures "could be a good solution for future commercial communication systems" due to their "flexibility, their potential for integration and their cheap and easy fabrication".

2.6 Conclusion

This chapter has covered the history and basics of all electronic components covered in this thesis. The components covered are transmission lines, waveguides, filters, mixers, multipliers, and antennas. The material covered in this chapter is intended to give background to the designs shown in Chapters 6 to 10.

Chapter 3: Numerical Methods

This section outlines the numerical methods and software used in this thesis. These are the finite difference time domain (FDTD) method, as used in Lucifer, and the method of moments (MOM), as used in Matlab and ADS (advanced design software).

3.1 Finite Difference Time Domain

The finite difference time domain method (FDTD) is common numerical analysis technique used to solve problems in electromagnetics. As the process is grid based, see Figure 22, the method is computationally intensive and therefore only appropriate when the characteristic dimensions of the domain are of the same order as the wavelength. FDTD simulations have been used to model a variety of THz antennas [48, 49, 50] where the dimensions are in the order of tens to hundreds of microns. This section will present the FDTD method and Lucifer simulator, that will be used to model the electromagnetic response of THz antennas in Chapter 6. Lucifer is open-source software [51] developed within our research group (prior to this thesis), which allows direct manipulation of simulation parameters. This is not usually possible in commercial simulation packages. However, this increased level of control requires an in-depth knowledge and understanding of the FDTD method to allow careful selection of parameters such as simulation geometry, source and monitor planes, boundary conditions, and dielectric properties.

3.1.1 The Finite Difference Time Domain Method

The finite difference time domain method, also known as Yee's method, is an approximate solution to Maxwell's equations over discretised space and time [52]. Yee [53] first suggested using second order finite difference equations to replace Maxwell's curl equations. This allows for an iterative approach to finding future values of magnetic and electric fields based on currently known values at adjacent nodes, as shown in Figure 22.

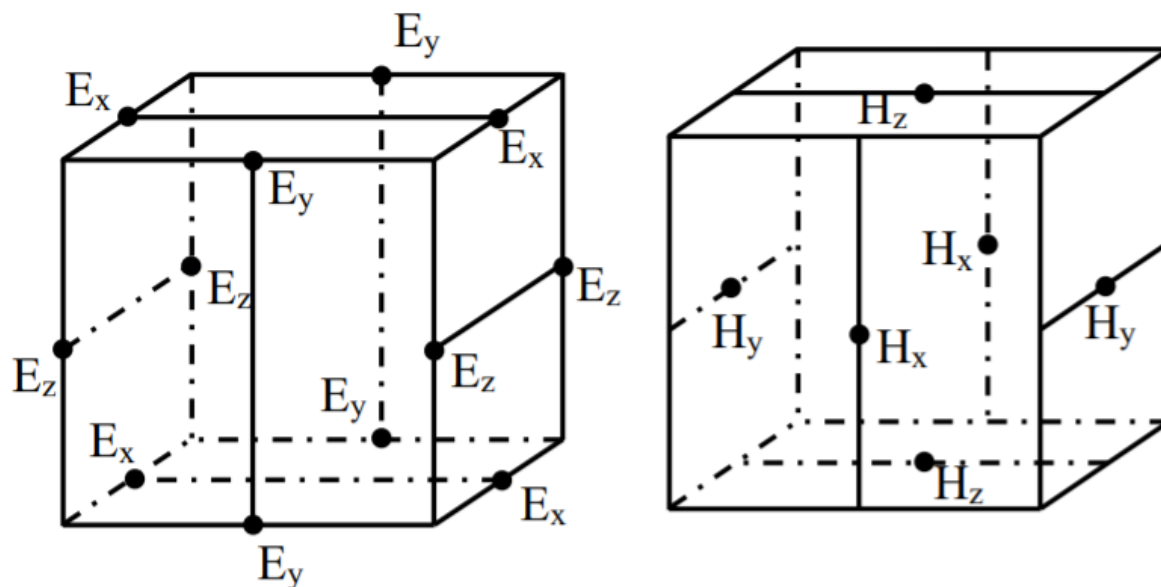


Figure 22: Yee's cell, used in the iterative finite difference time domain method. The FDTD method starts with known electric and magnetic fields in one location, then calculates the surrounding fields iteratively across the rest of the domain. The cells on the left and right show the electric (E) and magnetic (M) fields respectively, and one cell of the discrete grid used to solve for them.

The discretised space must be able to resolve both the smallest wavelength and smallest feature in the model. This creates a fine grid, restricting the maximum domain size due to computational time, removing the capability of the FDTD to calculate the far-field. However, this can be approximated from the near-field results using the geometric mean method, as outlined in Schneider [52].

Energy in a FDTD simulation cannot propagate further than one spatial step in each time step, as each node's electric and magnetic fields are calculated as a function of their neighbours. The constant relating the spatial and time steps is called the Courant Number (S_c):

$$S_c = \frac{c\Delta t}{\Delta x} \quad (3.1)$$

where c is the speed of light in free space, Δt is the time step, and Δx is the spatial step. In a 1-dimensional FDTD simulation, the Courant number must therefore be less than one, to keep energy propagation below the speed of light. In a 3-dimensional simulation, the distance between farthest adjacent nodes is $\sqrt{3}\Delta x$. The time taken to communicate between these is $3\Delta t$. Therefore, the Courant number is [54]:

$$S_c = \frac{c\Delta t}{\Delta x} = \frac{1}{\sqrt{3}} \approx 0.577 \quad (3.2)$$

If a Courant number of exactly $\frac{1}{\sqrt{3}}$ is chosen, there is no numerical dispersion. However, choosing an irrational number would give instability in simulations. Choosing a large Courant number, within these limits, minimises the number of timesteps required to cross the total 3D geometry, therefore minimising computational time.

Solutions have been found to minimise reflection at the end of the physical space. Absorbing boundary conditions (ABC) or periodic boundary conditions (PBC) can be applied to nodes at the end of the physical space. The ABC acts as if the dimension is infinite. The PBC continues any effect to the opposite side of the domain. Though initially these solutions could not stop all reflection, solutions such as Berenger's perfectly matched layer (PML) [55], found in the 1990s, perfectly match absorption. This is not implemented in Lucifer, as reflection observed from using an ABC is already well below the reflection expected from practical experimentation.

Any computational simulation introduces errors due to storing numerical data with a finite number of digits. The constantly increasing computational power available has decreased these errors over time. Higher computational power also allows higher order approximations of Maxwell's equations to be used. This further reduces computational errors in later implementations of the FDTD.

3.1.2 Lucifer

Lucifer, an open-access Durham-developed FDTD software, is used for the antenna simulations in Chapter 6. It is written in C code, with Python and Matlab interfaces and is designed to simulate structures under different electromagnetic inputs. Parameters and geometries are accessible at a very low level, which makes it ideal for the simulations shown

here, where we require full control over simulation geometry, boundary conditions and dielectric properties. It does not automatically provide a graphical output, but the simplified interface of the output fields makes it easy to integrate with Matlab. As with most FDTD simulations, only the near field electric and magnetic fields are provided, but the far field can be calculated in post-processing from the methods outlined in Schneider [52].

In the simulations presented in this thesis a 5 μm cubic grid is used across the domain, the size of which varies on the antenna dimensions under test. The substrate and ground layers reach to the edges of the x and y domain.

Lucifer uses a configuration, geometry, and source file to characterise one simulation. The configuration file specifies basic requirements such as simulation size and time. The simulation time is set in the range of tens of picoseconds but is varied to allow the source wave to fully cross each domain size. The cell size can be set to any value, depending on the frequency range and the dimensions of the object under analysis. In all simulations outlined in this thesis, the cell size is set to 5 μm . This allows simulation of the smallest features used without excessively increasing computational time.

The configuration file is also used to specify the boundary conditions. The top and bottom of the domain are designated as ABCs, which stops reflections impeding the simulations. All sides are set as PBCs, which gives equivalence to infinite space and reduces the computational demand by allowing the domain size to be kept small.

The geometry file allocates each cell a material, either by specifying the dielectric constant of individual cells or of grouped entities such as a cylinder or sphere. A function was added to the geometry file, "*mat2plane*", which converts a 2-dimensional matrix to a list of entries for the material index matrix. The entries of the array are used to decide what materials are placed where, i.e. 0 is vacuum, 1 is metal and 2 is silicon. A frequency-independent dielectric constant of 3.43 is used to represent SU8 as the dielectric layer material [56].

The source file specifies the characteristics of the input wave. In Lucifer, all configurations are ‘illuminated’ by a 0.78 ps pulse, shaped to the first derivative of a Gaussian function and linearly polarised along the x-axis. This pulse shape imitates that generated by a time domain system (TDS) has zero magnitude at DC. This is set in Lucifer to allow comparison between simulations and TDS experiments. The simulation configuration and pulse shape can be seen in Figure 23.

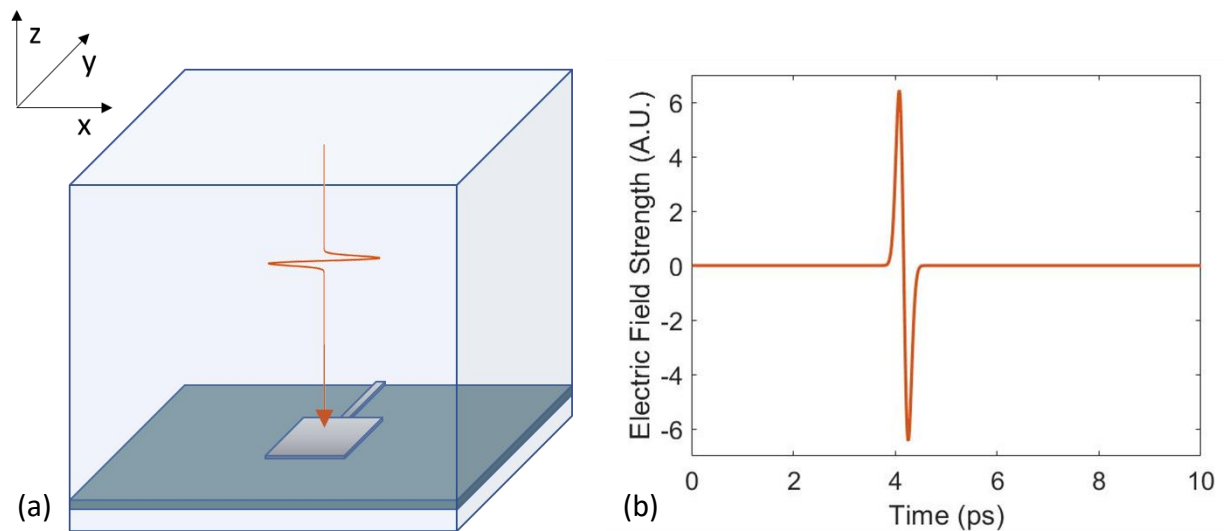


Figure 23: (a) Simulation configuration with source wave shown in red. Also shown is simulation boundary and example antenna under test. (b) shows the source wave in terms of electric field strength over time.

As shown in Figure 23(a) the source was located above the antenna and directed along the z-axis. An example of a simulation is seen in Figure 24. The figure shows the (x, y) plane of the FDTD simulation, 10 μm below the surface of the substrate.

While the FDTD code is not written in the process of this thesis, all instances of its' use, including edits to the configuration, geometry and source files were completed during this work.

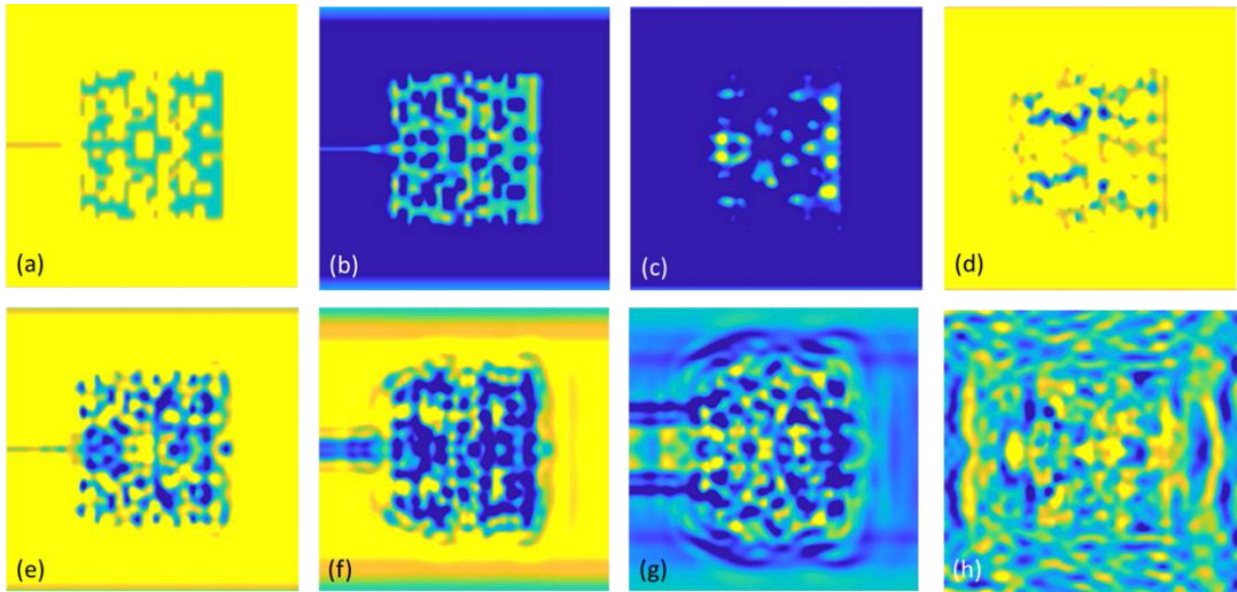


Figure 24: Lucifer FDTD simulation of an patterned patch antenna captured at (a) 2.6 ps (b) 3.0 ps (c) 3.4 ps (d) 3.8 ps (e) 4.2 ps (f) 4.6 ps (g) 5.4 ps (h) 12.0 ps after the application of the input pulse at 5.63 ps. Blue represents areas of high intensity electric field, and yellow low intensity.

Blue represents areas of high intensity electric field, and yellow low intensity. As the source wave overlaps the antenna, there are oscillating peaks of high and low intensity, mirroring the shape of the patterned metallic patch. This happens quickly to start with, but the effect slows as the wave is absorbed by the antenna and scattered off both the periodic boundary conditions of the simulation and the antenna itself.

3.2 Method of Moments

The method of moments (MOM) produces matrix equations in finite space to approximate functional equations in infinite space. These matrices can then be solved using linear algebra. The first example of this is from Galerkin in 1915 [57]. It was not initially popular due to the high computational load associated with matrix algebra. However, due to the improvements in personal computers, this is now a standard method for solving functional equations. MOM was first applied to electromagnetic field equations in the 1960s by Mei and Van Bladel [58] and has progressed to be the main technique for electromagnetic simulations in both Matlab and ADS [59, 60].

Both FDTD and MOM can be used to solve electromagnetic surface or volume integral equations. MOM differs from FDTD in that this is completed in the frequency domain and only

the electromagnetic sources (surface or volume currents) are of interest. Consequently, MOM is commonly used for solving radiation and scattering problems [61].

3.2.1 Matlab

In Chapter 6 the antenna toolbox within Matlab is used to simulate THz antennas, thereby using the method of moments. The antenna toolbox has a hard-coded 200 GHz frequency limit. Simulations can be converted to a lower frequency provided the dimensions of the component under test are appropriately increased, due to the MOM being characteristically scalable. Alternatively, under request, Matlab will provide replacement files to increase this frequency limit. This is advantageous as can reduce the time taken scaling complicated configurations. This process is outlined in Appendix 1.

3.2.2 Agilent Advanced Design System

Agilent (now Keysight) Advanced Design System (ADS) Method of Moments (Momentum) electromagnetic simulator is a 3-D planar EM simulation software for electronics and antenna analysis. It is a partial differential equation solver of Maxwell's electromagnetic equations based on MOM. Magnetic and electric Green's functions follow from Maxwell's equations to account for all coupling, radiation and dispersion effects in the substrate. This means all capacitors and inductors are modelled as complex and frequency dependant [60]. Momentum is considered a 2.5D EM simulator, as there are planar restrictions on current flow along conductors, but vias may be used to connect planar layers.

The Layout environment of ADS directly supports Momentum simulations. These are simple to set up as the user can directly specify the circuit in the Layout GUI or directly import from the Schematic environment. There is no limit on frequency range and s-parameter results can be plotted directly in the simulator.

A basic use model can be seen in the figure below.

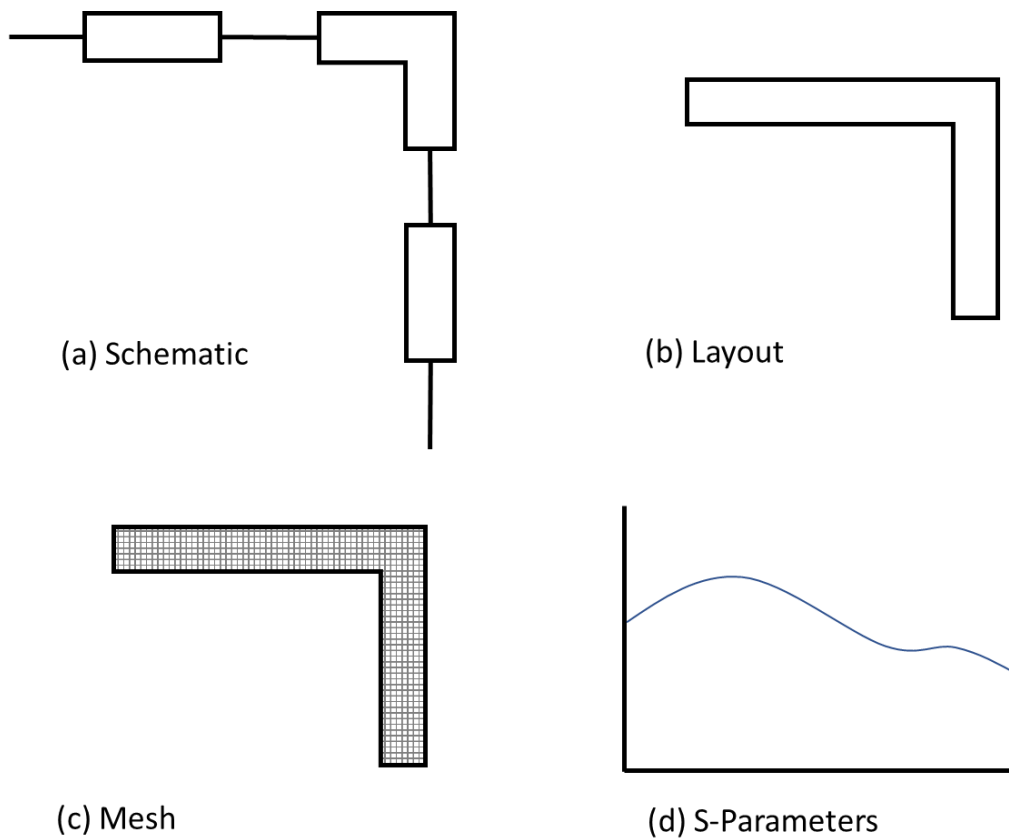


Figure 25: Basic use model of Agilent ADS, showing (a) drawing of a schematic (b) conversion to layout (c) meshing and (d) calculation of S-Parameters.

ADS circuit design is usually started by (a) drawing a schematic of the approximate features and (b) converting this to a layout. The layout feature on ADS allows visualisation of the dimensions the circuit will assume. From the layout, the momentum window allows mesh (c) generation, with frequency specified by the user. Once a mesh is generated it will appear superimposed on the geometry outline. Simulations, or “Momentum” analysis, can then be run to calculate S-parameters (d) and plot output data in the graphics server [62].

3.3 Conclusion

This section outlined the numerical methods and software used in this thesis. These are the finite difference time domain (FDTD) method, as used in Lucifer, and the method of moments (MOM), as used in Matlab and ADS (advanced design software).

Chapter 4: Measurement Techniques and Fabrication Methods

This chapter is an overview of the techniques employed for experimental work in this thesis. These can be split into two principal topics: measurement techniques, and fabrication methods. The techniques outlined in this chapter are used throughout the thesis and are not particular to any one experiment. Experimental work at post-5G frequencies requires state of the art equipment and processes, as devices are increasingly miniaturised and require high-rate analysis tools.

4.1 Measurement Techniques

The measurement techniques introduced here rely on the concept of a two-port network; the simplest of which can be seen in Figure 26.

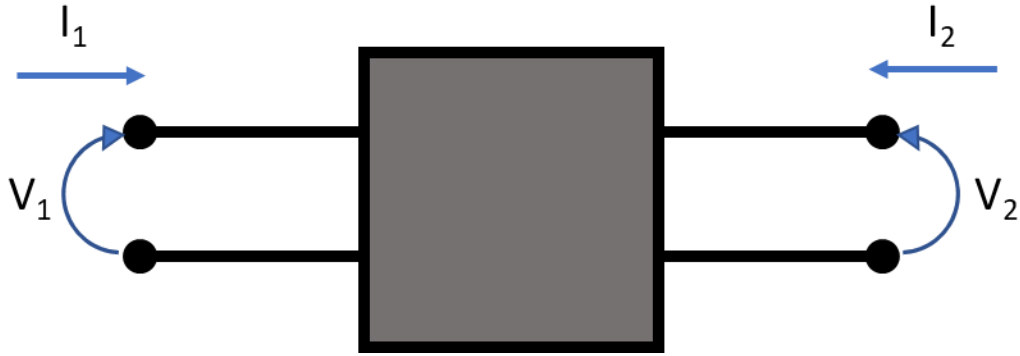


Figure 26: Simplest form of two-port network, where there are two current inputs and two voltages. The central "black box" can be described as a matrix of impedances.

In this network, the voltages can be described in terms of the input current and the impedance matrix.

$$\begin{pmatrix} V_1 \\ V_2 \end{pmatrix} = \begin{pmatrix} z_{11} & z_{12} \\ z_{21} & z_{22} \end{pmatrix} \begin{pmatrix} I_1 \\ I_2 \end{pmatrix} \quad (4.1)$$

This is a conveniently simple equation but does not allow the networks to be cascaded into a more complex transmission system. For this, the network in Figure 27 can be used. Here the current on Port 2 has been reversed to allow cascading [13].

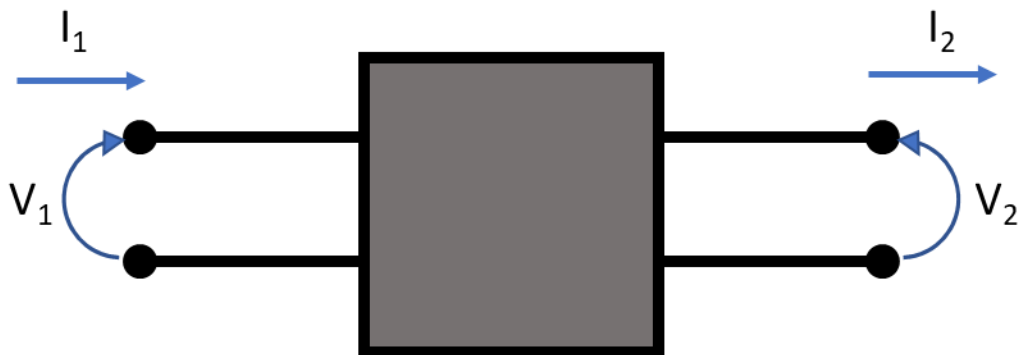


Figure 27: More complex two-port network, where the network can be described by an admittance matrix. This matrix is shown in equation 4.2 [13].

In this case, the voltage and current at port 1 can be calculated from those at port 2 via the admittance (or ABCD) matrix [13],

$$\begin{pmatrix} V_1 \\ I_1 \end{pmatrix} = \begin{pmatrix} A & B \\ C & D \end{pmatrix} \begin{pmatrix} V_2 \\ I_2 \end{pmatrix} \quad (4.2)$$

For a transmission line, the ABCD matrix can be expressed as [13],

$$\begin{pmatrix} A & B \\ C & D \end{pmatrix} = \begin{pmatrix} \cos(g) & iZ_L \sin(g) \\ iZ_L^{-1} \sin(g) & \cos(g) \end{pmatrix} \quad (4.3)$$

Where [13],

$$g = -i\gamma_L l \quad (4.4)$$

and γ_L is the propagation constant of the transmission line and l is the line length.

These impedance or admittance matrices are usually calculated from IV characteristics, but these can be difficult to measure at high frequencies, where behaviours become less linear. Therefore, modern systems such as Vector Network Analysers (VNAs) rely on s (scattering)-parameters.

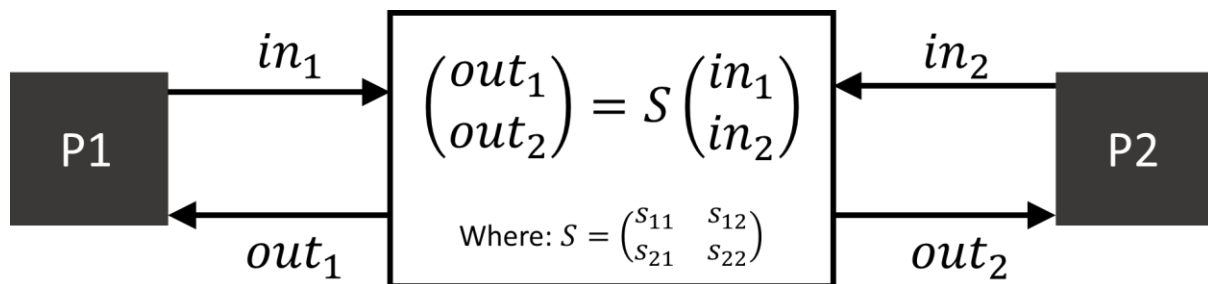


Figure 28: Theoretical description of s -parameters for a two port (P1 and P2) network. These can be used to determine the reflection and transmission characteristics between the ports.

The scattering matrix, S , quantifies how power propagates through a multi-port network. For the two-port network shown in Figure 28 there are four scattering parameters in this matrix. Parameters s_{11} and s_{22} describe the reflection into ports P1 and P2 respectively. The transmission between ports can be calculated with either s_{21} (i.e., port P1 was the source and port P2 the receiver) and s_{12} (i.e., port P2 was the source and port P1 the receiver). Alternatively, the s -parameters can be calculated from the ABCD matrix using the conversion in [63].

4.1.1 Vector Network Analyser

A VNA or Vector Network Analyser is an instrument used to measure network parameters, such as amplitude and phase properties, of electrical networks to calculate s -parameters. The VNA used in this thesis is an Agilent Technologies N5224A PNA with WR1.0-VNAX frequency extension modules. A simple electrical network is shown below.

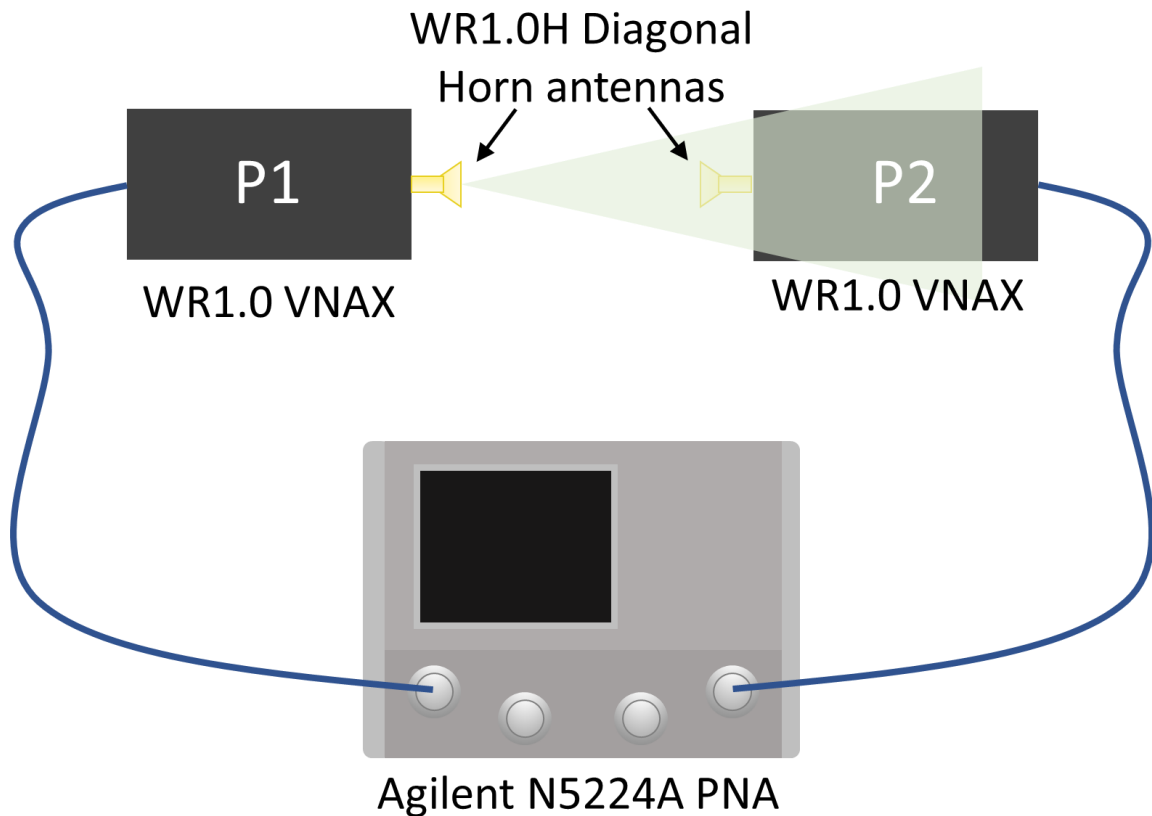


Figure 29: VNA module and frequency extenders used for s-parameter testing in this thesis. The PNA is specified for use in the region 10 MHz to 43.5 GHz, and the VNAX modules extend this to 0.75 THz to 1.1 THz.

The VNA module is specified for use between 10 MHz to 43.5 GHz. It is designed to measure s-parameters, as seen in Figure 28.

4.1.2 Frequency Extenders

WR1.0 VNAX modules with WR1.0H Diagonal Horn antennas allow the frequency of the VNA to be extended to between 0.75 THz and 1.10 THz. To allow for free space transmission measurements WR1.0H Diagonal Horn antennas with an 11° divergence are added to each extension module waveguide.

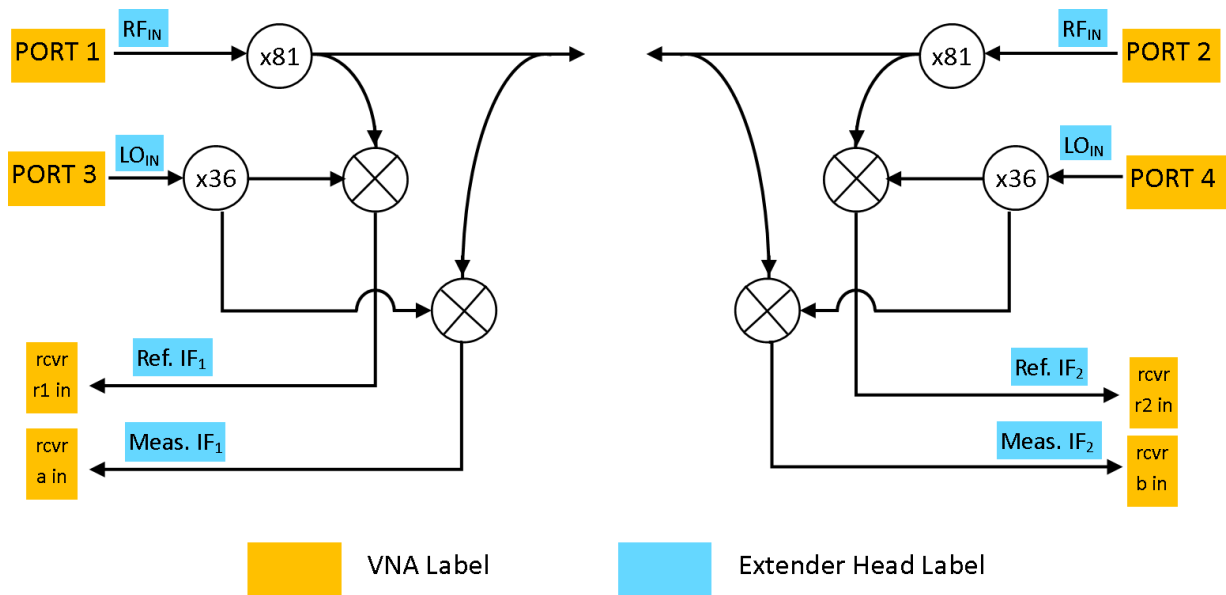


Figure 30: Simplified extender head module diagram with multipliers and mixers shown, alongside connection information for combining with Agilent N5224A PNA. Extender head 1 shown on left, 2 on right.

The VNA outlined in Section 4.1.1 provides inputs to RF_{IN} and LO_{IN} for both extender heads. The input frequencies can be varied, to allow combination with external analysis equipment. The default RF_{IN} frequency is 12.3 GHz and the default LO_{IN} is 300 MHz.

The extender heads each provide two outputs: Meas_{IF} and Ref_{IF}. The measured output (Meas_{IF}) is the received signal from the alternative extender head. This is normalised by the reference output (Ref_{IF}) of the extender head in question, within the VNA, to calculate the transmitted s-parameters.

4.1.3 Calibration

The VNA and extender heads can be calibrated as a single module, using a Short-Open-Load-Through (SOLT) calibration. This allows for losses up to but not including the horn antennas. The Virginia Diodes WR1.0 calibration kit provides three one-port reflection standards (shorted termination, open and load) and one transmission standard (1" through). These devices have been found to have an experimental standard deviation of up to 0.10 when measuring the reflection coefficient [64].

4.1.4 Additional equipment

An additional VNA which is used in conjunction with the VNA N5224A outlined above when an experiment requires greater than two inputs. It is Hewlett Packard 85047A S-parameter test set [65] with frequency range of 200 kHz to 6 GHz. In this thesis it is used purely as an additional signal generator, as the input analysis of the VNA N5224A is sufficient. A Tektronix RSA306B Real-Time Spectrum Analyzer is also used in this laboratory to analyse RF inputs between 9 kHz and 6.2 GHz.

A Giga-tronics Synthesized signal generator model 7100 was used for the testing of frequency multipliers as it can generate an input sine, square or triangle wave within a range of 10 MHz to 20 GHz [66]. The low harmonic content, -55 dBc between 50 MHz and 20 GHz, made this an ideal signal generator for testing frequency multipliers, which are characterised by their ability to produce and amplify harmonics from a clean signal.

The output of the frequency multipliers was analysed using a Keysight EXA Signal Analyzer N9010A, which functions from 10 Hz to 44 GHz [67]. This range allows frequency triplers to be analysed with an input of up to 11 GHz.

4.2 Fabrication Techniques

There are two key fabrication techniques explored in this thesis. The first is microlithography, a microfabrication process most used in the semiconductor industry to pattern devices with an accuracy of approximately 10 μm . Durham University has a clean room equipped for microfabrication using lithography techniques. The techniques used in this thesis are fully explored in Chapter 7: Antenna Fabrication and Testing.

The second fabrication technique is PCB printing. This is much faster, as it is fully automated. The majority of PCB printing machines require only a gerber input file to fully produce the specified PCB. However, the PCB printer used here is a LPKF laser and electronics s60 which only has an accuracy of approximately 200 μm , due to the size of tools accepted. The following section analyses the potential of PCB printing to produce the microdevices that are designed in this thesis.

4.2.1 Lithography

For many fabrication techniques, the pattern generation is completed using lithography. This is a printing technique, where the material properties of the “ink” cause it to remain in only specified locations when exposed to specific conditions. There are many types of lithography, such as x-ray and electron beam, which are also used in micro fabrication. Here, we analyse optical lithography, one of the most common techniques, and the one that has been applied in this thesis.

Optical or photo-lithography relies on the photo-dependent material properties of photoresist. When exposed to UV light, photoresist becomes either more or less soluble depending on its type. Here, we use positive photoresist, in which exposed areas become more soluble. Alternatively, negative resist would become less soluble under exposure of UV light.

The photolithographic process can be seen in Figure 31.

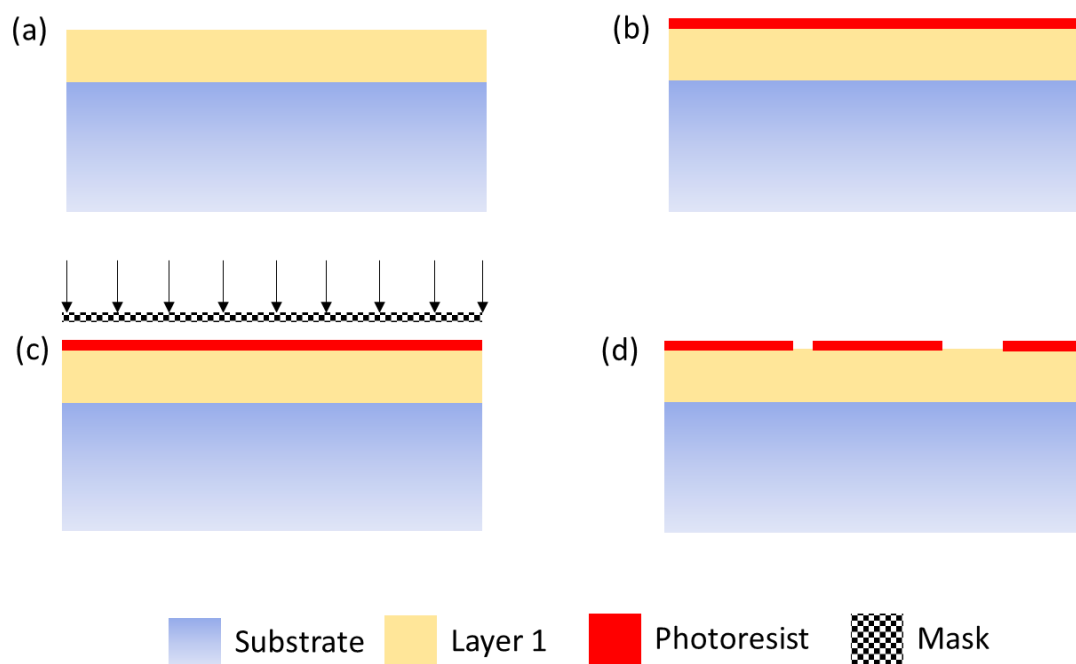


Figure 31: Overview of photolithographic printing process. (a) A layer that requires patterning is deposited onto a substrate; (b) photoresist is applied; (c) the photoresist is exposed to UV light through a mask; (d) exposed areas of photoresist are removed with developer. This mask can now be used to apply a pattern to or etch Layer 1.

With reference to Figure 31, a layer that requires patterning is deposited onto a substrate (a). Positive photoresist is applied in an even coating across this layer (b). The photoresist is exposed to UV light through a mask (c). Masks are printed acetate or glass sheets, depending

on the number of patterns to be printed. The printed areas on the mask block the UV light, and the clear areas allow transmission. The positive photoresist that has been exposed has increased solubility.

Photoresist developer is applied to the sample, which removes the soluble photoresist (d). There is now a pattern, in photoresist, on the sample. The remaining photoresist is simple to remove at any time with an acetone solution.

Dependant on the device under fabrication, the sample could now be etched. This etches the printed patten onto the layer below. Alternatively, an additional layer could be applied, before removing the photoresist underneath and leaving a patterned second layer. This is a technique known as lift-off.

4.2.2 Optical Lithography Limitations

The key limitation in optical lithography is the resolution that the pattern can be applied to the substrate to. According to Rayleigh's Criterion, "the minimum resolvable detail of two images through an optical system is diffraction-limited." This minimum resolvable detail, R , can be described by [68],

$$R = k_1 \frac{\lambda}{d}$$

Where λ is the wavelength of light, and d is the diameter of the circular aperture. Therefore, for a decreased wavelength, the minimum resolvable detail is smaller. k_1 is known as the k_1 factor, which is a constant used to describe environmental impacts on the resolution.

Therefore, not only can the resolvable detail be improved by decreasing the optical wavelength, but the k_1 factor can also be decreased. For standard geometries, these can be simplified to constants. If the diffraction is due to a circular aperture, the k_1 factor is 0.61, and for a slit is 0.5, The theoretical k_1 factor limit for a pattern of holes with space between equal to the hole diameter, is 0.25. The k_1 factor includes anything that can improve the imaging resolution, not just in optics but also by changing the surface layer and photomasks. This includes using phase-shifting masks, decreasing the surface roughness of the photoresist layer and applying antireflective coatings [68].

The fabrication process undertaken here includes a spin-coated layer of SU8. This produces a layer, where the thickness in the center is higher than at the edges. While the thickness was within the realms for acceptable antenna performance, lithography relies on a known gap between the resist and the mask. Variations in this thickness causes distortions of the pattern [69]. This effect was reduced by confining the pattern to the, relatively uniform, center portion of the substrate.

4.2.3 Printed Circuit Boards

PCBs are patterned using a technique known as PCB printing. The metal, usually copper, is removed either using a laser or milling bit to leave the specified tracks. In this thesis, PCB printing is completed using an LPKF laser and electronics s60 machine, with a microcutter 200 μm drill bit fitted. Vias are either added automatically using the s60 machine or manually with a pillar drill and 400 μm drill bit.

In this section, the capability of the PCB printing machine is tested. As the machine is used with a 200 μm drill bit it should therefore be capable of printing features of this size. Three track widths and gaps are investigated: 500 μm , 200 μm and 100 μm . 500 μm is chosen to view the usual capability of the printer, 200 μm to test at the extremes of the printer's capability, and 100 μm to see if this limit can be stretched. Figure 32 shows the test boards printed using the s60 machine.

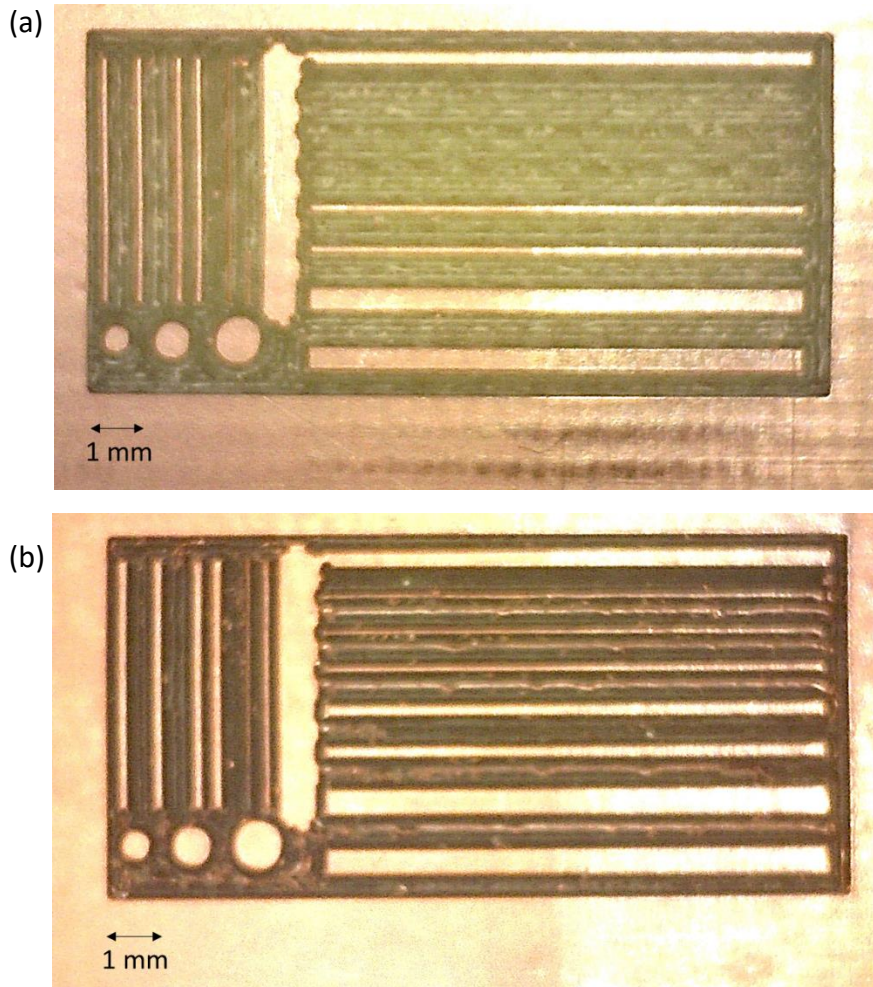


Figure 32: Test print boards with microstrips of varying width and gap size. Printed on (a) FR4 and (b) RT/duroid 5870.

Two PCB materials are tested. The first is FR4, shown in Figure 32(a), which is the standard substrate used with this machine. FR4 has a thickness of $400\ \mu\text{m}$, including two layers of copper with a thickness of $35\ \mu\text{m}$ [70], and a dielectric constant of 4.2 at around 3 GHz, but this varies considerably with frequency [71]. The second is RT/duroid 5870, shown in Figure 32(b). This has a low dissipation factor dielectric constant of 2.33, which is constant from 8 GHz to 40 GHz [72]. This makes it an ideal candidate for microstrip circuit design if PCB printing can be proved simple and effective under current standard manufacturing conditions. This is thinner than FR4, with a thickness of $127\ \mu\text{m}$ and a copper thickness of $18\ \mu\text{m}$ [72], and so fabrication settings in the s60 PCB printing machine must be adjusted for this.

Figure 33(a) shows the surface roughness of the FR4 test board, taken with a Dektak surface profilometer. The profilometer has a diamond stylus that is kept in contact with the test surface while scanning horizontally. The vertical profile is measured as a function of position. The Dektak can measure features from $0.01\ \mu\text{m}$ to $65\ \mu\text{m}$ [73].

This does not give a full profile of track width, as the material removed with the s60 is not restricted to copper, and some substrate is taken in the process. Therefore Figure 33(b) and Figure 33(c) are included, as these are microscope images of the 500 μm and 200 μm tracks respectively.

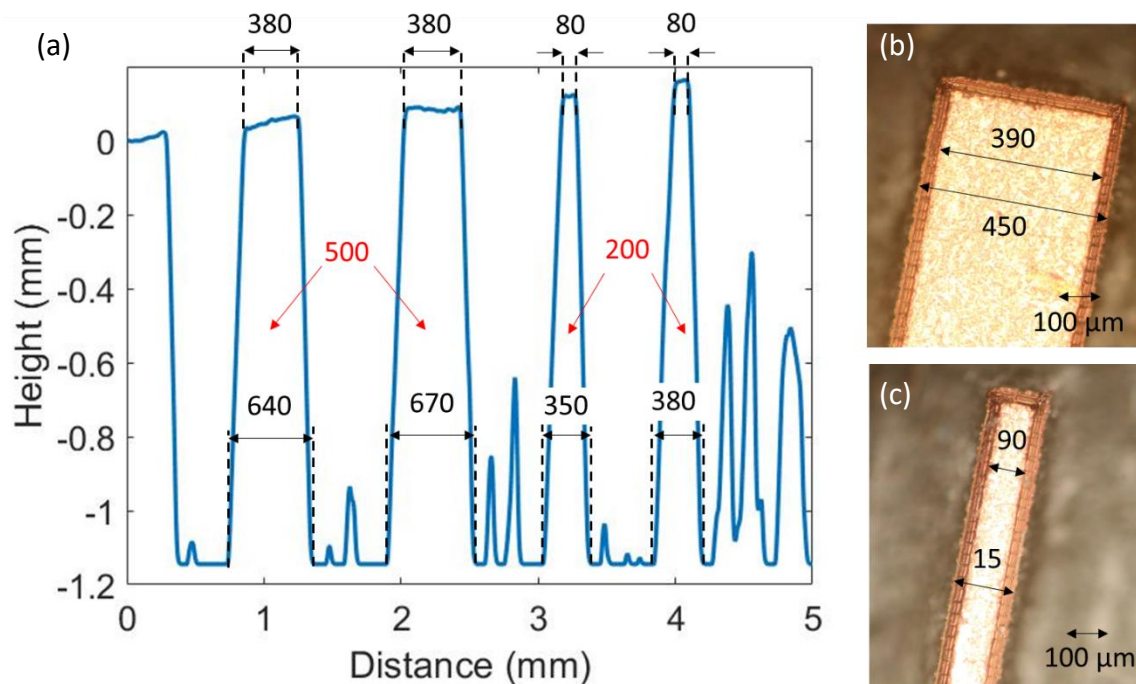


Figure 33: Analysis of PCB printing of tracks on FR4. (a) Profilometer measurements, red writing shows specified size, black shows measured size (b) microscope photo of 500 μm track, and (c) microscope photo of 200 μm track. Dimensions in μm . Peaks on right of (a) are rough surface of FR4 material after the top copper layer is etched.

As shown in Figure 33 the copper strips have been manufactured significantly smaller than specified. The inner measurements agree with the optical microscope measurements to within 10 μm . However, the outer measurement for both widths is significantly larger than that measured with the optical microscope. The clear conclusion from this is that the drill encroaches into the substrate material and does not merely remove the copper layer. As the drill has a tapered tip, the copper on top is drilled to a thinner track width than specified. Therefore, the mean of the microscope measurements is taken as the actual gap width.

The 500 μm line is fabricated with a width of 420 μm , and the 200 μm line fabricated to a width of 120 μm . Therefore, the print width is consistently 80 μm smaller than specified. The 100 μm tracks have not been included in this analysis, as they have not been successfully defined.

This same analysis can be repeated for the gap between tracks. Figure 34 shows the profilometer measurements and microscope photos for the 500 μm and 200 μm gap respectively.

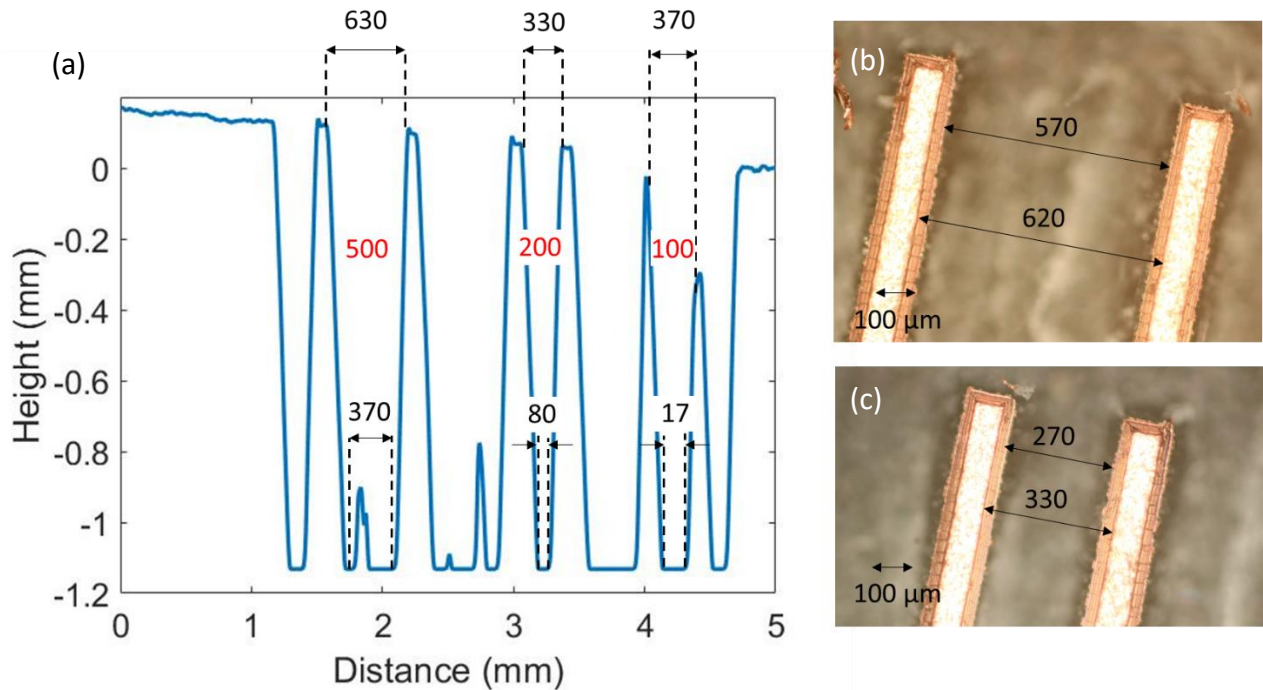


Figure 34: Analysis of PCB printing of gap between tracks on FR4. (a) Profilometer measurements, red writing shows specified size, black shows measured size (b) microscope photo of 500 μm gap, and (c) microscope photo of 200 μm gap. Dimensions in μm .

Both gap sizes are larger than specified, which is expected due to the smaller track width. Once again, the mean of the microscope measurements is taken as the actual gap width. Therefore, the 500 μm gap is measured as 600 μm and the 200 μm gap is measured as 300 μm . This shows a consistent over-mill of 100 μm . The 100 μm gap is not successfully fabricated, as the milling tip clearly cuts into the tracks on either side of the gap.

RT/Duroid substrates are designed with lower dielectric constants, which reduces parasitic capacitances between the ground plane and tracks. This is important for circuit design at GHz frequencies and above, where parasitic capacitances can cause components to act as short circuits. Figure 35 (a) shows the surface roughness of the RT/Duroid 5870 test board. Figure 35 (b) and (c) show microscope images of the 500 μm and 200 μm tracks, respectively.

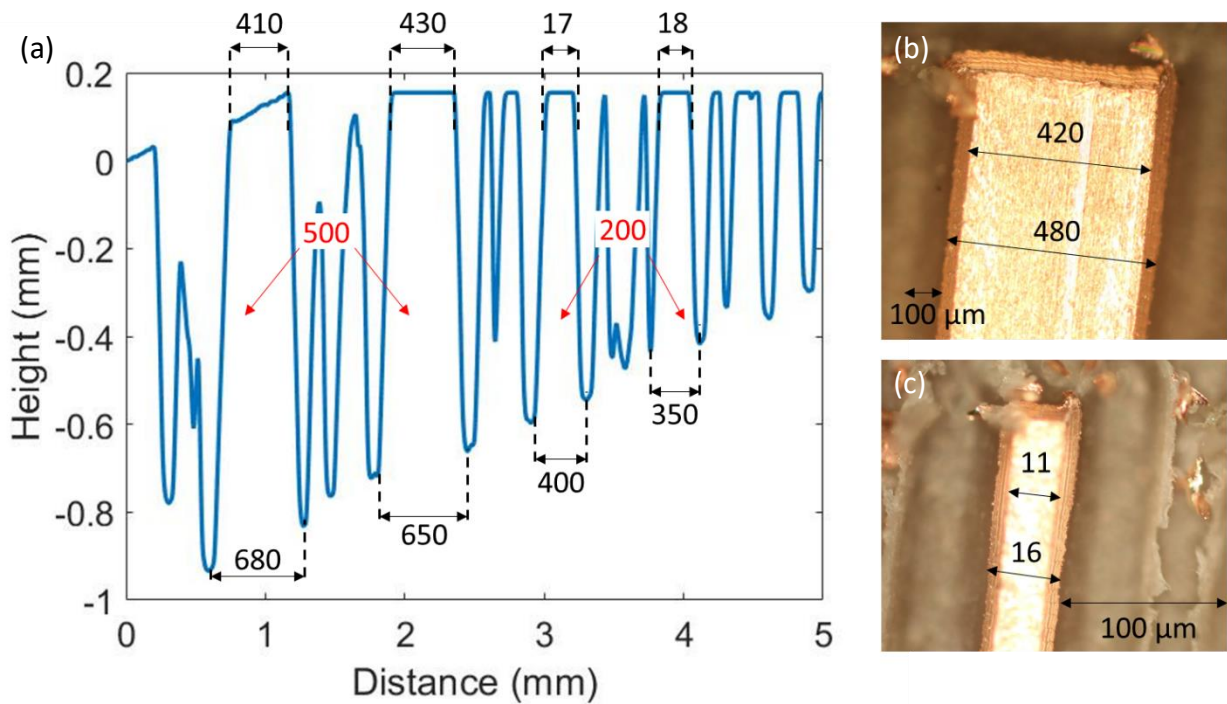


Figure 35: Analysis of PCB printing of tracks on RT/Duroid 5870. (a) Profilometer measurements, red writing shows specified size, black shows measured size (b) microscope photo of 500 μm track, and (c) microscope photo of 200 μm track. Dimensions in μm .

The 500 μm track is measured as 450 μm and the 200 μm track as 140 μm mm. Therefore, track fabrication is approximately 0.05 mm smaller than specified. This is half the error from the FR4 test board. This is perhaps lower, as RT/Duroid is thinner than FR4, and the PCB thickness is programmed in to the s60 PCB printing machine to avoid unnecessary cutting. For larger, lower frequency PCBs, this error is acceptable, but for fabrications with dimensions close to the limit of 200 μm , this must be accounted for.

Figure 36 shows the profilometer measurements and microscope photos for the 500 μm and 200 μm gap, respectively.

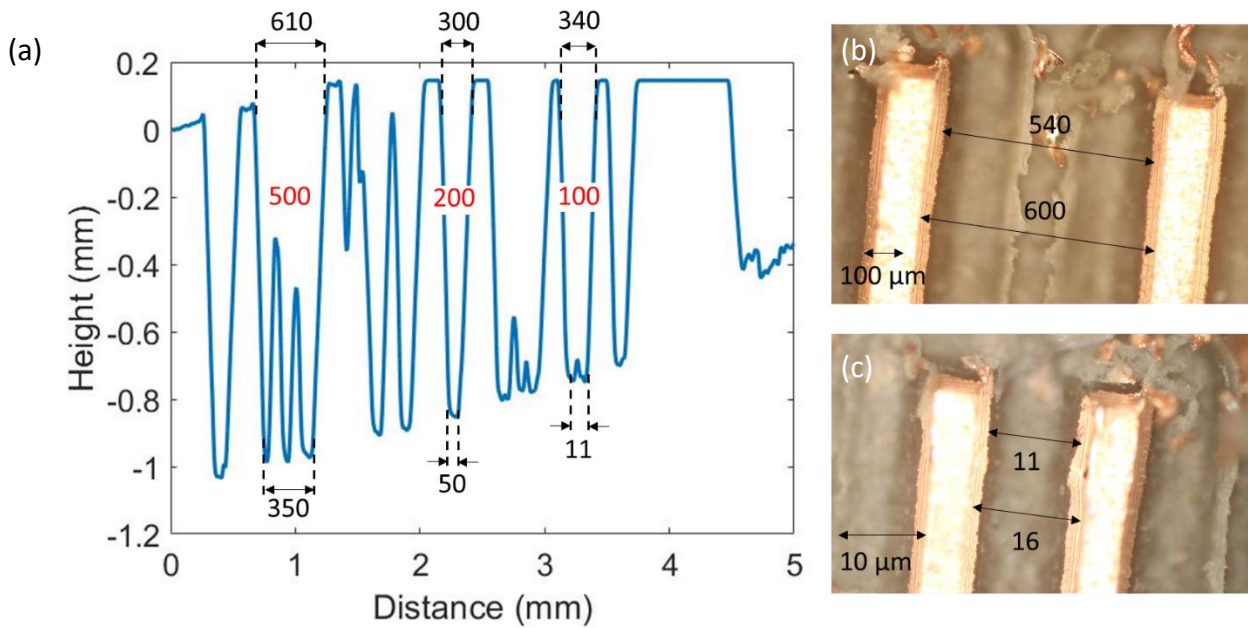


Figure 36: Analysis of PCB printing of gap between tracks on RT/Duroid 5870. (a) Profilometer measurements, red writing shows specified size, black shows measured size (b) microscope photo of 500 μm gap, and (c) microscope photo of 200 μm gap. Dimensions in μm.

The 500 μm gap was fabricated as 570 μm, and the 200 μm gap 140 μm. This shows inconsistent gap fabrication, highlighted further by the visible 100 μm gap on the profilometer measurement. This shows a measured gap of 340 μm, larger than the gap shown when 200 μm was specified. Therefore, the s60 is not capable of producing consistent gap sizing at 200 μm and below, and fabrication of components that require precise manufacturing such as coupled-line bandpass filters should possibly be avoided.

4.3 Conclusion

This section has covered the measurement and fabrication techniques that are used in this thesis. The measurement techniques include using a vector network analyser, frequency extenders and other additional measurement equipment in both the Durham University terahertz laboratory and communications laboratory. The fabrication techniques are primarily lithography and PCB printing. The in-depth lithographic processes are covered in Chapter 7 with the fabrication on terahertz antennas. The PCB printing on FR4 and TR/Duroid 5870 is fully analysed in this chapter, especially in reference to the accuracy in printing 500 μm, 200 μm and 100 μm microstrip lines. For FR4, there is found to be a consistent overmilling of 80 μm, and for RT/Duroid 5870 an overmill of 50 μm. For both PCB boards, this meant milling microstrip lines of 100 μm was unfeasible.

Chapter 5: Genetic Algorithms

This section introduces the concept of a genetic algorithm, and presents Agenoria, a GA developed for the purpose of optimising electromagnetic components without requiring prior in-depth knowledge of their operating procedure.

5.1 Background

The concept of a “*learning machine*”, which could reflect the principles of evolution was proposed by Alan Turing in 1950 [74]. He suggested, instead of trying to imitate an adult mind through computing, “*why not rather produce one which simulates the child’s?*” He drew similarities between trying to simulate the brain of a child and the evolutionary process as such:

“Structure of the child machine = Hereditary material

Changes of the child machine = Mutations

Natural selection = Judgement of the experimenter”

These three statements clearly show the building blocks on which all computational genetic algorithms have been based. Turing goes on to state that survival of the fittest is a slow procedure, that this method, with the inclusion of an “*experimenter*”, should be able to speed

up by providing external intelligence on the most important parts of the child machine's structure and honing these through targeted mutations.

While Turing's paper focused purely on the theoretical concept of computation evolution, it was only 4 years before computer simulation of evolution began. Nils Aall Barricelli published "*Esempi Numerici di processi di evoluzione*" in 1954 [75] (republished in English in 1957 [76]). This released the results of a simulation, ran at the Institute for Advanced Study in Princeton, NJ, in 1953. The simulation is based on a grid of numbers, where the numbers move around the grid based on rules specific to each number. When a "*collision*" occurs between two numbers reproductive algorithms occur (generating a new child number from two parent numbers). Barricelli used this basis to produce a series of evolutionary algorithms optimising gaming strategies, specifically in the game Tac Tix [77, 78]. The algorithm produced results with little practical use, as could be easily beaten by a human beginners' tactics.

At a similar time, geneticist Alex Fraser, published a series of papers on computational simulation of biological organisms [79]. The first of these was in 1957 [80] and is the first recorded use of computers to study genetic systems. The focus was on artificial selection of organisms to optimise a measurable trait.

At a similar time to Fraser's introductory paper, Box [81] suggests using evolutionary algorithms to optimise factory production. Minute changes are applied to online systems with the changes in production process recorded as a fitness. This could be viewed as the first use of mutation in an evolutionary algorithm. Fogel and Maxfield [82] uses this concept to design a Mealy finite state machine via a genetic algorithm including both reproduction and mutations. The state machine's fitness is tested on its ability to predict its environment, i.e. the next symbol received.

The combination of these research areas, fore fronted by Barricelli and Fraser can be seen as the precursor to genetic algorithms. These are first seen in their current form in the work of Hans-Joachim Bremermann. His series of papers, published in the 1960s, attempt to optimise a variety of problems [83]. However, instead of focusing on finding a particular result, Bremermann mostly focused on optimising the algorithm itself. This has led to a wide range of uses and his techniques are still reflected in many modern genetic algorithms.

The optimization of passive THz components, such as filters and antennas, is typically based on the well-established numerical methodologies developed for microwave frequencies. However, these methods are not well-suited for optimisation against a target performance (e.g., power efficiency) at THz frequencies, as they tend to result in more complex geometries that cannot be readily realised at the micrometre-scale. Genetic algorithms (GAs) have been successful at developing new devices and antennas at MHz and GHz frequencies [84, 85] but their use in THz component design is still largely unexplored.

Compared to other numerical methods, GAs are more likely to scale well to THz frequencies because they can optimise within many constraints at once. The challenge of manufacturing at the micrometre scale can be avoided by specifying constraints such as minimum feature size. Another advantage of GAs is that they can optimise over a wide band of frequencies concurrently, which is difficult to achieve using conventional design techniques.

Genetic Algorithms have many advantages over more traditional optimization techniques. These include the ability to be applied to any problem, whether they have continuous or discrete parameters, and regardless of whether the data is collected through simulation or experiment. The number of variables is no barrier and no prior knowledge of the problem is required, which means problems with complex cost functions can also be optimised. They provide analysis over the entire solution space to give a list of possible results, not just a single answer [85]. Finally, they can be easily parallelised to allow increased speed of optimisation. For these reasons, GAs have been investigated for a wide variety of disciplines, such as aerospace [86], astrophysics [87] and psychology [88]. In electromagnetics, optimisation has included the geometry of antennas and arrays [89], Electromagnetic compatibility problems [90] and impedance matching [91].

5.2 Introduction to Genetic Algorithms

GAs use Darwinian evolution as a metaheuristic computational technique to find optimised solutions to a variety of problems. The algorithm is initialized with a collection (or population) of designs (referred to as individuals), represented by a vector (the genome) which contains all the required parameters (the chromosomes).

The population of n genomes can be written as

$$[G_1, G_2, G_3 \dots G_n] \quad (5.1)$$

For the individual with Genome, G_2 , with m Chromosomes, K, could be written as.

$$G_2 = [K_1, K_2, K_3 \dots K_n] \quad (5.2)$$

For a given fitness test, the probability that genome G_2 is chosen to reproduce via combination could be written as

$$P(C_{G_2}) = 2P(Ccombination Selection) \quad (5.3)$$

The probability of combination is usually set for each algorithm, based on theory presented in section 5.2.1. This probability is doubled as two individuals are selected each time.

The probability that chromosome C_{53} is carried forward to the next generation, given its host individual has been selected for combination is

$$P(C_{C_{53}})|P(C_{G_2}) = 0.5 \quad (5.4)$$

Given that each chromosome of the two individuals has equal chance of being picked.

For a given fitness test, the probability that genome G_2 is chosen to reproduce via mutation is simply,

$$P(M_{G_2}) = P(Mutation Selection) \quad (5.5)$$

The probability of an individual being selected for mutation is also set for each particular algorithm use case.

If an individual has been selected for mutation of two individuals, the probability that chromosome C_{53} is carried forward to the next generation is

$$P(M_{C_{53}})|P(M_{G_2}) = 1 - M \quad (5.6)$$

Where M is usually the mutation variable, which describes how much mutation is required in a given individual. The probability of the chromosome being passed to the next generation unaltered is therefore 1-M.

Therefore, the probability of any given chromosome, x , from genome, y , being passed to the next generation unaltered (given both mutation and combination are allowed to happen to the same individual) is

$$P(C_x) = P(C_{C_{53}}) + P(M_{C_{53}})$$

$$P(C_x) = P(\text{Combination Selection}) + (1 - M)P(\text{Mutation Selection}) \quad (5.7)$$

This is an iterative process where the individuals of each generation are used as the parents for the next (their progeny). The initial population is often randomly generated. The individuals are subject to selection through a fitness test; the fittest individuals are used to create another generation using genetic reproduction. The algorithm is terminated at a set fitness level, number of generations, or after maximum fitness stagnation [92]. The best output is normally called an evolved result or device. This procedure is outlined in the flow diagram shown in Figure 37. These algorithms can be written to evolve the shape of components to maximise a specific fitness function which describes the desired component behaviour.

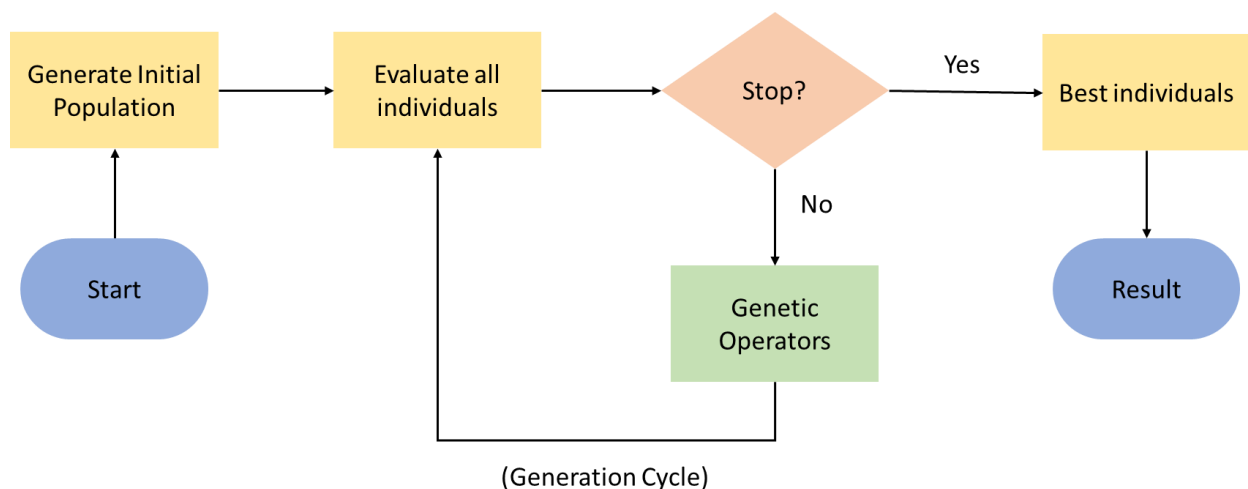


Figure 37: Basis of a genetic algorithm, shown as a flow diagram. The algorithm is initialised by generating the first population. The individuals of this population are evaluated based on their performance. If the performance has reached an acceptable level, the algorithm is stopped, and the best individuals outputted. If not, genetic operators are applied, which produce a new generation of individuals, ready to be evaluated. This cycle continues until an acceptable solution has been found.

The initial generation is designed to include a cross-section of a likely population. It is vital that there is sufficient variation in this population, so the algorithm does not immediately converge on a non-optimal solution. This initial generation can be generated manually or through machine learning techniques but is usually generated at random.

The population evaluation entirely depends on the optimisation problem to be solved. In Barricelli [77], the evaluation would depend on the result of an automated game, whereas in electromagnetic optimisation scenarios this could be the output of a simulation based on Maxwell's equations.

5.2.1 Genetic Operators

Genetic reproduction consists of three operators: *cloning*, *crossover*, and *mutation*. Cloning is the duplication of an individual so that the progeny has the same chromosomes as the single parent. Crossover is the combination of two parents to produce a single progeny. Mutation is the application of localised, often random, changes to the genome of a single parent to produce one new individual. Before the individuals can be mutated or combined, the parents must be selected.

Crossover

The purpose of crossover is to combine favourable characteristics from well performing individuals. There are varying crossover methods that have unique benefits. Fraser's [80] reproduction algorithm uses a one-point crossover algorithm, where variable positions between genomes on the genetic string have a set probability of breaking to combine with another individual's broken genetic string. This is useful when consecutive genomes have an impact on each other and therefore it is ideal to keep local sets of genomes intact. Bremermann [83] implements crossover with each chromosome (bit) within the genome considered in isolation. Each progeny chromosome is selected independently with equal probability from either parent's corresponding chromosome. This is useful when genomes have little to no effect on each other. This technique has the benefit of being very fast at finding local maxima.

Mutation

Mutation is used to add new, unique chromosomes. This can be used to increase variation in a population, or to tweak one well performing individual in the hopes of locating which genome causes this high performance. The rate of mutation in a human population, calculated through genome sequencing from a family consisting of two siblings and their

parents, is estimated to be in the order of 10^{-8} per position per haploid genome (half set of paired chromosomes) [93]. Mutations in genetic algorithms are usually set at around 10^{-3} , as they attempt to speed up the evolutionary process. Higher mutation rates reduce the tendency of genetic algorithms to quickly converge on local optima. Instead, a wider range of prospective designs are considered, so increasing the probability of finding global optima.

Fogel and Maxfield [82] shows the algorithm converges slower if multiple mutations are allowed. They set the likelihood of mutation as function of the range of fitness score. When individuals start to converge, greater effort is given to finding another peak through the creation of “*radical*” offspring. These are offspring with a previously unseen set of chromosomes, unlikely to occur through reproduction. Fogel and Maxfield [82] also shows larger populations and more surviving offspring produces more possible peaks but at a lower efficiency.

Parent Selection

Fraser [80] explores different techniques of optimisation through varying methods of parent selection. Function maximisation is fastest when only the fittest parents are chosen, otherwise known as “*hard selection*”. This causes the algorithm to climb localised peaks with no concern for global optima. However, selection can be stabilised through choosing mean fitness individuals, or through “*soft selection*”. This slows peak climbing by ensuring greater effort goes to locating alternative peaks. Therefore, by keeping a minority of less fit individuals, a reasonably fast but stable approach towards function maxima is achieved.

Pincus [94] and Galar [95, 96, 97] analyse the effect of using either hard or soft selection on early peak convergence. Pincus [94] notes that soft selection reduces stagnation around peaks, leading to quicker rates of escaping local minima. Hard selection is more efficient at finding local maxima. Galar [95] shows that radical individuals and small fitness peaks are more likely to be created from the mutants of mutants formed in a soft selection process. Galar [96] [97] analyses time taken to cross between maxima peaks in a multimodal fitness landscape. Soft selection completes this, on average, 30 times faster than hard selection. Galar [97] suggests algorithms should switch between the two techniques to optimise convergence rate and saddle crossing rate alternatively.

5.2.2 Algorithm Termination

The algorithm can be terminated whenever the user sees fit. This could be at a target goal, for example, Barricelli [77] would stop the algorithm after a successful win, or a set number of generations. This is most useful when the evaluation procedure is computationally intensive, and the run time spans over several days or weeks. The final option is to wait for a fitness convergence. This may not always occur, but once it does there is no option but to stop the algorithm as further improvement is unlikely. Great effort is often put into ensuring premature convergence does not occur for this reason.

5.3 Agenoria

Agenoria is a genetic algorithm developed during this PhD, for the purpose of designing electromagnetic components. This is open-source software and available on to use on GitHub [98]. It allows optimisation of a wide variety of passive components, such as filters, circulators, and impedance matching networks [99, 100]. The fitness test is the only major component of the algorithm that needs to be specifically adapted to the individual use case. The reproductive stages are entirely self-adapting. The fitness test provides one score for each simulated individual, combining weighted simulation outputs. For instance, weighting antenna gain at the frequency of interest against that across the remaining spectrum.

Figure 38 gives an overview of the working principle of Agenoria. It is similar to the generic GA shown in Figure 37. The primary difference is the choice of a FDTD- finite difference time domain simulator, which will be used for all simulations. This has been chosen as all systems optimised with Agenoria are electromagnetic based.

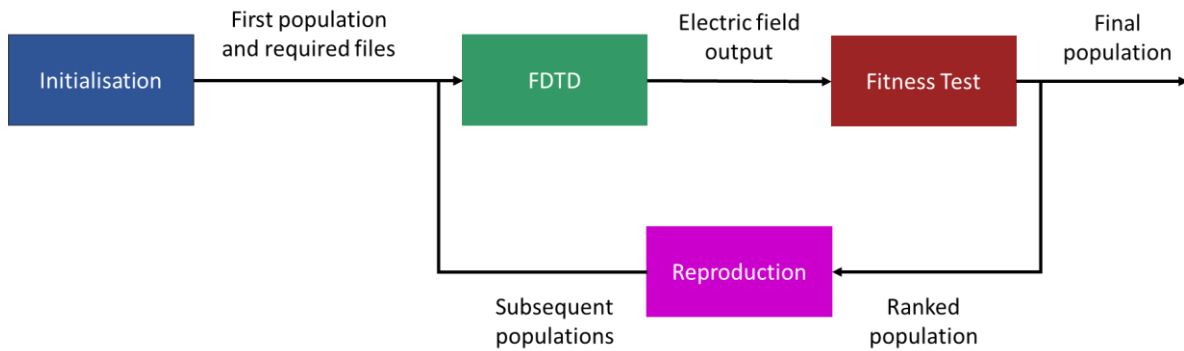


Figure 38: Overview of the genetic algorithm, written for this project. The algorithm is initialised with a population of individuals, and the required files (config/ geometry) generated. The individuals are passed through an FDTD algorithm to determine their EM response. The output of this influences their score in a fitness test, which ranks the population from best to worst. The algorithm is then either stopped (if the generation has been sufficiently high performing) or continued to reproduction algorithms. These are applied to produce a new generation of individuals containing features previously found to be successful. These individuals are passed through the FDTD, and this cycle continues.

The number and the size of generations is varied based on parameters such as the number of constraints, the required convergence time, and the disk space available. The initial generation is formed of 2D or 3D arrays describing the set of objects to be optimised. This could be an antenna, waveguide or other THz device, but must be describable in cubic elements.

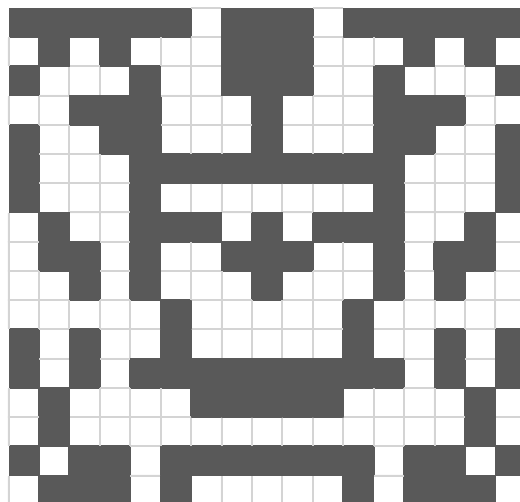


Figure 39: Example of an array/individual to be optimised in the genetic algorithm, where grey represents one material (i.e metal) and white another (i.e free space).

The cubic elements are each allocated a binary value, which describes their material. The list of binary entries can be written as a string, or a “genome”. Therefore, every individual can be described by a unique genome representing their shape.

5.3.1 File Allocation

Before the algorithm is initialised, all files are automatically produced via Matlab script, as shown in the figure below. The files, *Produce_files.m*, *initial_generation.m*, *Runlucifer*, *Fitness_Test.m*, *GA.m*, *Mutation.m* and *Crossover.m* start in the folder used for that simulation. Folders Gen1 to Gen50 inclusive are then produced by running *Produce_files.m*, which then populates these folders by producing a *Config*.py* and *Geom*.py* file for each individual and copying a generic *Source.py* file into each generation. The bash script *Runlucifer* is then executed, which first runs the file *initial_generation* to produce all individuals in the first generation, then begins to execute the genetic algorithm, as will be explained in this section.

The *initialisation* step of the algorithm produces a population of individuals, each represented by a binary array of randomly generated chromosomes. With reference to Figure 38, in this step, the required configuration, geometry and source files are also produced.

These individuals are passed into the *FDTD* simulator, *Lucifer*, which uses the generated files to subject the individuals to a described set of simulation conditions. The output of this simulation is the measured electric field at a described location.

This electric field output is used to influence the fitness test, *Fitness_Test.m*, which ranks the individuals from best to worst based on their performance.

This ranked list is passed to the *reproduction* stage, which uses genetic operators to combine characteristics of high performing individuals to produce the next generation. To complete this, the *Runlucifer* bash script calls a Matlab file, *GA.m*, which specifies the rate of mutation and combination in any given generation. The *GA.m* script is responsible for calling the scripts *mutation.m* and *combination.m* as appropriate. Finally, the loop continues, and the data files produced by the previous generation are deleted as one generation can take up to 300 GB of space. This is an iterative process where each generation is used as the parents for the next. The algorithm is terminated at a set fitness level, number of generations, or after maximum fitness stagnation [92].

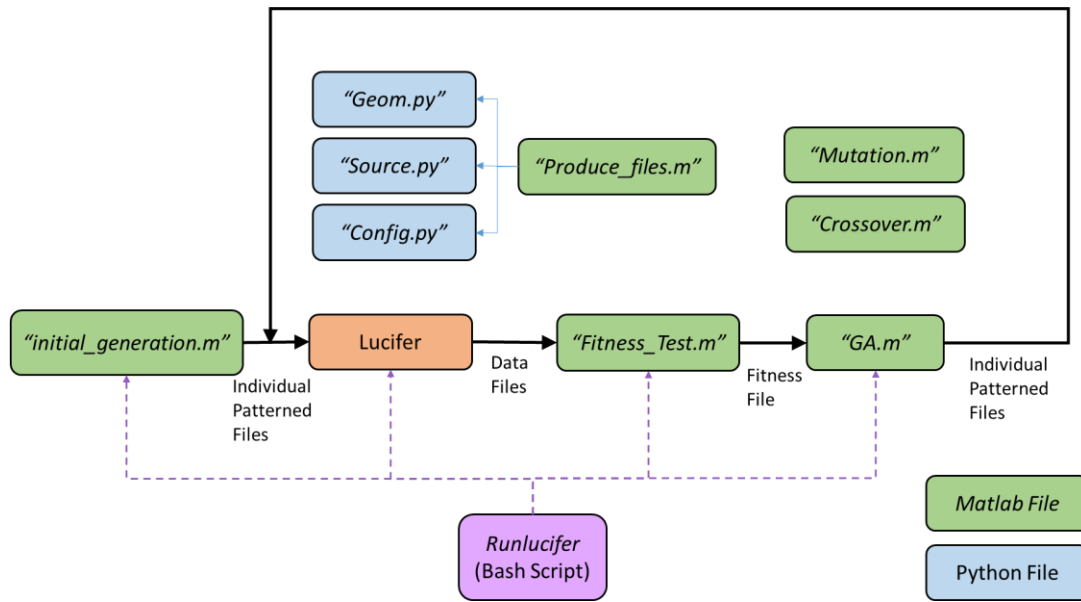


Figure 40: Genetic algorithm file system. Geometry, source and configuration python files are generated specifically for each individual using a Matlab script. Then a bash script, 'Runlucifer' is used to run each of the required files in turn, until a set number of generations. At this point, the result is analysed in person, to decide if further generations would be productive.

The next section describes how each of these stages have been implemented.

5.3.2 Initialisation

Figure 41 describes the initialisation through first generating a population of individuals (stage 1), and then a configuration and geometry file for each individual (stage 2). As each generation is held in a separate folder, a source file is also copied into each generation.

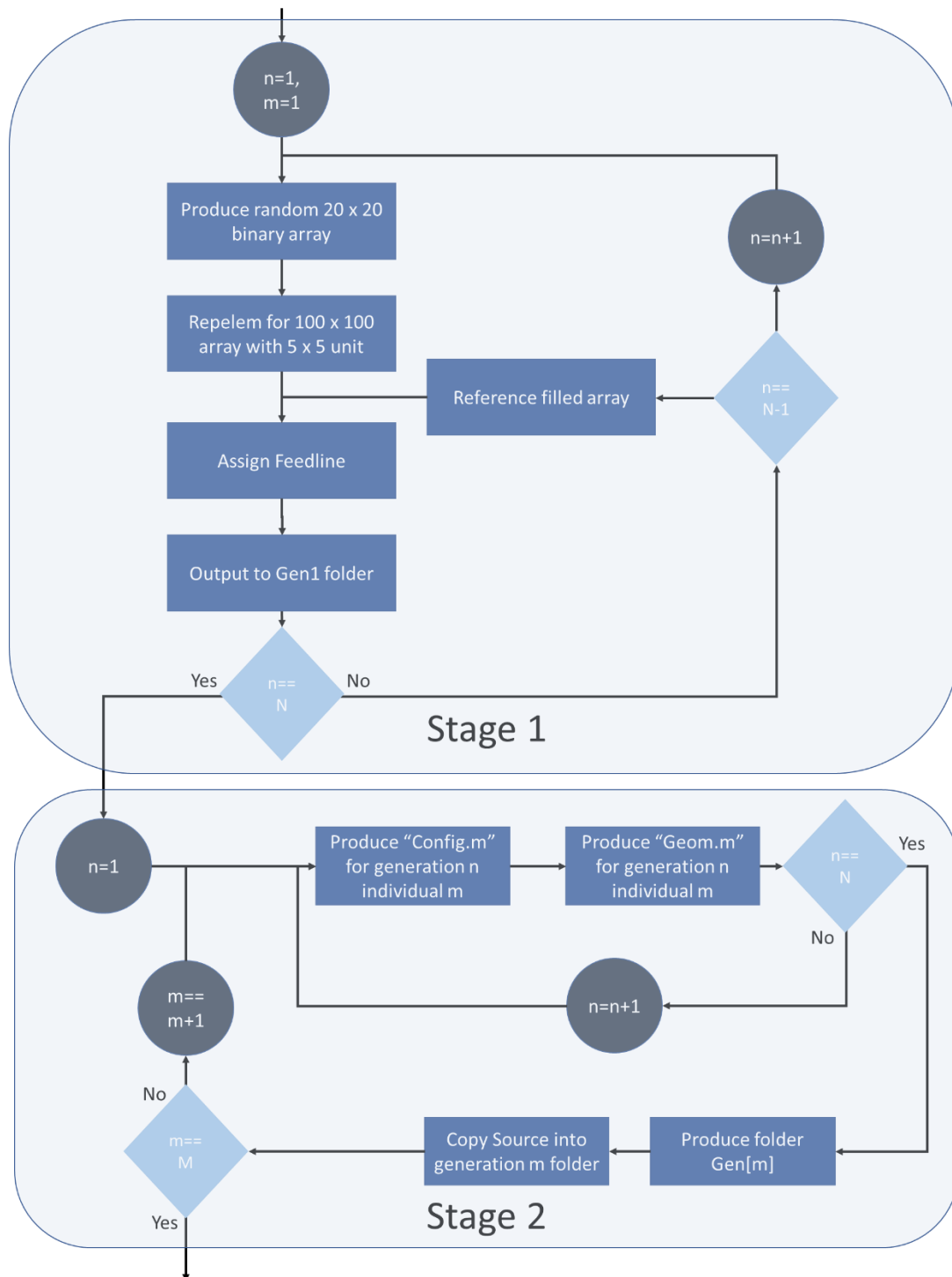


Figure 41: Initialisation of Genetic Algorithm, where N is the number of individuals in the first generation. n is used as an integer to cycle through stage 1 of the algorithm, until all individuals have been generated, m is used to cycle through stage 2, which generates the configuration, geometry and source files required for the algorithm.

The loop, *Stage 1* describes the production of the randomly generated first generation of individuals. This is completed through a Matlab file, *initial_generation.m*, which randomly produces every individual patterned file in the first generation. For a 100 μm by 100 μm (x by y) shape, with cell size 1 μm , the array is initialised with a random 100 by 100 binary array

using the *randi* function. If a minimum feature size is required, a smaller array is made first, then magnified using the *repelem* function. The feed is then assigned to the full-size array, and the array written to a binary file using *dlmwrite*. A reference fully filled array is also included.

Stage 2 describes the production of the configuration and geometry files for each individual, which is completed using a Matlab file, *Produce_files.m*, which produces the python scripts required for simulating of all the individual throughout the algorithm. It starts by making folders for a specified number of generations and produces every configuration and geometry file required for each of these. The configuration and geometry files are individual to each individual configuration. The source file is identical for all simulations in one algorithm and so this is copied into each generation's folder rather than generated uniquely.

Finite Difference Time Domain (FDTD)

A finite difference time domain simulator will be used for all optimisations presented in this thesis. The FDTD method has been outlined in full in Section 3.1. However, this genetic algorithm has also been integrated with Matlab simulations successfully [99].

Fitness Test

This is the only part of the algorithm that must be changed depending on what device is being optimised and its required characteristics. Each fitness test will be expanded upon in Chapter 6 with the relevant results.

5.3.3 Genetic Operators

The reproduction algorithm receives a ranked list of every individual in the generation. This list is used to inform the creation of the next generation. Genetic reproduction was performed in MATLAB and consisted of three operators: *cloning*, *crossover*, and *mutation*. Cloning is the duplication of an individual so that the progeny has the same chromosomes as the single parent. Crossover combines two parents to produce a single progeny. This is implemented as in Bremermann [83], where each chromosome (bit) within the genome is considered in

isolation. Each progeny chromosome is selected independently with equal probability from either parent's corresponding chromosome. Mutation applies random changes to the genome of a single parent to produce one new individual. The mutation algorithm is implemented by inverting a small number of chromosomes within the parent genome. Each bit has a 5% probability of being inverted.

These three operators are used to create progeny from parents as follows:

- 1) The best 10% of individuals are carried through to the next generation unaltered (cloned); this ensures that there is never a decrease in fitness score between generations. This technically happens in the fitness test stage, as the fitness scores are copied from one generation to the next.
- 2) The top 50% undergo crossover and mutation to produce new designs, combining favourable characteristics from well-performing individuals. These account for 85% of the next generation. When the algorithm starts to converge, as detected by a decrease in the range of fitness scores, the ratio of progeny produced by mutation compared to that produced by crossover increases. This reduces the probability of premature convergence on local maxima by producing *radical* offspring. These are individuals with a previously unseen set of chromosomes, which are unlikely to occur through crossover alone.
- 3) A small, random sample of individuals from across the whole parent generation (including the bottom 50%) undergo crossover to produce the remaining 5% of the progeny; this maintains design variation, to further guard against premature convergence.

Figure 42 describes this process in full.

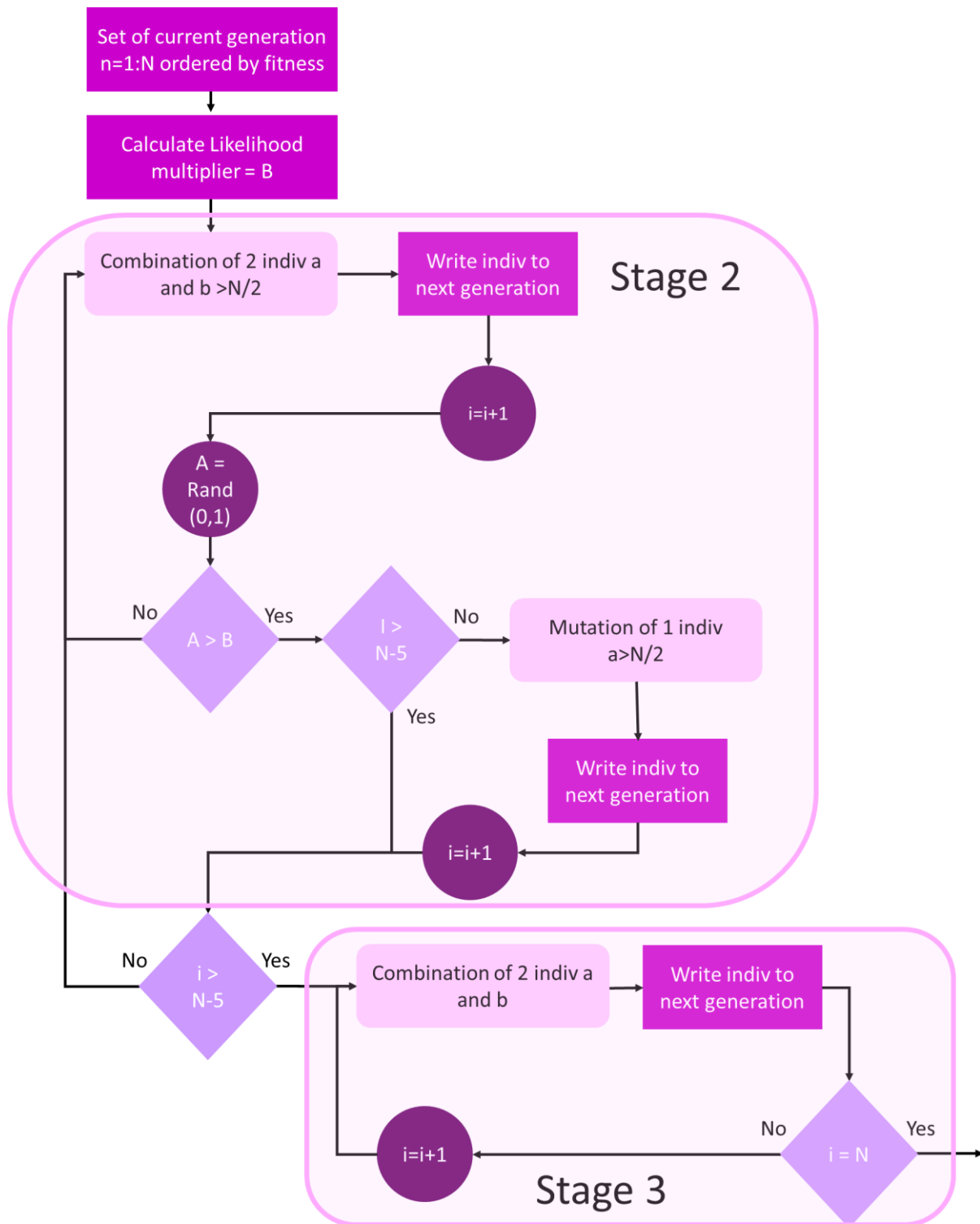


Figure 42: Reproduction algorithm flow diagram. Stages 2 and 3 refer to numbered list above diagram.

After the ranked generation has been loaded, the first step is to calculate the likelihood multiplier, B , which is used to calculate the likelihood of mutation in each generation. This is calculated from the range of fitness scores in the generation, and ensures if the designs are converging, there is a higher chance of mutated, and therefore radical, individuals. Individuals

are then selected from the top 50% for crossover. For every individual that undergoes crossover there is a possibility (based on the likelihood multiplier) that one individual from the top 50% will undergo mutation. When the population has been filled to ~90% (or 5 spaces remaining), depending on generation size, the final spaces are populated with individuals from individuals ranked in the bottom 50%.

Figure 43 describes the combination algorithm in full.

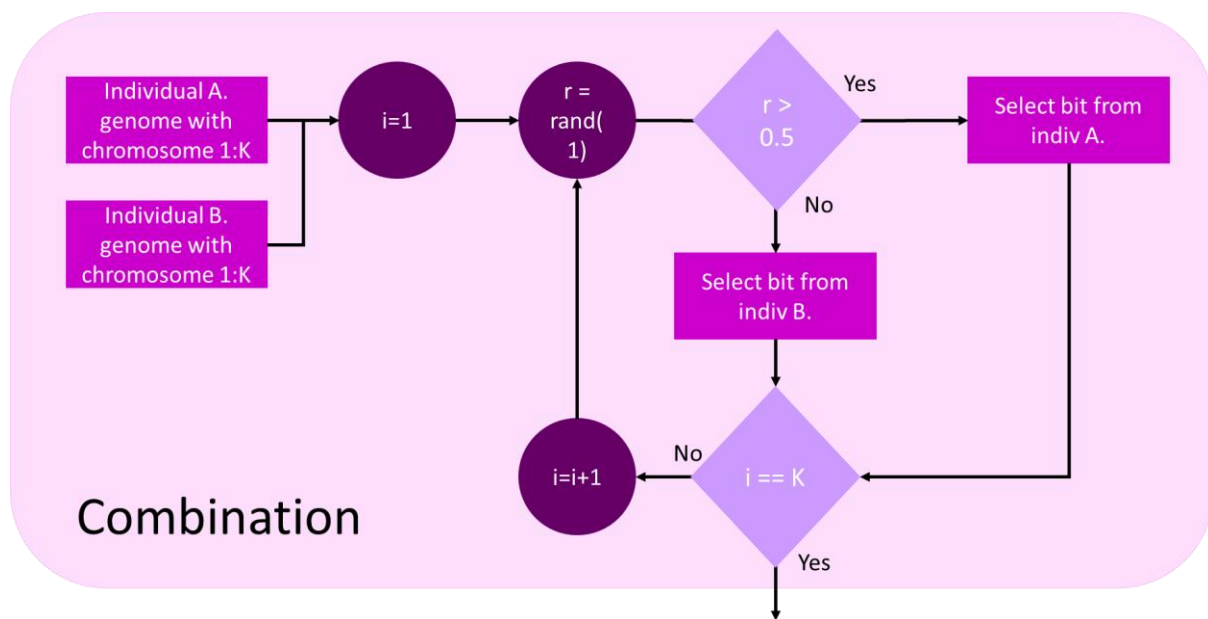


Figure 43: Combination algorithm flow diagram. Two individuals, A and B are selected to undergo combination to produce a child design. A random number generator, r , between zero and one is used to select which individual will provide the first bit or chromosome. If $r > 0.5$, individual A is chosen, if $r < 0.5$ individual B is chosen. The first bit of the chosen individual is then copied to the child design. This process is repeated until the child has an identical number of chromosomes to the parents.

Figure 44 describes the mutation algorithm in full.

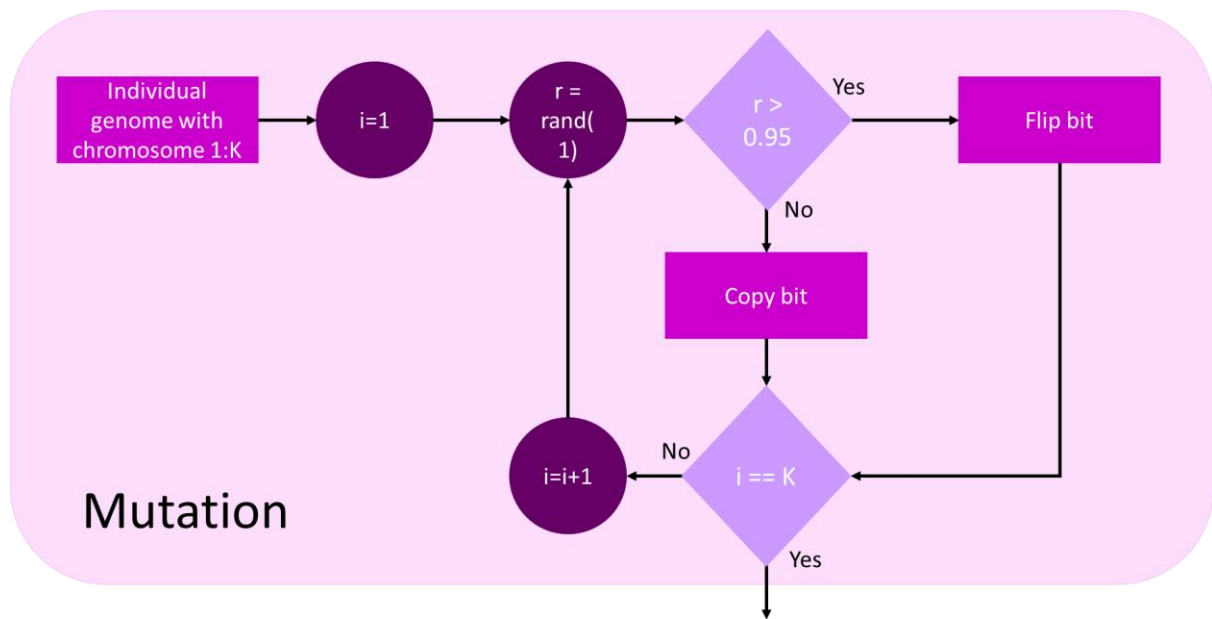


Figure 44: Mutation algorithm flow diagram. One individual is selected to undergo mutation, and the first bit selected. A random number generator, r , then produces a number between zero and one. If this number is smaller than 0.95, the selected bit is copied to the child design with no change. The algorithm then increments to select the next bit. If r is larger than 0.95, the parent's bit is "flipped" (from 0 to 1 or from 1 to 0) before being allocated to the child. This process is repeated until the child has an identical number of chromosomes to the parent.

5.4 Conclusion

A genetic algorithm, Agenoria, coupled to a finite difference time domain simulator, is presented for the optimisation of passive THz devices. This is a generic GA, designed to be capable of use with a variety of electromagnetic devices, only requiring that the dimensions or configuration under optimisation can be represented as an array. Genetic algorithms were chosen as, compared to other numerical methods, they are more likely to scale well to THz frequencies due to being able to optimise within many constraints at once. The challenge of manufacturing at the micrometre scale can be avoided by specifying constraints such as minimum feature size. The algorithm presented here will be implemented in Chapter 6 to generate a variety of candidate THz antennas.

Chapter 6: Antenna Optimisation

In this chapter, we present the optimisation of antennas using a GA. The antennas presented here are planar patch antennas. Conventionally, the patch is continuous, but this limits the performance of the antenna to narrow-band operation. By creating apertures in the patch, the antenna bandwidth can be extended, and its impedance tailored. This technique has been used before, such as by Islam [12]. This section investigates the viability in using genetic algorithms to design the location of these apertures.

6.1 Patch Antenna Principles

Patch antennas, designed by Howell [43], consist of a silicon substrate sandwiched between a flat metallic ground plane and a “patch” of metal, as shown in Figure 45. These are the most common cell phone antenna, as they are small (at microwave frequencies), two dimensional, and can be easily manufactured through microfabrication techniques such as lithography. Kleine-Ostmann and Nagatsuma [47] states planar structures “*could be a good solution for future commercial communication systems*” due to their “*flexibility, their potential for integration and their cheap and easy fabrication*”.

The two metal planes, either side of the substrate, act as a microstrip transmission line, therefore patch antennas are also referred to as microstrip antennas. As in a microstrip transmission line, waves generated within the dielectric are reflected by the metal layers. In a microstrip antennas, these reflections are radiated from fringing fields at the edge of the patch. Therefore, most of the radiation occurs output of the boundaries of the microstrip, which increases the effective length of the patch. The patch is commonly designed to have an effective length of a half-wavelength. This resonates the lowest order mode TM_{10} [101], causing interference in the fringe fields and increasing the magnitude of the radiated power.

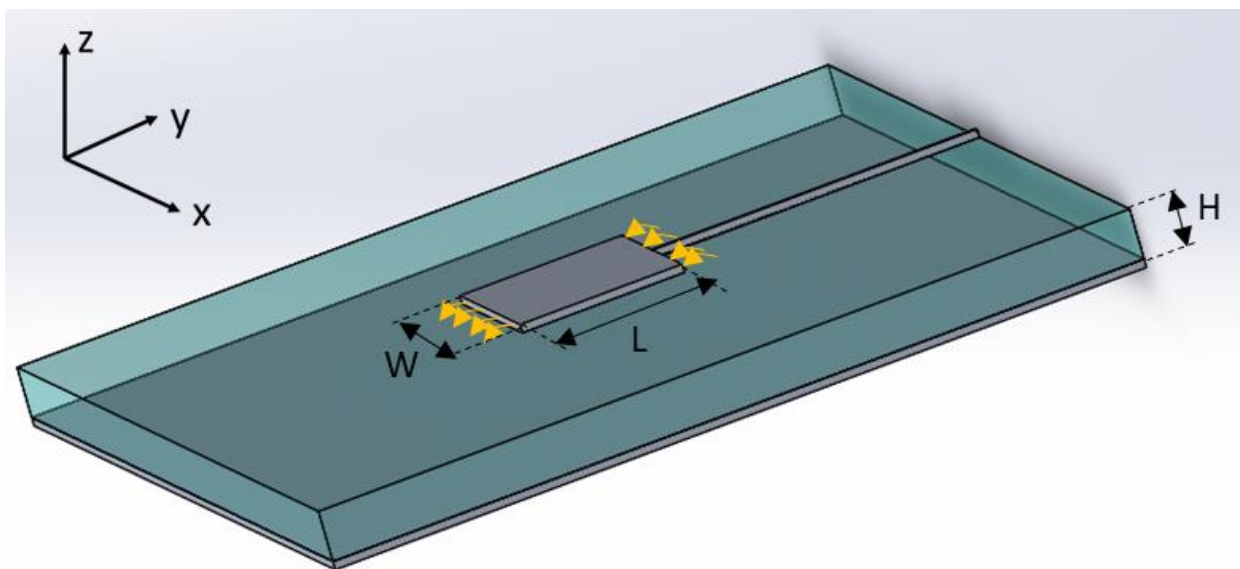


Figure 45: Patch antenna, substrate shown in blue with ground and patch (with feedline) shown top and bottom in grey. Electric field lines shown in orange.

Further development of patch antennas includes fractal patch antennas, where fractal geometry surrounds or replaces the simple patch. Sivia and Bhatia [102] states that the main advantages of these include “circular and linear polarization, low profile, light weight, low fabrication cost and mechanically robust when mounted on stiff surfaces.” Another popular antenna is the compact, multiband microstrip antenna. Shah et al. [103] shows that a multiband microstrip antenna can be miniaturised by shorting the patch and ground plane and using a defected ground structure created from a combination of U and L-shaped slots. This miniaturisation makes the antenna ideal for mobile communications. Singh et al. [104, 105, 106] focuses on high frequency planar antennas, above 80 GHz, in his series on THz microstrip antennas and Herrero et al. [107] developed a patch antenna at 122 GHz with 6 dBi gain, and 140 GHz patch antenna array with gain 11 dBi.

A key advantage of microstrip antennas is that multiple patches can be combined on the same substrate to create complex structures. This makes them excellent candidates for mmWave and mobile communications, as this technique can be used to produce high gain antenna arrays and phased arrays. When combined with beam steering this allows the creation of complex and highly controlled beam shapes. There are two popular methods for the combination of patch antennas. The first is a series fed linear array, mostly used in radar [108], shown here in Figure 46(a). The second, shown in Figure 46(b), is a more traditional antenna array configuration, mostly used for increasing bandwidth in mobile communications [109].

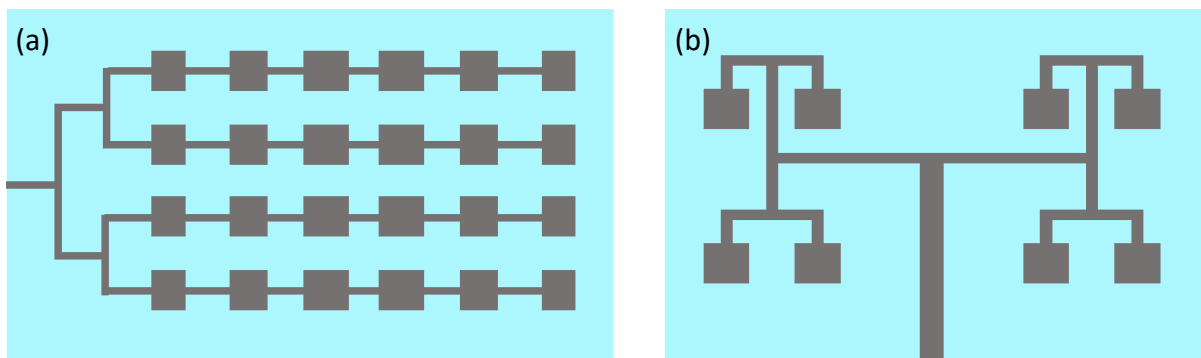


Figure 46: Common array structures for the combination of microstrip antennas (a) series fed linear array, (b) traditional array configuration.

6.2 Application of Genetic Algorithm

This section describes the implementation of Agenoria to develop patch antennas for a variety of frequencies and bandwidths. The antenna design is comparable to a patch antenna on an SU8 substrate. SU8 is chosen as it is flexible and has low dielectric losses at THz frequencies [110]. An array is mapped onto the top surface in lieu of the usual patch. An example of this allocation is shown in Figure 47.

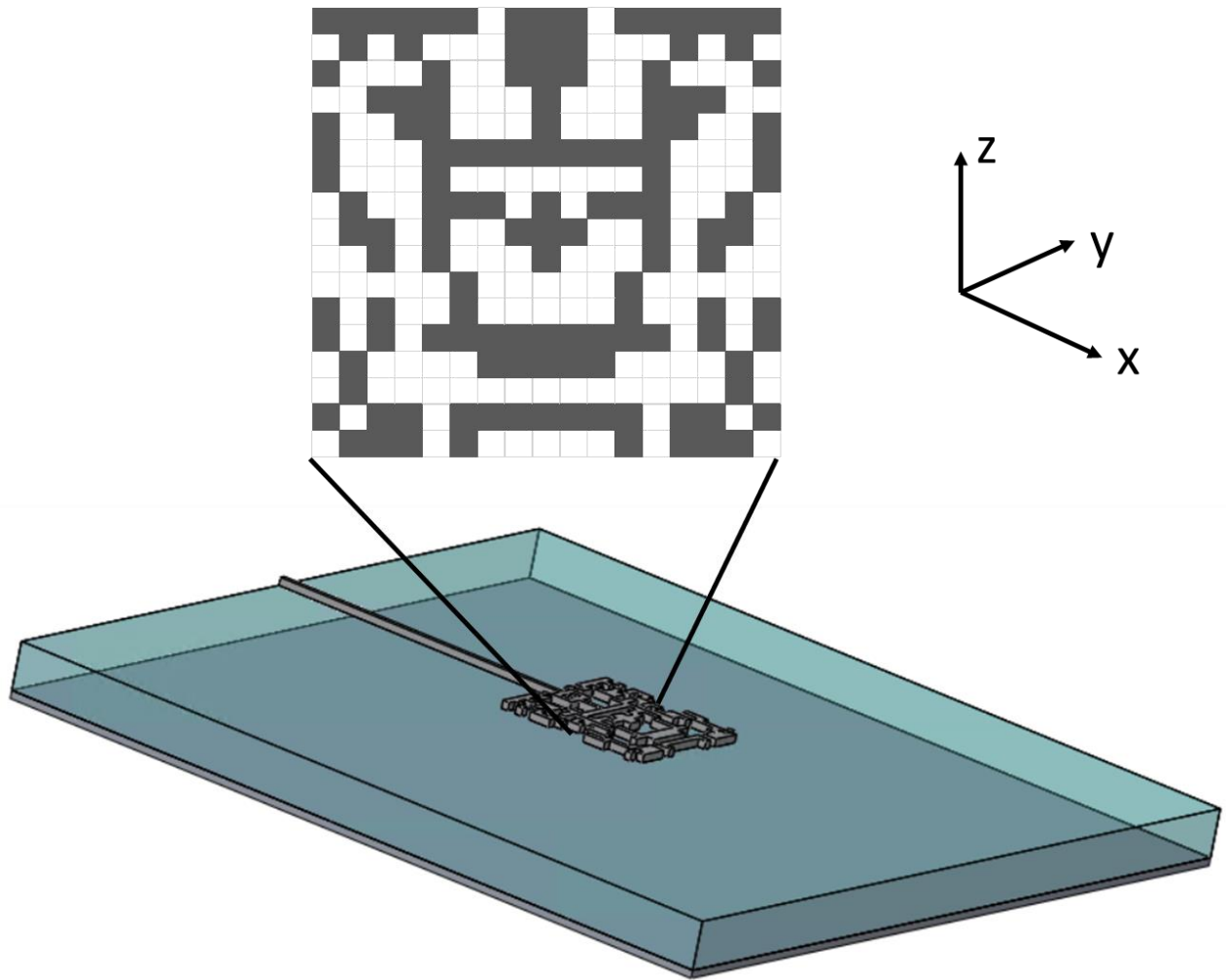


Figure 47: Patch antenna with substrate in blue modelled as an SU8 layer and metal in dark grey modelled as a perfect conductor.

The metal patch in the centre of the antenna is a $500\ \mu\text{m}$ by $500\ \mu\text{m}$ array, divided into 400 $20\ \mu\text{m}$ by $20\ \mu\text{m}$ sections. These sections are each allocated a binary value, to describe whether they are filled with metal or not. The list of binary entries can be written as a string, or a “genome”. Therefore, every individual antenna can be described by a unique genome representing the shape of the metal patch. The dimensions are varied depending on the frequency and bandwidth the antenna is being optimised for. Each design will be outlined in Section 6.3.

The parameters that are not already set by Agenoria will also be discussed, namely the population size and fitness test. The choice of population size is a balance between the characteristic effects of both small and large populations. Larger population sizes increase computational time as this is directly proportional to the number of antennas tested.

However, smaller population sizes can lead to the simulation converging prematurely on a non-optimal solution.

Alander [111] recommends that population size is the same as the length of the binary string. The length of the binary string used to analyse most of the antennas included here is either 400 or 200 (the array shown in Figure 47 can be described by half the number of bits if symmetry is forced across the feed line). The workstation used for simulations is a Intel® Xeon® CPU E5-2650 v3 with 128 GB of RAM. To reduce computational time and complexity of the analysis files, the output files of an entire generation of individuals must be stored concurrently. To store the output of 200 individuals would reduce the maximum file size to 0.64 GB, equivalent to a run time of 9 ps. As the input pulse is not applied until 5.63 ps into the simulation the minimum frequency resolution for this run time is approximately 300 GHz. The minimum frequency required for the simulations detailed here is 100 GHz. Consequently, a simulation time of 30 ps has been chosen, with a minimum frequency resolution of approximately 40 GHz. To account for this, the population size is reduced to between 60 and 90 individuals.

The fitness test is unique for each instance of the algorithm, as it must be changed depending on the chosen bandwidth and ideal output. The input to the fitness test is the electric field across the domain specified in the FDTD. The Matlab file *Fitness_Test.m* uses this to calculate the power transmitted through the feedline of each antenna. The power spectral density (PSD) is then calculated by taking the Fourier transform of this time series using the inbuilt *fft* function, which is then normalised against the input source. The normalised PSD of each antenna is then assessed at chosen frequencies to give each candidate antenna design a fitness score.

6.3 Algorithm Examples

The antennas that are demonstrated here are:

1. A broadband patch antenna optimized from 100 GHz to 5.00 THz
2. A single peak patch antenna optimized for at 1.00 THz
3. A dual peak patch antenna optimized for 1.00 THz and 1.20 THz

Other algorithms that are not included here, but used the same algorithm basis:

1. A dual peak patch antenna optimized for 0.85 and 0.95 THz
2. A bowtie antenna optimised from 100 GHz to 5.00 THz

6.3.1 A broadband patch antenna optimized from 100 GHz to 5.00 THz

The first antenna to be optimised is a broadband patch antenna. The optimised frequency range is 100 GHz to 5.00 THz to test the algorithm's capability across the entire frequency range it is likely to be used for. The fitness test evaluates the performance of the antenna as a broadband power receiver, without a specific frequency response. As such, the fitness test measures the overall power collection efficiency of the antenna between 0.1 THz and 5.0 THz by evaluating the power spectral density received in the feedline compared to that of the input.

The population size is set at 90, as the frequency range is so large, it is ideal to keep the diversity in antenna design as high as possible as there are many local optima to avoid if an acceptable global solution is to be located. As this is the maximum population size, given storage constraints, the pattern optimised here is set as symmetrical around the feedline. This reduces the solution space, decreasing the number of local optima, and therefore the likely optimisation time.

For the fitness test, the spectrum is split into 2 sections: the region of interest and the discarded region. The region of interest (R_1) is between 0.10 THz and 5.00 THz. The discarded region (R_2) is any other measured value.

$$Fit_{R1} = \int_{5.00\ THz}^{0.10\ THz} \frac{|fft(E_{meas})^2|}{|fft(E_{in})^2|} \quad (6.1)$$

$$P_{out} = 10 \log_{10}(Fit_{R1}) \quad (6.2)$$

Where E_{meas} is the electric field measured at the antenna output (feedline), E_{in} is the electric field impulse used to excite the antenna.

The fitness convergence pattern can be seen in Figure 48.

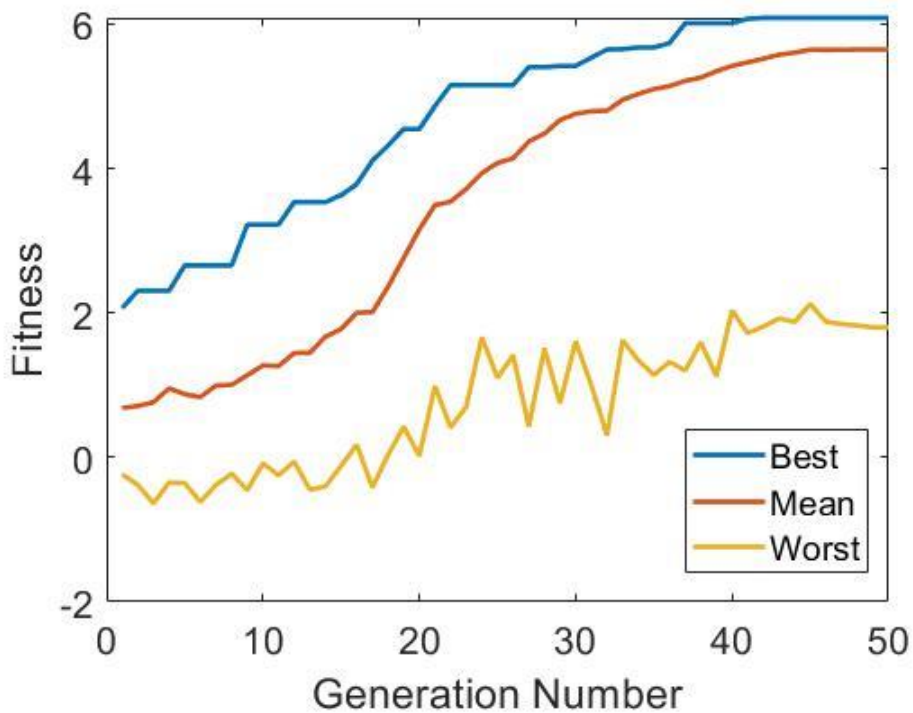


Figure 48: Genetic algorithm fitness variation, for a broadband patch antenna, until stabilisation at 50 generations. Fitness score is measured in arbitrary units. Reference antenna has a fitness (F) = 2.1, which is the best of the first generation.

The algorithm ran for 50 generations, stagnating after generation 42 with a fitness score of 6.08. This shows a 294% improvement from the best fitness score of 2.06 from the first generation. As shown in Figure 49, the best antenna design from generation 1 is a reference plain patch antenna.

The GA converged in only 50 generations, which is relatively fast compared to other, similar algorithms, and followed a typical convergence pattern [112, 113]. There was slow progress until generation 17, with the lowest worst fitness score of -0.637 recorded at generation 3. Between generations 17 and 21 the largest increase in fitness score is seen, before progress tails off as the algorithm converges.

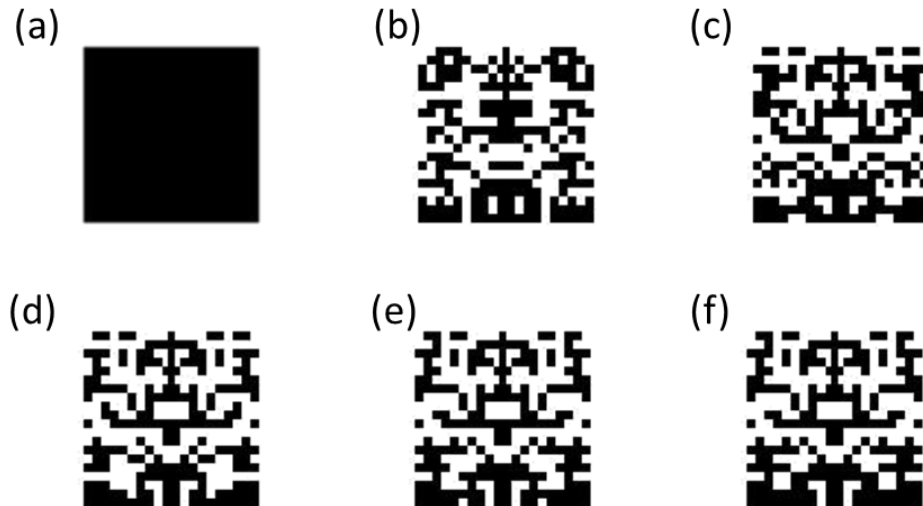


Figure 49: Best candidate antenna designs, for a broadband patch antenna, from their respective generations: (a) 1 (b) 10 (c) 20 (d) 30 (e) 40 and (f) 50, with fitness scores of: (a) 2.06 (b) 3.22 (c) 4.55 (d) 5.42 (e) 6.01 and (f) 6.08.

The antenna pattern here is set to be symmetrical. This both reduces the number of bits in the metal patch to be optimised from 400 (20 x 20 array) to 200 (20 x 10 array) and enables clearer features to be seen. These features become clearer and more coherent with each generation. Figure 49(f) shows the final evolved design, which includes patterns akin to ring and slot structures, such as those used to optimise radiation patterns and impedance matching in conventionally designed patch antennas [114, 115].

Figure 50 shows the normalised (against input power) output power of the evolved and reference antenna designs.

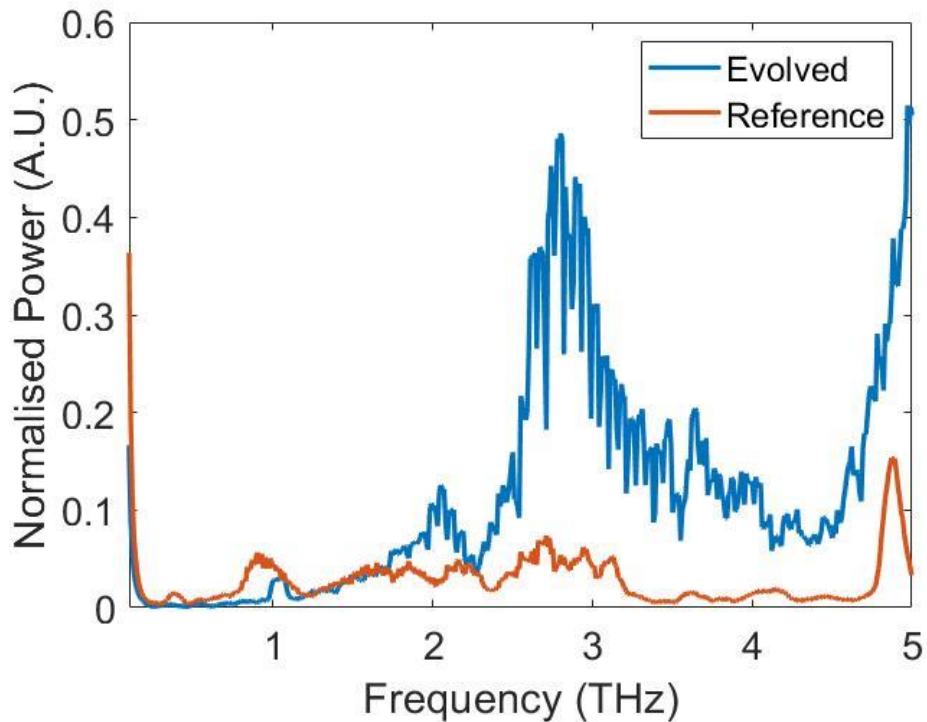


Figure 50: Normalised power output of evolved broadband antenna from generation 50 compared to the best antenna from generation 1 (here a plain patch antenna).

The antenna has been optimised to improve performance over the entire region, with no specific frequency response. As shown in Figure 50, most of this improvement is achieved around 3 THz.

In Figure 51, the simulation has been run for an increased time (100 ps) and the electric field measurements converted to a voltage, windowed, and converted to decibels. This is to provide a comparison for the experimental work completed in Chapter 7. While this gives a better comparison for experimental results, Figure 50 better reflects the data used for generating the fitness score, where calculations are kept minimal and approximate.

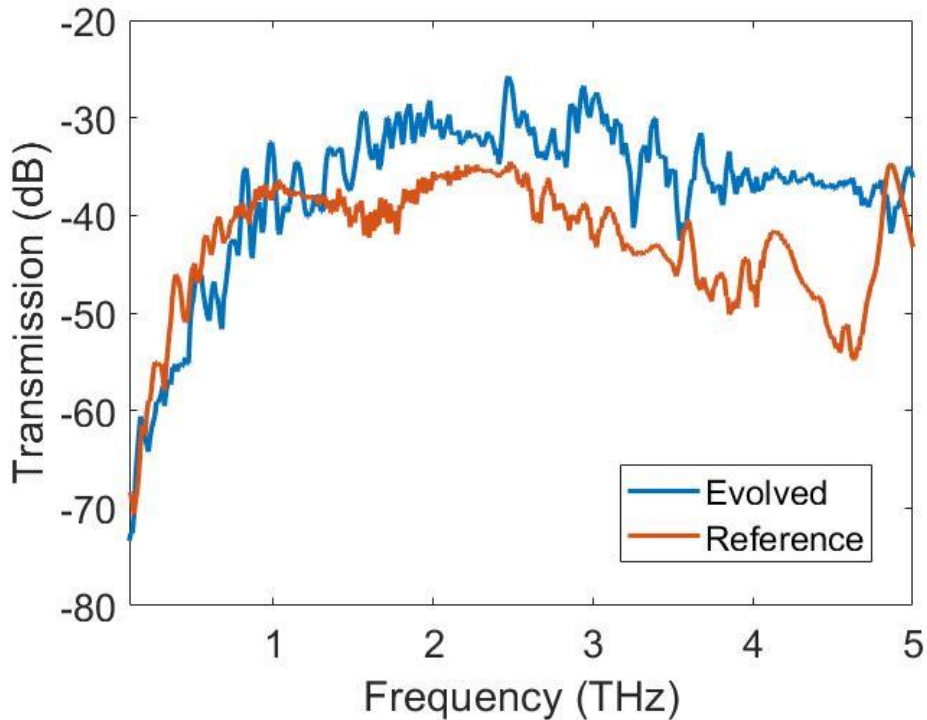


Figure 51: Transmission of evolved broadband antenna from generation 50 compared to the best antenna from generation 1 (here a plain patch antenna).

The transmission showed a mean improvement of 5.3 dB seen in the GA over the optimised region, 0.1 THz to 5.0 THz, optimising 79% of the spectrum within this range.

6.3.2 A single peak patch antenna optimized for at 1.00 THz

The second antenna to be optimised is a single peak patch antenna. The fitness test evaluates the performance of the antenna as a narrowband power receiver (without a specific frequency response). The fitness test measures the overall power collection efficiency of the antenna, at $1.00 \text{ THz} \pm 30 \text{ GHz}$, by evaluating the power spectral density in the feedline compared to the input.

The frequency range to be optimised is small, so there are a low number of local optima to avoid, and less diversity is required in the population. Therefore, the population is set at the reduced size of 60, and the pattern to be optimised asymmetric. Any noticeable symmetries are therefore due to the algorithm.

The spectrum is split into 2 sections: the region of interest and the region to be minimised. This is different to the broadband patch in that any region outside of that of interest is actively suppressed. The region of interest (R_1) is an approximately 30 GHz range either side of the 1.00 THz: 0.967 THz to 1.034 THz. The region to be minimised (R_2) is any other measured value between 0.50 THz and 2.00 THz.

First, the peak prominence must be determined. This is the height of the desired peak above the noise level. The fitness due to the desired peak is:

$$Fit_{R1} = \int_{1.03 \text{ THz}}^{0.97 \text{ THz}} P_{int} \quad (6.3)$$

And due to the surrounding noise:

$$Fit_{R2} = \int_{0.97 \text{ THz}}^{0.50 \text{ THz}} P_{int} + \int_{2.00 \text{ THz}}^{1.03 \text{ THz}} P_{int} \quad (6.4)$$

The peak prominence is the difference in these:

$$Peak \ Prominence = Fit_{R1} - Fit_{R2} \quad (6.5)$$

If the peak prominence is positive, there is a peak at the desired frequency above the noise level. If the peak prominence is negative, there is no noticeable peak here.

For a negative peak prominence, the fittest individuals should score the smallest negative number. Two additional measures, Fit_3 and Fit_4 , are included to ensure any unwanted peaks have an increased negative impact factor. Fit_3 is the sum of surrounding points above the main peak and Fit_4 the sum of surrounding points above the noise floor. Points included in Fit_3 are also in Fit_4 , to give extra weighting to these.

For a positive peak prominence, the fittest individuals should score the largest positive number. Two additional measures, Fit_3 and Fit_4 , are included to ensure any successfully suppressed peaks have an increased positive impact factor. In this case Fit_3 is the sum of surrounding points below the main peak, and Fit_4 the sum of surrounding points below the noise floor. Points included in Fit_4 are also in Fit_3 , to give extra weighting to these.

The total fitness is:

$$Fit = \frac{Peak\ Prominence \times (Fit_3 + Fit_4)}{Peak\ Variance} \quad (6.6)$$

The convergence pattern, due to the algorithm and fitness function, can be seen in Figure 52.

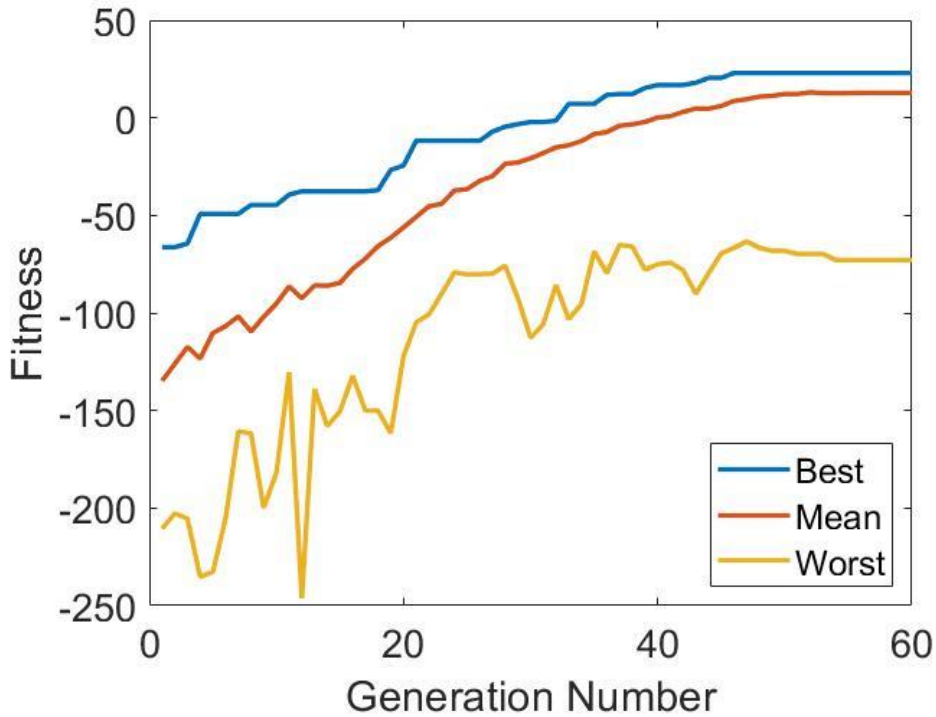


Figure 52: Genetic algorithm fitness variation, for a single peak patch antenna, until stabilization at 50 generations. Fitness score is measured in arbitrary units.

As in Figure 48, Figure 52 shows a standard convergence pattern, with the fitness score improvements in the middle generations noticeably larger than the slow improvements at the start and end of the algorithm. This algorithm was terminated at 60 generations, with a fitness score of 22.95, as it had stagnated after generation 46.

Due to the active suppression of surrounding peaks (those at any frequency not between 0.97 THz and 1.04 THz) the first generation has only negative fitness scores, with a best of -66.35. This means there are no candidate antenna designs that have a peak around 1.00 THz above the general noise level. The lowest fitness score exhibited is -246.2 from a design in generation 12. This is due to a design where the power collection at 1.00 THz is significantly lower than the surrounding spectrum.

The best fitness crosses zero at generation 33 with a score of 7.127, this is a key moment in the convergence as there is now a visible peak at 1.00 THz. After a further 13 generations, the fitness has stagnated at 22.95, and the candidate antenna design can be seen in Figure 53.

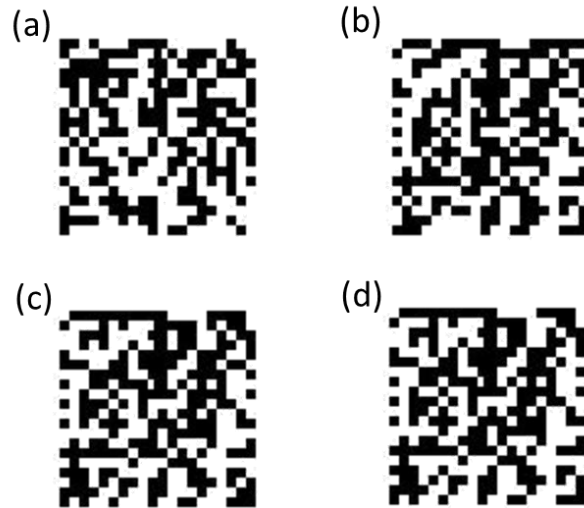


Figure 53: Best candidate antenna designs, for a single peak patch antenna, from their respective generations: (a) 1 (b) 20 (c) 40 and (d) 60, with fitness scores of: (a) -66.35 (b) 24.47 (c) 16.79 (d) 22.95.

These candidate antenna designs have no forced symmetry to see if symmetrical features appear into the array when optimised. Due to the asymmetry of the designs, specific features in the antenna pattern are less obvious. Clearly, the resulting patterns do not express symmetry. This is a key advantage of evolved architectures, as genetic algorithms produce architectures unlikely to have been designed by man.

Figure 54 shows the normalised power output of the evolved and reference antenna designs. The reference antenna design is the best performing design from generation 1, shown in Figure 53(a).

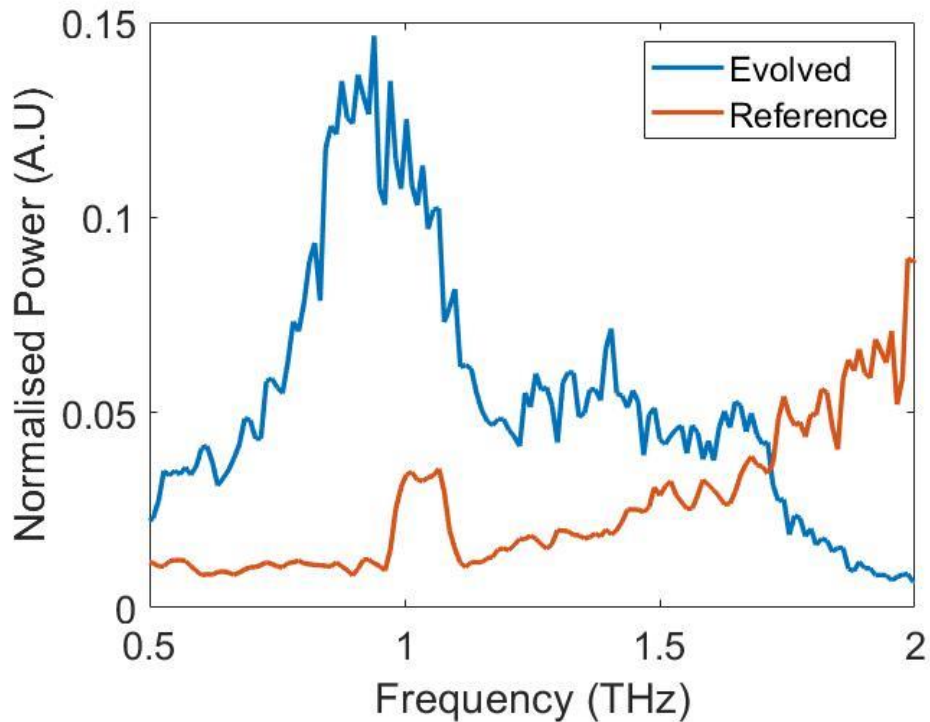


Figure 54: Normalised power output of evolved single band antenna from generation 60 compared to the best antenna from generation 1.

The evolved antenna's simulated power output is considerably higher than that of the reference case, with an improvement at 1 THz of 267%. Though the background noise has also increased between 0.5 and 0.97 THz and between 1.03 and 1.72 THz, the peak prominence has improved as the peak around 1 THz in the evolved case is consistently above the surrounding noise level.

6.3.3 A dual peak patch antenna optimized for 1.00 THz and 1.20 THz

The second antenna to be optimised is a dual peak patch antenna. The fitness test evaluates the performance of the antenna as a narrowband power receiver over two regions simultaneously. The fitness test measures the overall power collection efficiency of the antenna, at $1.00 \text{ THz} \pm 30 \text{ GHz}$ and at $1.20 \text{ THz} \pm 30 \text{ GHz}$, by evaluating the power spectral density received in the feedline compared to that of the input. The population size is set at 90, as the frequency range to be optimised is larger than that of the single peak case and therefore there are an increased number of local optima to avoid, and so more diversity is required in the population.

The first stage of the dual peak optimisation is to find the “peak prominence”, this is the height of the two wanted peaks above the surrounding noise level. To find the peak height, an approximately 30 GHz range is taken either side of the two peaks. 0.967 THz to 1.034 THz and 1.167 THz to 1.234 THz.

$$Fit_{R1} = \int_{1.03 \text{ THz}}^{0.97 \text{ THz}} P_{int} + \int_{1.23 \text{ THz}}^{1.17 \text{ THz}} P_{int} \quad (6.7)$$

The region to be minimised is the spectrum between 0.50 THz and 2.00 THz that is not included in either of the two peaks.

$$Fit_{R2} = \int_{0.97 \text{ THz}}^{0.50 \text{ THz}} P_{int} + \int_{1.17 \text{ THz}}^{1.03 \text{ THz}} P_{int} + \int_{2.00 \text{ THz}}^{1.23 \text{ THz}} P_{int} \quad (6.8)$$

The peak prominence is the difference in the two fitness measurements,

$$Peak \ Prominence = Fit_{R1} - Fit_{R2} \quad (6.9)$$

There is an additional component in optimising for dual peaks, the peak variance, which is the absolute difference in the two desired peaks.

$$Peak \ Variance = \left| \int_{1.03 \text{ THz}}^{0.97 \text{ THz}} P_{int} - \int_{1.23 \text{ THz}}^{1.17 \text{ THz}} P_{int} \right| \quad (6.10)$$

This is intended to be minimised, so the absorption in both wanted parts of the spectrum has similar magnitude. The overall fitness is therefore given by:

$$Fit = \frac{Peak \ Prominence \times (Fit_3 + Fit_4)}{Peak \ Variance} \quad (6.11)$$

The descriptions of Fit_3 and Fit_4 can be seen in Section 6.3.2.

The fitness convergence of the genetic algorithm, using the above fitness function, can be seen in Figure 55.

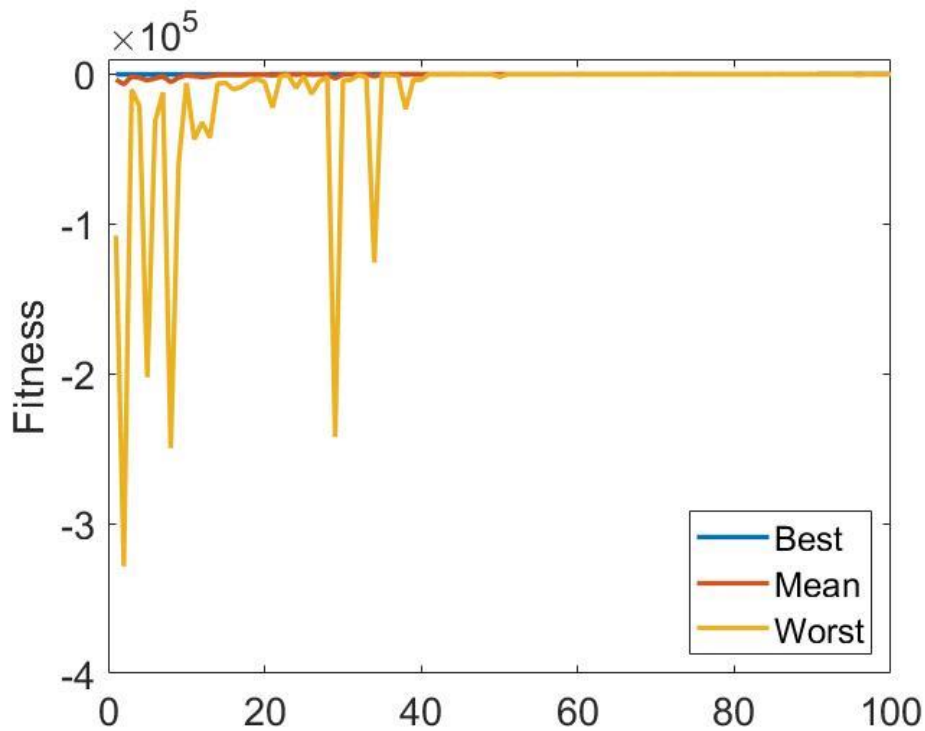


Figure 55: Genetic algorithm fitness variation, for a dual peak patch antenna, until stopped at 100 generations. Best, mean and worst of each generation is shown.

The oscillations in worst fitness score are due to the increased rate of mutation when the fitness scores in any given generation have a low range, as shown in Figure 42. This increases the probability of finding novel candidate antenna designs and therefore reduces premature stagnation in fitness. As the worst fitness score here is -328,600, at generation 2, the best fitness scores from each generation have been plotted separately in Figure 56.

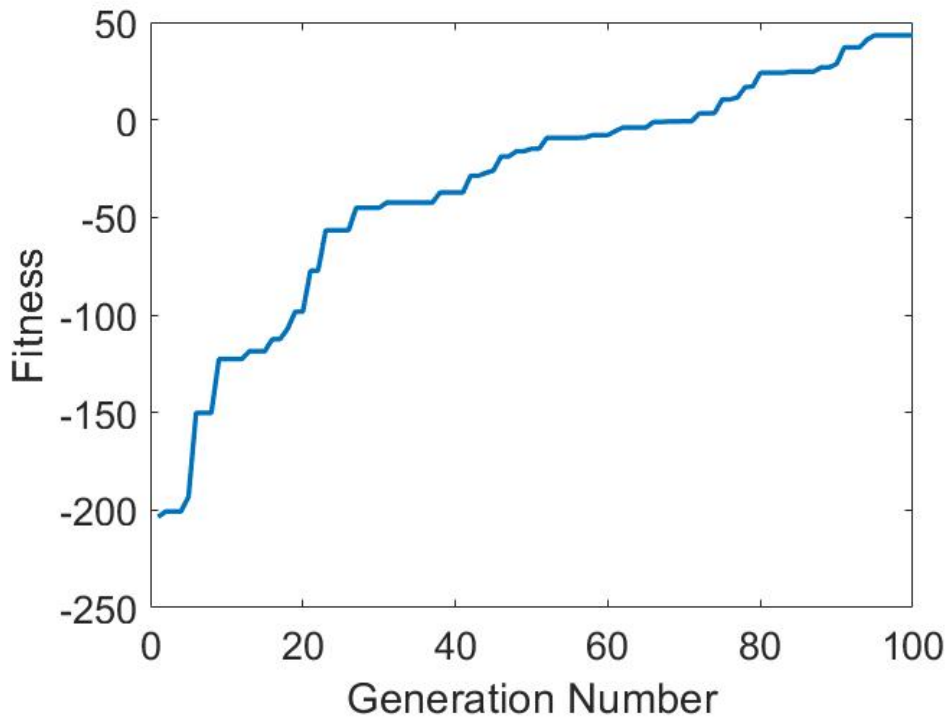


Figure 56: Genetic algorithm fitness scores of the best candidate antenna design in each generation, for a dual peak patch antenna.

Figure 56 shows a typical genetic algorithm convergence, where improvements are quick at first, improving from a score of -203.6 to -77.3 in the first 20 generations, but slow with number of generations. The improvement in the final 20 generations is from 10.4 to 43.3, only 26.1% of the improvement shown in the initial 20 generations. The algorithm reaches a fitness of 43.3 at 95 generations and then stagnates. Here, up to 100 generations are shown, but an additional 10 generations were run to prove the algorithm had converged.

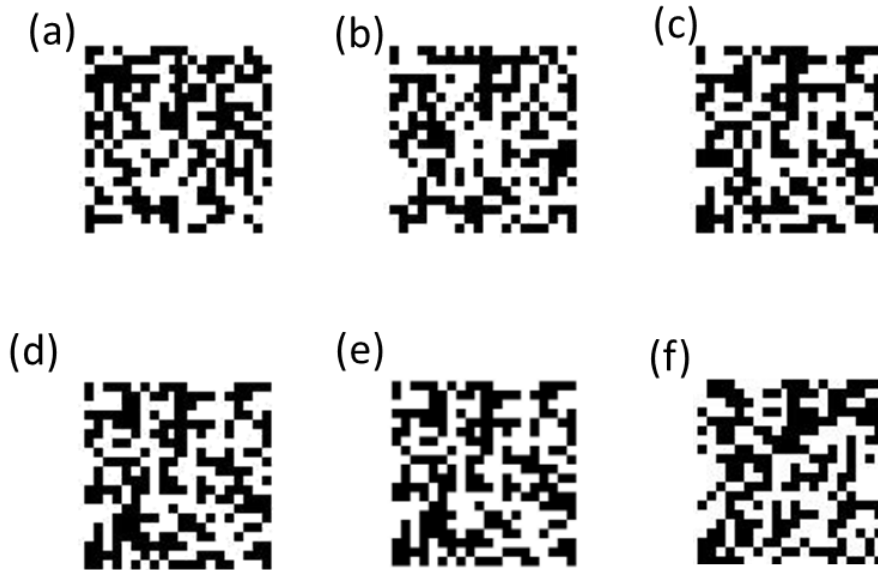


Figure 57: Best candidate antenna designs, for a dual peak patch antenna, from their respective generations: (a) 1 (b) 20 (c) 40 (d) 60 (e) 80 and (f) 100, with fitness scores of: (a) -203.5 (b) -98.3 (c) -37.2 (d) -7.9 (e) 24.1 and (f) 43.3.

As in Section 6.3.2, this antenna design is also asymmetrical, and so analysed by a 400-bit array. The increased time taken to optimise this array is clear by the 100-generation algorithm shown in Figure 56.

Figure 58 shows the normalised (against input power) power output of the evolved and reference antenna designs. The reference antenna design is the best performing design from generation 1, shown in Figure 57(a).

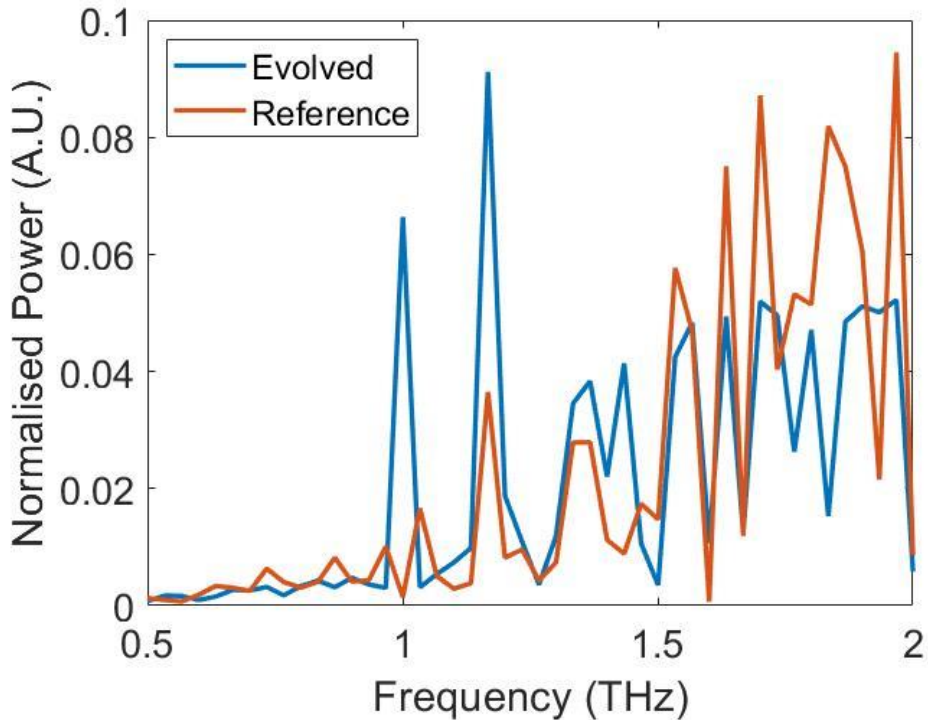


Figure 58: Normalised power output of evolved dual band antenna from generation 100 compared to the best antenna from generation 1.

Figure 58 shows clear peaks in normalised power for the evolved antenna design at 1 THz and 1.2 THz of 0.066 and 0.091 respectively. Compared to the peaks due to the reference antenna at these frequencies, of 0.0014 and 0.037 respectively, this shows improvements of 4,510% and 250%. The mean normalised power absorption in the minimised region for the reference antenna is 0.024, which is reduced to 0.020 in the evolved antenna spectrum.

6.4 Conclusion

In this chapter, a series of planar patch antennas have been optimised for power collection using Agenoria, a genetic algorithm presented in Section 5.3. The first is a broadband antenna, optimised between 100 GHz and 5.0 THz, where 79% of the spectrum shows some improvement. The second antenna is optimised for a single peak at 1.0 THz. The evolved antenna's simulated power output is considerably higher than that of the reference case, with an improvement at 1 THz of 267%. The third antenna is a dual peak antenna, with peaks optimised at 1.0 THz and 1.2 THz showing a 4,510% and 250% improvement on the reference case from the first generation.

Chapter 7: Antenna Fabrication, Testing and Results

In Chapter 3, a genetic algorithm, Agenoria, is introduced. This is designed to optimise THz components, and a selection of evolved THz antenna designs are presented. In this chapter, one antenna design is experimentally verified in a restricted frequency range, based on available hardware. The antenna is a broadband patch antenna, optimised between 0.1 THz and 5.0 THz, as shown in Section 6.3.1. The fabrication method, experimental configuration, and results are presented.

A vector network analyser (VNA) with two bidirectional VDI WR 1.0 frequency extenders with high-gain horn antennas operating between 0.75 THz and 1.10 THz was used for testing. Both the measured antenna transmission and angular dependence is compared with simulated results. In addition, the losses due to the antenna microstrip feedlines are characterised to analyse the effect of the feedline on the antenna transmission gain.

7.1 Antenna Fabrication

The evolved antennas are arranged in pairs, as shown in Figure 59. One antenna acts as the receiver, the other the transmitter, with the signal transferred between by a 20 μm wide microstrip feedline with a characteristic impedance of 49.9 Ω . The connecting microstrips are of varying lengths, to allow independent characterisation of the feedline.

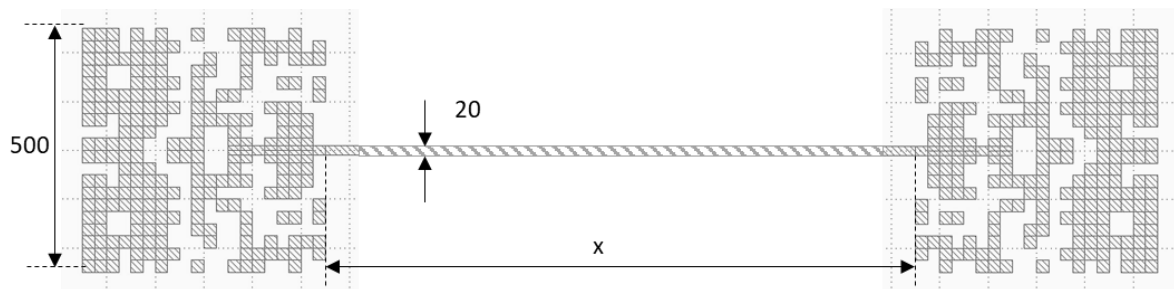


Figure 59: Mask design for antenna pairs, dimensions in μm , $x=50, 75, 100, 125$ and 150 mm.

The microstrip connecting the antennas is defined by five different lengths, 50, 70, 100, 125 and 150 μm .

7.1.1 Fabrication Process

The fabrication process for the antennas in Figure 59 is shown in Figure 60.

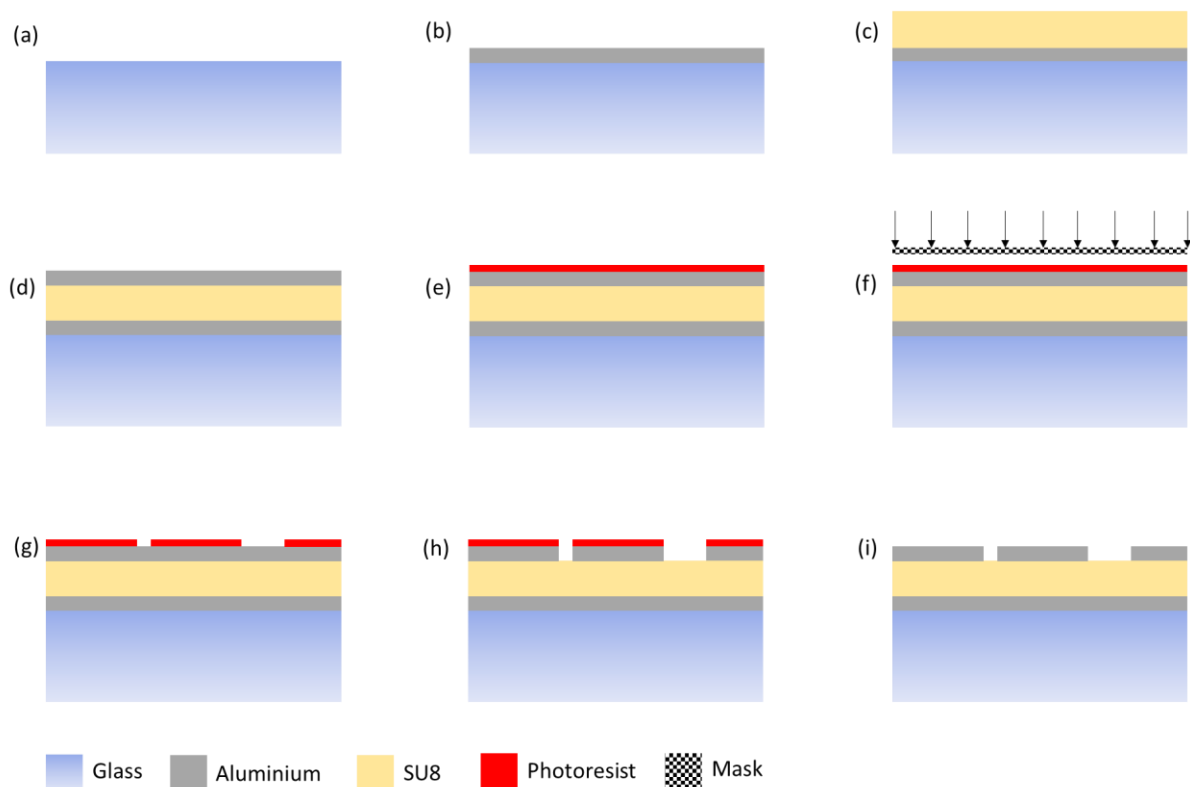


Figure 60: Antenna fabrication process (a) glass substrate (b) aluminium ground plane (c) SU8 dielectric layer (d) aluminium top layer (e) photoresist (f) UV applied through mask (g) selective photoresist removal (h) aluminium etch (i) remaining photoresist removal.

A 2" borosilicate glass substrate (Figure 60(a)) is sputter coated with a 100-nm- thick aluminium ground plane (Figure 60(b)), as determined by the crystal thickness monitor internal to the sputtering system. A nominal 30- μm thick SU8 layer (as determined through [116]) is spin coated onto the ground plane (Figure 60(c)), before an additional 100-nm thick sputter coated aluminium layer deposited (Figure 60(d)). The patches are defined using a photolithographic process: the top aluminium layer is covered with S1813 positive photoresist (Figure 60(e)), exposed through a mask (Figure 60(f)), developed (Figure 60(g)), and finally etched (Figure 60(h)). Optionally, the remaining photoresist is removed (Figure 60(i)). This process is outlined in full in Appendix 2.

Borosilicate glass is chosen as a substrate as it is a flat, non-reactive surface that can be easily coated with aluminium using metal evaporation. The electrical characteristics are not significant, as the substrate will be coated with a ground plane. Aluminium was chosen for all metallic components as it is cheap, has good electrical conductivity and is easy to process.

SU8 is used as the dielectric material due to its relatively low dielectric losses at THz frequency [110] and because a selection of well-defined processes and protocols is available in-house.

7.1.3 Fabricated Antenna

A fabricated antenna can be seen in Figure 61.

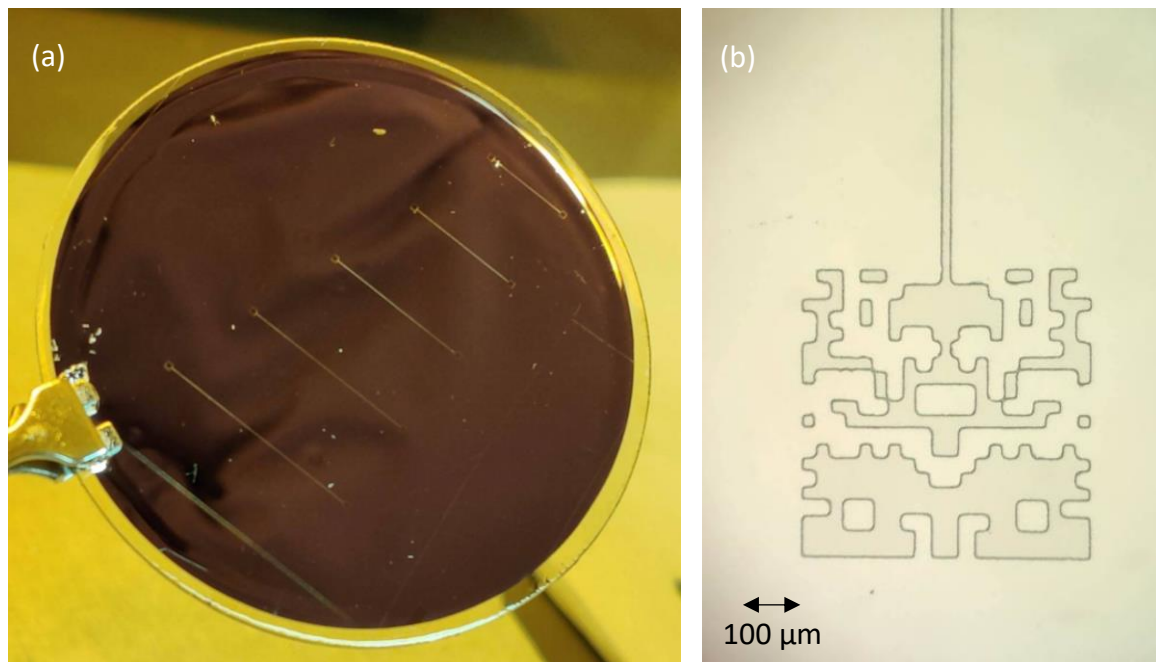


Figure 61: Fabricated antennas (a) pairs shown connected by feed line (b) single antenna photographed under microscope.

The fabrication produced a set of five antenna pairs, with continuous feedlines and antennas featuring the same pattern as outlined in Figure 49 (Section 6.3.1). The key difference with the fabricated antenna in Figure 61 and the design shown in Section 6.3.1 is the curved corners visible on each cell in the fabricated version. This is a common feature of the etching process, and could be removed by using a lift-off method. The 25 μm binary features were measured under a microscope to show a mean fabricated width of 23.2 μm and standard deviation of 1.73 μm. Additionally, the 20 μm feedline showed a mean fabricated width of 19.8 μm with a standard deviation of 0.25 μm. This shows a small but consistent over etching, which is difficult to account for in the fabrication as it is a higher priority to avoid underetching, where unwanted surface aluminium remains.

Figure 62 shows some common fabrication errors associated with these processes and materials.

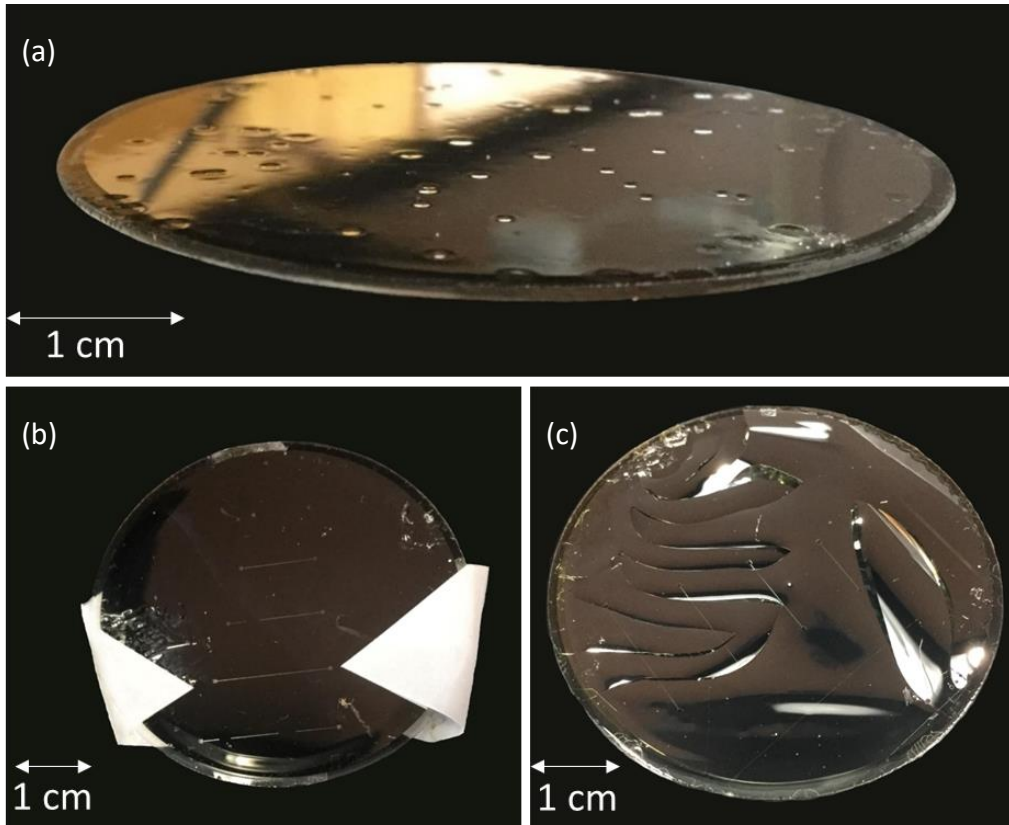


Figure 62: Examples of common issues seen in the manufacturing process: (a) Air bubbles introduced during the spinning of SU8 (b) over-etching and (c) cracking.

(a) As SU8 is an extremely viscous liquid, air bubbles form easily and expand when under the high rotational speeds encountered in the spin coating process. These can be reduced or avoided by allowing the SU8 to settle for at least 20 minutes after transfer to a new bottle or surface and ensuring that surface is properly cleaned and dried before application.

(b) This image shows feedline erosion due to over-etching of the antenna during the step shown in Figure 60(h). The etching solution outlined in Appendix 2 completes a full etch of the 100 nm exposed aluminium in 10-12 seconds. By diluting this solution, and therefore extending the etch time, a more uniform etch can be achieved.

(c) After baking SU8 and allowing it to return to room temperature, the sample cannot be taken above the hardbake temperature without introducing additional stress. As shown in Figure 62(c), this can cause cracking in top layers due to the stress gradients below. This effect can be avoided by ensuring a high enough hard bake of the SU8 to account for all processes and use cases of the device after SU8 application.

7.2 Antenna and Feedline Characterisation

A vector network analyser (VNA) with two bidirectional VDI WR 1.0 frequency extenders with high-gain horn antennas operating between 0.75 THz and 1.10 THz was used for testing. This equipment is described in Section 4.1.1. Due to the extremely broadband nature of the antenna (0.1 THz to 5.0 THz), it is not possible to validate the simulated performance across the entire frequency range. Therefore, the verification is completed at a frequency band within the optimised range. This section presents the experimental configuration and results of the antenna transmission measurements and feedline characterisation within the range of the WR.1.0 frequency extenders.

7.2.1 Experimental configuration

The experimental setup for measuring the antenna response is shown in Figure 63. The frequency response between 0.8 THz and 1.05 THz was determined by measuring the transmission output of two antennas connected by a microstrip. The extremes of the frequency extenders (0.75 to 0.8 THz and 1.05 to 1.1 THz) are not considered due to the increased noise in these regions. The extenders were vertically polarized; therefore, the feed lines connecting the antenna pairs needed to be orientated vertically. With reference to Figure 63, port P1 transmitted to mirror M1, which focused the signal onto the upper antenna (blue beam path). The microstrip sent the received signal down to the lower antenna, which re-transmitted the signal. This was collimated and focused by the mirror pair M2-M3 onto port P2 (red beam path).

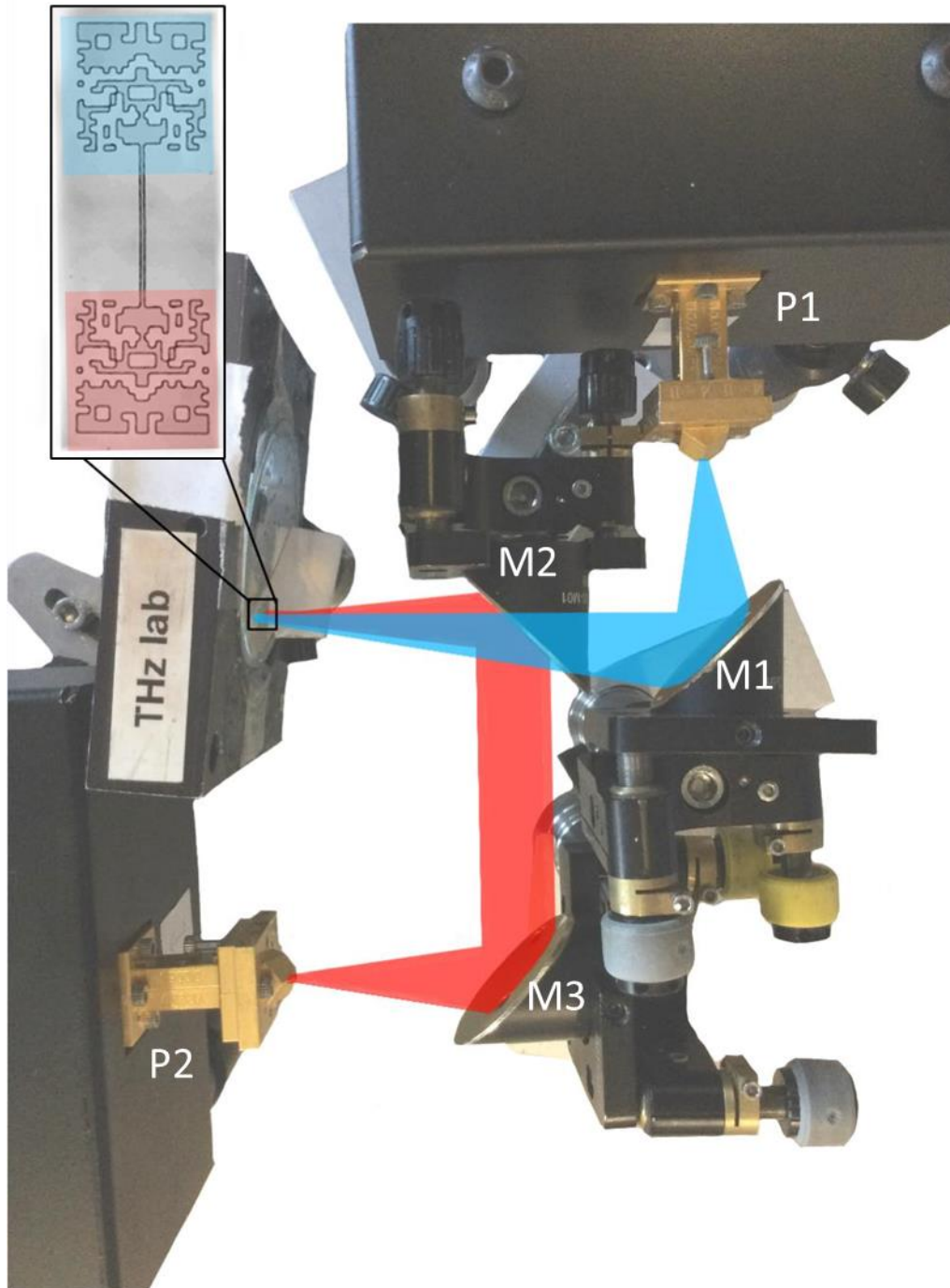


Figure 63: Antenna testing. Antennas are orientated vertically on upper left-hand side. The blue trace shows the higher transmission path from port P1 to the upper antenna. The red trace shows the lower transmission path from the bottom antenna to port P2.

The power losses associated with transmission in air are reduced by decreasing the signal path length by using the compact experimental configuration seen in Figure 63. However, the focal lengths of mirrors and adequate access space (to adjust alignment) must be accounted for. All mirrors on the blue patch (M1) are aligned 15mm higher than on the red path (M2 and

M3). The path length could be further reduced by moving the mirror M2 closer to the antennas, but this would cause the mirror M2 to obstruct the signal path between M1 and the test antennas.

The experimental configuration is simple to ensure ease of alignment. Experimental set-ups with one mirror on both signal paths (blue and red) were considered. Due to the short length of the feedlines, the two mirrors would have to adjoin each other to both sit perpendicular to the antenna pairs. While accounting for standard mirror housing this was impossible, and the set-up seen in Figure 63 developed.

7.2.2 Antenna Transmission

The comparison between the measured response of the reference patch and evolved antenna is shown in Figure 64.

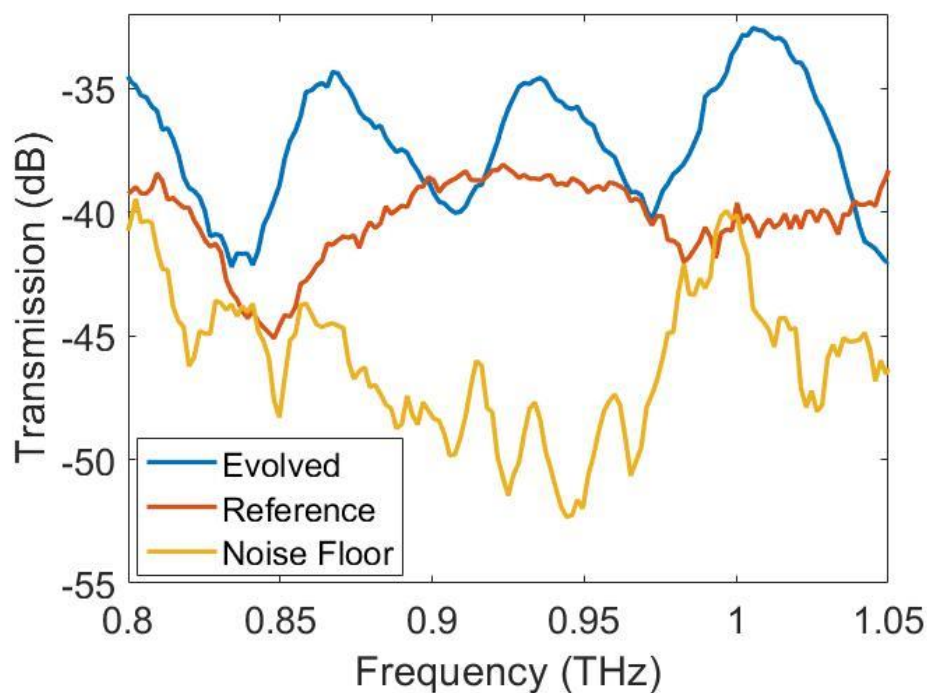


Figure 64: Experimental results from manufactured broadband evolved and reference patch antennas.

The scattering matrix, S , quantifies how power propagates through a multi-port network. This is fully described in Section 4.1.1. For the two-port network used here, there are four scattering parameters in this matrix. Parameters s_{11} and s_{22} describe the reflection into ports P1 and P2 respectively. The transmission between ports can be calculated with either s_{21} (i.e. port P1 was the source and port P2 the receiver) or s_{12} (i.e. port P2 was the source and port P1 was the receiver).

P1 the receiver). In Figure 64, the transmission, T , was determined from the modulus scattering parameters: $T = |s_{21}|^2 \cong |s_{12}|^2$. The transmission, calculated with either, showed very good agreement. A 10-point moving average was applied to the data shown in Figure 64, to smooth local peaks due to noise.

Figure 65 shows the comparison of the results obtained in the experiment detailed in this chapter and the FDTD simulations from Section 6.3.1.

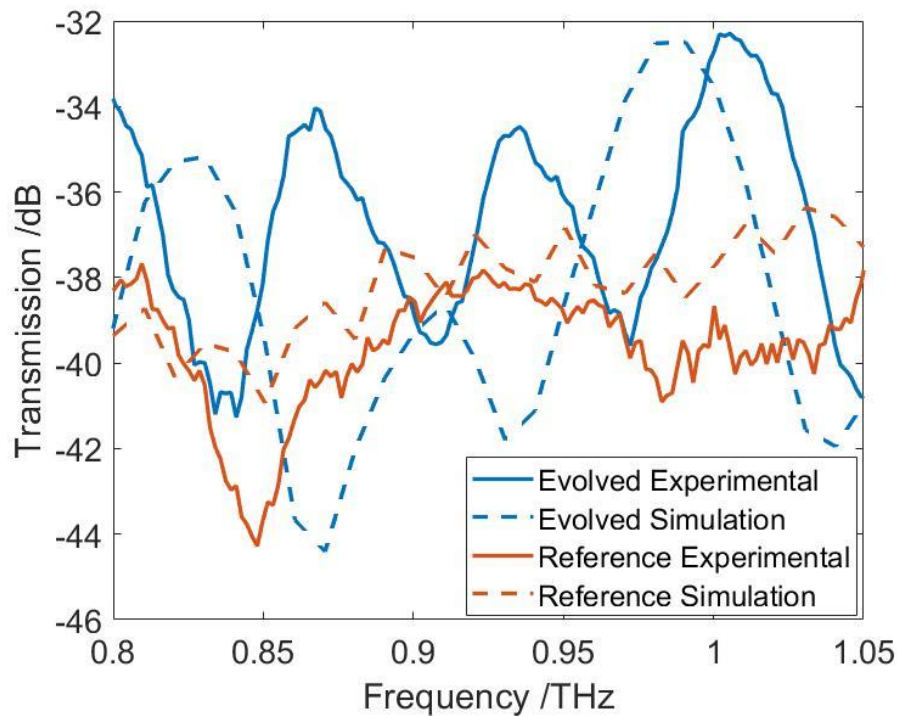


Figure 65: Experimental and simulated results of both evolved and reference patch antennas.

Figure 65 shows comparable levels of transmission for each antenna type. The variations in spectrum were expected due to the variations in antenna fabrication (i.e., slight curving of corners due to etching process). The small frequency shift is likely due to changes in SU8 thickness between fabricated and simulated antennas. The measured average thickness, using a Dektak 3 Profilometer [73], of the SU8 was $32.8 \mu\text{m}$, with standard deviation of $7.8 \mu\text{m}$.

7.2.3 Feedline losses

Microstrips of different lengths were used to connect antenna pairs, to allow the microstrip to be characterised independently, as seen in Figure 66. The experimental set-up is identical to that used in Figure 63, with S-parameters measured between P1 to P2. Figure 66 shows

the losses measured between these ports, while the feed length connecting the antennas under test is varied. The power transfer is calculated from the mean of S_{12} measurements between 0.8 THz and 1.0 THz, and the error bars calculated from repeated measurements using different sets of fabricated antennas. To calculate the impact of the feedline, it is assumed the loss due to the receiving and transmitting antennas under test is identical for the entire experiment. Therefore, the power loss per length is calculated from the gradient of the trendlines seen in Figure 66.

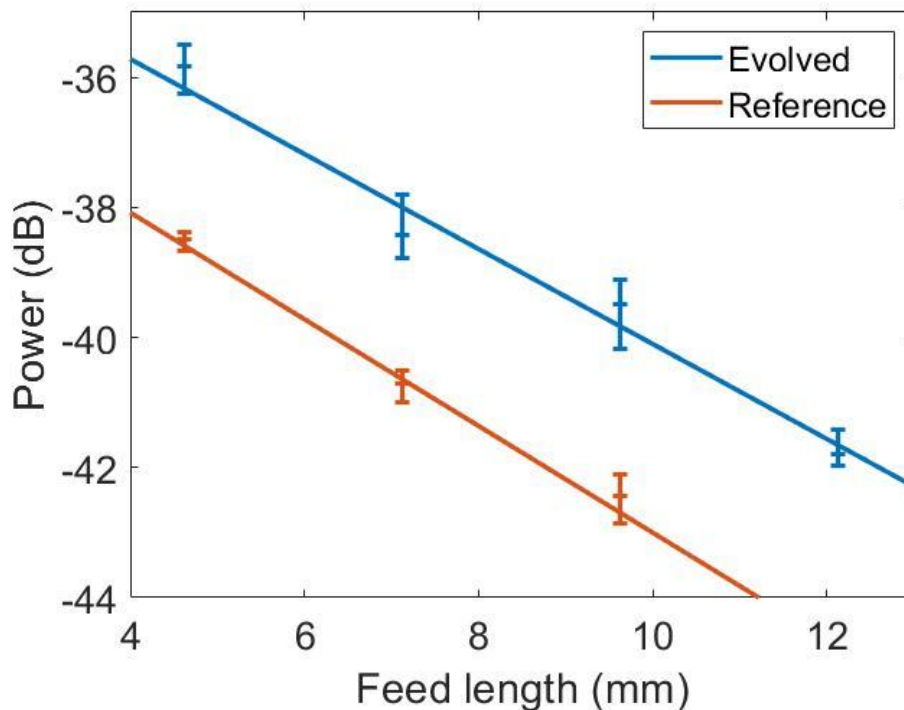


Figure 66: Feedline characterization calculated from scattering parameter s_{21} using antenna pairs with varying lengths of microstrip between.

The loss calculated from the gradients in Figure 66 was 0.79 ± 0.06 dB/mm, which shows excellent agreement between the reference and evolved samples and promisingly low losses. For comparison, state-of-the-art gold-plated TE₀₁ waveguides have losses ranging from 0.13 dB/mm at 0.75 THz to 0.088 dB/mm at 1.10 THz [117]. However, these waveguides require precision manufacturing and cannot be easily integrated. The microstrip presented here added no extra cost and required no dedicated process for its integration. The relatively low loss of the feedline compared to the system gain implies that the measured transmission shown in Figure 64 is almost entirely a function of the antennas.

7.3 Radiation Pattern

The radiation pattern of an antenna is a measure of its directional variation in intensity. This is a useful metric as it can determine the use case of the antenna. Highly directional antennas, those with a narrow main lobe, are useful for line-of-sight transmissions, where reducing interference or even the possibility of interception is key. Alternatively, omnidirectional antennas are ideal for covering a larger area and where the aim is to transmit to all users, in all directions.

7.3.1 Experimental Configuration

Radiation pattern measurements are normally completed by moving the scanning port across the path of the antenna under test [118]. However, due to the space constraints in this experiment, the measurement is configured as in Figure 67. A slit is passed in front of the transmitting antenna (red path). Here, the signal is diverging, to be collimated by mirror M2. Therefore, moving a slit is equivalent to slicing an angled section of the beam.

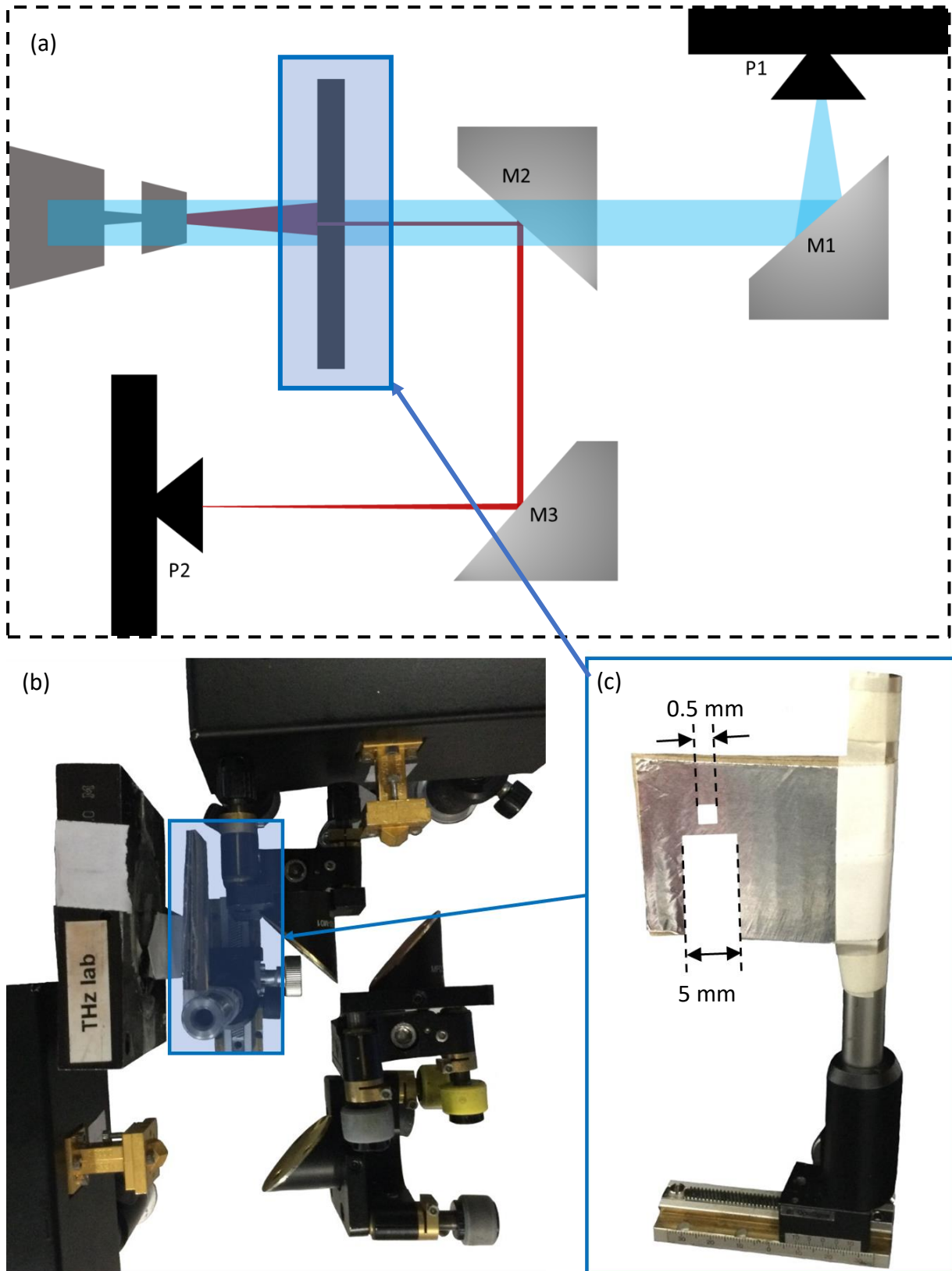


Figure 67: Radiation pattern experimental configuration (a) configuration diagram with signal path shown (b) photo of experimental set-up with scanning tool highlighted (c) scanning tool with two sized slits.

The scanning tool shown in Figure 67(c) has two sizes of slit. The first is a 0.5 mm slit, the second a 5 mm. The first was intended for accurate measurement, but due to low level of signal in the associated path (< -50 dB), these measurements were too close to the noise floor, and discounted. The second, larger, slit was much more successful, and measurements of the antenna radiation pattern are taken using this.

7.3.2 Comparison of Simulated and Experimental Measured Angular Dependence

The simulated radiation pattern and measured angular dependence are shown in Figure 68. Two frequencies are shown, 0.85 and 0.95 THz. The radiation pattern was simulated using MATLAB's antenna toolbox (with adjustments for THz frequency simulations). All patterns were plotted from 45° to 135° as this was the maximum range allowed by our experimental setup shown in Figure 67.

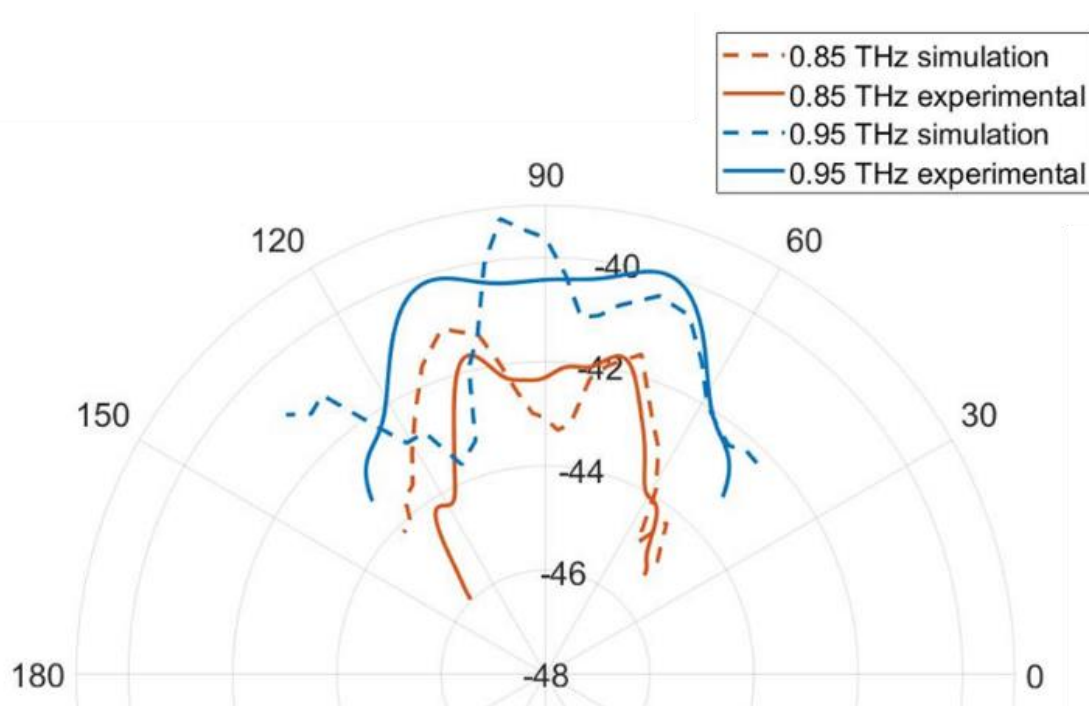


Figure 68: Radiation patterns of evolved antennas at 0.85 THz and 0.95 THz. Solid line shows measured angular dependence experimentally examined through moving of 5.0 mm slit. Dotted line shows radiation pattern simulated using MATLAB's antenna toolbox.

To allow simulation and measured patterns to be plotted on the same axis, the simulated radiation pattern has been shifted in magnitude to account for path losses obtained in the experiment. Figure 68 shows that the simulated radiation pattern and measured angular dependence have similar trends at 0.85 THz and 0.95 THz. This agreement provides evidence

that the antenna's performance over the entire simulated frequency range would be reproducible experimentally.

7.4 Calibration

To calibrate component height, a Class 1A visible laser is first calibrated to the same height as the port antennas. The laser is visibly aligned to the port while adjacent, then the port and laser slowly separated to ensure the laser beam remains aligned up to 50 cm and is therefore providing a horizontal beam for the path length of this experiment. The laser is then used to adjust the height of the mirrors and antenna pairs. There are two lasers used in this way, one for each path height. Using this method, vertical alignment was achieved to within ± 0.5 mm. This ensures most in-experiment adjustment is horizontal.

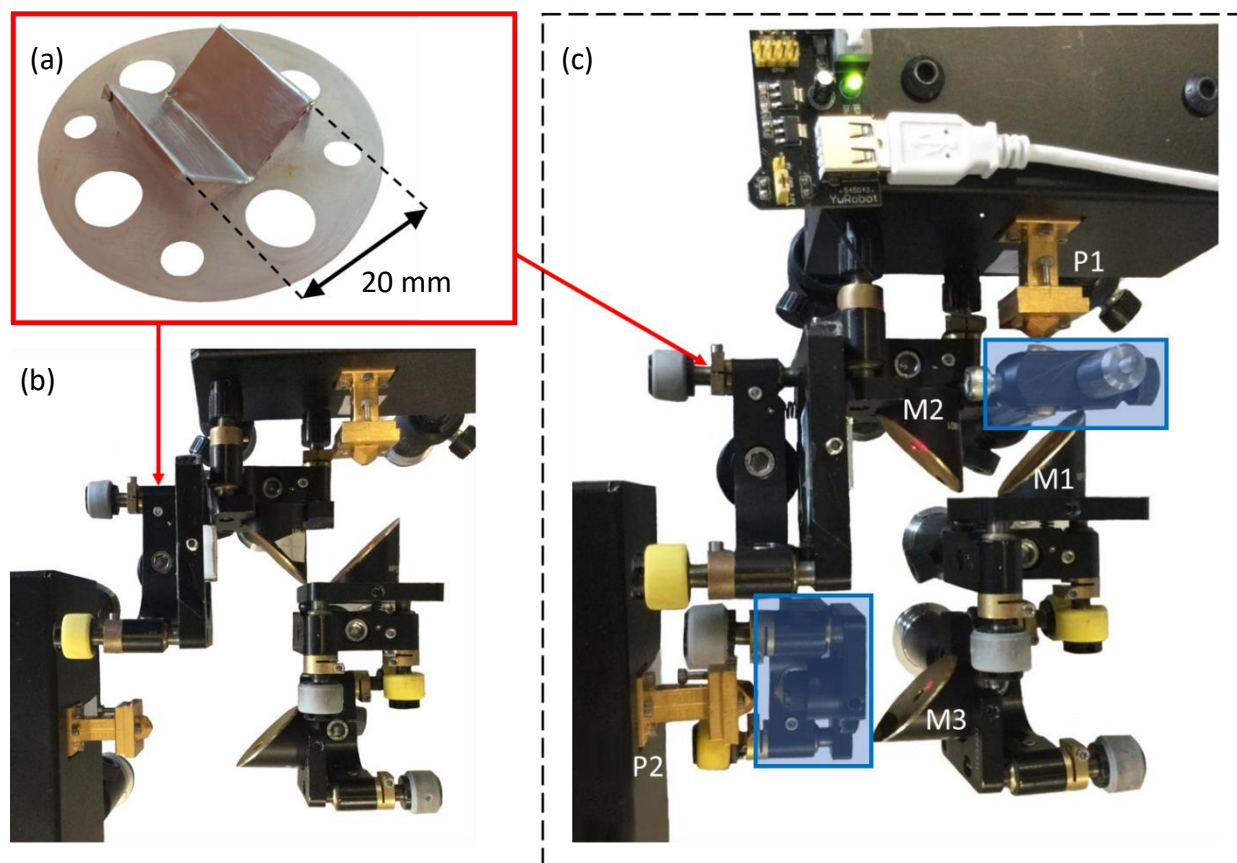


Figure 69: Alignment of experimental set-up, with (a) alignment tool (b) tool in situ and (c) tool and visible lasers (highlighted in blue) in situ.

After vertical alignment, the equipment is set up as seen in Figure 69(b). This shows an alignment tool (Figure 69(a)) in place of the antennas. This tool has been 3D-printed in

polyethylene terephthalate glycol (PETG) and covered with reflective aluminium tape. This tool is designed to be used in place of the antennas during the alignment process, as it does not require absorption or retransmission via the antenna pair, and so the power transmission is higher. This makes for easier alignment as a measurable power level is more likely with initial alignments.

After the initial alignment has shown a clear transmission path from P1 to P2, visible lasers are placed in front of the ports. These are adjusted to establish a continuous visible path between the two ports. The alignment tool can then be removed and replaced by the antenna pairs. The antennas are adjusted, while the lasers' location is maintained, to align each antenna in a pairing to its respective port. With lasers removed, an approximate alignment should be achieved. This is apparent due to a low level of transmission visible on the VNA (which is measuring the scattering parameters between the two ports). The mirrors are then adjusted until a local maximum in the signal is located.

As the antenna pairs and feedlines have associated power loss, specular reflections from the ground plane could produce a larger power output than that due to transmission through the antenna pairs. The possibility of this is reduced by carefully aligning mirror height to ensure minimum adjustment is required throughout the experiment.

To ensure the VNA is not measuring specular reflections, a small metallic plate is used to cover areas of the fabricated device. If the set-up is correctly aligned to an antenna pair, only by covering either of the antennas in this pair will the signal be reduced. If the set-up is not correctly aligned then covering other areas of the device will reduce the signal magnitude, as it will block the specular reflections.

7.5 Conclusion

The genetic algorithm, Agenoria, is verified by fabricating and experimentally analysing an evolved antenna. The antenna is a broadband patch antenna, optimised from 0.1 GHz to 5.0 GHz, as shown in Section 6.3.1. The fabrication method and experimental configuration were presented in this chapter. Due to the extremely broadband nature of the antenna, it was not possible to validate the simulated performance across the entire frequency range. Therefore,

the verification was completed at a frequency band of 0.8 THz to 1.0 THz, within the optimised range.

A vector network analyser (VNA) with two bidirectional VDI WR 1.0 frequency extenders with high-gain horn antennas operating between 0.75 THz and 1.10 THz was used for testing. Feedline losses were investigated using the experimental set-up shown in Figure 63. The loss calculated from the gradients in Figure 63 was 0.79 ± 0.06 dB/mm, which shows excellent agreement between the reference and evolved samples and promisingly low loss in both cases. For comparison, state-of-the-art gold-plated TE01 waveguides have losses ranging from 0.13 dB/mm at 0.75 THz to 0.088 dB/mm at 1.10 THz [117]. However, these waveguides require precision manufacturing and cannot be easily integrated. The microstrip presented here added no extra cost and required no dedicated process for its integration. The relatively low loss of the feedline compared to the system gain implies that the measured transmission shown in Figure 63 is almost entirely a function of the antennas.

Using the same configuration, the antenna transmission was measured for both the evolved antennas and a reference plain patch antenna. When compared to simulation results, these were found to concur, with variations in spectrum attributed to imperfections in the antenna fabrication (i.e., slight curving of corners due to etching process). The angular dependence of the antennas was also measured. Excellent agreement between simulated and experimental measurements was shown at both 0.85 THz and 0.95 THz. The combination of these antenna measurements verifies the simulation output within the region 0.8 THz to 1.0 THz. It is therefore assumed the simulations would match experimental results across the entire simulated range.

This verification supports the mean improvement of 5.3 dB seen in the GA over the optimized region, 0.1 THz to 5.0 THz, as seen in Section 6.3.1. As the GA improved 79% of the spectrum within this range, it can be concluded that this algorithm would be a good candidate for creating future antenna designs, with bandwidths within this region.

7.5.1 Experimental Adjustments

Other experimental configurations were considered, to simplify the set-up shown in Figure 63. One of these is the experimental design shown in Figure 70. The antenna pairs were

intended to be fabricated on a flexible substrate and curved around a 10 mm thick aluminium sheet. This is opaque to THz radiation and ensures no line-of-sight transmission between ports.

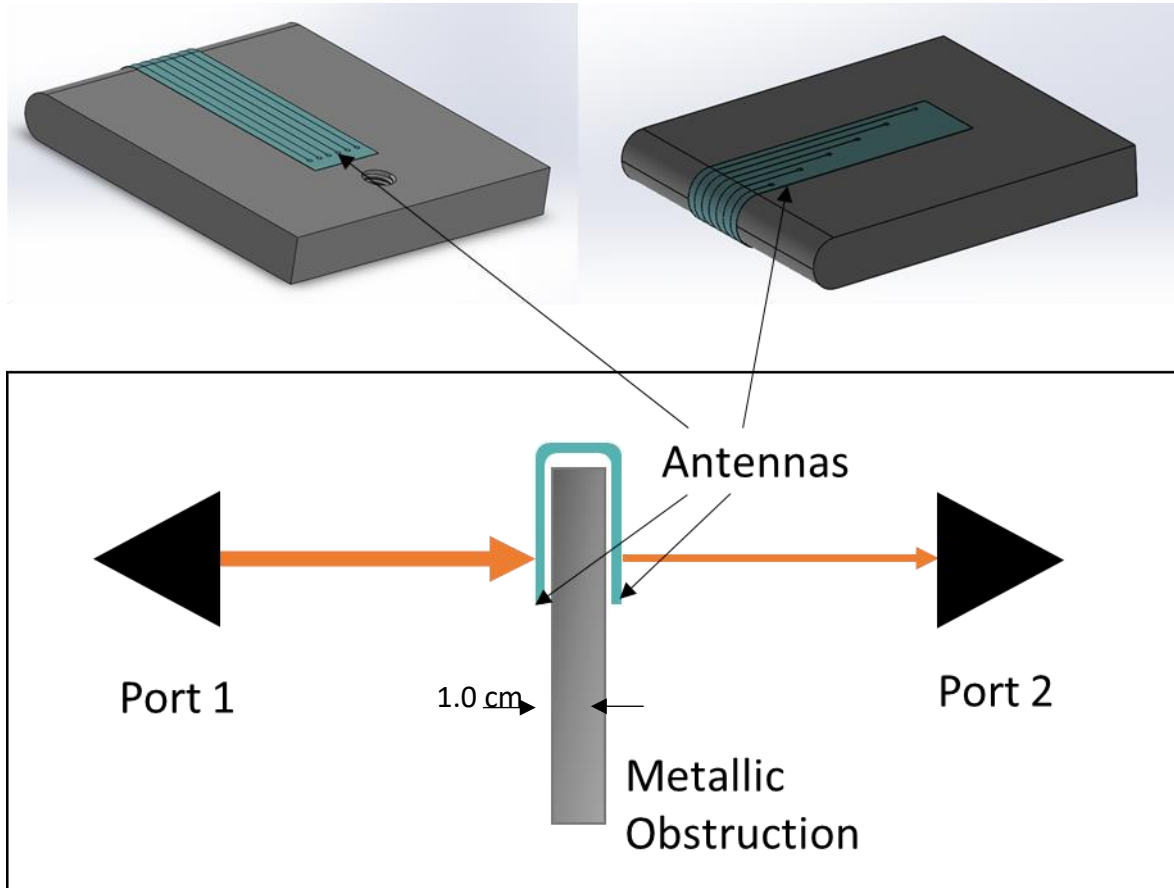


Figure 70: Proposed antenna testing set-up using flexible substrate, port 1 and 2 are VDI WE 1.0 frequency extenders connected to a VNA.

The substrate chosen was acetate, as it is cheap, very flexible, and easy to cut down to size. 2 inch by 2 inch squares were used. However, acetate has a glass transition temperature of 185°C [119]. This caused an issue with the SU8 process, as the hard bake temperature of 200°C could not be reached without damaging the acetate. The fabrication attempt is shown in Figure 71.

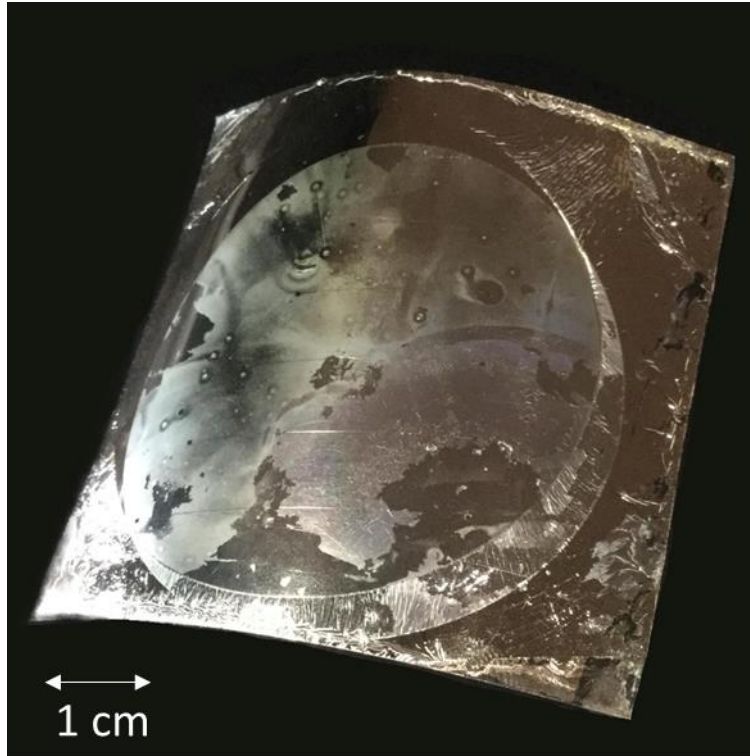


Figure 71: Attempted fabrication of antennas on acetate substrate. Unwanted effects include cracking, bubbling and uneven deposition.

Due to the difficulties in flexible substrate manufacture, the original set-up is maintained, and all results shown obtained using rigid substrates.

Chapter 8: On-Off Modulation

On-Off keying (OOK) has been in use since the first commercial telegraph, demonstrated by Cooke and Wheatstone in 1837 [120]. It is the simplest form of modulation, equivalent to amplitude modulating between only two levels. This method is famously used in morse code transmission over radio frequencies. More recently, OOK has been mostly used for optical systems, both through fibre [121] and wireless [122] networks. The limitations of OOK are spectral inefficiency and susceptibility to interference. However, OOK systems can be designed for high energy efficiency [122] as coherent receiver architectures are not required, therefore an oscillator does not need to be continuously powered. Low power applications where OOK has been explored include medical implants [123], remote sensor networks [122] and for chip to chip communication [124].

In this chapter, an on-off modulator is designed and simulated for a 12.3 GHz carrier wave, corresponding to the RF input of the extender heads. This is then fabricated and tested both alone and in conjunction with the VNA and frequency extenders.

8.1 Concept

The intended use-case of the designed on-off modulator in conjunction with the frequency extenders is seen in Figure 72.

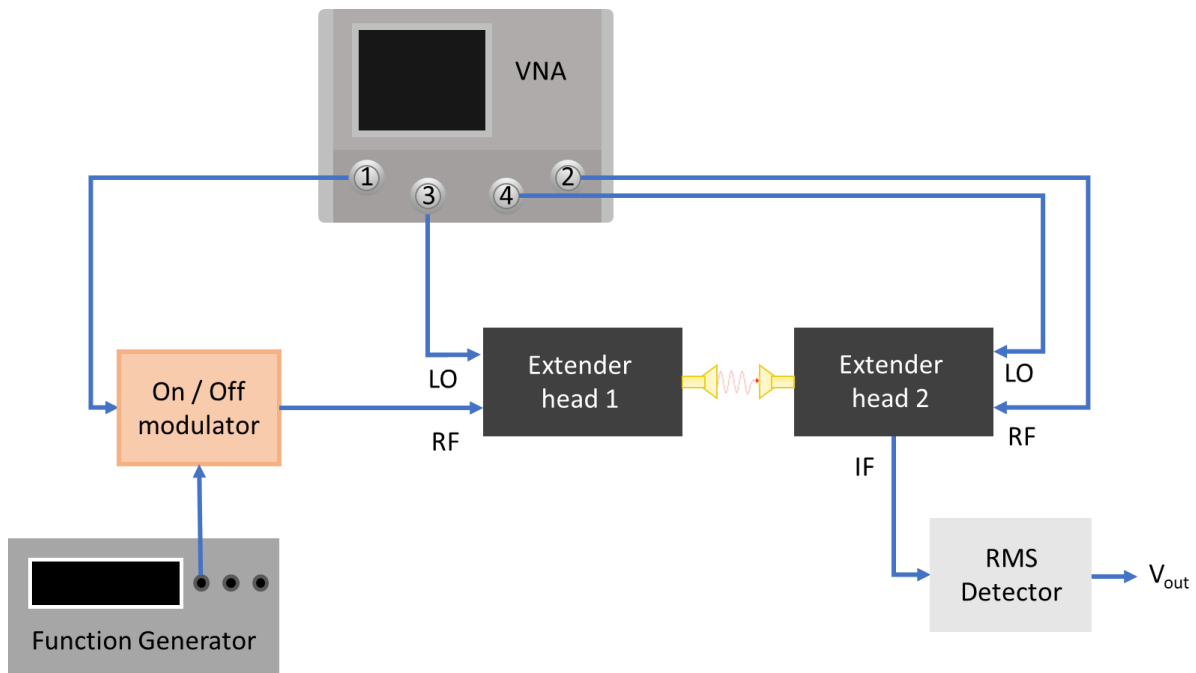


Figure 72: Diagram of modulator and power detector used in conjunction with WR1.0-VNAX THz frequency extenders. A VNA is used to measure S parameters of the system, the output of which is fed directly as the carrier signal into an on-off modulator. This is modulated by a switching signal from a function generator, and the switched signal passed to a pair of frequency extenders before being received as the input to the VNA.

The VNA supplies an LO frequency of 12.3 GHz to the on-off modulator, which is modulated by a frequency set by the function generator, before being passed to the frequency extender (Extender head 1). The extender head multiplies the modulated signal in frequency to form a THz pulse. This THz pulse is transmitted using a horn antenna to a second extender head (Extender head 2) which downconverts the signal to an IF output at 315 MHz. This is received by an RMS detector designed in Section 8.2, which is used to detect the power in the signal. 315 MHz is chosen as it is central to the 312 MHz to 318 MHz range the RMS detector is optimised for.

To ensure the frequency extenders can receive a modulated signal a chopper wheel is placed between the two extender heads, which replicates a simple on-off switching mechanism. This preliminary check is required as the amount of filtering inside the extender heads is unknown, and it is plausible any frequencies lower than the desired transmission band will be removed from the output. A 1 kHz chopper frequency, generated by a lock-in amplifier, was successfully transmitted through the receiving frequency extender. The received signal at the lock in amplifier was between 993 and 987 Hz. This frequency decrease is likely due to power losses in the chopper wheel driver. The phase difference of chopper and lock in amplifier

fluctuated between 0.0° and 1.5°. The magnitude of the received signal from the PCB at 1 kHz was $54.5 \mu\text{V} \pm 1.0 \mu\text{V}$, significantly above the $0.5 \mu\text{V}$ noise level.

8.2 RMS Detector

RMS detectors are used to measure the RMS power in a time-domain signal. These produce a voltage proportional to the average signal power. They are useful for power detection in modulated waveforms where the amplitude of the signal can vary significantly. The RMS detector presented here is designed to convert power outputs from the extender heads into a measurable voltage. This is a convenient component, as it measures the IF output of the frequency extender heads without significantly degrading the SNR.

The power detector is designed for use between 312 and 318 MHz as this is within the IF range of the VNA shown in Figure 30. The proposed circuit diagram for the RMS detector can be seen in Figure 73.

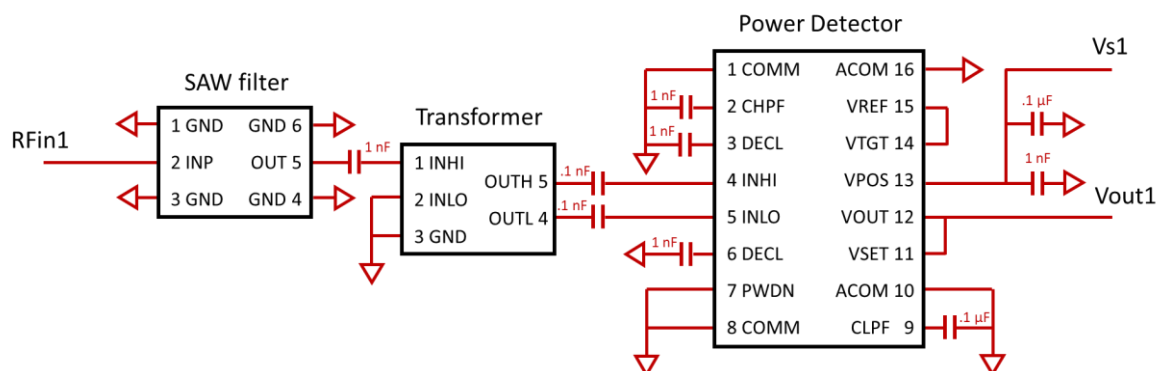


Figure 73: RMS detector circuit diagram, featuring B3722 SAW filter, ETC.1.64-2-3 transformer and AD8362 power detector.

The component B3722 [125] is a SAW filter optimised for use between 312 MHz and 318 MHz. This device is chosen as the frequency is within the range that the VNA can supply as an IF frequency. The filtered signal is transformed by the ETC.1.6-4-2-3 transformer [126] from an unbalanced input to the balanced input required by the AD8362 power detector [127]. The power detector has a frequency range of 50 Hz to 3.8 GHz and is used to convert the balanced power input to a voltage output. The capacitors shown in Figure 73 are as specified by the component use guides [125, 127]. The printed design on FR4 can be seen in Figure 74.

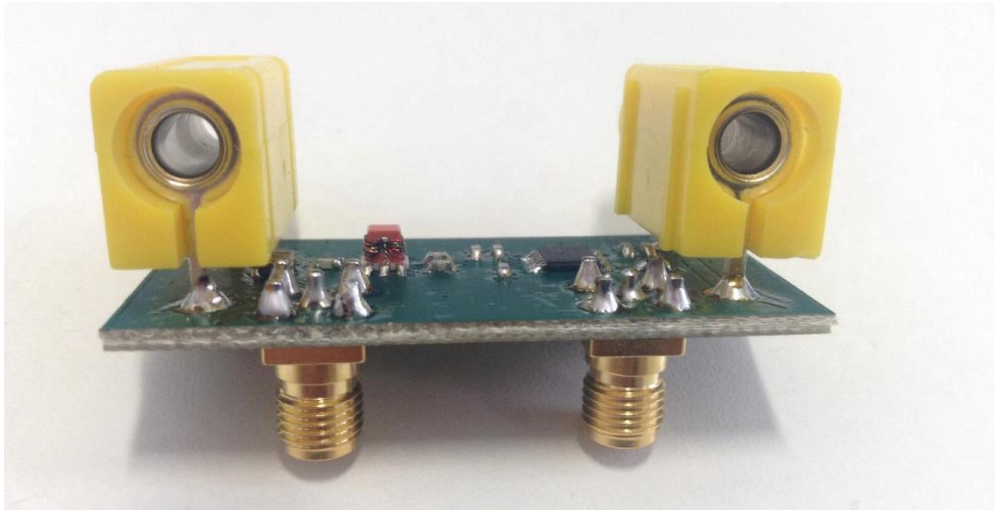


Figure 74: Photograph of fabricated RMS detector PCB on FR4.

The circuit connectors can be clearly seen in Figure 74. The two SMA connectors underneath are for RFin1 and Vout1 (with reference to Figure 73). The two banana connectors on top of the PCB, GND1 (0 V) and Vs1 (5 V), are to supply power to the AD8362 power detector.

The circuit is tested using an RF input between 300 and 330 MHz. The power input is varied between -40 and -20 dBm, to approximate common outputs from the VNA. The resulting graphs are shown in Figure 75.

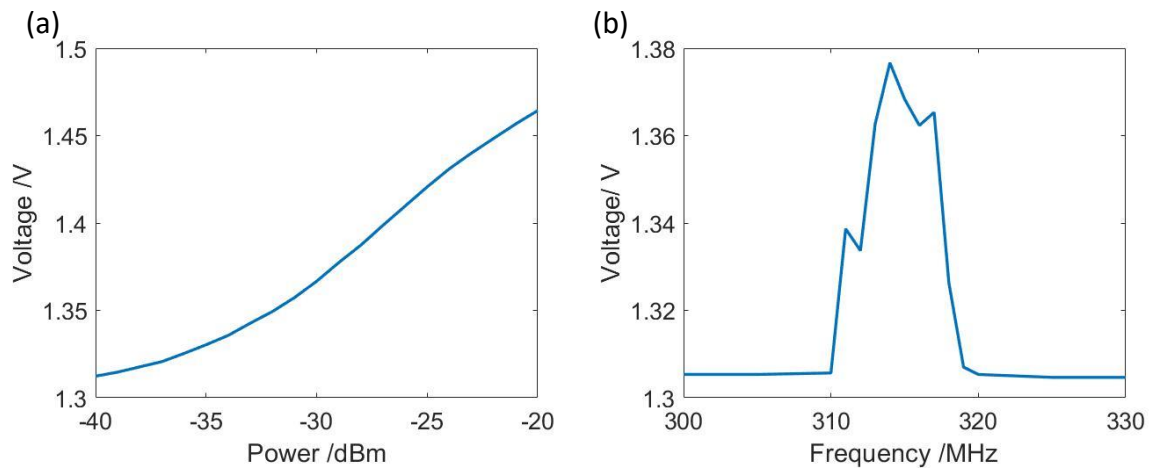


Figure 75: Experimental results of power detector test, (a) voltage performance with varying input power at 315 MHz, (b) voltage performance with varying input frequency with power of -30 dBm.

The power dependence of the graph can be seen in Figure 75(a). The highest rate of voltage to power variation is seen between -35 and -25 dBm. The frequency dependence of the device can be seen in Figure 75(b). A clear peak can be seen between 310 and 320 MHz, of 1.38 V at 314 MHz. This is within the range of 312 MHz to 318 MHz the board is design for. The voltage

supply to the PCB was set at 5.00 V but fluctuated between 4.98 V and 5.13 V. The output fluctuations of the RMS detector were ± 0.003 V.

8.3 On-Off Modulator

8.3.1 On-Off Modulator Design

The switch is designed with two back-to-back PIN diodes, as shown in Figure 76(a). PIN diodes have a faster switching speed than other devices, such as field-effect transistors (FETs) and so are more suitable for GHz frequencies [128]. PIN diodes differ from a standard PN junction in that they have an intrinsic region between the two heavily doped regions. At lower frequencies, they act purely as a diode, as this depletion region has enough time to fully charge and discharge. However, at higher frequencies, the depletion region never fully discharges, and the device acts akin to a capacitor.

As shown in Figure 76(b), when the switching input is off, the diodes are reversed biased and act as capacitors. This suppresses the RF signal. When the switching input is on, as shown in Figure 76(c), the diodes are forward biased and therefore act as resistors in parallel with a high capacitance. Therefore, the RF signal can pass easily.

The circuit design is shown in Figure 76(d) with the component values shown the result of optimisation through Keysight ADS. The radial stubs act as an open circuit to the RF input frequencies, as discussed in Section 2.2.2. By attaching the stubs to the main transmission line by a $\lambda/4$ transformer, the intersections between the main transmission line and the three perpendicular lines all act as a short circuit. The resultant effect is one of a bandpass filter, with the frequencies around the RF input passed with low impedance. As shown in Figure 76(d), the radial stub filter on the switching input, shown bottom middle, is larger than the other two filters to accommodate the impedance of the two diodes. In addition, there is a capacitor on each of the high frequency ports to decouple the DC current and a resistor on the switch input to bias the diode pair.

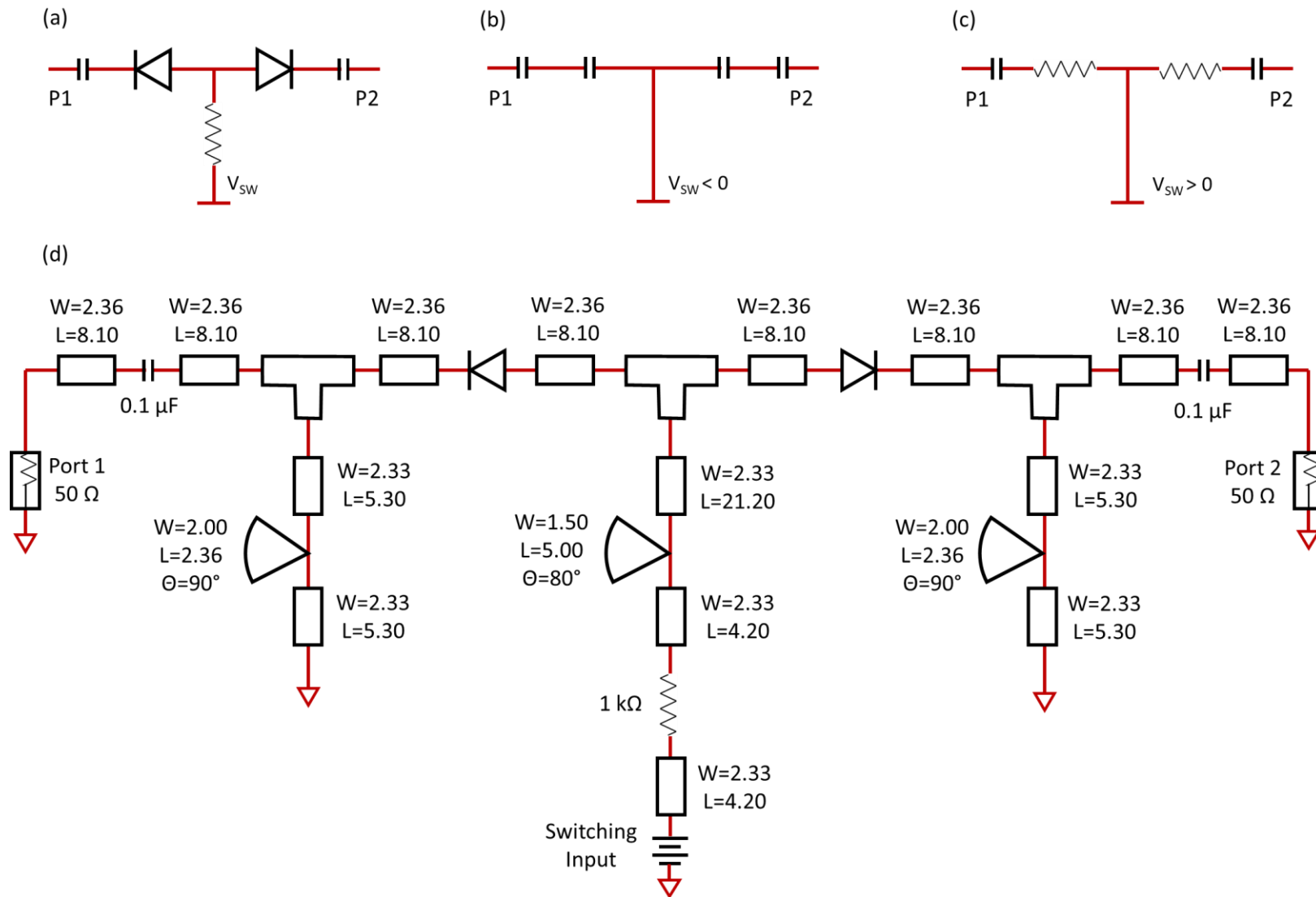


Figure 76: (a) Concept circuit diagram of switch, (b) equivalent circuit of (a) when switch is off, (c) equivalent circuit of (a) when switch is on, and (d) ADS schematic view of an on-off modulator designed to switch a 12.3 GHz signal.

8.3.2 Simulation

The switch is designed to work on the 12.3 GHz RF input to the extender heads. The switch will therefore be optimised around this frequency. The circuit shown in Figure 76 is simulated between 10 GHz and 15 GHz to calculate the s-parameters of the system in both the off and on states. The s-parameters are calculated between the port seen on the left of Figure 76 (Port 1) and that on the right (Port 2). The on-off switching occurs by changing the input of the voltage supply, seen bottom centre, between 0 V and 1 V. As the design is symmetric, s_{12} and s_{21} , and s_{11} and s_{22} are identical. The transmission s-parameters in both the on and off states can be seen in Figure 77.

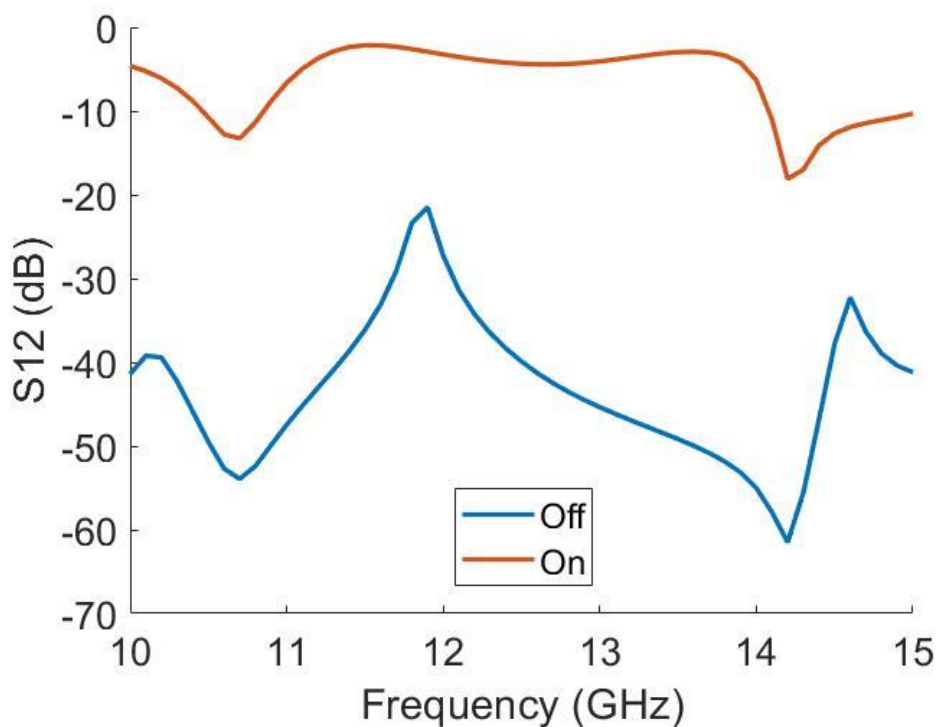


Figure 77: Transmission s-parameters of the switching circuit in both the ON and OFF states.

The switch has been optimised for use at 12.3 GHz, where S_{12} is -4.1 dB in the ON state and -36.5 dB when OFF. The ideal switching location is between 11.5 and 13.5 GHz, where the ON state is consistently above -5.0 dB. The reflection s-parameters in both the on and off states can be seen in Figure 77.

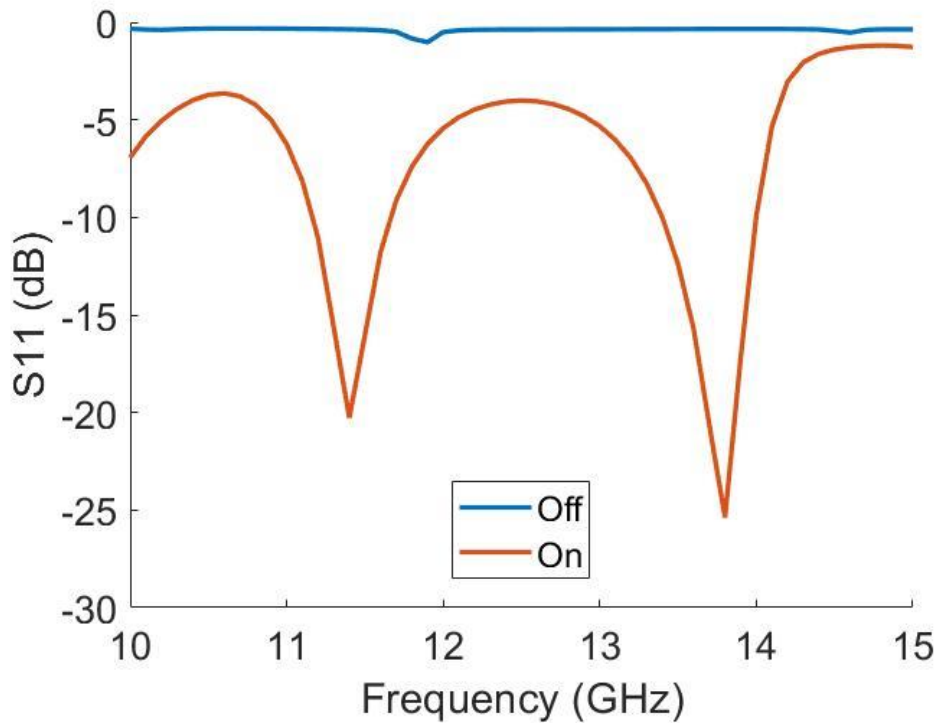


Figure 78: Reflection s-parameters of the switching circuit in both the On and Off states.

At 12.3 GHz, S11 is -4.2 dB in the on state and -0.4 dB when off. This shows there is high reflection even when the switch is on.

8.3.3 Fabrication

The on-off modulator was fabricated in the electronics workshop on RT/Duroid 5870 using techniques outlined in section 4.2.3. The PIN diodes and connectors were soldered by hand. Two SMA connectors are used for the higher frequency ports (ports 1 and 2 in Figure 79), and a BNC connector used for the lower frequency switching port (port 3).

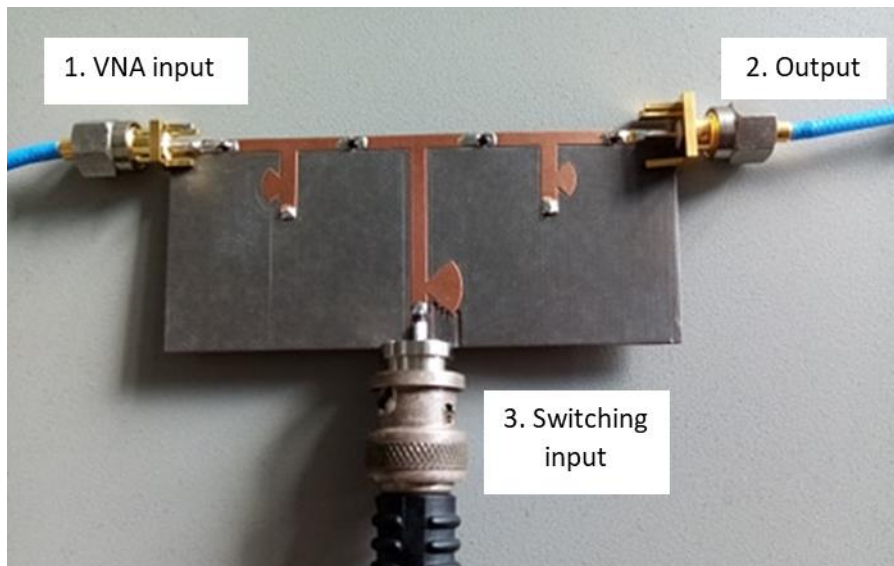


Figure 79: Fabricated modulator with ports labelled.

8.3.4 On-Off Modulator Characterisation

The experimental set-up for the characterisation of the on-off modulator can be seen in Figure 80. A function generator is used to supply the switching input to port 3 and the VNA used to analyse the s-parameters between ports 1 and 2.

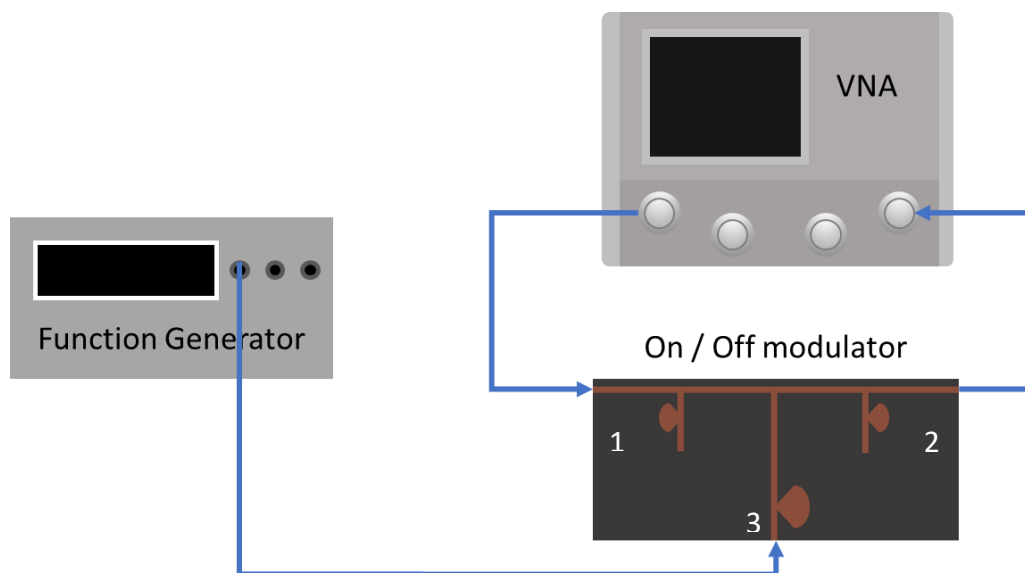


Figure 80: Experimental set-up for on-off modulator characterisation. A function generator is used to supply the switching signal and the VNA to can the power output between ports 1 and 2 for frequencies between 9 GHz to 15 GHz.

A square (with 50 % duty cycle) wave was provided by the function generator. This had an amplitude of 1.5 V and were used as the switching input to port 3. 1.5 V was chosen to increase the output power variation between states and so make switching effects more pronounced. The VNA scanned power output between 9 GHz and 15 GHz, using receiver port

'B' on VNA port 2 (refer to Figure 30), which is a non-normalised port. The switching input was oscillated at 10 Hz during the scanning to produce the graph shown in Figure 81.

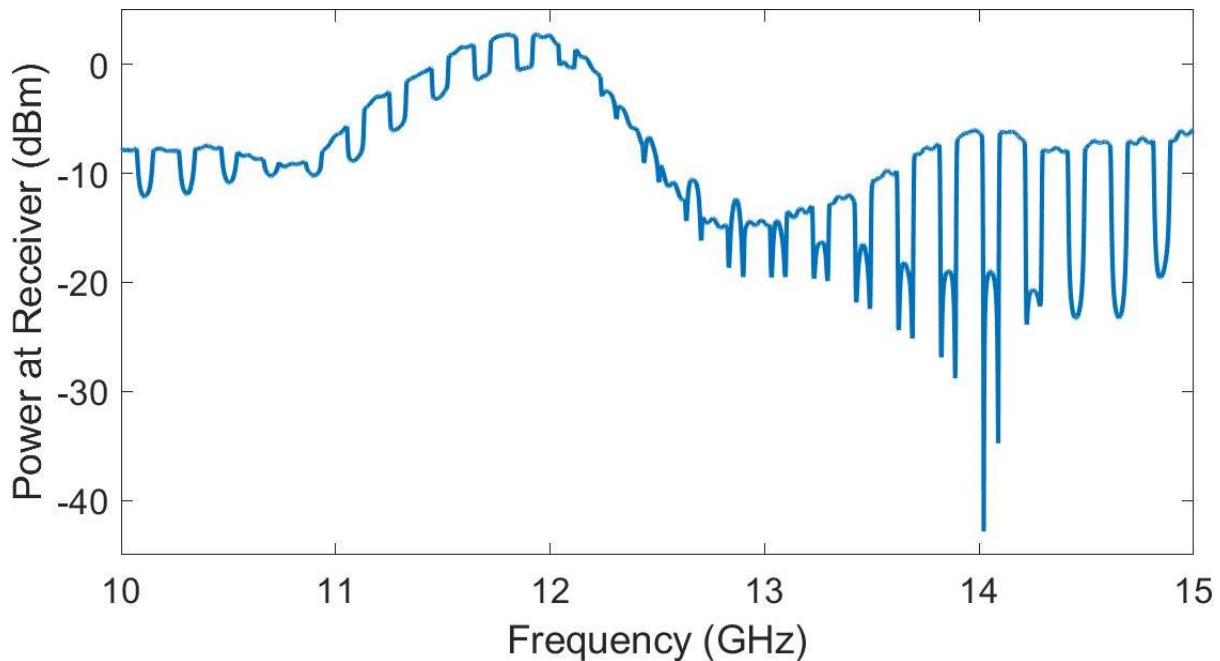


Figure 81: The behaviour of the switch between 9 GHz and 15 GHz for a square wave input. Top right shows the switch response to a 10 Hz switching input.

Figure 81 shows the on-off modulator response to a 10 Hz switching input across a large frequency range, 9 GHz to 15 GHz. The response shows a clear switching of the spectrum between higher and lower power levels as the spectrum is scanned.

8.3.5 Extender head modulation

This section investigates the capability of the frequency extenders to transmit an on-off modulated signal. The experimental configuration shown in Figure 76 is used to test whether switching can be seen at the output of extender head 2. The extender heads take a few seconds to turn on once plugged in, therefore switching (at a rate above 0.1 Hz) by removing the input could be impossible. Additionally, as the extender heads are only designed to transmit between 0.75 and 1.1 THz, low frequency switching signals could easily be filtered on the output. This experiment allows the determination of whether switching between on and off states through the HF port (Figure 30) is possible at frequencies in the Hz to MHz region. If successful, this means future modulators could be tested within the current set-up, without an inhouse multiplier chain established to replace the extenders.

The function generator is used to supply 1 Hz sine and square waves, with a duty cycle of 50 % and an amplitude of 1.5 V. This input is fed to port 3 (Figure 79) of the modulator as the switching frequency. Port 1 receives a 12.3 GHz carrier wave from the VNA, which also analyses the output of the extender heads with the switching applied. Figure 82 shows the on-off modulated signal plotted on the VNA in time over a 5 second interval.

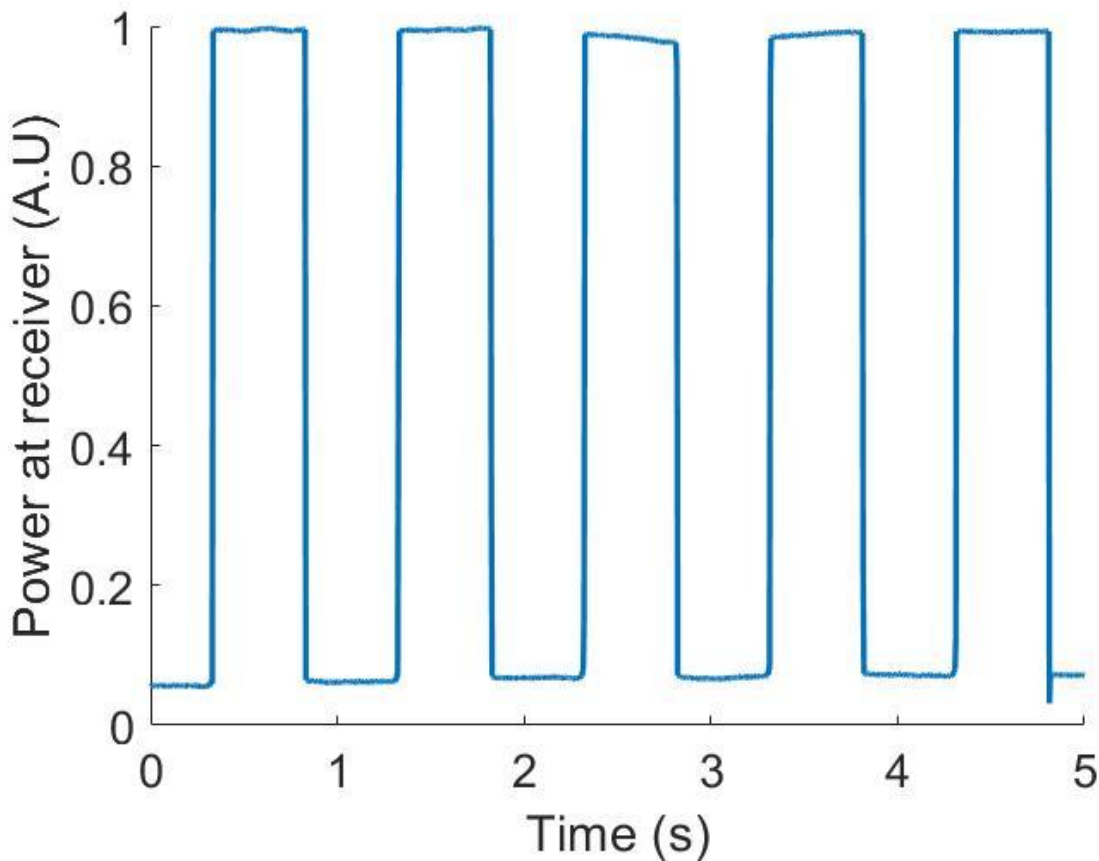


Figure 82: On-off modulated signal response to a square wave switching input, passed through frequency extenders as seen in Figure 72.

Figure 82 shows that the 1 Hz modulation of the extender heads is successful. The traces have been normalised between 1 and 0 to allow the rise/fall shapes to be seen clearly. Further experimental characterisation of the modulator was restricted due to the covid-19 pandemic.

8.4 Conclusion

A simple modulation platform for THz communications has been developed to be used in conjunction with WR1.0-VNAX frequency extenders. This consists of an on-off switching board, designed and simulated for a 12.3 GHz carrier wave, corresponding to the RF input of

the extender modules, and a power detector board, designed for the 315 MHz output of the extenders.

The power detector was successfully designed and fabricated in house. It was characterised, and a clear peak seen between 310 and 320 MHz, of 1.38 V at 314 MHz. This PCB was then used in the characterisation of the on-off keying capabilities of the VNA and extender heads.

The feasibility study of on-off keying between the extender heads was successful, with a 1 kHz signal measured on the extender head output. Therefore, a switch was designed and simulated for a 12.3 GHz carrier wave, corresponding to the RF input of the extender heads. Finally, this switch was fabricated and tested both alone and in conjunction with the VNA and frequency extenders. The switch was found to work best at 10 kHz but can modulate the VNA 12.3 GHz input at frequencies between 1 Hz and 1 MHz.

Chapter 9: Frequency Multipliers

Compared to other regions of the electromagnetic spectrum, the terahertz region has been underutilised due to the low number of available sources [129]. Traditional direct generation sources within the terahertz gap include backward wave oscillators and far infrared lasers, however these are both bulky and provide poor bandwidth [130]. A common alternative to producing high frequency signals is to multiply lower frequencies using frequency multipliers.

Frequency multipliers utilise non-linear circuits to distort an input signal and generate harmonics. The multiplication factor depends on which harmonic is generated due to the distortion. In this chapter, we investigate the viability of using diodes as a non-linear component to produce a successful passive diode tripler.

This chapter describes the design, optimisation and experimental verification of triplers. First, the experimental procedure is outlined. Then the anti-parallel diode tripler is described. Then an analysis of the potential diodes, followed by potential filters. A combination of two filter designs and three diode types are fabricated for a total of six multipliers. Finally, the simulation and experimental results of these six boards are presented.

9.1 Experimental Procedure

All multipliers will be tested with a Giga-tronics Synthesized signal/function generator model 7100, 2 SMK coaxial cables and Keysight EXA Signal Analyzer N9010A. A diagram of the set up can be seen in Figure 83.

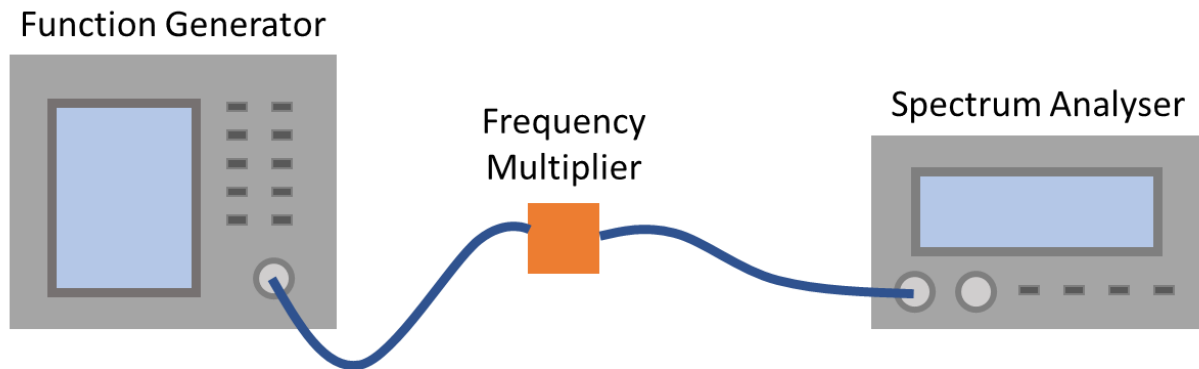


Figure 83: Experimental set-up for frequency multipliers, coaxial cables shown in blue. The input is controlled by a function generator and the output is plotted on spectrum analyser.

The function generator can supply signals up to 30 GHz with 15 dBm power. The spectrum analyser can plot up to 40 GHz. This will allow testing up to 13 GHz while plotting the 3rd harmonic (39 GHz for a 13 GHz input) on the spectrum analyser.

The SMK connections with coaxial cables have unknown linearity. Figure 84 shows the harmonic content measured at the spectrum analyser due to purely the source, connectors, and cables. The cables shown here are used for all frequency multiplier testing, so can be used as a baseline comparison for multiplier performance. A male-male SMK connector has been used in place of the frequency multiplier in Figure 83 to connect the cables under test. This will cause additional, unmeasured distortion, but no more than seen due to connections to PCB boards used to test the multipliers themselves.

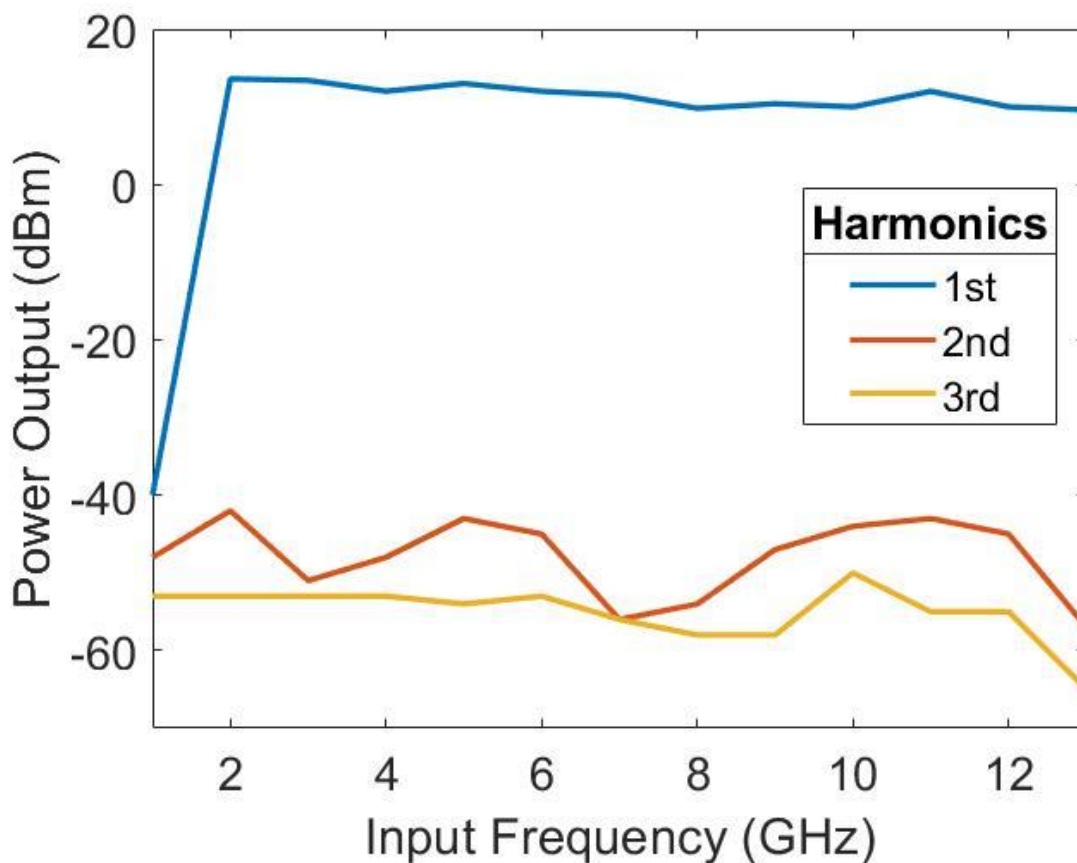


Figure 84: Harmonic distortion measured over frequency, due to signal generator output, connectors and coaxial cables.

The first harmonic is greatly distorted at 1 GHz but has a mean 11.4 dBm output above this. The power output from the function generator is 15 dBm at the fundamental frequency, therefore, above 1 GHz, 3.9 dBm has been attenuated between source and spectrum analyser. Both the second and third harmonics have significant magnitude without any PCB present, their mean magnitude being -47.9 dBm and -55.1 dBm respectively. There is a small peak in the 3rd harmonic at 10 GHz, this is 5.5 dBm above the mean of the other readings. Any measured peak at 10 GHz in multiplier testing will have to be greater than this to be verifiable.

9.2 Multiplier Design

This section describes the diode-based tripler design. The diode choice is predominantly between step recovery diodes, PIN diodes and Schottky barrier diodes. Step recovery diodes can be used in either forward or reverse bias, where they look like a large capacitor (low impedance) or small capacitor (high impedance) respectively. The transmission between low

and high impedance happens in the diode transition time. This produces a narrow voltage pulse; however, the output frequency is limited by the transition time.

PIN diode frequency multipliers can be used in a variety of configurations. A single PIN diode is useful for low cost or high frequency waveguide structures where the fundamental frequency is easy to reject. However, balanced PIN diodes have increased output power and inherent rejection of the fundamental frequency and of certain unwanted harmonics.

Schottky barrier diodes have high switching speeds and are therefore ideal for high frequency applications. They can be used for both frequency doublers and triplers and are very cheap to buy. Schottky diodes are the non-linear component of choice for this section and will be used in a tripler configuration. Typical diode multiplier configurations can be seen in Figure 85.

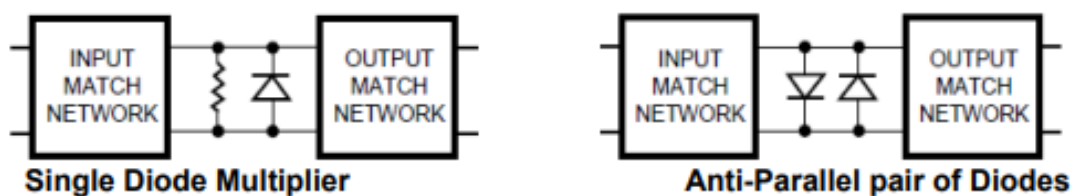


Figure 85: Passive diode multiplier layout, with single and anti-parallel configurations shown. Image from reference [28].

In the anti-parallel pair of diodes, each diode effectively shorts the other at the second harmonic and so all even harmonics are rejected. This can only be used as an odd-order multiplier and requires a filter to reject the fundamental frequency. This will form the basis of the multiplier, when in combination with an input and output filter.

While this chapter focused on multipliers for microwave frequencies, the intention is to extend these into the THz range. The basis of these designs is appropriate for higher frequencies, as the filter designs are only based on microstrip lengths which can easily be reduced with micro-fabrication methods, but interconnections such as soldering of diodes must be removed. As even a small amount of solder can resonate and therefore act as an antenna at these frequencies. Therefore, on chip Schottky diodes are a requirement. These have already been proven within the THz range for detectors [131, 132], and so there is good evidence to show this is plausible. The challenge to move to the THz range, is the integration of suitable rectifiers on chip. Besides conventional Schottky diodes, a more novel solution is to use metal, insulator, metal (MIM) junctions, such as those developed at Durham [133, 134]

9.3 Diodes

Three types of surface mount Schottky barrier diodes have investigated for use in the frequency tripler. The first is a HSMS-2852-BLKG Broadcom diode [135] that is rated up to 1.5 GHz. The second is a HSMS-2829 Broadcom diode [136] that is advertised as being “*optimized for use in RF applications, such as’... ‘Mixers and frequency multipliers up to 6 GHz*”. The third and final diode is a SMS7630-079LF Skyworks Solutions which “*May be used at frequencies up to 24 GHz*” [137]. Figure 86 shows a summary of the characteristic variables for each diode.

Spice Parameter		Unit	Diode 1	Diode 2	Diode 3
B _V	Reverse Breakdown Voltage	V	3.8	15	2
C _{JO}	Zero-bias Junction Capacitance	pF	0.18	0.7	0.14
E _G	Energy Gap	eV	0.69	0.69	0.69
I _{BV}	Current At Reverse Breakdown Voltage	A	3 E-4	1 E-4	1E-4
I _S	Saturation Current	A	3 E-6	2.2 E-8	5 E-6
N	Emission Coefficient	-	1.06	1.08	1.05
R _S	Ohmic Resistance	Ω	25	6	20
P _B (V _J)	Junction Potential	V	0.35	0.65	0.34
P _T (XTI)	Saturation-current Temperature Exponent	-	2	2	2
M	Grading Coefficient	-	0.5	0.5	0.4
TT	Transit Time	sec	0	0	1 E-11
F _C	Forward-bias Depletion Capacitance Coefficient	-	0.5	0.5	0.5

Figure 86: Simulation parameters for each diode. Where default value is used: shown as bold in the table.

Each of the diodes shown in Figure 86 will be simulated, first alone to ensure simulation is accurately matching the datasheet characteristics, then in a anti-parallel configuration, as shown in Figure 85, to test its capability as a tripler. Below, the first test set up is shown. This is a DC simulation of a diode, where voltage is varied and current measured. All simulations are completed with Keysight ADS, for full details refer to Section 3.2.2.

The simulation configuration shown in Figure 87 is for the harmonic analysis of an antiparallel diode pair. This is to show the capability of the diodes in the chosen frequency tripler configuration, with no associated filtering.

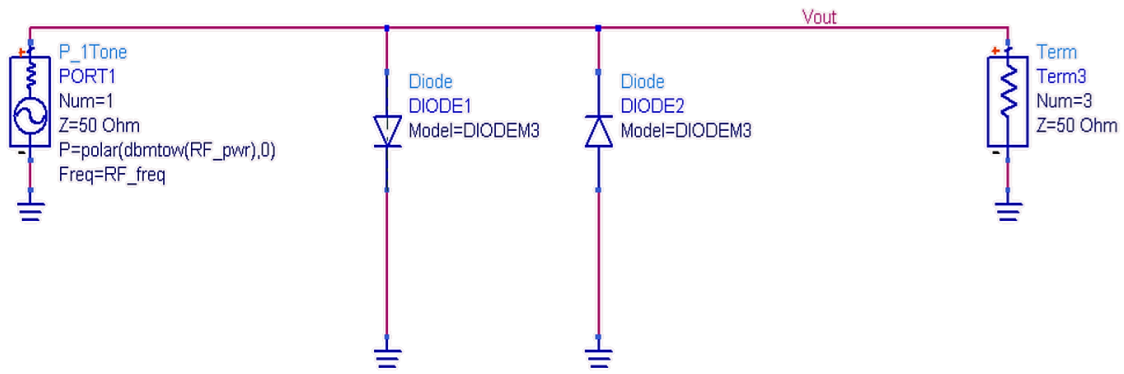


Figure 87: Harmonic analysis ADS simulation set-up for antiparallel diode testing.

The 1st and 3rd harmonics have been plotted in Figure 88. The second harmonic has been omitted from this graph as the mean power (across all three diodes) is -335 dBm.

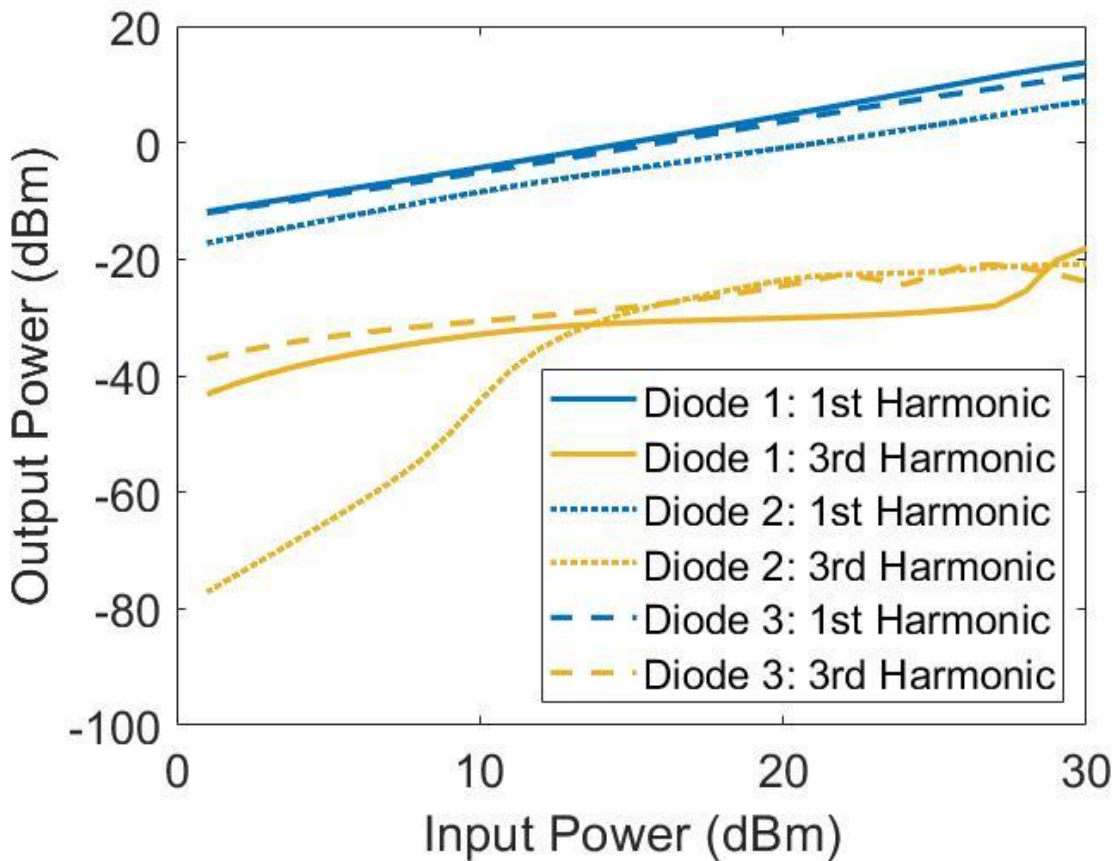


Figure 88: Harmonic content produced by different diodes in antiparallel configuration with 15 dBm input.

The output power increases with the input power for all diodes. At 12 dBm to 16 dBm the 3rd harmonic for all diodes under test has similar magnitude. Below 10 dBm the output power of the 2nd diode greatly decreases and would not be the ideal candidate for frequency tripler with an expected low power input.

Figure 89 shows the simulation power response to a varied frequency input. 15 dBm has been selected as the input for variable frequency testing, this is the upper power limit of our function generator and should allow the largest range of signals to be seen on the spectrum analyser. The frequency input varies between 1 and 13 GHz to reproduce what is possible to test with available experimental equipment.

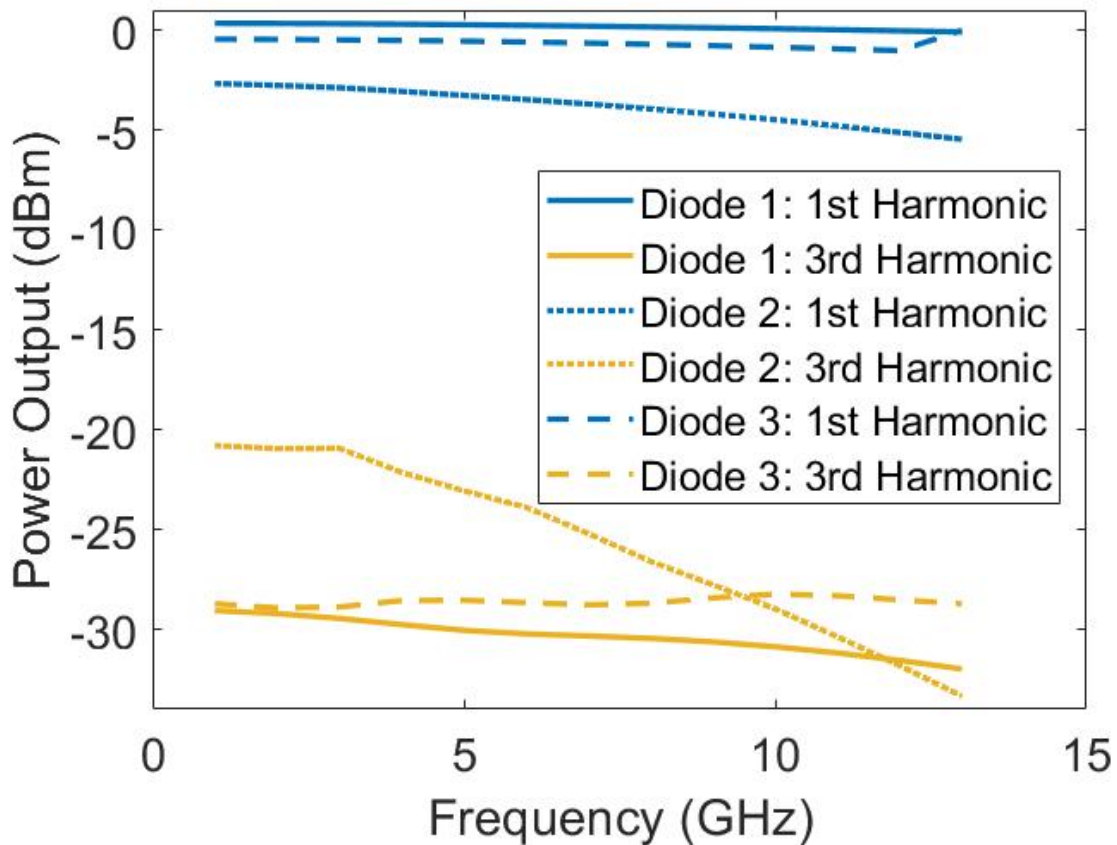


Figure 89: ADS simulated harmonic response to anti-parallel diodes with no associated filtering.

Diodes 1 and 3 have consistent power output across the frequency range tested, compared to diode 2 for which power output decreases for both the first and third harmonic as power is increased. This could predict a poorer tripler efficiency at the higher end of the tested spectrum.

Figure 90 shows a PCB designed to experimentally test the diodes in anti-parallel configuration, without filtering any harmonics. Figure 90(a) shows the ADS model used to test this design, and Figure 90(b) the manufactured board with diode 1 under test. All PCBs are fabricated in house on RT/Duroid 5870 using techniques outlined in Section 4.2.3.

Three of each PCB were fabricated, so each diode type had its own test board. This was for ease of re-test but has the advantage of random errors in manufacture not impeding the characterisation of the board. This means any similarities between the boards are legitimately due to design and not due to random error in manufacture. All diodes will be tested, even the poorer performing diode 2, to judge whether simulations are accurate replications of experiment.

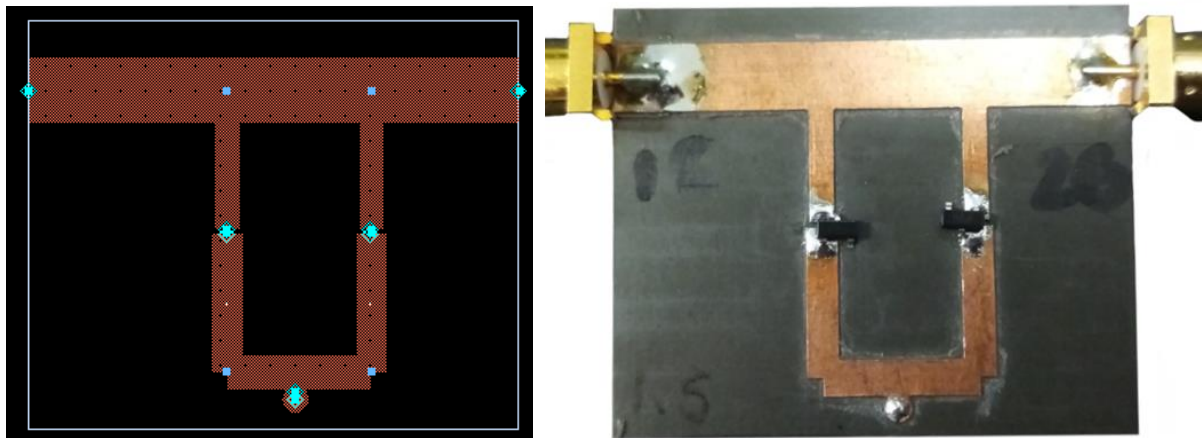


Figure 90: (a) ADS model and (b) fabricated PCB of antiparallel diode test board.

Figure 90(a) shows the ADS simulation model. Port 1 is on the top left and supplies 15 dBm power at varying frequencies to the anti-parallel test board. The two diodes are located inside the loop, one facing upwards and one downwards (ergo anti-parallel). Port two is on the top right and is where the diode's response is measured from. Figure 90(b) shows the fabricated version of this test board. Ports 1 and 2 can be seen with SMK connectors to attach into the experimental test set-up shown in Figure 83, and the two diodes seen soldered towards the centre of the board.

Figure 91 shows the experimentally measured harmonic response of the diodes, housed in the PCB shown in Figure 90(b).

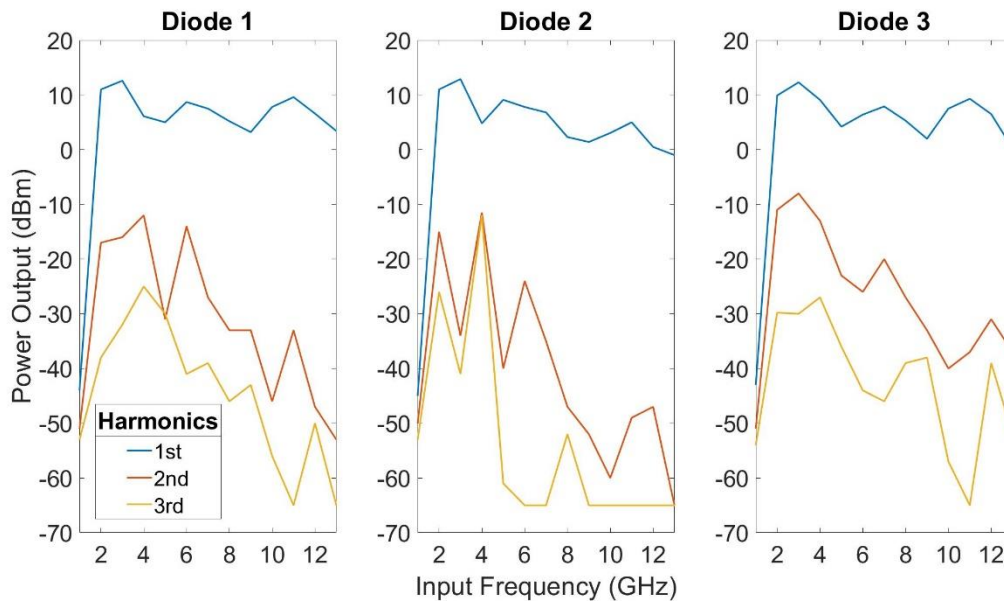


Figure 91: Experimentally measured harmonic response to anti-parallel diodes with no associated filtering.

For all diodes, the first harmonic has a similar response, peaking at 3 GHz with a power of approximately 12 dB. This reflects the losses shown due to the experimental equipment in Figure 83.

The second harmonic in Figure 88 is much higher for all diodes in experiment than the simulated -335 dBm. This could be due to the frequency generator having higher harmonic content than the simulated source. The harmonic content of the signal generator is quoted as -55 dBc between 50 MHz and 20 GHz, and the simulated harmonic content is non-existent.

The third harmonic is much less consistent than the reference Figure 83, which had a stable output of approximately -53 dB. Figure 91 shows harmonics have indeed been produced, as much higher third harmonics are seen, peaking at -13 dB for the 4 GHz measurement of diode 2.

9.4 Filters

The frequency multipliers discussed so far have no associated filtering, and so are not optimised around any one frequency. The aim of this chapter is to produce a tripler with an input of 10 GHz.

Filtering is required at both the input RF frequency and the output harmonic frequency. A bandpass filter will be designed for both. As we will be integrating the multiplier onto a PCB, the chosen filters must be easy to implement and integrate. Two filter types will be tested. They are both microstrip filters, and so have no components that must be soldered, which reduces risk of excess solder causing interference at the desired frequencies.

The first is a coupled line bandpass filter and the second is a stub filter. These are optimised concurrently with the anti-parallel diodes. This is to increase the possibility of other frequencies contributing positively to the 30 GHz required output, and to decrease optimisation time. However, to view the filters more simply, the multipliers are divided into three sections: namely, input filter, antiparallel diode pair and output filter. The input filter is designed to inherently isolate 10 GHz as this is the required signal to be tripled. The output filter is optimised for 30 GHz.

9.4.1 Filter A

Filter A is a coupled line filter [138], optimised to multiply a 10 GHz signal to 30 GHz. As shown in Figure 92(a), it is formed of five filters in total. Two are on the input, three on the output. The output has an additional filter due to the added difficulty of ensuring the harmonic frequency is removed. There is an added ground plane in the centre to make it easier to solder the larger diodes into the same ground port.

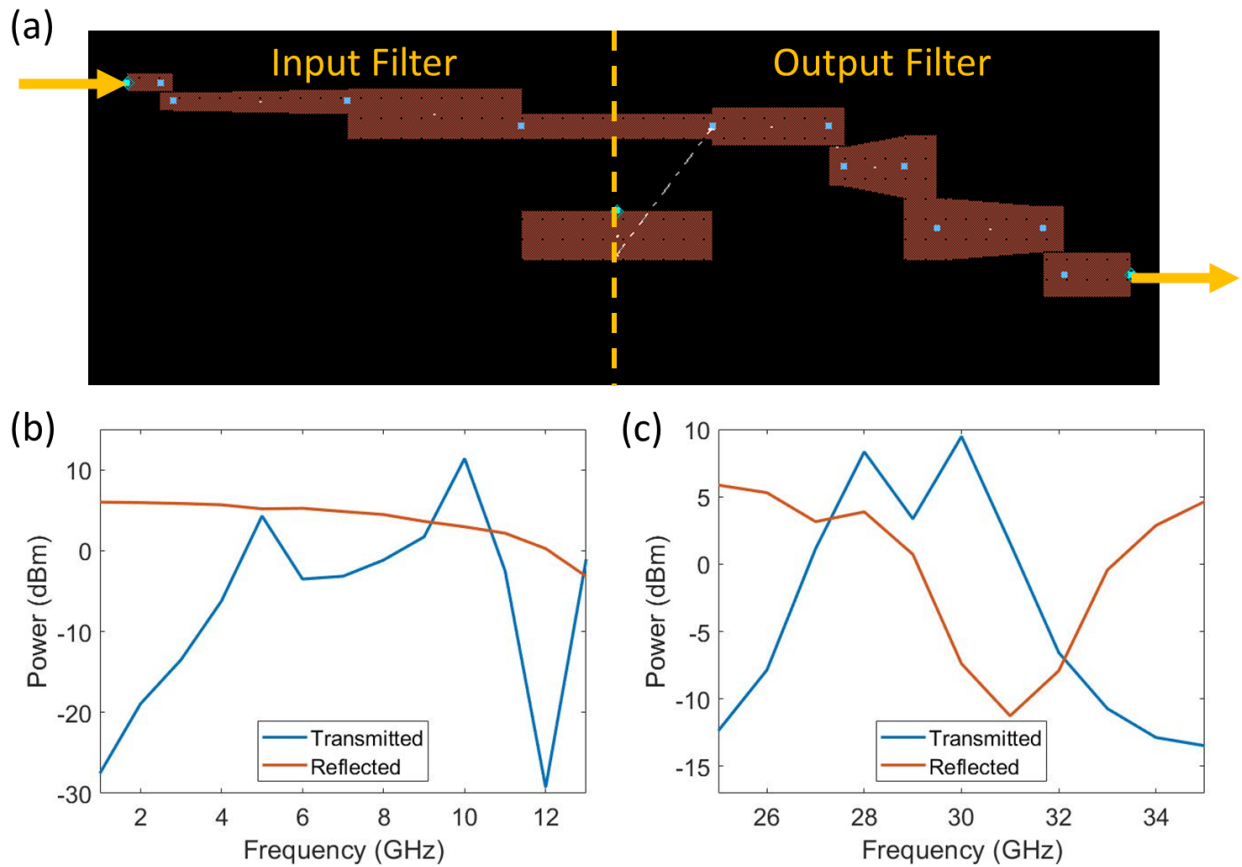


Figure 92: (a) First filter design showing both halves of the filter, and the simulated transmitted and reflected power responses of the (b) input and (c) output filters between 1 GHz and 13 GHz.

Figure 92(b) shows the power response of the input filter and Figure 92(c) that of the output filter. For both input and output, the transmitted power has a clear peak at the desired frequency, 10 GHz and 30 GHz respectively. The transmitted power for the input of filter C at 10 GHz is 11.4 dBm and the reflected power is 3.0 dBm. The transmitted power for the output of filter C at 30 GHz is 9.5 dBm and the reflected power is -8.6 dBm.

Figure 93 shows the ADS harmonic simulation of the entire tripler, for all three diodes, including input and output filtering.

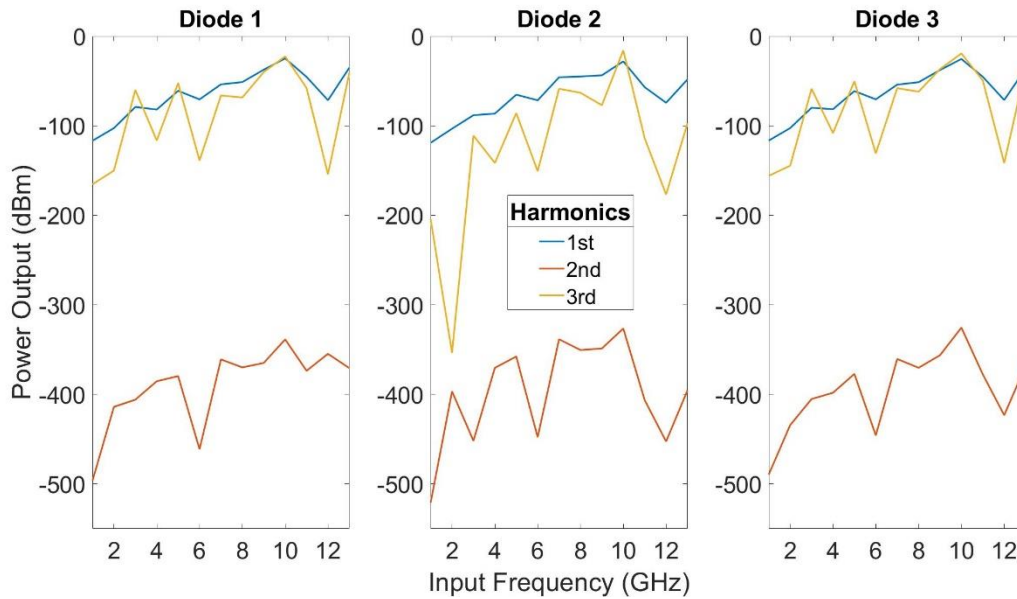


Figure 93: ADS harmonic simulation of anti-parallel diode frequency tripler with diodes 1-3 and filter A.

The multiplier has been successfully optimised as the 3rd harmonic is highest for each diode at 10 GHz. The fabricated PCB can be seen in Figure 94.

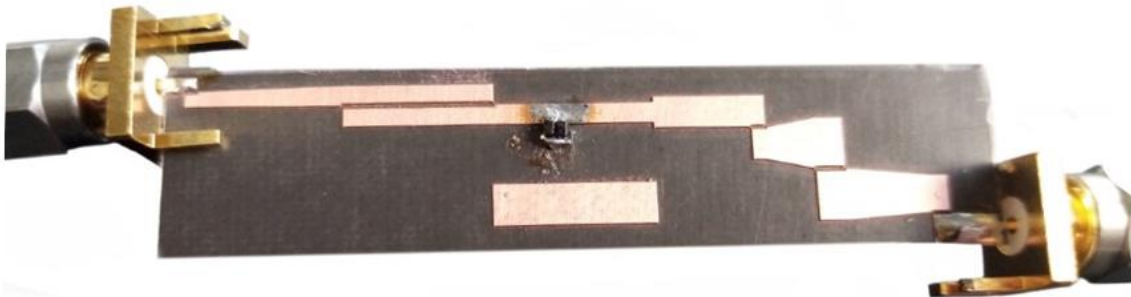


Figure 94: Fabricated anti-parallel diode frequency tripler with Filter A.

The output for the third harmonic was lower than the noise level for the entire frequency region tested. This is likely due to all slithers between coupled line sections being manufactured to 0.4 mm, regardless of the size specified in the Gerber. Alternate milling tools were tested, but with no success on increasing the accuracy of the printing.

9.4.2 Filter B

Filter B is designed with grounded stub filters [138], with a 0.5 mm continuous transmission line. Figure 9(a) shows the final design of the filters for the multiplier.

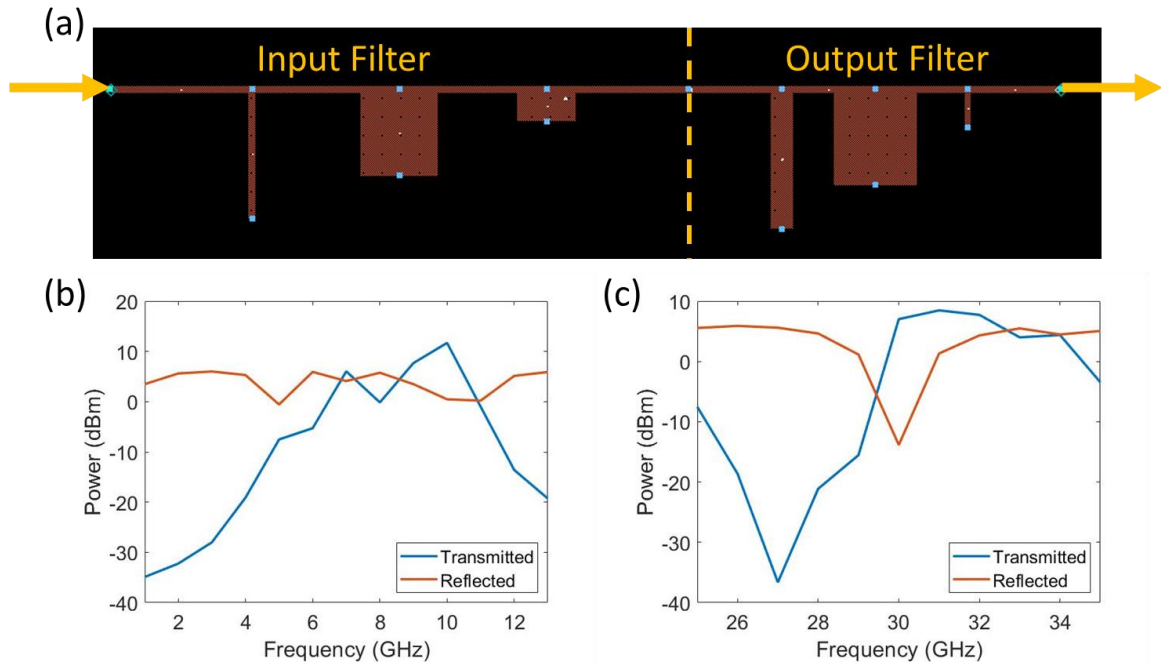


Figure 95: (a) Second filter design showing both halves of the filter, and the simulated transmitted and reflected power responses of the (b) input and (c) output filters between 1 GHz and 13 GHz.

Figure 95(b) shows the power response of the input filter, with a 15 dBm input. The input filter is simulated around the expected transmission peak at 10 GHz. An ideal filter would transmit all available power at this frequency. The transmitted power of this filter is 11.7 dBm; the reflected power is 0.5 dBm.

Figure 95(c) shows the transmitted and reflected power due to the output filter, with a 15 dBm input. The transmitted power at 30 GHz is 7.0 dBm and the reflected power is -14.1 dBm.

Figure 96 shows all three diodes, as outlined in Figure 86, tested with filter B.

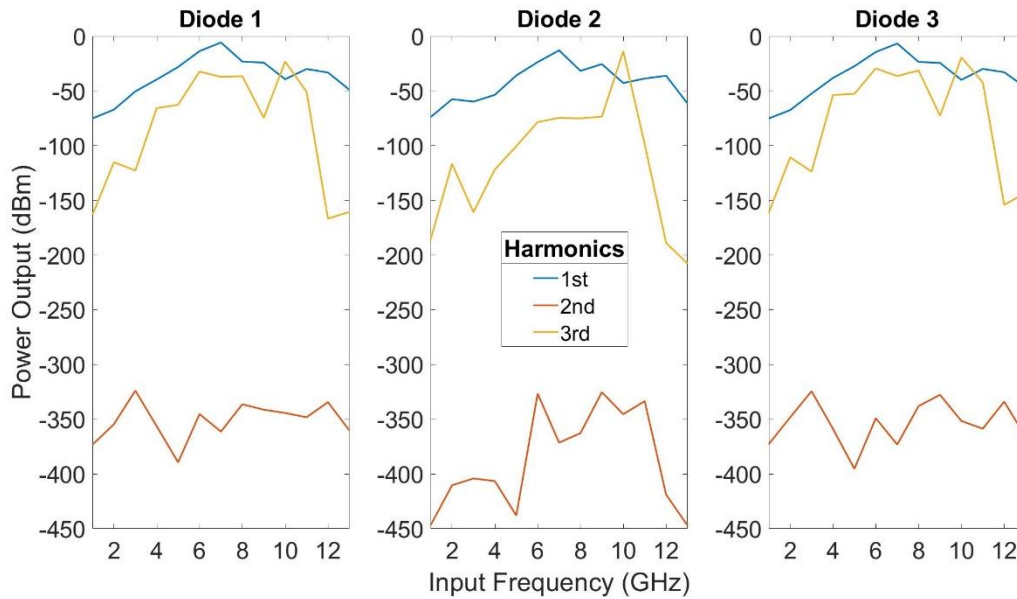


Figure 96: ADS harmonic simulation of anti-parallel diode frequency tripler with diodes 1-3 and filter B.

The first harmonic has the largest power output magnitude, except at 10 GHz which the frequency tripler has been optimised for. At this frequency, the 3rd harmonic is dominant for all three diodes tested. The magnitude is -23.1 dBm, -13.7 dBm and -19.4 dBm for diodes 1, 2 and 3 respectively. However, the 1st harmonic is still very high at 10 GHz so the output filter is not suppressing this as much as would be ideal. The 2nd harmonic has negligible magnitude as expected, the mean is -351 dBm, -387 dBm and -354 dBm for diodes 1, 2 and 3.

Figure 97(a) shows the fabricated first filter design, with the experimentally measured transmitted power at harmonics 1-3 shown in Figure 97(b).

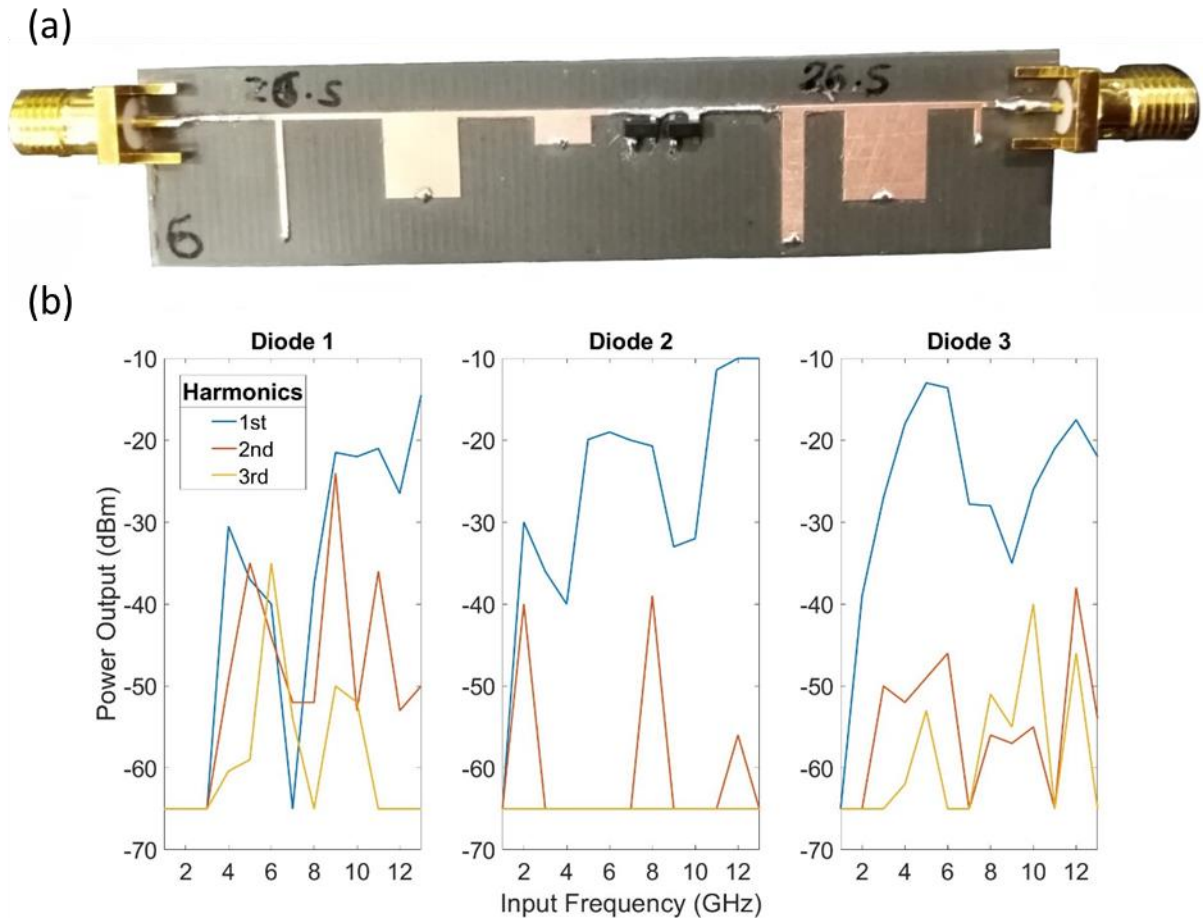


Figure 97: (a) shows the fabricated antiparallel diodes with filter B and (b) the experimentally measured harmonic response to this frequency multiplier.

The experimental results in Figure 97 are different to those simulated in Figure 96. The 10 GHz peaks in 3rd harmonic are suppressed for all three diodes: -52 dBm, -65 dBm and -40 dBm for diodes 1, 2 and 3 respectively. The second harmonic is significantly larger for diodes 1 and 3 than in simulation. This could be the result of the non-perfect function generator input. As the simulation assumes no harmonic content on the input, the filter is not optimised to remove this. Another possibility is that the PCB is not acting as a purely odd-order multiplier. This could be due to the arrangement of the diodes. In simulation they are located directly next to each other with no track length between. In reality this is not possible, and the small length of track between the diodes could make the diodes appear as if in parallel configuration at certain frequencies.

One way to negate this effect would be to rearrange the placement of the diodes, for instance having one soldered above the line and one below. This would allow the diodes to be soldered at the same point, therefore closer replicating the simulation conditions.

9.5 Conclusion

Frequency multipliers have been designed and simulated in the 10 to 30 GHz frequency range. Simulations consistently showed a strong third harmonic while others were successfully filtered by on-chip microstrip filters. However, the preliminary experimental results show a stronger effect of the filter output due to tolerances than had been predicted. These tolerances are fully investigated in Section 4.2.3, however complications due to the Covid-19 pandemic prevented a further round of fabrication and experiment to characterise the effect of the machining tolerances on the filter performance. It would be recommended to produce an identical set of multiplier designs fabricated through the more accurate technique of photolithography. This has successfully been utilised in the manufacture of antennas in Chapter 7 and have been used for micro-PCB fabrication previously [139] with patterning from 1 to 6 μm with accuracy $\pm 0.2 \mu\text{m}$.

Chapter 10: Frequency Mixers

Mixers are described in Pozar [13] as “a three-port device that uses a nonlinear or time-varying element to achieve frequency conversion”. They are a vital part of most microwave systems as it is difficult to both generate and analyse the RF signal directly. The principle of mixing signals can be traced back to the early 1900’s. However, interest in the field spiked in World War II, where military radars were being produced for microwave frequencies [29].

One of the most predominant achievements in the subsequent years is the full characterisation of mixer theory. By the late 1950’s the “theoretical underpinnings of mixer design” were settled [30]. The improvements thereafter are mostly characterised by improvements in diode technology; Young and Irvin designed the first high frequency GaAs Schottky diodes in the mid-1960s [140], This greatly increased the frequencies RF mixers could achieve, with Fetterman [141] demonstrating a fifth harmonic mixing at 1757.5 GHz in 1974.

In the 1980’s Bishop [142] designed the first planar THz Schottky diode, which has led to applications such as sub-mm-wave heterodyne instruments and THz imaging radar and instruments, and in the 2010’s more sophisticated mixer topologies were made possible by the invention of low-parasitic diodes [143].

This chapter describes the design, fabrication and testing of a series of planar balanced mixers. For an introduction to mixer theory, refer to Section 2.4.

10.1 Design

The frequency mixer shown here is designed for an RF input of 20 GHz. This is to allow easy adaptation to common post-5G frequencies: 60, 90 or 270 GHz, with a final mixer stage. This final stage will not be presented here as cannot be tested with our available equipment. The required output IF frequency is 315 MHz so the RMS detector presented in Section 8.2 can be used to analyse the output.

The down conversion from 20 GHz to 315 MHz will be split between two mixers. The first has inputs 20 GHz (f_{RF1}) and 18 GHz (f_{LO1}) and will be filtered for an output of 2 GHz (f_{IF1}). This will be referred to as the 20 GHz mixer. The second has inputs 2 GHz ($f_{RF2} = f_{IF1}$) and 1.685 GHz (f_{LO2}) and will be filtered at 315 MHz (f_{IF2}). This will be referred to as the 2 GHz mixer. The LO frequencies have been chosen as they are both possible to generate using the VNA, and the IF frequencies are chosen to be able to plot on the 3 GHz spectrum analyser. There are two main physical advantages to splitting the mixing process. The first is the reduction in overall noise on the output, and the second is if the signal has been significantly attenuated it is possible to amplify between mixer stages. Another advantage is that simulation time is greatly reduced by having a smaller frequency range to analyse each stage over.

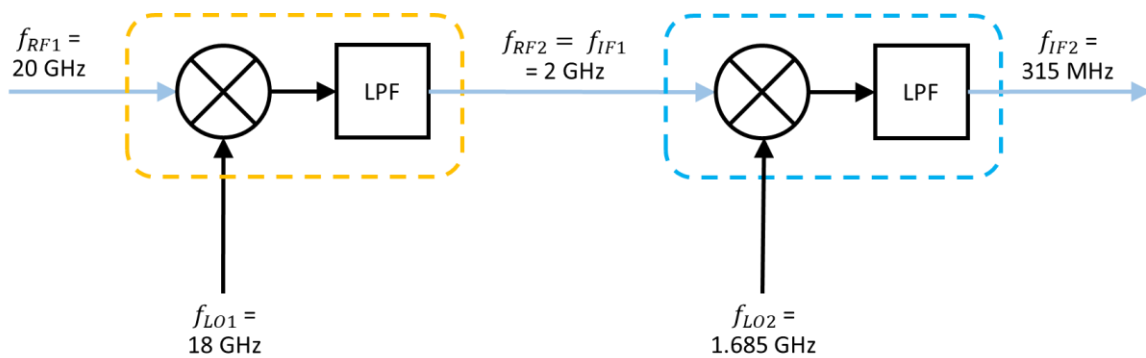


Figure 98: Diagram of intended mixer layout. The first mixer (yellow) downconverts a 20 GHz RF input to a 2 GHz IF frequency using a LO of 18 GHz. The second mixer uses the 2 GHz output as the input, which it downconverts to 315 MHz using a 1.685 GHz LO frequency.

Figure 98 shows complete diagram of the intended mixer layout. The yellow and blue sections highlight the areas that will each be fabricated on a single PCB. The mixers consist of a rat-race coupler, with a 2nd order Butterworth low pass filter.

10.1.1 Rat Race Mixer

A rat-race mixer, or ring hybrid, is a circular device, with two inputs, F_1 and F_2 spaced $\lambda/2$ apart from each other. By using a $\lambda/4$ transformer on each input, the output appears to have the inverse of the input, or by applying a $\lambda/2$ transformation the output is identical to the input. Therefore, the combinations of F_1-F_2 or F_1+F_2 can be achieved by adding transmission lines to the ring specific intervals of $\lambda/4$ away from the inputs.

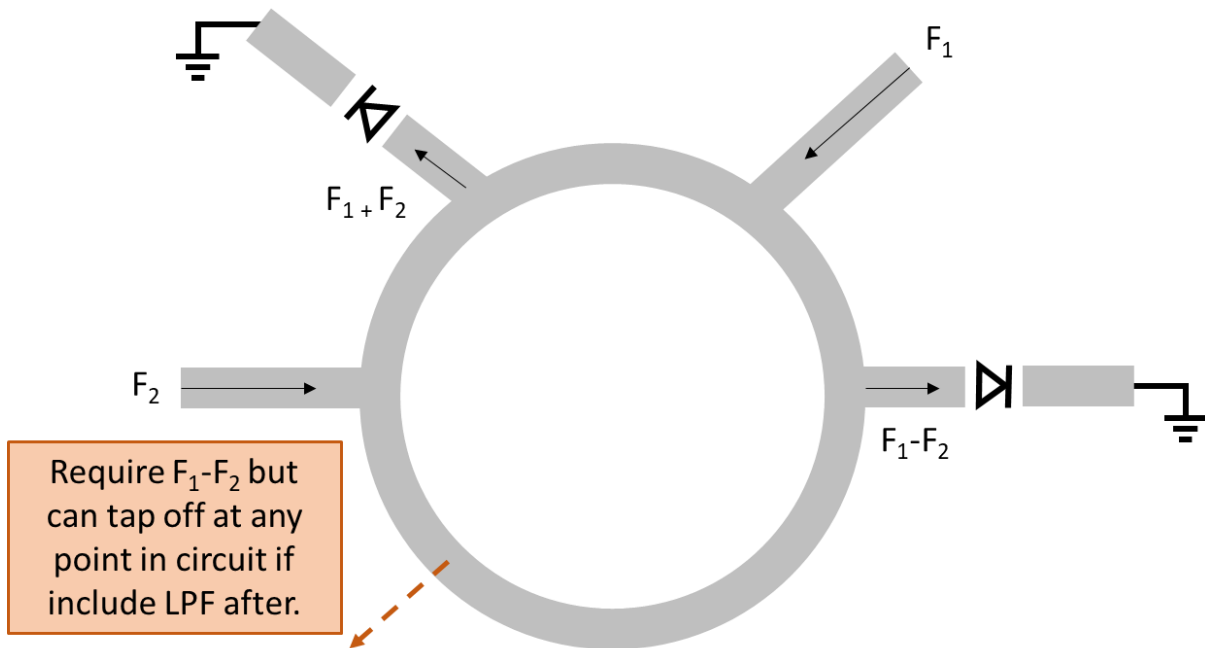


Figure 99: Concept diagram of a rat race mixer with two different frequency inputs F_1 and F_2 .

The two outputs F_1-F_2 and F_1+F_2 are grounded, via Schottky diodes, to allow the output F_1-F_2 to be produced from any part of the ring if a low pass filter is applied after. This type of mixer was chosen as it is easy to integrate and manufacture on a microstrip and does not require many components to be soldered.

While this chapter focused on mixers for microwave frequencies, the intention is to extend these into the THz range. The rat race mixer is an ideal design to be reduced down to THz wavelengths. This is because its function is primarily reliant on microstrip lengths, which using micro-fabrication techniques, can easily be reduced in size. The only other required alteration is the Schottky diodes, which would have to be produced on chip, to avoid solder interconnections, as these can cause high losses at THz frequencies. As discussed in section 9.2, producing Schottky diodes for THz frequencies is already achievable.

10.1.2 Simulation and Optimisation

The basic design of the mixer is decided before fine optimisation completed. The dimensions of the rat-race coupler are confined by the output frequency, and the bandwidth of the ring is generally around 20-30% regardless of the size (pozar). The low pass filter chosen is a Butterworth filter, as they are simple to design and easy to optimise.

All simulations and fine tuning were completed in ADS, as described in Section 3.2.2. The mixers were optimised for the largest output at either 315 MHz or 2 GHz, for the low and mid frequency mixers respectively. The suppression of the input frequencies was also optimised for. This was completed by plotting the magnitude of the FFT of the voltage output, as shown:

$$Y = \text{mag}(\text{fft}(V_{out})) \quad (10.1)$$

Where Y is the output to be optimised, calculated from V_{out} : the output voltage.

10.1.3 Fabrication

All PCBs are fabricated with the techniques for PCB printing outlined in Section 4.2.3. There are 2 designs, one using FR4 as a substrate and one with RT/duroid. The FR4 is a thicker substrate and is expected to perform worse than the RT/duroid PCB. However, it is significantly cheaper and more readily available, so will be used as a test to validate the circuit design, i.e., the rat race coupler and 2nd order Butterworth low pass filter combination. If found to be a successful design, the circuit will then be optimised for the RT/Duroid substrate and manufactured and tested using this.

10.1.4 Experimental Procedure

Figure 100 shows the experimental set-up used to characterise both the low and mid frequency mixers.

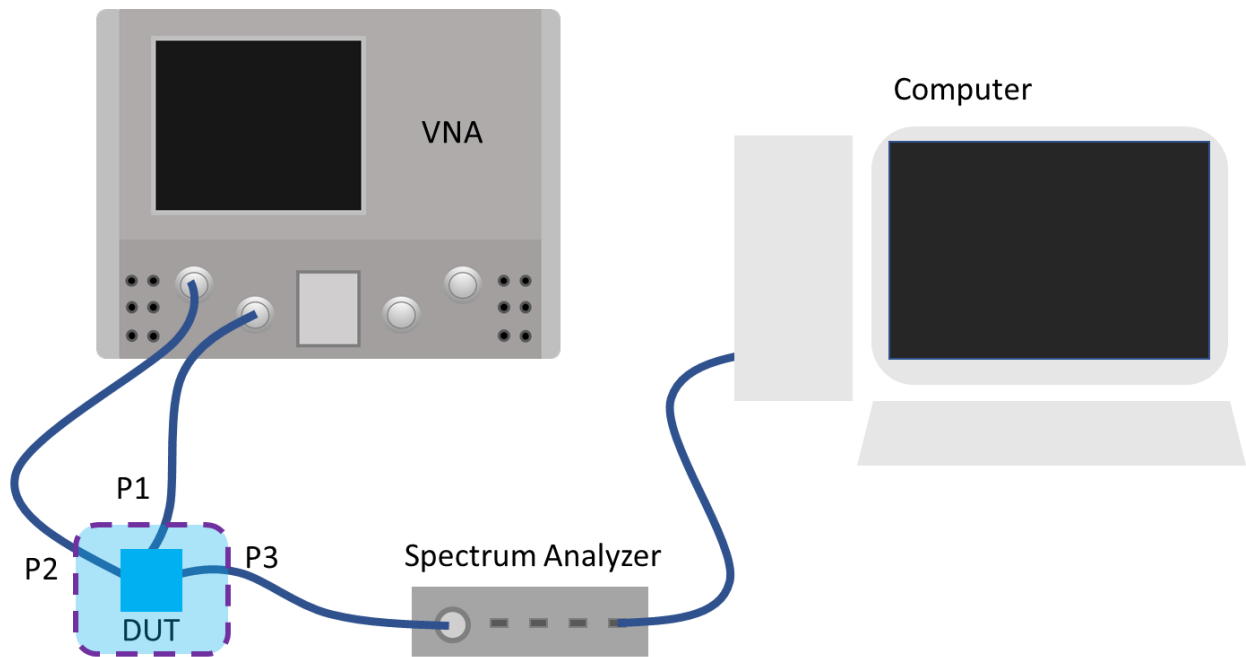


Figure 100: Experimental configuration for characterisation of mixers. The two frequency inputs (P1 is RF input, P2 is IF input) are supplied by the VNA. The output is analysed by a spectrum analyser in conjunction with an external PC.

An Agilent N5224A PNA is used as the inputs to both input ports (P1 and P2) of the mixer. The output port, P3, is connected to a Tektronix RSA306B Real-Time Spectrum Analyzer, which works in conjunction with an external computer and screen. When testing the 2 GHz mixer, the VNA supplies a 2 GHz RF input to port P1 and a 1.685 GHz LO input to port P2. The 315 MHz output from port P3 is then plotted by the spectrum analyser. For testing the 20 GHz mixer, the VNA supplies an RF input of 20 GHz to port P1 and an LO input of 18 GHz to port P2. The spectrum analyser is used to analyse the 2 GHz IF output from port P3. The spectrum analyser has a frequency range of 9 kHz to 6.2 GHz, which is more than sufficient for our maximum output frequency of 2 GHz.

10.2 2 GHz Mixer

10.2.1: On FR4 Substrate

Figure 101 shows the mixer and Butterworth filter design for the 2 GHz mixer.

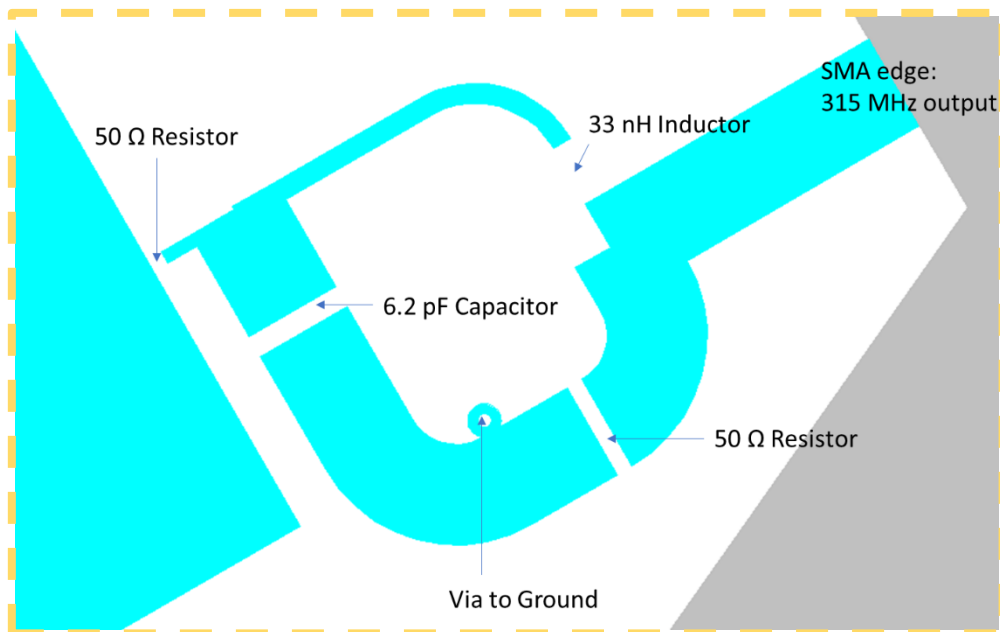
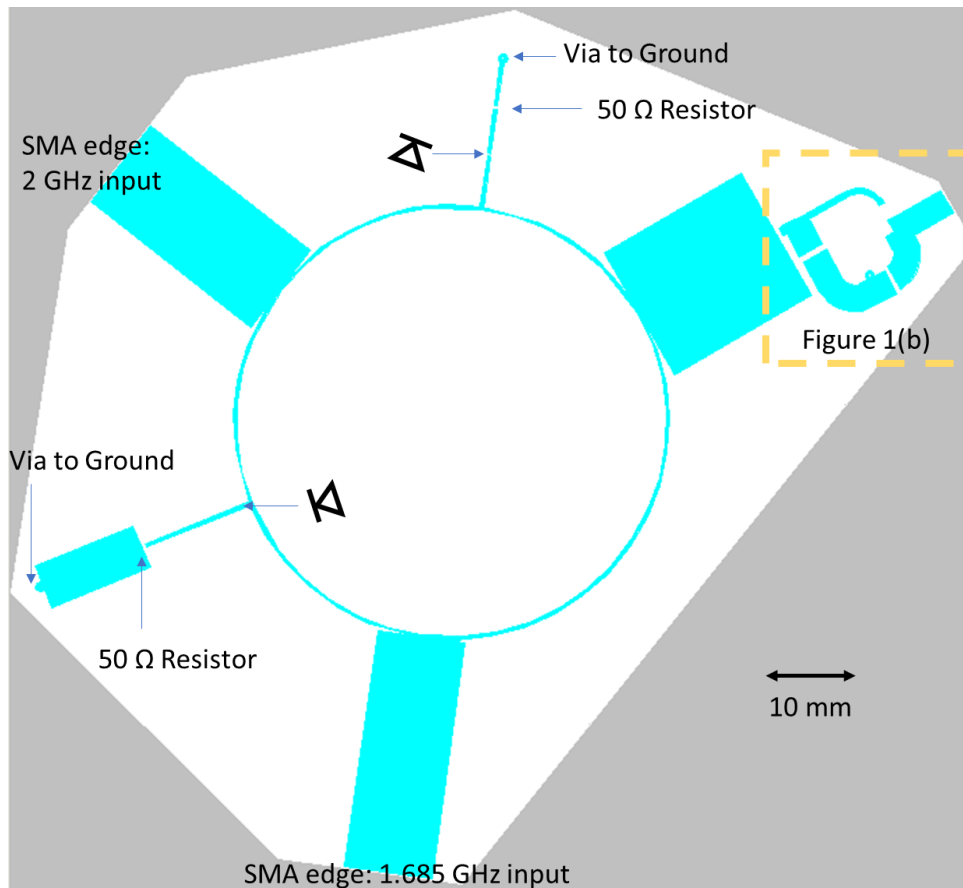


Figure 101: Diagram of 2 GHz rat race mixer with low-pass filter for 315 MHz output, optimised using Keysight ADS for a FR4 substrate. Expanded sections shows Butterworth filter design.

The component values are all shown in Figure 101. SMA connectors are chosen to include the highest frequency transmitted at each port. The diodes are Skyworks Solutions Schottky Diodes [137], rated up to 24 GHz.

This circuit was simulated in ADS over the frequency range 0 GHz to 2.1 GHz, to see the frequency composition of the 315 MHz output. The input at both RF and IF ports was a 1 V RMS sine wave. The output can be seen in Figure 102.

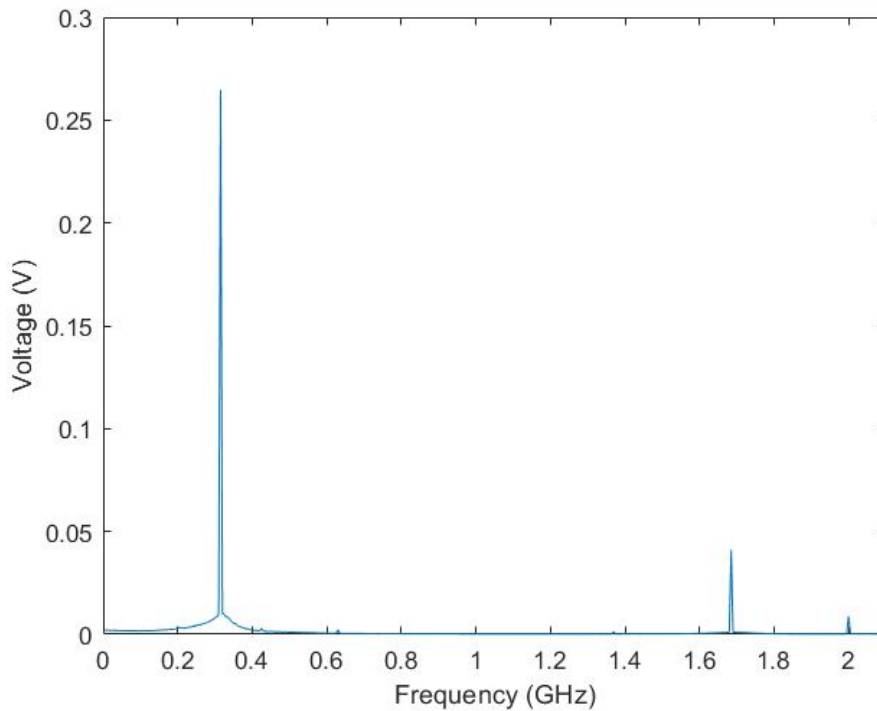


Figure 102: Simulated frequency response of 2 GHz mixer on FR4 substrate, as shown in Figure 101, with 315 MHz output.

The peak at 315 MHz is 0.265 V, and clearly higher than the two inputs at 1.685 and 2 GHz. These have been successfully filtered, the output at 1.685 GHz being 0.041 V and at 2 GHz is 0.009 V. The circuit design seen in Figure 101 was then fabricated using PCB printing methods outlined in Section 4.2.3. A photograph of the resulting fabricated board can be seen in Figure 103.



Figure 103: Fabricated 2 GHz mixer on FR4 substrate. Design shown in Figure 101.

The 2 GHz RF port can be seen bottom left, the 1.685 GHz LO port centre top, and the 315 MHz output port bottom right. The ring mixer is clearly visible in the centre, and the Butterworth filter seen adjacent to the output port. This board was characterised using the experimental configuration shown in Figure 100. The frequency response around the 315 MHz output is plotted in Figure 104. Both input ports have a power of 0 dBm.

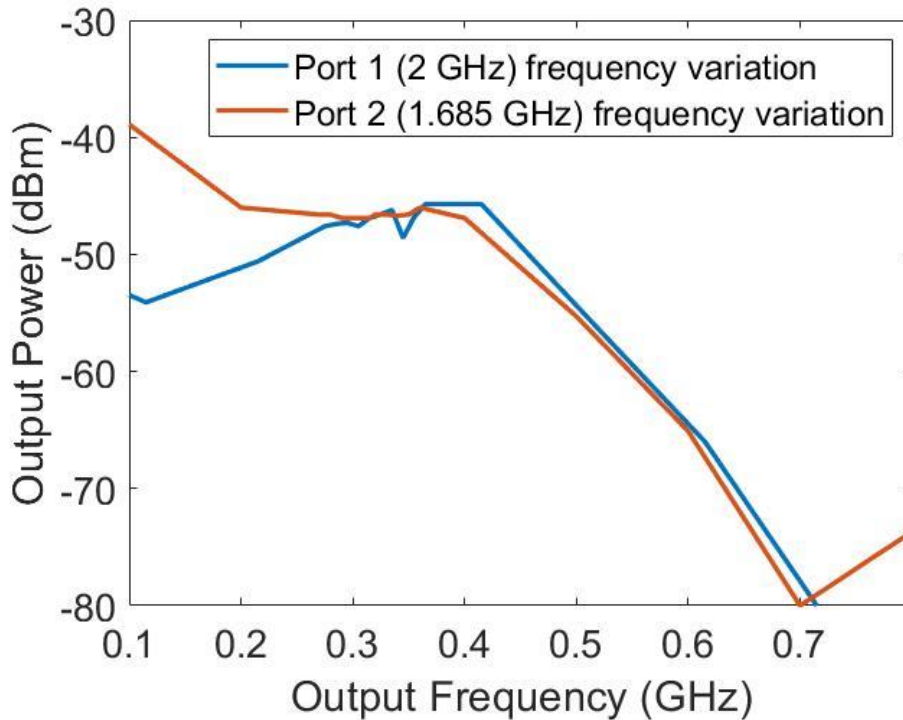


Figure 104: Frequency response of 2 GHz mixer on FR4 substrate. Both RF and LO input frequencies are varied, and the output plotted. Note: a 2.1 GHz RF input and 1.685 GHz IF input would give an output of 415 MHz.

There is a global peak of -38.9 dBm at 0.100 GHz. However, this only occurs under the variation of Port 2 (red trace), which is the LO input of 1.685 GHz. This is unlikely to occur in practice, as the IF is kept constant to allow for a varying RF input. Therefore, the Port 1 frequency variation (blue trace) is a far more accurate representation of the mixers use-case.

The output power, under Port 1 frequency variation, at 0.315 GHz, where the mixer is optimised for, is -46.9 dBm. The region 0.225 MHz to 0.460 MHz has a relatively flat frequency response, all above -50 dBm, and peaking at 0.415 GHz with a power of 45.7 dBm. This flat response is useful as the mixer is still functional under small frequency fluctuations in the RF input. There is a steep drop off in power above 0.415 GHz due to the low-pass filter on the output.

10.2.2 On RT/Duroid 5870 Substrate

The mixer design concept has been proved by its functionality on FR4. This section uses the same concept but applied to a different substrate: RT/Duroid 5870. The adjusted optimised design can be seen in Figure 105.

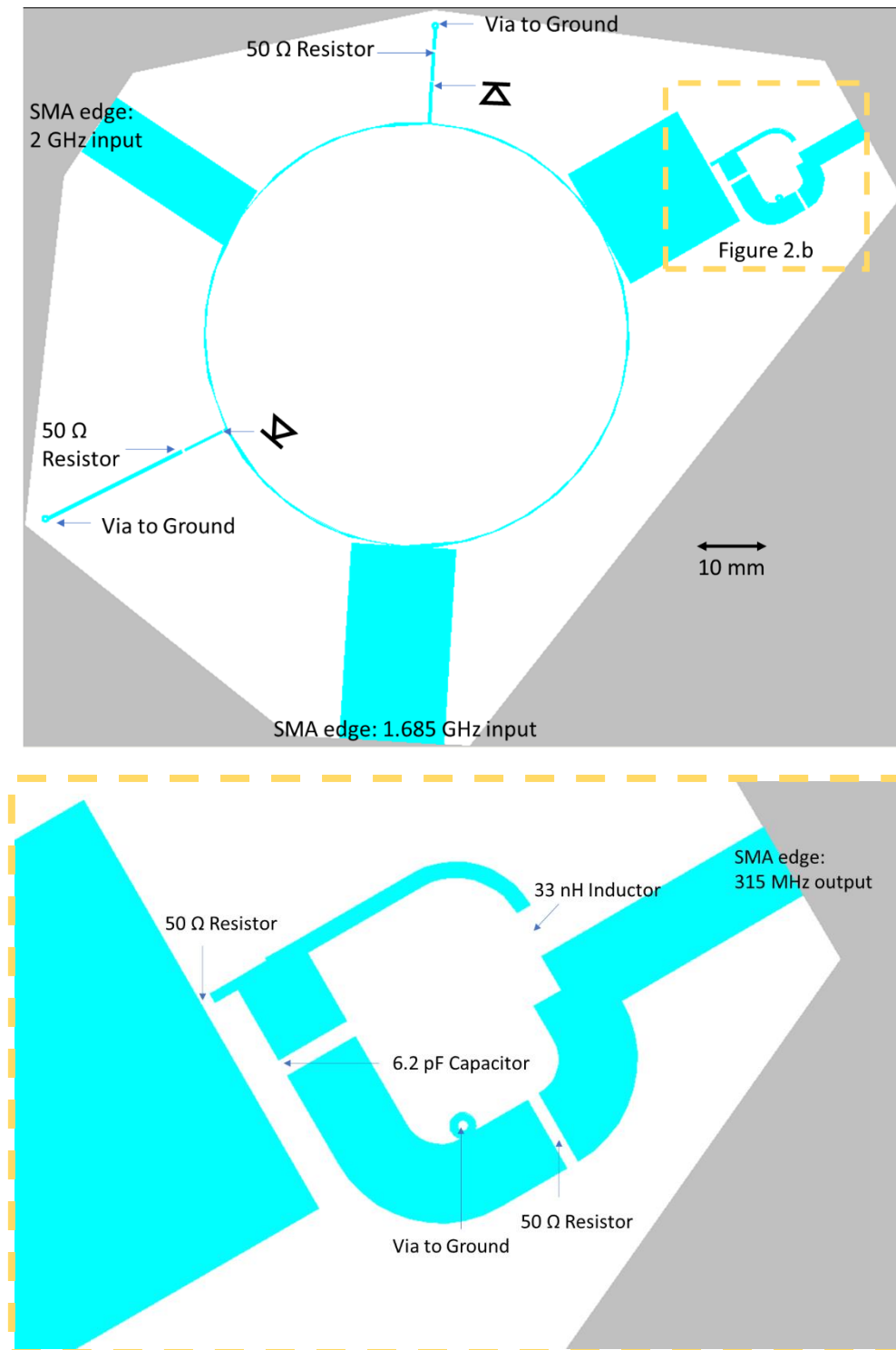


Figure 105: Diagram of 2 GHz mixer with low-pass filter for 315 MHz output, optimised for RT/Duroid 5870 substrate using Keysight ADS. Expanded section shows Butterworth output filter.

The component values are all shown in Figure 105, these are identical to those optimised for FR4 in Figure 101. The dimensions of the transmission lines have been altered to allow for the thinner substrate with a lower dielectric constant. The SMA connectors have once again been chosen to include the highest frequency transmitted at each port.

This circuit was simulated in ADS over the frequency range 0 GHz to 2.1 GHz, to see the frequency composition of the 315 MHz output. The input at both RF and IF ports was a 1 V RMS sine wave. The output can be seen in Figure 106.

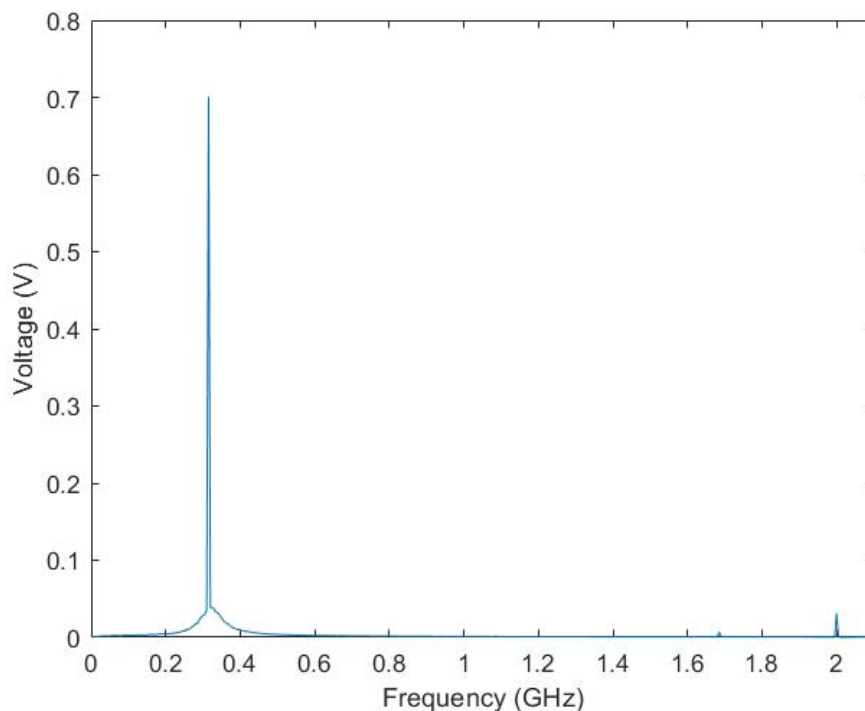


Figure 106: Simulated frequency response of 2 GHz mixer on RT/Duroid 5870, as shown in Figure 105, with 315 MHz output.

The voltage output at 315 MHz is 0.700 V. This is much higher than the 0.265 V simulated peak on the FR4 substrate. Both the 1.685 and 2 GHz inputs have been successfully filtered, with output amplitudes of 0.007 V and 0.031 V respectively. The circuit design seen in Figure 105 was then fabricated on RT/Duroid using PCB printing methods outlined in Section 4.2.3. A photograph of the fabricated board can be seen in Figure 107.

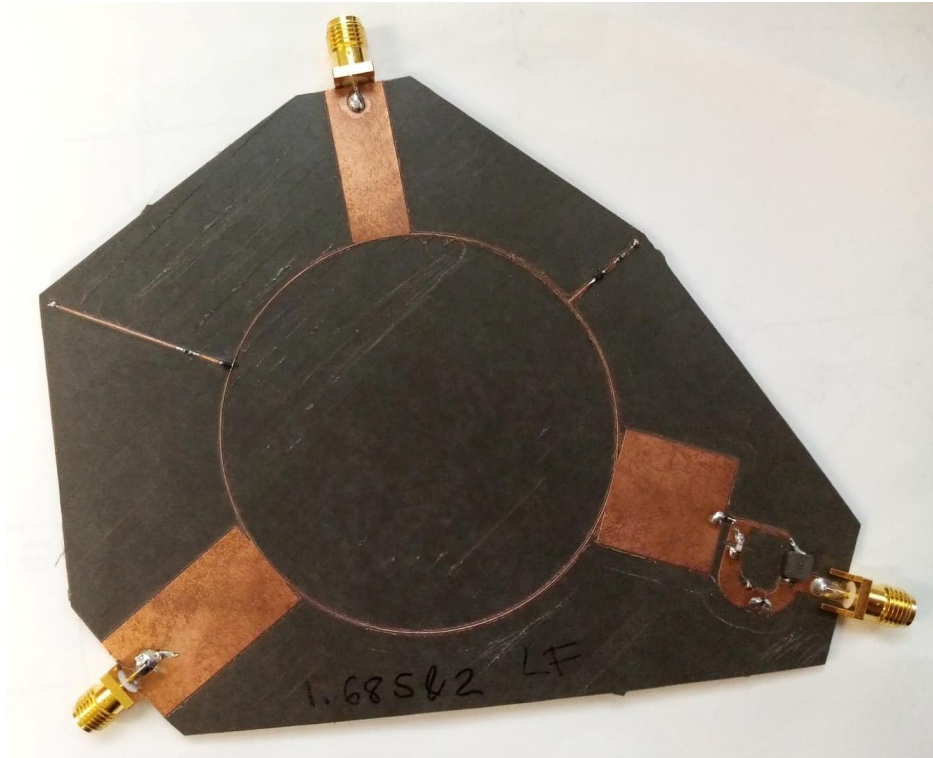


Figure 107: Fabricated 2 GHz mixer on RT/Duroid 5870 substrate. Design shown in Figure 105.

The 2 GHz RF port can be seen bottom left, the 1.685 GHz LO port centre top and the 315 MHz output port bottom right. The ring mixer is clearly visible in the centre, and the Butterworth filter seen adjacent to the output port. This board was characterised using the experimental configuration shown in Figure 100. The frequency response around the 315 MHz output is plotted in Figure 108. Both input ports have a power of 0 dBm.

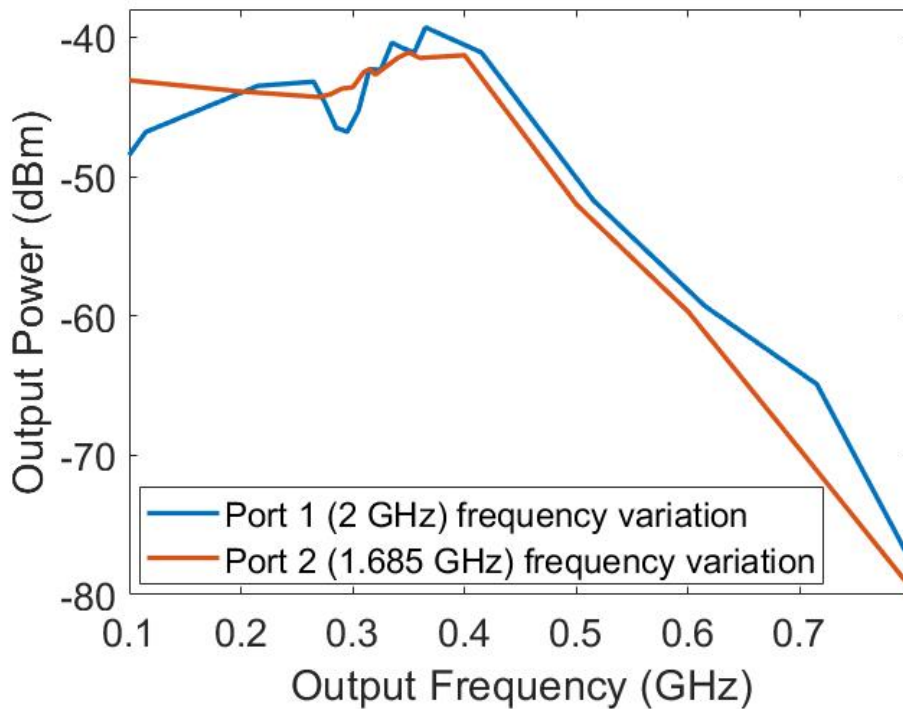


Figure 108: Frequency response of 2 GHz mixer on RT/Duroid 5870 substrate. Both RF and IF input frequencies are varied and the output plotted. Note: a 2.1 GHz RF input and 1.685 GHz IF input would give an output of 415 MHz.

The output power at 0.315 GHz, where the mixer is optimised for, is -42.3 dBm. This is a 4.6 dBm improvement on the is -46.9 dBm seen at this frequency on the FR4 board. The output is consistently higher, being above -50 dBm between 0.115 GHz and approximately 0.500 GHz for the blue trace. The global peak is -39.3 dBm at 0.365 GHz, whilst varying the frequency at Port 1. Additionally, the peak output power whilst varying the frequency at Port 2 is -41.1 dBm at 0.350 GHz. As in Figure 104, the Port 1 frequency variation (blue trace) is a more accurate representation of the mixers use-case.

10.3 20 GHz Mixer

The mid-frequency mixer is designed for an RF input of 20 GHz and an IF of 18 GHz. The output 2 GHz is isolated with a low-pass Butterworth filter. The required output IF frequency is 2 GHz MHz to be fed into the mixer presented in Section 10.2. The design is directly optimised for an RT/Duroid 5870 substrate as this is designed for higher frequency circuitry.

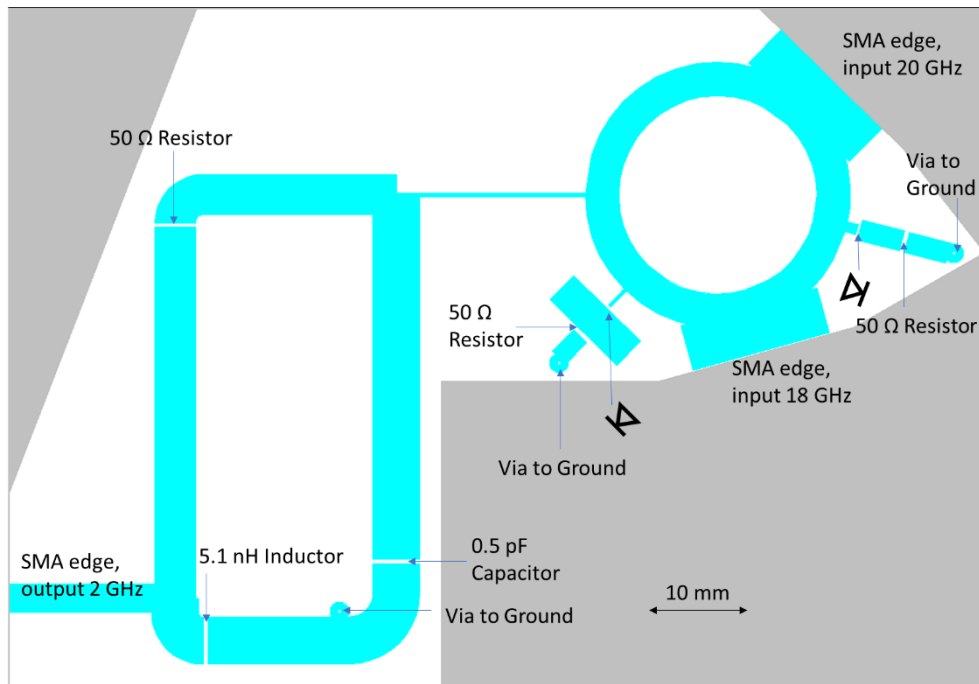


Figure 109: Diagram of 20 GHz mixer with low-pass filter for 2 GHz output, optimised for RT/Duroid 5870 substrate using Keysight ADS. Output Butterworth filter shown on left hand side.

The component values are all shown in Figure 109. SMA connectors are chosen to include the highest frequency transmitted at each port. The diodes are Skyworks Solutions Schottky Diodes [137], rated up to 24 GHz. This circuit was simulated in ADS over the frequency range 0 GHz to 21 GHz, to see the frequency composition of the 2 GHz output. The input at both RF and IF ports was a 1 V RMS sine wave. The output can be seen in Figure 110.

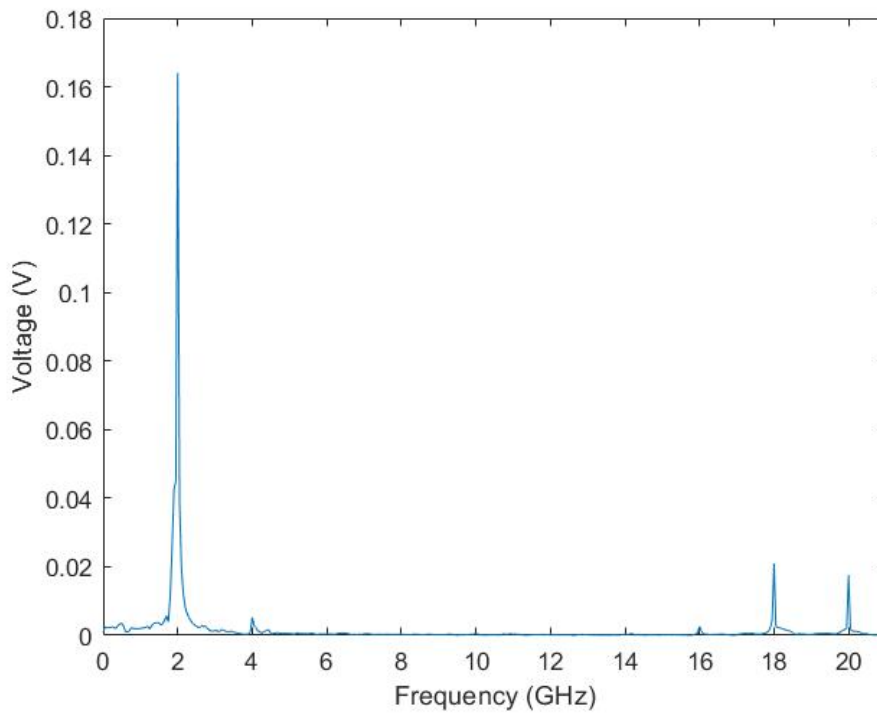


Figure 110: Simulated frequency response of 20 GHz mixer on RT/Duroid 5870, as shown in Figure 109, with 2 GHz output.

The voltage output at 2 GHz is 1.641 V. Both the 18 and 20 GHz inputs have been successfully filtered, with output amplitudes of 0.021 V and 0.018 V respectively. The circuit design seen in Figure 109 was then fabricated on RT/Duroid 5870 using PCB printing methods outlined in Section 4.2.3. A photograph of the fabricated board can be seen in Figure 111.



Figure 111: Fabricated 20 GHz mixer on RT/Duroid 5870 substrate. Design shown in Figure 109.

The 20 GHz RF port can be seen top right with the 18 GHz IF port directly below and the 315 MHz output port bottom right. The ring mixer is visible on the right-hand side, and the Butterworth filter on the left. The output 2 GHz port is bottom left, at the output of the filter. This board was characterised using the experimental configuration shown in Figure 100. The frequency response around the 2 GHz output is plotted in Figure 112. Both input ports have a power of 0 dBm.

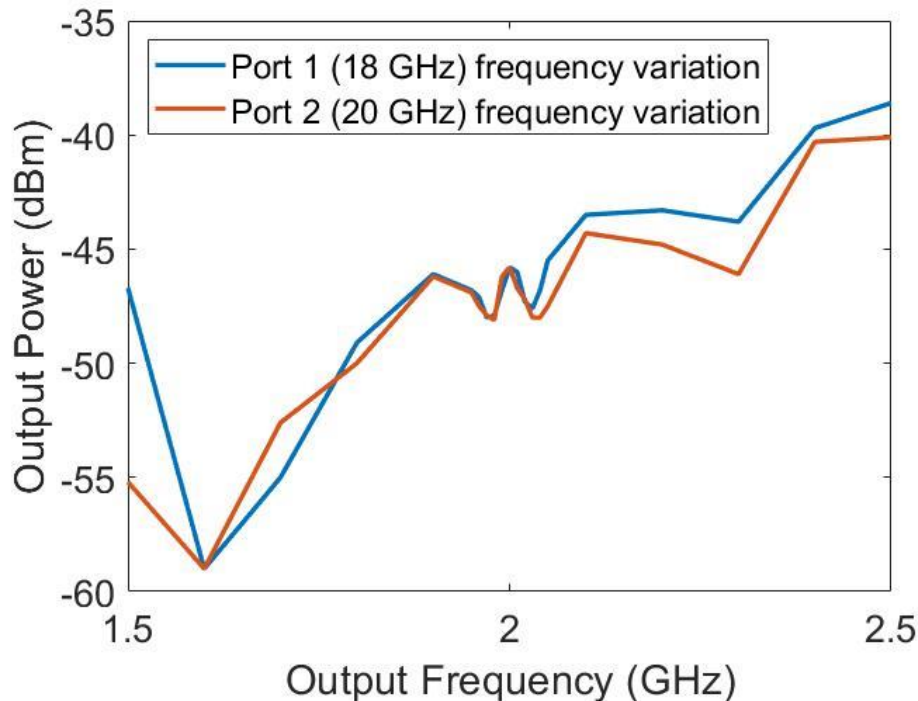


Figure 112: Frequency response of 20 GHz mixer on RT/Duroid 5870 substrate. Both RF and IF input frequencies are varied and the output plotted. Note: a 20.1 GHz RF input and 18 GHz IF input would give an output of 2.1 GHz.

The output power at 2.00 GHz, where the mixer is optimised for, is -45.8 dBm. There appears to be filtering of approximately 2 dB directly either side of the central 2.00 GHz peak. However, the overall output power trend is to increase with frequency, demonstrated by the global peak being -38.6 dBm at 2.5 GHz, whilst varying the frequency at port 1. As in Figure 104, the Port 1 frequency variation (blue trace) is a more accurate representation of the mixers use-case.

10.4 Conclusion

In this chapter, three mixers at two separate frequency ranges were designed, optimised, fabricated and experimentally characterised. These were tested with 0 dBm power on both

input ports. The low frequency mixers, combining 2 GHz and 1.685 GHz signals, had a measured output power of -42.3 dBm at 0.315 GHz, where the mixer is optimised for. A mid-frequency mixer, designed to combine frequencies of 20 GHz and 18 GHz to produce a 2 GHz output signal, produced an output power of -45.8 dBm at the optimised frequency. The advantage of splitting the mixing process into stages, other than providing more flexibility, is that intermediate frequencies can be amplified before once again being mixed.

The next stage of this project is to design a high frequency mixer, with an output frequency of 20 GHz. This would be then passed to the mid and low frequency mixers in turn. The ideal frequency for this high frequency mixer would be around 270 GHz (combined with an IF of 250 GHz). This would allow a full THz test bed to be produced in house. A diagram of the potential mixer chain can be seen in Figure 113.

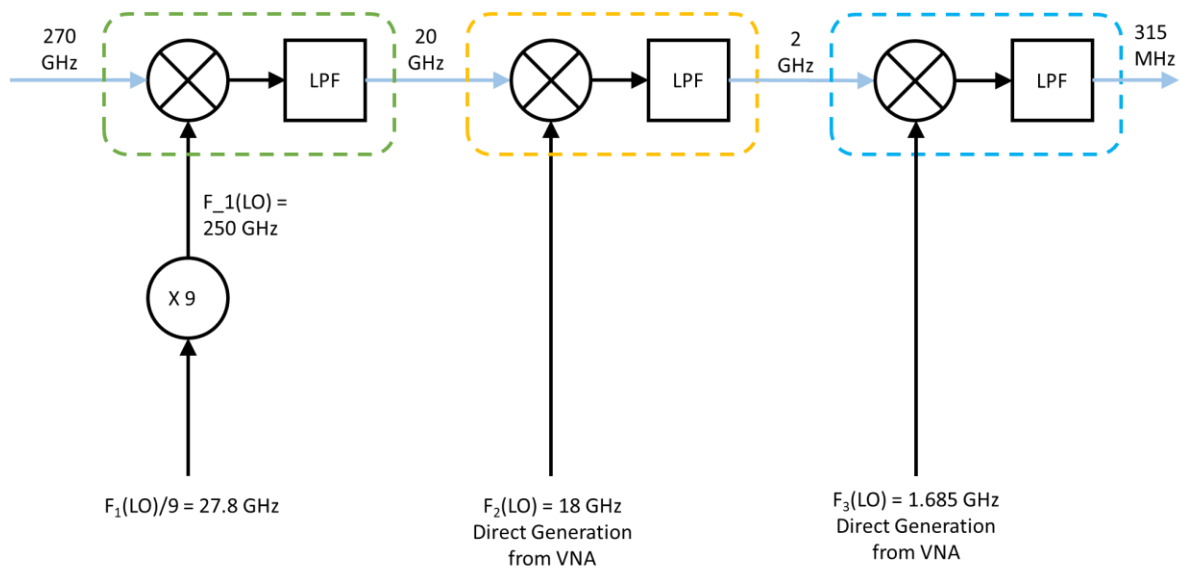


Figure 113: Theoretical mixer chain to downconvert a 270 GHz signal to 315 MHz, based on the mixers designed in this chapter. The first mixer downconverts the 270 GHz RF signal to 20 GHz, which is passed to the second mixer to be downconverted to 2 GHz, before a final mixer stage to provide a 315 MHz output.

Chapter 11: Conclusions and Further Work

11.1 Conclusions

This thesis presents mm-wave and terahertz components that can be used in small hand-held devices, fabricated using traditional microfabrication techniques and easily integrated with other components. The optimisation techniques integrated within ADS and a genetic algorithm are employed for the purpose of designing these components.

A genetic algorithm, Agenoria, coupled to a finite difference time domain simulator, is presented for the optimisation of passive THz devices. This is used to optimise a series of planar patch antennas for power collection. The first is a broadband antenna, optimised between 100 GHz and 5.0 THz, where 79% of the spectrum shows some improvement. The second antenna is optimised for a single peak at 1.0 THz. The evolved antenna's simulated power output is considerably higher than that of the reference case, with an improvement at 1 THz of 267%. The third antenna is a dual peak antenna, with peaks optimised at 1.0 THz and 1.2 THz showing a 4,510% and 250% improvement on the reference case from the first generation.

This genetic algorithm is verified by fabricating and experimentally analysing an evolved broadband patch antenna. A vector network analyser (VNA) with two bidirectional VDI WR

1.0 THz frequency extenders with high-gain horn antennas operating between 0.75 THz and 1.10 THz was used for testing. The antenna transmission and angular dependence were measured and found to concur with simulated results for both the evolved antennas and a reference plain patch antenna. Feedline losses were investigated using the experimental set-up shown in Figure 63. The calculated loss of the microstrip line, connecting the antenna pairs, is 0.79 ± 0.06 dB/mm, which shows promisingly low losses. The combination of these antenna measurements verifies the simulation output within the region 0.8 THz to 1.0 THz.

An RMS detector was successfully designed for use between 312 and 318 MHz and fabricated in-house. It was characterised between 310 and 320 MHz, with a clear peak of 1.38 V seen at 314 MHz. This PCB was then used in the characterisation of the on-off keying capabilities of the VNA and WR1.0-VNAX frequency extenders. An on-off modulator was designed and found to successfully modulate the VNA 12.3 GHz input at frequencies between 1 Hz and 1 MHz.

A selection of frequency triplers were designed and simulated in the 10 to 30 GHz frequency range. Simulations consistently showed a strong third harmonic whilst the first and second were successfully filtered by on-chip microstrip filters. However, the preliminary experimental results disagreed with simulation due to manufacturing tolerance issues. The PCB printing on FR4 and TR/Duroid 5870 was found to have a consistent overmilling of 80 μm and 50 μm respectively. For both PCB boards, this meant milling microstrip lines of below 200 μm was unfeasible, which made fabrication in the 10 to 30 GHz frequency range unworkable. Furthermore, restricted laboratory access due to the Covid-19 pandemic prevented an additional round of fabrication and experimentation to characterise the effect of the machining tolerances on the filter performance.

Frequency mixers at two separate frequency ranges were designed, optimised, fabricated and experimentally characterised. The first, combining 2 GHz and 1.685 GHz signals, had a measured output power of -42.3 dBm at 0.315 GHz. The second, designed to combine frequencies of 20 GHz and 18 GHz, produced an output power of -45.8 dBm at 2 GHz.

11.2 Further Work

This work may be extended by integrating the components presented into a sub-THz communications system. This would provide a test bench for signal processing methods to be investigated, which is currently difficult due to the filtering associated with off-the-shelf devices. A possible frequency region for this test bench is the unlicensed 265 to 275 GHz band, which has already been allocated for mobile use [144] and has ongoing component research [145, 146, 147].

Genetic algorithms, the genetic algorithm, has been shown to successfully produce THz antenna designs. This work may easily be extended to produce candidate antenna designs optimised for power collection at 270 GHz. A pair of 270 GHz antennas would then be fabricated to produce a wireless link between the transmitting and receiving parts of the communications system. As the frequency would be reduced from those fabricated in Chapter 7, the feature size would be increased and therefore the fabrication process shown here may be reapplied.

The mixers presented in Chapter 10 may be extended to downconvert the received signal from the 270 GHz antenna. A 270 to 20 GHz subharmonic mixer could be designed and fabricated, to be followed by the two mixers presented in Chapter 10 to convert to a 315 MHz output. This would be received by the power detector designed in Section 8.2.

As discussed in Chapter 9, Traditional direct generation sources within the terahertz gap are often bulky and provide poor bandwidth [130]. A common alternative to producing high frequency signals is to multiply lower frequencies using frequency multipliers. A 10 to 30 GHz multiplier design was presented herein, but fabrication work not completed due to fabrication errors introduced by PCB printing methods. It would be recommended to first fabricate the same set of multiplier designs using the more accurate technique of photolithography. This has successfully been used in the manufacture of antennas in Chapter 7 and has been used for micro-PCB fabrication previously with patterning from 1 to 6 μm with accuracy $\pm 0.2 \mu\text{m}$ [139]. This work could then be extended to add a second and third frequency multiplier, 30 to 90 GHz, and 90 to 270 GHz respectively.

After completion of a sub-THz communications system, it would be beneficial to continue the work of Chapter 8 and implement an on-off modulation device to transmit data across the wireless link. This may then be extended to various modulation techniques, such as QAM.

Appendices

Appendix 1: Increasing frequency range of Matlab Antenna Toolbox

Under request, Matlab will provide a replacement “checkFrequency.p” file from the directory: “toolbox/antenna/antenna/+em/@MeshGeometry”. Replacing this allows the hard coded 200 GHz limit to be bypassed. This limit is only in place to stop small mesh sizes rendering simulations too computationally intensive to run. However, the reduced size of most THz devices means this should not be an issue. Though, other files may need to be adjusted to allow for the smaller dimensions and constants likely to occur at these frequencies. These include the maximum sliver tolerance in the shape file: “\toolbox\antenna\antenna\+antenna\shape” and the loss tangent in the dielectric file: “\toolbox\antenna\antenna\dielectric.m”.

Appendix 2: Fabrication procedure for terahertz antennas.

A 2” borosilicate glass substrate is cleaned with a 2% decon 90, 98 % di water mix. This ensures the removal of any small traces of dirt on the surface, as with each layer, the effects of these increase, and can damage features on subsequent layers. The samples are submerged in the cleaning solution for 15 minutes, at 45°C in an ultrasonic bath. The samples are inspected for foreign matter using an optical microscope, then purified using di water for 15 minutes. The samples are then dried, either using nitrogen or a vacuum oven.

A 100nm aluminium layer is sputter coated onto the clean substrate. This is heated to 200°C for 15 minutes, to ensure the sample is impervious to fracture up to this temperature.

A 30 µm SU8 dielectric layer is applied. Both SU8 2025 [116] and SU8 3025 [148] are capable of being spun to 30 µm, but here the fabrication of SU8 3025 is outlined.

- 1) Apply 1ml resist for each inch² of substrate. This equates to 4ml on our 2-inch substrate.
- 2) Spin at 500 rpm for 7seconds, with an acceleration of 100 rpm/s.

- 3) Spin at 2500 rpm (SU8 3025 [149]) or 3000 rpm (SU8 2025 [116]) for 30 seconds, with an acceleration of 300 rpm/s.
- 4) Soft bake at 65°C for 1 minute, then at 95°C for 5 minutes. Slowly increasing the temperature minimises the probability of fracture.
- 5) Flood exposure at 150 mJ/cm² with a wavelength greater than 350 nm.
- 6) Post Exposure Bake at 65°C for 1 minute, then at 95°C for 3 minutes.
- 7) Hard bake at 200°C for 15 minutes

A 100 nm aluminium layer is sputter coated on top of the dielectric layer to form the base of the antenna pattern. The antenna is patterned using a photolithography process. Positive photoresist (S1813) is applied using a spin coater, first at 500 rpm for 10 seconds to ensure the photoresist covers the entire wafer and then at a higher speed of 3700 rpm for 60 seconds to give a consistent film thickness. The sample is then baked at 95°C for 5 minutes to cure the photoresist.

The resist is exposed through a glass mask of the antenna pattern, to 80 mJ using the LEV. Photoresist developer is applied to remove the photoresist in any exposed region. The sample is thoroughly washed with di water to remove any excess developer.

The sample is wet-etched in a solution of 100 ml Phosphoric acid, 6 ml Nitric acid and 10 ml water for 10 seconds, to remove unwanted metal.

The pattern is viewed under a microscope to ensure the feed lines are continuous and checked with an multimeter to evaluate if any unwanted aluminium remains. This cannot be completed with just a visual check due to the metallic ground plane being visible through the clear SU8 dielectric layer.

If unwanted aluminium is present, the sample is bathed in the etchant solution for an additional second before rechecking. Once the etch is satisfactory, the sample is dipped into an acetone bath for 30 seconds to remove the remaining photoresist.

Bibliography

- [1] M. Van Exter, C. Fattering and D. Grischkowsky, "Terahertz time-domain spectroscopy of water vapor," *Optics letters*, vol. 14, no. 20, pp. 1128-1130, 1989.
- [2] Ericsson, "Ericsson Mobility Report," Ericsson, 2022.
- [3] I. Akyildiz, J. J. and C. Han, "TeraNets: Ultrabroadband communication networks in the terahertz band," *IEEE Wireless Communications*, vol. 21, no. 4, pp. 130-135, 2014.
- [4] Ofcom, "Enabling mmWave spectrum for new users," 2022.
- [5] "Technical Specification Group Radio Access Network; Study on Scenarios and Requirements for Next Generation Access Technologies (Release 15)," 2018.
- [6] T. S. Rappaport, Y. Xing, O. Kanhere, S. Ju, A. Madanayake, S. Mandal, A. Alkhateeb and T. G. C, "Wireless communications and applications above 100 GHz: Opportunities and challenges for 6G and beyond," *IEEE Access*, vol. 7, pp. 78729-57, 2019.
- [7] X. Wang, L. Kong, F. Kong, F. Qiu, M. Xia, S. Arnon and G. Chen, "Millimeter Wave Communication: A Comprehensive Survey," *IEEE Communications Surveys & Tutorials*, vol. 20, no. 3, pp. 1616-1653, 2018.
- [8] H. Aghasi, S. M. H. Naghavi, M. Tavakoli Taba, M. A. Aseeri, A. Cathelin and E. Afshari, "Terahertz electronics: Application of wave propagation and nonlinear processes," *Applied Physics Reviews*, vol. 7, no. 2, 2020.
- [9] T. W. Crowe, D. W. Porterfield, J. L. Hesler, W. L. Bishop, D. S. Kurtz and K. Hui, "Terahertz sources and detectors," in *SPIE Defense and Security*, Orlando, Florida, United States, 2005.
- [10] "National Radio Astronomy Observatory, Charlottesville, VA., Atacama Large Millimeter Array," [Online]. Available: <http://www.alma.nrao.edu/>.

- [11] G. Miller, "Momentum Optimization," 10 September 2008. [Online]. Available: <https://edadocs.software.keysight.com/display/ads2009/Momentum+Optimization>. [Accessed 22 September 2022].
- [12] M. T. Islam, M. N. Shakib and N. Misran, "Multi-slotted microstrip patch antenna for wireless communication," *Progress In Electromagnetics Research*, vol. 10, pp. 11-18, 2009.
- [13] D. M. Pozar, *Microwave Engineering*, John Wiley & Sons, 2012.
- [14] R. M. Barrett, "Microwave Printed Circuits - A Historical Survey," *IRE Transactions on Microwave Theory and Techniques*, vol. 3, no. 2, pp. 1-9, March 1955.
- [15] D. D. Grieg and H. F. Engelmann, "Microstrip-A New Transmission Technique for the Kilomegacycle Range," *Proceedings of the IRE*, vol. 40, no. 12, pp. 1644-1650, December 1952.
- [16] "Microwave Engineering, 4th Edition (radfiz.org.ua)".
- [17] O. Heaviside, "On the electromagnetic effects due to the motion of electrification through a dielectric," *The London, Edinburgh, and Dublin Philosophical Magazine and Journal of Science*, vol. 27, no. 167, pp. 324-339, 1889.
- [18] D. F. Williams and S. E. Schwarz, "Design and Performance of Coplanar Waveguide Bandpass Filters," *IEEE transactions on microwave theory and techniques*, vol. 31, no. 7, pp. 558-566, July 1983.
- [19] R. E. Collin, *Foundations for microwave engineering*, John Wiley & Sons, 2007.
- [20] Quadrivium, "History of Filter Theory," [Online]. Available: <https://www.quadrivium.nl/history/history.html>. [Accessed 31 12 2021].
- [21] M. I. Pupin, "Wave transmission over non-uniform cables and long-distance air-lines," *Transactions of the American Institute of Electrical Engineers*, no. 17, pp. 245-307, May 19, 1900.

- [22] M. Reed, "Electrical Wave Filters," *Experimental Wireless & the Wireless Engineer*, no. 7, Series of 6 articles, pp. 78-83, 122-445, March-August 1930.
- [23] S. Darlington, "Synthesis of reactance 4-poles which produce prescribed insertion loss characteristics.," *Journal of Mathematics and Physics*, vol. 18, pp. 257-353, 1939.
- [24] S. Butterworth, "On the theory of filter amplifiers," *Experimental Wireless & the Wireless Engineer*, vol. 7, no. 85, pp. 536-541, October 1930.
- [25] G. L. Matthaei, I. Young and E. M. T. Jones, *Microwave Filters, Impedance-Matching Networks, and Coupling Structures*, Dedham, Mass: Artech House, 1964.
- [26] P. I. Richards, "Resistor-Transmission Line Circuits," *Proceedings of the IRE*, vol. 36, pp. 217-220, February 1948.
- [27] J. G. Hong and M. J. Lancaster, *Microstrip filters for RF/microwave applications*, John Wiley & Sons, 2004.
- [28] I. Rosu, "Frequency Multipliers," QSL, [Online]. Available: https://www.qsl.net/va3iul/Frequency_Multipliers/Frequency_Multipliers.pdf. [Accessed 13 July 2022].
- [29] T. H. Oxley, "50 years development of the microwave mixer for heterodyne reception," *IEEE Transactions on Microwave Theory and Techniques*, vol. 50, no. 3, pp. 867-876, March 2002.
- [30] S. A. Maas, *Microwave mixers*, Norwood, 1986.
- [31] C. Poole and I. Darwazeh, "Microwave mixers," in *Microwave active circuit analysis and design*, Academic Press, 2015, pp. 589-616.
- [32] W. L. Stutzman and G. A. Thiele, *Antenna theory and design*, John Wiley & Sons, 2012.
- [33] J. Ramsay, "Highlights of antenna history," *IEEE Communications Magazine*, vol. 19, no. 5, pp. 4-8, 1981.

- [34] H. Hertz, "Die Kräfte electrischer Schwingungen, behandelt nach der Maxwell'schen Theorie," *Annalen der Physik*, vol. 272, no. 1, pp. 1-22, 1889.
- [35] J. C. Maxwell, "VIII. A Dynamical Theory of the Electromagnetic Field," *Philosophical transactions of the Royal Society of London*, vol. 155, pp. 459-512, 1865.
- [36] G. Marconi, "Improvements in Transmitting Electrical impulses and Signals, and in Apparatus therefor". British Patent 12,039, 1897.
- [37] K. Fujimoto, *Mobile Antenna Systems Handbook*, Artech House, 2008.
- [38] H. Yagi and S. Uda, "Projector of the sharpest beam of electric waves," *Proceedings of the Imperial Academy*, vol. 2, no. 2, pp. 49-52, 1926.
- [39] P. P. Viezbicke, *Yagi antenna design*. Vol. 688., US Government Printing Office, 1976.
- [40] K. S. Packard, "The origin of waveguides: A case of multiple rediscovery," *IEEE Transactions on Microwave Theory and Techniques*, vol. 32, no. 9, pp. 961-969, 1984.
- [41] "Virginia Diodes, Inc., Nominal Horn Specifications," [Online]. Available: http://vadiodes.com/VDI/pdf/VDI%20Feedhorn%20Summary%202006_05.pdf. [Accessed 2 September 2022].
- [42] S. Lim and A. H. Naqvi, "A beam-steering antenna with a fluidically programmable metasurface," *IEEE Transactions on Antennas and Propagation*, vol. 67, no. 6, pp. 3704-3711, 2019.
- [43] J. Howell, "Microstrip antennas," *IEEE Transactions on Antennas and Propagation*, vol. 23, no. 1, pp. 90-93, 1975.
- [44] E. Rufus, A. C. Zachariah and P. V. Chaitanya, "A modified bow-tie antenna for microwave imaging applications," *Journal of Microwaves, Optoelectronics and Electromagnetic Applications*, vol. 7, no. 2, pp. 115-122, 2008.

- [45] S. Gupta, A. Samer and C. Christophe, "Microwave analog real-time spectrum analyzer (RTSA) based on the spectral–spatial decomposition property of leaky-wave structures," *IEEE Transactions on Microwave Theory and Techniques*, vol. 57, no. 12, pp. 2989-2999, 2009.
- [46] E. R. Brown, C. D. Parker and E. Yablonovitch, "Radiation properties of a planar antenna on a photonic-crystal substrate," *JOSA B*, vol. 10, no. 2, pp. 404-407, 1993.
- [47] T. Kleine-Ostmann and T. Nagatsuma, "A review on terahertz communications research," *Journal of Infrared, Millimeter, and Terahertz Waves*, vol. 32, no. 2, pp. 143-171, 2011.
- [48] J. Zhang, "Characterization of the terahertz photoconductive antenna by three-dimensional finite-difference time-domain method," *arXiv preprint*, 2014.
- [49] C. Zhang, Z. Ninkov, G. Fertig, R. Kremens, A. Sacco, D. Newman, K. Fourspring, P. Lee, Z. Ignjatovic, J. Pipher and C. McMurtry, "Optical simulation of terahertz antenna using finite difference time domain method," *Terahertz Physics, Devices, and Systems IX: Advanced Applications IX: Advanced Applications in Industry and Defense*, vol. 9483, pp. 48-58, 2015.
- [50] M. Nazeri and R. Massudi, "Study of a large-area THz antenna by using a finite difference time domain method and lossy transmission line," *Semiconductor science and technology*, vol. 25, no. 4, 2010.
- [51] C. Balocco, "Lucifer," 19 April 2018. [Online]. Available: <https://github.com/claudiobalocco/lucifer>.
- [52] J. B. Schneider, Understanding the finite-difference time-domain method, School of electrical engineering and computer science Washington State University, 2010.
- [53] K. Yee, "Numerical solution of initial boundary value problems involving Maxwell's equations in isotropic media," *IEEE Transactions on antennas and propagation*, vol. 14, no. 3, pp. 302-307, 1966.
- [54] C. Hill and A. Kim, *Simulation and Testing of Metallic Aperture Arrays at Terahertz Frequencies*, Diss. Durham University, 2016.

- [55] J. Berenger, "A perfectly matched layer for the absorption of electromagnetic waves," *Journal of computational physics*, vol. 114, no. 2, pp. 185-200, 1994.
- [56] M. Naftaly and R. E. Miles, "Terahertz Time-Domain Spectroscopy for Material Characterization.," *Proceedings of the IEEE*, vol. 95, no. 8, pp. 1658-1665, 2007.
- [57] R. F. Harrington, "The Method of Moments in Electromagnetics," *Journal of Electromagnetic Waves and Applications*, vol. 1, no. 3, pp. 181-200, 1987.
- [58] M. G. Andreasen, "Scattering from parallel metallic cylinders with arbitrary cross sections," *IEEE transactions on Antennas and Propagation*, vol. 12, no. 6, pp. 754-764, 1964.
- [59] MathWorks, "Method of Moments Solver for Metal Structures," MathWorks, 2021. [Online]. Available: <https://uk.mathworks.com/help/antenna/ug/method-of-moments.html>. [Accessed 21 February 2022].
- [60] "Theory of Operation for Momentum," Keysight, 15 November 2011. [Online]. Available: <https://edadocs.software.keysight.com/display/ads2011/Theory+of+Operation+for+Momentum>. [Accessed 21 February 2022].
- [61] W. C. Gibson, *The Method of Moments in Electromagnetics*, Boca Raton: Chapman and Hall, 2021.
- [62] "ADS Momentum Basics," 19 February 2018. [Online]. Available: https://nanopdf.com/download/the-momentum-user-interface_pdf. [Accessed 21 February 2022].
- [63] D. A. Frickey, "Conversions between S, Z, Y, h, ABCD, and T parameters which are valid for complex source and load impedances," *IEEE Transactions on Microwave Theory and Techniques*, vol. 42, no. 2, p. 205, 1994.
- [64] N. M. Ridler and R. G. Clarke, "Investigating connection repeatability of waveguide devices at frequencies from 750 GHz to 1.1 THz," in *82nd ARFTG Microwave Measurement Conference*, 2013.
- [65] "Hewlett-Packard Company, HP 85047 A S-Parameter Test Set," xdevs, May 1992. [Online]. Available:

- www.xdevs.com/doc/HP_Agilent_Keysight/HP%2085047A%20Operating%20Only.pdf. [Accessed 25 July 2022].
- [66] “Advanced Test Equipment Corporation, Gigatronics 7100 Synthesized Signal Generator,” [Online]. Available: <https://www.atecorp.com/products/gigatronics/7100>. [Accessed 25 July 2022].
- [67] “Keysight Technologies, N9010A EXA X-Series Signal Analyzer,” 26 March 2018. [Online]. Available: <https://www.keysight.com/gb/en/assets/7018-01558/data-sheets/5989-6529.pdf>. [Accessed 25 July 2022].
- [68] Z. Cui, *Nanofabrication: Principles, Capabilities and Limits*, Springer, 2016.
- [69] A. Zawadzka and P. Regina, “Limitations of optical lithography on non-planar surfaces,” *Materials Science in Semiconductor Processing*, vol. 143, p. 106548, 2022.
- [70] “RS Components, AAC20, Single-Sided Photoresist Board FR4 Datasheet,” 13 November 2008. [Online]. Available: <https://uk.rs-online.com/web/p/copper-clad-boards/2926932>. [Accessed 1 September 2022].
- [71] E. L. Holzman, “Wideband measurement of the dielectric constant of an FR4 substrate using a parallel-coupled microstrip resonator,” *IEEE transactions on microwave theory and techniques*, vol. 54, no. 7, pp. 3127-3130, 2006.
- [72] “Rogers Corporation, RT/duroid® 5870 Laminates,” 2017. [Online]. Available: <https://rogerscorp.com/-/media/project/rogerscorp/documents/advanced-electronics-solutions/english/data-sheets/rt-duroid-5870---5880-data-sheet.pdf>. [Accessed 14 July 2022].
- [73] “INRF Integrated Nanosystems Research Facility, Dektak 3 Profilometer,” [Online]. Available: <https://www.inrf.uci.edu/facility/equipment/characterization/dektak-3-profilometer/>. [Accessed 1 September 2022].
- [74] A. M. Turing, “Computing machinery and intelligence,” *Mind*, vol. LIX, no. 238, pp. 433–460, 1950.

- [75] N. A. Barricelli, "Esempi numerici di processi di evoluzione," *Methodos*, p. 45–68, 1954.
- [76] N. A. Barricelli, "Symbiogenetic evolution processes realized by artificial methods," *Methodos*, p. 143–182, 1957.
- [77] N. Barricelli, "Numerical testing of evolution theories: Part I: Theoretical introduction and basic tests," *Acta Biotheoretica*, vol. 16, no. 1-2, pp. 69-82, 1962.
- [78] N. Barricelli, "Numerical testing of evolution theories: Part II: Preliminary tests of performance, symbiogenesis and terrestrial life," *Acta Biotheoretica*, vol. 16, no. 3-4, pp. 99-126, 1963.
- [79] D. Fogel, *Evolutionary computation: the fossil record*, Wiley-IEEE Press, 1998.
- [80] A. Fraser, "Simulation of genetic systems by automatic digital computers. I. Introduction," *Aust. J. Biol. Sci.*, vol. 10, no. 4, p. 484–491, 1957.
- [81] G. Box, "Evolutionary operation: A method for increasing industrial productivity," *Applied statistics*, pp. 81-101, 1957.
- [82] A. Maxfield and L. Fogel, "Artificial intelligence through Simulated Evolution," in *Biophysics and Cybernetics Systems: Proceedings of the Second Cybernetics Sciences*, Washington DC, Spartan Books, 1965, pp. 227-298.
- [83] H. Bremermann, M. Rogson and S. Salaff, "Global properties of evolution processes," *Natural automata and useful simulations*, pp. 3-41, 1966.
- [84] G. Hornby, A. Globus, D. S. Linden and J. D. Lohn, "Automated antenna design with evolutionary algorithms," *AIAA Space*, pp. 19-21, September 2006.
- [85] S. C. Panagiotou, S. C. A. Thomopoulos, T. Christos and N. Capsalis, "Genetic Algorithms in Antennas and Smart Antennas Design Overview: Two Novel Antenna Systems for Triband GNSS Applications and a Circular Switched Parasitic Array for WiMax Applications Developments with the Use of Genetic Algorithm," *International Journal of Antennas and Propagation*, December 2014.

- [86] A. Oyama, S. Obayashi and T. Nakamura, "Real-coded adaptive range genetic algorithm applied to transonic wing optimization," *Applied Soft Computing*, vol. 1, no. 3, pp. 179-187, 2001.
- [87] L. Xiao-Lin, J. Feng and H. Zhang, "A genetic algorithm for astroparticle physics studies," *Computer Physics Communications*, vol. 250, pp. 1-7, 2020.
- [88] E. Hedwig, S. O. Lilienfeld and T. Yarkoni, "Using a genetic algorithm to abbreviate the Psychopathic Personality Inventory–Revised (PPI-R)," *Psychological Assessment*, vol. 27, no. 1, p. 194, 2015.
- [89] H. T. Chou, Y. C. Hou and W. J. Liao, "A dual band patch antenna design for WLAN and DSRC applications based on a genetic algorithm optimization," *Electromagnetics*, vol. 27, no. 5, pp. 253-262, 2007.
- [90] M. H. Oktem and B. Saka, "Design of multilayered cylindrical shields using a genetic algorithm," vol. 43, no. 2, p. 170–176, 2001.
- [91] W. P. du Plessis and P. L. D. Abrie, "Lumped impedance matching using a hybrid genetic algorithm," *Microwave and Optical Technology Letters*, vol. 37, no. 3, pp. 210-212, 2003.
- [92] G. C. Onwubolu and B. V. Babu, *New optimization techniques in engineering*. vol. 141, Springer, 2013.
- [93] J. C. Roach, G. Glusman, A. F. Smit, C. D. Huff, R. Hubley, P. T. Shannon, L. Rowen, K. P. Pant, N. Goodman, M. Bamshad and J. Shendure, "Analysis of genetic inheritance in a family quartet by whole-genome sequencing," *Science*, 2010.
- [94] M. Pincus, "An evolutionary strategy," *Journal of Theoretical Biology*, vol. 28, no. 3, pp. 483-488, 1970.
- [95] R. Galar, "Handicapped individua in evolutionary processes," *Biological cybernetics*, vol. 53, no. 1, pp. 1-9, 1985.
- [96] R. Galar, "Global random search with soft selection," *Cybernetics and Systems: Present and Future*, pp. 817-820, 1987.

- [97] R. Galar, "Evolutionary search with soft selection," *Biological Cybernetics*, vol. 60, no. 5, pp. 357-364, 1989.
- [98] V. Fenlon, "Agenoria genetic algorithm," 2020. [Online]. Available: <https://github.com/claudiobalocco/agenoria>. [Accessed 16 February 2021].
- [99] J. McCubbin, V. J. Fenlon and C. Balocco, "Impedance Matching Networks Designed by Evolutionary Algorithms," in *44th International Conference on Infrared, Millimeter, and Terahertz Waves (IRMMW-THz)*, Paris, 2019.
- [100] V. J. Fenlon, M. Cooke, A. Gallant and C. Balocco, "Genetic Algorithms for the Design of THz Components," in *45th International Conference on Infrared, Millimeter, and Terahertz Waves (IRMMW-THz)*, Buffalo, 2020.
- [101] T. A. Milligan, *Modern Antenna Design*, John Wiley & Sons, 2005.
- [102] J. S. Sivia and S. S. Bhatia, "Design of fractal based microstrip rectangular patch antenna for multiband applications," in *Advance Computing Conference (IACC), IEEE International*, 2015.
- [103] S. I. H. Shah, S. Bashir, A. Altaf and S. D. H. Shah, "Compact multiband microstrip patch antenna using defected ground structure (DGS)," *Direct and Inverse Problems of Electromagnetic and Acoustic Wave Theory (DIPED)*, pp. 96-99, 2014.
- [104] A. Sharma, V. K. Dwivedi and G. Singh, "THz rectangular patch microstrip antenna design using photonic crystal as substrate," in *Progress in Electromagnetic Research Symposium*, Cambridge, USA, 2008.
- [105] A. Sharma and G. Singh, "Rectangular microstrip patch antenna design at THz frequency for short distance wireless communication systems," *Journal of Infrared, Millimeter, and Terahertz Waves*, vol. 30, no. 1, pp. 1-7, 2009.
- [106] K. R. Jha and G. Singh, "Microstrip patch array antenna on photonic crystal substrate at terahertz frequency," *Infrared Physics and Technology*, vol. 55, no. 1, pp. 32-39, 2012.

- [107] P. Herrero, J. Martin and S. Joerg, "Planar antennas and interconnection components for 122 GHz and 140 GHz future communication systems," *Frequenz*, vol. 62, no. 5-6, pp. 128-131, 2008.
- [108] Y. I. Chong and D. O. U. Wenbin, "Microstrip series fed antenna array for millimeter wave automotive radar applications," in *IEEE MTT-S International Microwave Workshop Series on Millimeter Wave Wireless Technology and Applications*, 2012.
- [109] G. L. Ramos, F. M. E. Camillo and H. X. Araújo, "Bandwidth Enhancement of a mmWave Microstrip Antenna Array Using a Metamaterial Structure.," in *MOMAG*, 2016.
- [110] C. Lin, C. Chang, Y. T. Cheng and C. F. Jou, "Development of a Flexible SU-8/PDMS-Based Antenna," *IEEE Antennas and wireless propagation letters*, vol. 10, no. 1108-1111, 2011.
- [111] J. T. Alander, "On optimal population size of genetic algorithms," *Proceedings computer systems and software engineering*, pp. 65-70, 1992.
- [112] F. Boschetti, M. C. Dentith and R. D. List, "Inversion of seismic refraction data using genetic algorithms," *Geophysics*, vol. 61, no. 6, pp. 1715-1727, 1996.
- [113] V. K. Koumoussis and C. P. Katsaras, "A saw-tooth genetic algorithm combining the effects of variable population size and reinitialization to enhance performance," *IEEE Transactions on Evolutionary Computation*, vol. 10, no. 1, pp. 19-28, 2006.
- [114] S. Chen, J. Row and K. Wong, "Reconfigurable square-ring patch antenna with pattern diversity," *IEEE Transactions on Antennas and Propagation*, vol. 55, no. 2, pp. 472-475, 2007.
- [115] A. N. da Silva, R. G. de Carvalho and A. G. D'Assunção, "A new technique using axially slotted microstrip line for antenna impedance matching designs," *Journal of Microwaves, Optoelectronics and Electromagnetic Applications*, vol. 18, pp. 208-218, 2019.
- [116] "Kayaku Microchem, SU-8 2000 Permanent Negative Epoxy Photoresist," [Online]. Available: <https://kayakuam.com/products/su-8-2000/>. [Accessed 25 July 2022].

- [117] “Virginia Diodes, Inc., VDI Waveguide Designations 2015.01 -WR – Frequency Multipliers (WR and D Series),” 2015.
- [118] A. K. Klein, A. Basden, J. Hammler, L. Tyas, M. Cooke, C. Balocco, D. Zeze, J. M. Girkin and A. Gallant, “Scattering of spoof surface plasmon polaritons in defect-rich THz waveguides.,” *Scientific reports*, vol. 9, no. 1, pp. 1-8, 2019.
- [119] P. I. C. Claro, A. R. S. Neto, A. C. C. Bibbo, L. H. C. Mattoso, M. S. R. Bastos and J. M. Marconcini, “Biodegradable blends with potential use in packaging: A comparison of PLA/chitosan and PLA/cellulose acetate films.,” *Journal of Polymers and the Environment*, vol. 24, no. 4, pp. 363-371, 2016.
- [120] B. Bowers, “Inventors of the Telegraph,” *Proceedings of the IEEE*, vol. 90, no. 3, pp. 436-439, March 2002.
- [121] F. Feng, Y. Jung, H. Zhou, R. Zhang, S. Chen, H. Wang, Y. Yang, S. U. Alam, D. J. Richardson and T. D. Wilkinson, “High-order mode-group multiplexed transmission over a 24km ring-core fibre with OOK modulation and direct detection.,” in *2017 European Conference on Optical Communication (ECOC)*, 2017.
- [122] D. C. Daly and A. P. Chandrakasan, “An Energy-Efficient OOK Transceiver for Wireless Sensor Networks,” *IEEE Journal of Solid-State Circuits*, vol. 42, no. 5, pp. 1003-1011, 2007.
- [123] J. Bohorquez, A. Chandrakasan and J. Dawson, “A 350 μ W CMOS MSK Transmitter and 400 μ W OOK Super-Regenerative Receiver for Medical Implant Communications,” *IEEE Journal of Solid-State Circuits*, vol. 44, no. 4, pp. 1248-1259, 2009.
- [124] H. Lee, J. Lee, C. Lee, T. Jang, H. Kim and C. Park, “High-speed and low-power OOK CMOS transmitter and receiver for wireless chip-to-chip communication,” in *IEEE MTT-S International Microwave Workshop Series on Advanced Materials and Processes for RF and THz Applications (IMWS-AMP)*, 2015.
- [125] TDK, “SAW Components: B3722,” 10 December 2012. [Online]. Available: https://www.mouser.com/datasheet/2/842/tdkc_s_a0001072838_1-2295288.pdf.
- [126] “MACOM Technology Solutions, ETC1.6-4-2-3 Transformer,” [Online]. Available: www.mouser.co.uk/ProductDetail/MACOM/ETC16-4-2-

3TR?qs=zQS7eqYV0KQEQp5tpaMokg%3D%3D&gclid=Cj0KCQjwxIOXBhCrARIsAL1QFCYi34I1laIX_ChvMaY4otnDJiKx3WRI8Mn7xDIO11hK82Dq6vb54_QaAsgjEALw_wcB.

- [127] A. Devices, "65 dB TruPwr™ Detector AD8362," 2015. [Online]. Available: <https://www.analog.com/en/products/ad8362.html?doc=ad8362.pdf>.
- [128] A. M. Street, "RF switch design," *IEE Training Course How to Design RF Circuits*, pp. 1-7, 2000.
- [129] P. Chevalier, A. Amirzhan, F. Wang, M. Piccardo, S. Johnson, F. Capasso and H. Everitt, "Widely tunable compact terahertz gas lasers," *Science*, vol. 366, no. 6467, pp. 856-860, 2019.
- [130] I. Mehdi, G. Chattopadhyay, E. Schlecht, J. Ward, J. Gill, F. Maiwald and A. Maestrini, "Terahertz multiplier circuits," *2006 IEEE MTT-S International Microwave Symposium Digest*, pp. 341-344, 2006.
- [131] J. L. H. H. X. A. W. L. a. R. M. W. L. Liu, "A Broadband Quasi-Optical Terahertz Detector Utilizing a Zero Bias Schottky Diode," *IEEE Microwave and Wireless Components Letters*, vol. 20, no. 9, pp. 504-506, 2010.
- [132] R. H. e. al., "Active Terahertz Imaging Using Schottky Diodes in CMOS: Array and 860-GHz Pixel," *IEEE Journal of Solid-State Circuits*, vol. 48, no. 10, pp. 2296-2308, 2013.
- [133] L. E. D. D. W. a. C. B. D. Etor, "An Ultrathin Organic Insulator for Metal–Insulator–Metal Diodes," *IEEE Transactions on Electron Devices*, vol. 63, no. 7, pp. 2887-2891, 2016.
- [134] J. e. a. Jin, "Metal-insulator-metal diodes based on alkyltrichlorosilane self-assembled monolayers," *AIP Advances*, vol. 9, no. 6, 2019.
- [135] "Broadcom / Avago HSMS-2852-BLKG," Mouser Electronics, 2022. [Online]. Available: <https://www.mouser.co.uk/ProductDetail/Broadcom-Avago/HSMS-2852-BLKG?qs=RQ9zk%252B50r5EwS8JI7M2U0A%3D%3D>. [Accessed 3 August 2022].

- [136] Farnell, "HSMS-2829-BLKG," 12 January 2017. [Online]. Available: https://uk.farnell.com/broadcom/hsms-2829-blkg/diode-rf-sch-cro-ov-quad-15v-sot143/dp/1843077?CMP=KNC-GUK-GEN-KWL-MAN-L5Pages-New-Structure-Control731-CatchAll&mckv=_dc|pcrid|517389657283|&gclid=EAlaIqobChMIqKbn-fqw9AIV4IBQBh3FFA_yEAAYASAAEgLU_D_BwE. [Accessed 3 August 2022].
- [137] "Skyworks Solutions, Inc. SMS7630-079LF," Mouser Electronics, 2022. [Online]. Available: <https://www.mouser.co.uk/ProductDetail/Skyworks-Solutions-Inc/SMS7630-079LF?qs=WMHGlxXAKT%2Fg1qGRez3v%252Bg%3D%3D>. [Accessed 3 August 2022].
- [138] D. M. Pozar, "Microwave Filters," in *Microwave Engineering*, John Wiley & Sons, Inc., 2012, pp. 380-450.
- [139] I. E. Obuh, *Low-Cost Fabrication Techniques for RF Microelectromechanical systems (MEMS) Switches and Varactors*, 2018.
- [140] D. T. Young and J. C. Irvin, "Epitaxial Diodes with a Novel Contacting Technique," *Proceedings of the IEEE*, pp. 2130-2131, 1965.
- [141] H. R. Fetterman, B. J. Clifton, P. E. Tannenwald, C. D. Parker and H. Penfield, "Submillimeter Heterodyne Detection and Harmonic Mixing Using Schottky Diodes," *IEEE Transactions on Microwave Theory and Techniques*, vol. 22, no. 12, pp. 1013-1015, 1974.
- [142] W. L. Bishop, K. McKinney, R. J. Mattauch, T. W. Crowe and G. Green, "A Novel Whiskerless Schottky Diode for Millimeter and Submillimeter Wave Application," *1987 IEEE MTT-S International Microwave Symposium Digest*, pp. 607-610, 1987.
- [143] I. Mehdi, J. V. Siles, C. Lee and E. Schlecht, "THz diode technology: Status, prospects, and applications," *Proceedings of the IEEE*, vol. 105, no. 6, pp. 990-1007, 2017.
- [144] "ECO Frequency Information System," European Communications Office, [Online]. Available: <https://efis.cept.org/>. [Accessed 11 October 2022].

- [145] D. Hou, J. Chen, P. Yan and W. Hong, "A 270 GHz× 9 multiplier chain MMIC with on-chip dielectric-resonator antenna," *IEEE Transactions on Terahertz Science and Technology*, vol. 8, no. 2, pp. 224-230, 2018.
- [146] K. Sekine, T. Hagiwara, K. Takano, S. Hara, A. Kasamatsu and Y. Umeda, "A 270 GHz CMOS Doubler-Based Up-Conversion Mixer with Output Amplitude Imbalance Detection," in *2021 IEEE International Symposium on Radio-Frequency Integration Tech*, 2021.
- [147] M. Wehbi, M. Margalef-Rovira, C. Durand, S. Lepilliet, A. L. Serrano and P. Ferrari, "Dual-Band Patch Filter 180/270 GHz on BiCMOS 55nm," in *2022 IEEE/MTT-S International Microwave Symposium-IMS 2022*.
- [148] "Kayaku Microchem, SU-8 3000 Permanent Epoxy Negative Photoresist," [Online]. Available: <https://kayakuam.com/products/su-8-3000/>. [Accessed 25 July 2022].
- [149] kayakuAM, "SU-8 3000 Technical Data Sheet," July 2020. [Online]. Available: <https://kayakuam.com/wp-content/uploads/2020/07/KAM-SU-8-3000-Datasheet-7.10-final.pdf>. [Accessed 20 February 2022].
- [150] G. Plastics, "What is Acetate?," Grafix Plastics, 2022. [Online]. Available: https://www.grafixplastics.com/grafix-plastics/plastic-film-plastic-sheet-faq/acetate_what/. [Accessed 20 February 2022].